

DESIGN OF PASSIVE MICROMIXERS IN MICROFLUIDIC SYSTEMS: A COMPUTATIONAL STUDY

A Dissertation
Presented to
The Academic Faculty

by

Mahmut Burak Okuducu

In Partial Fulfillment
of the Requirements for the Degree
Doctor of Philosophy in the
School of Civil and Environmental Engineering

Georgia Institute of Technology
December 2020

COPYRIGHT © 2020 BY MAHMUT BURAK OKUDUCU

DESIGN OF PASSIVE MICROMIXERS IN MICROFLUIDIC SYSTEMS: A COMPUTATIONAL STUDY

Approved by:

Dr. Mustafa M. Aral, Advisor
School of Civil and Environmental
Engineering
Georgia Institute of Technology

Dr. Xing Xie
School of Civil and Environmental
Engineering
Georgia Institute of Technology

Dr. Sotira Yiacoumi
School of Civil and Environmental
Engineering
Georgia Institute of Technology

Dr. Sven Simon
School of Earth and Atmospheric
Sciences
Georgia Institute of Technology

Dr. Yongsheng Chen
School of Civil and Environmental
Engineering
Georgia Institute of Technology

Date Approved: 08/06/2020

This dissertation is dedicated to my nieces, Hatice Buglem and Elif Asel. Thank you for your unconditional love.

ACKNOWLEDGEMENTS

First and most importantly, I would like to thank my thesis Advisor, Dr. Mustafa M. Aral, without whose never-ending support and guidance I could not achieve my academic goals. During the time that I spent with Dr. Aral, not only have I gained experience in my research field, but also I have broadened my horizons in life. I would like to sincerely express that it has always been an honor for me to know Dr. Aral and to be able to work with him. I also would like to thank my Ph.D. Advisory Committee members, Dr. Sotira Yiacoumi, Dr. Yongsheng Chen, Dr. Xing Xie, and Dr. Sven Simon for both instructive lecture times and their constructive comments in my Ph.D. study. My gratitude also goes to my best friends, Dr. Yasemin Kaya and Mustafa Cevher Unuz, for their consistent emotional support during my education at GaTech.

TABLE OF CONTENTS

ACKNOWLEDGEMENTS	iv
LIST OF TABLES	vii
LIST OF FIGURES	viii
SUMMARY	xvii
CHAPTER 1. INTRODUCTION	1
1.1 Background	1
1.2 Motivation and Objectives	7
1.3 Thesis Scheme	11
CHAPTER 2. LITERATURE REVIEW	13
2.1 Introduction	13
2.2 Passive Mixing and Micromixer Designs	13
2.3 False Diffusion Effects in Numerical Passive Micromixer Studies	22
2.4 Materials and Fabrication	29
CHAPTER 3. MATHEMATICAL-NUMERICAL METHODS and SIMULATION DEFINITIONS USED	31
3.1 Introduction	31
3.2 Mathematical Modelling of Fluid Flow and Passive Scalar Transport in Microchannels	31
3.3 Dimensionless Numbers	34
3.4 Simulation Setup and Numerical Solution of Governing Equations	36
3.5 Quantification of The Degree of Mixing in Micromixers	42
3.6 Mesh Refinement Study and Quantification of Numerical Diffusion Errors	45
3.7 Validation Studies	50
3.8 Summary	53
CHAPTER 4. NUMERICAL DIFFUSION ERROR ANALYSIS IN NUMERICAL SIMULATIONS OF PASSIVE MICROMIXERS	55
4.1 Introduction	55
4.2 Background	57
4.3 Qualitative Description of The Numerical Diffusion Problem in FVM	60
4.4 Computational Evaluation of Numerical Diffusion Errors for Different Mesh Types, Discretization Schemes and Numerical Techniques in A 3-D T-Shape Passive Micromixer	65
4.4.1 Micromixer design and case setup	65

4.4.2	Results and discussion	70
4.4.3	Conclusions	104
4.5	Computational Evaluation of Numerical Diffusion Errors for Different Grid Levels of Hexahedron Element Type and Peclet Number Scenarios in 3-D Swirl-Generating Passive Micromixers	106
4.5.1	Micromixer design and case setup	106
4.5.2	Results and discussion	109
4.5.3	Conclusions	129
CHAPTER 5.	NOVEL 3-D T-SHAPED PASSIVE MICROMIXER DESIGN WITH HELICOIDAL FLOWS	132
5.1	Introduction	132
5.2	Micromixer Design for Helicoidal Flow Generation	133
5.3	Case Setup	134
5.4	Results and Discussion	136
5.4.1	Grid study	136
5.4.2	Classical-T (CT) micromixer	139
5.4.3	Convex Semi-Circular-Ridge (CSCR) Micromixer	144
5.4.4	Alternative micromixer configurations	156
5.4.5	Discussion	159
5.5	Conclusions	161
CHAPTER 6.	NOVEL 3-D FLUID OVERLAPPING PASSIVE MICROMIXER DESIGN	164
6.1	Introduction	164
6.2	Overlapping Micromixer Design	165
6.3	Case Setup	168
6.4	Results and Discussion	170
6.4.1	Grid study	170
6.4.2	Fluid mixing in the CSFO–A and CSFO–B micromixer configurations	173
6.4.3	Fluid mixing in the CSFO–C micromixer configuration	180
6.4.4	Discussion	184
6.5	Conclusions	188
CHAPTER 7.	CONCLUSIONS AND FUTURE WORK	190
7.1	Conclusions	190
7.1.1	False diffusion errors in numerical passive micromixer studies	191
7.1.2	The convex semi-circular-ridge (CSCR) passive micromixer design	193
7.1.3	The circular-shaped fluid overlapping (CSFO) passive micromixer design	194
7.2	Recommendations for Future Works	195
APPENDIX A.	PUBLISHED ARTICLES	197

LIST OF TABLES

Table 3.1	Boundary conditions and physical fluid properties.....	38
Table 3.2	Simulation parameters employed in CFD solver validation.	51
Table 4.1	Test cases and simulation parameters for hexahedral, prism, and tetrahedral mesh configurations.	68
Table 4.2	Mesh properties and grid study results for $Re = 100$ case.	72
Table 4.3	Estimated prism and tetrahedron element numbers in the computational domain to reach predetermined thresholds of false mixing and numerical diffusion when $Re = 100$ and $Pe = 3.33 \times$ 10^5	91
Table 4.4	Comparisons of numerical (D_N), effective (D_E), and molecular diffusion (D_M) constants with respect to L1 level of all mesh types and Re scenarios.....	93
Table 4.5	Mesh properties and densities for six different levels.....	108
Table 4.6	Test cases for two-inlet and four-inlet micromixer designs.....	109
Table 4.7	Numerical (D_N) and effective (D_E) diffusion constants for different micromixer designs, flow scenarios, and mesh densities when $D_M =$ $3 \times 10^{-10} \text{ m}^2/\text{s}$	122
Table 5.1	Fluid flow and passive scalar transport test scenarios.	135
Table 5.2	Mesh properties tested in grid study.	137
Table 6.1	Fluid flow and passive scalar transport test scenarios.	170
Table 6.2	Mesh properties used in the grid study.	171
Table 6.3	The comparison of the CSFO–A configuration with the micromixers reported in the literature in terms of mixing performance in very low flow conditions ($Re < 10$).	185

LIST OF FIGURES

Figure 2.1 Enhancement of contact surface area in molecular diffusion-based passive micromixer designs. Red and blue line arrows represent different fluids. Green color shows the contact surface and diffusive interaction between different fluids.	15
Figure 2.2 Typical passive micromixer designs. All designs have a height perpendicular to the plane. Red and blue line arrows represent different fluids in the inlet channels. Green line arrows represent mixed fluids at the outlet.	17
Figure 3.1 Uniform and non-uniform distribution of scalar concentration in a parabolic velocity profile.	44
Figure 3.2 Classical T-shaped (CT) passive micromixer design.	51
Figure 3.3 Outlet mixing efficiency vs. Re number, obtained from the experimental studies and numerical simulations.	52
Figure 3.4 The distribution of scalar concentration at the outlet of the CT passive micromixers obtained from numerical simulations.	53
Figure 4.1 Schematic description of numerical diffusion and dispersion errors for a pure advection scalar transport in a classical T-shape passive micromixer.	58
Figure 4.2 Transported scalar distributions in different grid-flow alignment conditions of the 2-D test: (a) square elements with 45° flow angle; (b) square elements with 0° flow angle (orthogonal); and (c) triangular elements with randomly changing flow-boundary angle.	62
Figure 4.3 Transported scalar distributions in different grid-flow alignment conditions of the extended 2-D test case for multi-inlet scenarios: (d) square elements with 45° flow angle; (e) square elements with 0° flow angle (orthogonal); (f) and (g) triangular elements with randomly changing flow-boundary angle with imposed flow fields $(u, v) = (0.01 \text{ m/s}, 0.01 \text{ m/s})$ and $(0.01 \text{ m/s}, 0)$ respectively.	65

Figure 4.4 3-D view of T-shape passive micromixer.....	66
Figure 4.5 3-D mesh element types and orientations in the computational domains: (a) Hexahedron; (b) Prism; (c) Tetrahedron.	67
Figure 4.6 Flow profile at the beginning of mixing channel (Figures show the region between $x = 0$ and $500 \mu\text{m}$ and $y = 250$ and $-250 \mu\text{m}$): (a) Separated (or stratified) flow at $\text{Re} = 0.1$; (b) Periodic (or Vortex) flow at $\text{Re} = 100$	69
Figure 4.7 Velocity profile at four different cross-sections in the mixing channel (i.e., $x = 100, 200, 500$, and $1000 \mu\text{m}$). All planes are normal to the x-direction and color ranges were set to that of $x = 200 \mu\text{m}$ plane: (a) $\text{Re} = 0.1$; (b) $\text{Re} = 100$	70
Figure 4.8 Velocity distribution on the yz-plane at $x = 200 \mu\text{m}$ (on the dashed line arrow I in Figure 4.4) from L1, L2, L3, and L4 mesh level simulations: (a) Hexahedral; (b) Prism; (c) Tetrahedral; (d) Hexahedral vs. Prism vs. Tetrahedral solutions at L1 mesh level.	73
Figure 4.9 Grid study results for different mesh structures (i.e., hexahedral, prism, and tetrahedral) and grid levels (i.e., L1, L2, L3, and L4): (a) maximum velocity magnitude (u_{max}) on the yz-plane at $x = 200 \mu\text{m}$; (b) pressure drop (Δp) in the micromixer; (c) and (d) difference between mesh levels when u_{max} and Δp are employed as the flow parameters respectively.....	74
Figure 4.10 Difference between mesh levels (L2, L3, and L4) with respect to the finest mesh level (L1) when u_{max} is the parameter vs. total mesh element number difference between mesh levels compared.....	75
Figure 4.11 Grid study results when outlet mixing efficiency is the parameter: (a) outlet MI of hexahedral, prism, and tetrahedral mesh types at L1, L2, L3, and L4 mesh levels; (b) Difference between mesh levels (L2, L3, and L4) with respect to the finest mesh level (L1) when MI is the parameter.....	78
Figure 4.12 Transported scalar distributions at the outlet of the T-shape micromixer for all mesh configurations ($\text{Re} = 100$).....	79

Figure 4.13 Grid study results between grid levels (L4, L3, and L2) with respect to the finest grid (i.e., L1) for MI vs. total mesh element number difference between grid levels and the finest grid.	81
Figure 4.14 Outlet scalar distributions along the width of the mixing channel at $z = 50 \mu\text{m}$ (on the dashed line arrow II in Figure 4.4) for L1 level of all mesh types at $\text{Re} = 100$ scenario.	85
Figure 4.15 Numerical and effective diffusions in L1, L2, L3, and L4 mesh levels of hexahedral, prism, and tetrahedral mesh structures: (a) numerical diffusion vs. MI; (b) effective diffusion vs. MI; (c) physical diffusion masking.	88
Figure 4.16 Change of numerical diffusion and false mixing with mesh density: (a) hexahedral; (b) prism; (c) tetrahedral.	91
Figure 4.17 The change of numerical and effective diffusion with Re number at L1 level of hexahedral, prism, and tetrahedral mesh structures: (a) numerical diffusion vs. Re; (b) effective diffusion vs. Re.	93
Figure 4.18 The change of outlet MI with respect to numerical and effective diffusion approximations at L1 level of all mesh structures and all Re scenarios: (a) numerical diffusion vs. MI; (b) effective diffusion vs. MI. Inserted numbers on the data points show corresponding Re numbers.	95
Figure 4.19 Velocity distributions on the yz-plane at $x = 200 \mu\text{m}$ (on the dashed line arrow I in Figure 4.4) in $\text{Re} = 100$ scenario: (a) FEM solutions of hexahedral mesh levels (i.e., L1, L2, L3, and L4); (b) comparison of FEM and FVM at L1 level of hexahedral mesh.	99
Figure 4.20 Outlet scalar distributions along the width of the outlet at $z = 50 \mu\text{m}$ (on the dashed line arrow II in Figure 4.4) for L1, L2, L3, and L4 levels of hexahedral mesh ($\text{Re} = 100$ and $\text{DM} = 3 \times 10^{-10} \text{ m}^2/\text{s}$): (a) FEM solution with consistent stabilization; (b) FVM solution.	100
Figure 4.21 Outlet scalar distributions along the width of the outlet at $z = 50 \mu\text{m}$ (on the dashed line arrow II in Figure 4.4) for L1, L2, L3, and L4 levels of hexahedral mesh ($\text{Re} = 100$ and $\text{D}_\text{M} = 3 \times 10^{-10} \text{ m}^2/\text{s}$).	

FEM solutions with inconsistent stabilization: (a) $\delta = 0.25$; (b) $\delta = 0.50$	101
Figure 4.22 Comparison of FVM and FEM simulations at $Re = 100$ ($D_M = 3 \times 10^{-10} \text{ m}^2/\text{s}$): (a) outlet scalar distributions along the width of the outlet at $z = 50 \text{ }\mu\text{m}$ (on the dashed line arrow II in Figure 4.4) for L1 level of hexahedral mesh; (b) MI at the outlet for L1, L2, L3, and L4 levels of hexahedral mesh.	102
Figure 4.23 Comparison of FVM and FEM simulations at $Re = 0.1$ ($D_M = 3 \times 10^{-10} \text{ m}^2/\text{s}$): (a) outlet scalar distributions along the width of the outlet at $z = 50 \text{ }\mu\text{m}$ (on the dashed line arrow II in Figure 4.4) for L1 level of hexahedral mesh; (b) MI (%) values at the outlet.	104
Figure 4.24 Swirl-generating passive micromixers: (a) four-inlet design and (b) two-inlet design. Dashed arrow lines I, II, III, and IV are edge-to-edge on the x-y plane at different z-heights; $z = 100, 500, 1000$, and $2000 \text{ }\mu\text{m}$ respectively.	107
Figure 4.25 Orientation of structured hexahedron mesh elements in the computational domains.	108
Figure 4.26 Grid study results for fluid flow: (a) and (b) pressure drop (Δp) in micromixers at $Re = 240$ and 120 for four-inlet and two-inlet designs respectively; (c) and (d) velocity distribution on x-y plane at the exit of mixing box (Line-I in Figure 3) at $Re = 240$ for four-inlet and two-inlet designs respectively.	110
Figure 4.27 Grid study results for scalar transport at $Re = 240$: (a) and (c) concentration distribution on x-y plane at the exit of the mixing box (Line-I in Figure 4.24) for four-inlet and two-inlet designs respectively; (b) and (d) concentration distribution on x-y plane at $z = 500 \text{ }\mu\text{m}$ (Line-II in Figure 4.24) for four-inlet and two-inlet designs respectively.	112
Figure 4.28 Grid study results for scalar transport at $Re = 120$: (a) and (c) concentration distribution on x-y plane at the exit of the mixing box (Line-I in Figure 4.24) for four-inlet and two-inlet designs	

respectively; (b) and (d) concentration distribution on x-y plane at $z = 500 \mu\text{m}$ (Line-II in Figure 4.24) for four-inlet and two-inlet designs respectively.	113
Figure 4.29 Mixing index (MI) values of different cross-sections along the mixing channel: (a) and (c) four-inlet and two-inlet designs at $Re = 240$ respectively; (b) and (d) four-inlet and two-inlet designs at $Re = 120$ respectively. Numbers above trendlines show x-axis values in plots.	115
Figure 4.30 Comparison of mesh levels (L2, L3, L4, L5, and L6) with L1 using at different heights in the mixing channel ($z = 500, 1000, \text{ and } 2000 \mu\text{m}$): (a) and (c) four-inlet and two-inlet designs at $Re = 240$ respectively; (b) and (d) four-inlet and two-inlet designs at $Re = 120$ respectively.	115
Figure 4.31 Fluid flow and scalar transport domains in the mixing channel of the four-inlet design: (a) $Re = 240$ (left two shapes) and (b) $Re = 120$ (right two shapes). Colored images show passive scalar transport solutions at the L1 mesh level.	117
Figure 4.32 Fluid flow and scalar transport domains in the mixing channel of two-inlet design: (a) $Re = 240$ (left two shapes) and (b) $Re = 120$ (right two shapes). Colored images show passive scalar transport solutions at the L1 mesh level.	119
Figure 4.33 Central plane of mixing box at $z = 50 \mu\text{m}$: (a) Four- and two-inlet micromixer designs at $Re = 240$ and (b) four- and two-inlet micromixer designs at $Re = 120$. Arrows in dashed rectangles show velocity vectors on the plane colored by scalar values. Colored images show passive scalar transport solution at the L1 mesh level.	120
Figure 4.34 Flow profile and multi-layer mixing structure in the mixing box of two-inlet design: (a) $Re = 240$ and (b) $Re = 120$. Colored images show passive scalar transport solution at the L1 mesh level.	121

Figure 4.35 Normalized effective diffusion constant vs. mesh levels: (a) D_E/D_M and (b) D_E/D_N . The numbers above and below the trend lines show Pe_Δ numbers for corresponding mesh levels and flow conditions.	123
Figure 4.36 The ratio of D_E/D_M vs. mesh levels (L1, L3, and L6): (a) and (c) four-inlet and two-inlet designs at $Re = 240$ respectively; (b) and (d) four-inlet and two-inlet designs at $Re = 120$ respectively. The semicolon-separated numbers above the trend lines (corresponding to line color) show Pe_Δ numbers (left) and y-axis values (right) for mesh levels.	126
Figure 4.37 Scalar concentration distribution on the x-y plane at $z = 500 \mu m$ (Line-II in Figure 4.24) for four-inlet design at $Re = 240$: (a) $D_M = 3 \times 10^{-10} m^2/s$ and (b) $D_M = 6 \times 10^{-8} m^2/s$	128
Figure 5.1 3-D micromixer geometries (a) Classical-T (CT) micromixer; (b) Convex semi-circular-ridge (CSCR) micromixer. Diagonal dashed line arrows I and II are on the y-z plane at $x = 100$ and $2000 \mu m$, respectively.	134
Figure 5.2 Inlet types, injection modes, and 2-D micromixer geometries.	136
Figure 5.3 Grid study outcomes: (a) difference (%) between mesh levels for the parameters tested; (b) development of mixing on different y-z cross-sections along the mixing channel; (c) and (d) velocity and concentration distributions at the exit, respectively (dashed line arrow II in Figure 5.1).	139
Figure 5.4 Flow regimes in the CT micromixer: separated, vortex, and engulfment. Blue and red colors are used to differentiate flow pathlines in inlet A and inlet B.	140
Figure 5.5 (a) Pressure drop vs. Re number in CT micromixer. The numbers before and after the semicolons represent Re number and pressure drop values, respectively; (b) MI vs. Re number for different molecular diffusion coefficients in CT-FI-RI.	141

Figure 5.6 MI vs. Re for CT-HS-AI, CT-HS-SI, CT-VS-AI, and CT-VS-SI micromixer configurations and D_1 , D_2 , and D_3 molecular diffusion scenarios.....	143
Figure 5.7 Outlet concentration distributions in CT-HS-AI, CT-HS-SI, CT-VS-AI, and CT-VS-SI micromixer configurations for D_1 molecular diffusion constant.	144
Figure 5.8 Helicoidal fluid flow in the mixing channel at $Re = 40$. Yellow and green colors show fluids, injected from inlet A and inlet B, respectively. Fluids, travelling in the lower and upper height of the inlet channel, are represented by blue and red curvy arrows, respectively.	146
Figure 5.9 Concentration distributions in the mixing channel for the CSCR-VS-AI configuration ($D = D_1$). Plane 1 and 8 represent cross-sections at $x = 100 \mu m$ and at the outlet, respectively. Planes from 2 to 7 show the cross-sections, $30 \mu m$ after the center of odd-number semi-circular ridges starting from the confluence region. All planes are normal to the x-direction.....	147
Figure 5.10 Pressure drop, Δp (kPa) vs. Re number in the CSCR micromixer. The numbers before and after the semicolons represent Re number and pressure drop values, respectively.....	148
Figure 5.11 Mixing index vs. Re number for different inlet and injection configurations of the CSCR micromixer.....	150
Figure 5.12 The utilization of rotational fluid flow depending on the splitting type ($Re = 5$ and $D = D_1$).	150
Figure 5.13 Concentration distributions at the outlet of the CSCR micromixer configurations examined ($D = D_1$).	152
Figure 5.14 (a) and (b) the ratio of mixing index and mixing performance, respectively. Mixing values, obtained from CSCR-VS-AI micromixer, are normalized by that of CT-VS-AI; (c) and (d) the development of mixing index along the mixing channel for CSCR-VS-AI and CT-VS-AI configurations, respectively ($D = D_2$).	154

Figure 5.15 Scalar concentration distributions on the x-y plane at $z = 50 \mu\text{m}$ in CSCR-VS-AI (left) and CT-VS-AI (right) micromixer configurations for all the Re scenarios simulated ($D = D_1$). All planes are normal to the z-direction. In each plane, y-direction is shown between $y = +200 \mu\text{m}$ and $y = -200 \mu\text{m}$	155
Figure 5.16 Alternative micromixer configurations with semi-circular (i.e., A, B, and C) and rectangular (i.e., D) ridges. Top and side views of the mixing channels (left). Outlet concentration distributions at $Re = 20$ and 40 for corresponding micromixer configurations (right).	158
Figure 5.17 Alternative fluid injection types in the CSCR passive micromixer. Red and blue colors show different fluids.....	160
Figure 5.18 Parametric study outcomes for the CSCR-VS-AI micromixer configuration at $Re = 40$. Central values are the actual dimensions that are used in the CSCR micromixer design.	161
Figure 6.1 3-D CSFO micromixer geometry.	166
Figure 6.2 Injection types tested in the CSFO micromixer design.	167
Figure 6.3 Circular and rectangular nested-type inlet structures.	168
Figure 6.4 Alternative injection scenarios and distribution of fluids in microchannels.	168
Figure 6.5 Grid study outcomes and the change of pressure drop in the CSFO micromixer: (a) difference, as a percentage, between L1 and L2, L3, L4 mesh densities with respect to Δp and MI parameters; (b) velocity distribution on the diameter of outlet cross-section obtained from L1, L2, L3, and L4 mesh level solutions; (c) development of mixing efficiency along the CSFO micromixer in L1, L2, L3, and L4 mesh solutions. MI values are computed on E1, E2, E3, E4, and E5 cross-sections which are normal to the z-direction; (d) Δp vs. Re number in the CSFO micromixer.	171
Figure 6.6 Flow pathlines on the yz-plane at the center of the CSFO micromixer (center) and 3-D flow domain in the CSFO micromixer	

(left and right). Red and blue colors show the fluids injected from core and outer inlets, respectively.	174
Figure 6.7 The distribution of injected fluids in the mixing units of the micromixer configurations (a) CSFO–A; (b) CSFO–B; and (c) CSFO–C. The dashed lines and curves show the contact surfaces formed between different fluids. Red and blue colors represent the fluids injected from core and outer inlets, respectively. Black arrows show flow directions.	175
Figure 6.8 The development of MI along the CSFO–A and CSFO–B micromixer configurations for all flow conditions (i.e., $Re = 0.1, 0.5, 1, 5,$ and 10) and molecular diffusion constants ($D_1, D_2,$ and D_3). MI values are calculated on the E1, E2, E3, E4, and E5 cross-sections which are normal to the z -direction.	178
Figure 6.9 The distribution of scalar concentrations on the outlets of CSFO–A (first three columns on the left) and CSFO–B (last three columns on the right) micromixer configurations.	179
Figure 6.10 The development of fluid mixing along the CSFO–A micromixer configuration for all flow scenarios of D_1 diffusion constant. Planes show the distribution of scalar concentration. E1, E2, E3, E4, and E5 show exit cross-sections which are normal to the z -direction.	180
Figure 6.11 The development of fluid mixing with respect to time at the exit of mixing units in the CSFO–C micromixer configuration when $Re = 1, 5,$ and 10 and $D = D_1, f = 0$ Hz plots (first row) show time-dependent solutions of CSFO–A micromixer. MI values are calculated on the E1, E2, E3, E4, and E5 cross-sections which are normal to the z -direction.	183
Figure 6.12 The distribution of fluids in a single mixing unit when the entire inlet surface is used to inject fluids sequentially.	187
Figure 6.13 The distribution of flow vectors and flow pathlines in single–mixing–box circular and square design configurations ($Re = 10$).	188

SUMMARY

In microfluidic systems, passive micromixers are employed to mix at least two fluids homogeneously exploiting the fluid flow energy in microchannels. In these microscale mixing units, strictly laminar fluid flow that is Reynolds (Re) $\ll 100$ and very low molecular diffusion constants—typically in the range of 10^{-9} – 10^{-11} m^2/s —fundamentally create tough conditions in terms of both yielding a high mixing efficiency over a short distance and controlling false diffusion errors in numerical simulations. In passive micromixers, developing special geometric designs are essential to increase mixing performance and reduce mixing length. In the current literature, although various passive micromixer configurations are proposed, the improvement of mixing in these designs is usually possible compromising at least one of the following criteria: short mixing length, low energy requirement, and design simplicity in terms of fabrication. Besides, in numerical passive micromixer investigations, the magnitude of false diffusion errors is usually disregarded or underestimated. Evaluation of the degree of mixing in these devices without appropriate analysis of the contribution of false diffusion cause over estimation of mixing performance. The objective of this research is to characterize the extent of false diffusion errors in numerical simulations of microscale mixing systems and develop efficient three-dimensional micromixer designs in which all the above standards are ensured in tandem.

In the first part of the study, a comprehensive research is performed on false diffusion errors in numerical simulations of passive micromixers. The effect of false diffusion is investigated in both simple unidirectional and complex three-dimensional fluid

flow conditions. Several test scenarios are established to monitor and quantify the extent of false diffusion generation in numerical solutions. It is shown that the scalar transport simulations produce considerably high numerical errors compared to the numerical solution of the flow field. Thus, the use of flow parameters in grid studies should be avoided. Instead, mixing efficiency needs to be employed as the parameter to show the actual discrepancy between different grid levels and to determine a feasible grid size that is computationally inexpensive and produces insignificant amount of false diffusion. Moreover, the difference between mesh densities should be high enough to be able to expose false diffusion errors accurately. The simulation results of different numerical algorithms show that while Finite Element Method (FEM) and Finite Volume Method (FVM) resolve the flow domain almost identically, both numerical techniques exhibit different false diffusion generation inclination in scalar transport simulations. In FVM, false diffusion errors are reduced substantially when the flow vectors are orthogonal to the cell faces in the computational domain. Hence, the lowest numerical diffusion errors are observed in cases where the flow is unidirectional in the micromixer and hexahedron mesh elements are used. When prism and tetrahedral mesh structures are applied, the physical effect of the molecular diffusion constant tested is overshadowed by false diffusion errors that are generated during the numerical solution of advection diffusion (AD) equation. In complex fluid flow conditions, even though computational domain is discretized with hexahedron elements, contribution of additional dimensions inherently prevent retaining a good mesh flow alignment in micromixers. Thus, the continuous violation of orthogonality in such flow regimes causes generating high amount of false diffusion in numerical solutions which in turn masks the physical effects of molecular diffusion and increase the

performance of micromixer unphysically. In FEM, the selection of an appropriate stabilization type, which is used to suppress the oscillations in the simulations, is crucial to control the false diffusion in numerical solutions. It is found that consistent stabilization option manages false diffusion generation successfully and provide almost identical outcomes with FVM whereas artificial stabilization approach offers a stable solution at a cost of excess unphysical diffusion in numerical solutions.

In the second part of the study, fluid mixing in 3-D classical T-shaped (CT) passive micromixers is investigated in a wide range of flow, scalar transport and fluid injection conditions. It is shown that the improvement of mixing performance in CT micromixer configurations is quite low due to inefficient manipulation of fluid bodies in the mixing channel. Although vortex and engulfment flow profiles are fed by alternative split type inlets, the degree of mixing is not raised beyond 40%. In addition, the above complex flows are developed at a cost of a high pressure drop in the CT micromixer. The pressure drops measured are around 8.5 and 15.1 kPa for the two highest flow conditions tested, i.e., $Re = 160$ and 240 , respectively. Considering the limitations in the CT geometry in terms of creating an effective complex flow profile, a novel convex semi-circular-ridge (CSCR) passive micromixer design is developed. It is demonstrated that the convex alignment of semi-circular elements yields a specific, helicoidal fluid motion along the mixing channel which in turn enhances fluid mixing. The CSCR design reduces inhomogeneity between fluids by offering a two-way mixing mode depending on the flowrate imposed. While a rapid interdiffusion between fluid bodies is ensured in low flow conditions, the increasing deformation rate of fluid bodies with rising flowrates improves fluid mixing due to chaotic advection. In test cases examined, homogeneous scalar concentration distributions with a

mixing efficiency over 80% and a pressure drop less than 5 kPa are obtained in a mixing length less than 2000 μm . When it is compared to the CT micromixer, the novel design developed increases mixing efficiency and mixing quality values by the factors of 8.7 and 3.3, respectively. It is also shown that different orientations of mixing elements in the mixing channel adversely affect the mixing performance by disturbing the formation of helicoidal-shaped flow profile.

In the third part of the dissertation, a novel fluid overlapping mixing method is introduced along with nested type inlets. By this diffusion-based mixing approach, the improvement of mixing efficiency over a short distance is aimed particularly in very low flow conditions, i.e., $\text{Re} < 10$, where the development of a complex flow profile is difficult. The behavior of fluid flow in rectangular and circular designs is analyzed based on the simulation outcomes of a single-mixing-box fluid overlapping micromixer configuration. It is shown that the circular geometry presents optimum conditions in terms of the uniform distribution of fluid flow over an impermeable surface in the mixing box. The mixing of fluids is investigated in a circular-shaped fluid overlapping (CSFO) passive micromixer in the Re number range of 0.1–10. In the CSFO design, different scalar transport scenarios and inlet types are tested for both constant and sequential fluid injection modes. The outcomes show that the CSFO micromixer design provides considerably high mixing efficiencies over a very short distance in the main streamwise direction. When $\text{Re} = 0.1$, 0.5 and 1 flow conditions are simulated with the constant scalar injection mode, almost complete mixing is observed in a mixing distance between 260 μm and 470 μm for the most difficult mixing condition tested. In higher molecular diffusion scenarios of $\text{Re} = 0.1$, 0.5 and 1 flow conditions, fluid mixing is completed in a mixing distance less than 260

μm . When the sequential scalar injection mode is applied at $\text{Re} = 1$, it is found that even the lowest injection frequency tested provides more than 90% mixing efficiency for the smallest molecular diffusion constant simulated. The effect of injection frequency is more visible in higher flow cases that are $\text{Re} = 5$ and $\text{Re} = 10$. Operating the CSFO design with sequential injection mode reduces the complete mixing distance noticeably. In the highest flow condition examined, the maximum pressure drop is measured to be less than 1.4 kPa between inlet and outlet of the CSFO micromixer.

Based on the studies reported in this thesis three technical papers are published in SCI indexed journals on the subject which already received numerous citations over a very short period.

CHAPTER 1. INTRODUCTION

1.1 Background

Over the last half-century, miniaturization trend of macroscale systems in diverse disciplines has transformed the technology and created revolutionary impacts globally. Advances in micro- and nanotechnology paved the way for a new era where sophisticated largescale systems were fitted in microscopic footprints and redefined therein. In this research area, microfluidics concept, in which fluids are manipulated typically at submillimeter confined channels, has emerged as a new multi-disciplinary field. The important scientific branches that are utilized in microfluidics field are microelectromechanical systems (MEMS), microfabrication technology, materials science and engineering, physics, chemistry, and several other disciplines of engineering (e.g., chemical, mechanical, and electronics).

The development of the earliest microfluidic devices has started with inkjet printing technology in 1950s where fluid streams are controlled accurately for printing quality and this sparked other analytical applications in the fields of chemistry and pharmaceuticals since 1970s (Gervais et al., 2011). During the past few decades, advancements in microfabrication technology (Mansur et al., 2008), successful implementation of complex processes at microscales (Streets and Huang, 2013) and progressive applications in various interdisciplinary research fields have led the development of microfluidic systems and initiated the research field on which it relies on. Micro total analysis systems (μ TAS) or lab-on-a-chip (LOC) devices (Park et al., 2009; Reyes et al., 2002) are generally used to

define a centimeter-size compact unit on which physical, chemical, and biological processes can take place separately or collectively in a microchannel network.

Microfluidic systems are extensively used in various fields, such as chemistry (Aubin et al., 2010; Reyes et al., 2002), biology and biotechnology (Nguyen and Wu, 2005; Suh and Kang, 2010), medical (Capretto et al., 2011; Gambhire et al., 2016), medicine and healthcare (Hu et al., 2014; Tran-Minh et al., 2014), pharmacy and biochemistry (Mansur et al., 2008; Lei Wang et al., 2012), drug development and food industry (Ward and Fan, 2015), and environmental applications (Cai et al., 2017). From a general viewpoint, typical practices in these fields incorporate chemical synthesis, sample concentration, extraction, polymerization, biological screening, biomedical and clinical diagnostics, sample preparation and analysis, cell and DNA studies, separation and detection, drug delivery and fuel cell applications (Farra et al., 2012; Herold and Rasooly, 2009; Kjeang et al., 2009; C.-Y. Lee and Fu, 2018; Prescott et al., 2006).

Microfluidic systems have received a great attention as a result of the superiority of these systems against the largescale equivalents (Y. Liu and Jiang, 2017) and widespread applications in both academia and industry. It was reported in several journal articles that the number of studies on microscale systems has grown exponentially (Capretto et al., 2011; Kumar et al., 2011; Nguyen and Wu, 2005). Point-of-care (POC) and microfluidic paper-based analytical devices (μ PADs), which have already been commercialized and commonly used for various in vitro diagnostic, analysis, and characterization purposes (Abdollahi-Aghdam et al., 2018; Streets and Huang, 2013), may be given as the tangible examples of microfluidic chip technology that are engineered and utilized. Some of the common practices in these devices include cell experiments (e.g., growth and analysis) in

molecular biology, determining several biomarkers and health parameters in a body fluid sample (e.g., blood glucose level, hormones, cardiac makers, infectious pathogens, and viruses etc.) (Gervais et al., 2011; Le The et al., 2015; Pandey et al., 2018; St John and Price, 2014), and detection of contaminants for environmental monitoring purposes (Lisak et al., 2015; L. Wang et al., 2009). It should be noted that the use of POC devices on a global scale—particularly for health care purposes—has considerably increased in recent years. While the global market value of POC devices was approximately 15 and 23.16 billion US dollars in 2011 and 2016 respectively, this value is projected to be around 36.96 billion US dollars in 2021 (St John and Price, 2014; Vashist, 2017). The growth of these figures will likely to continue increasingly with the development of new techniques and devices in the following decades. The expanding potential of microfluidic devices mainly lies behind the several noteworthy benefits that are intrinsically presented by small scales.

Notably, the most remarkable influence of microfluidic chip concept is to present an effective process environment in a very small form factor, and therefore eliminate complex largescale equipment requirement for applications which in turn enables portable, rapid, convenient, low cost, safe, and clean operations. As reported in several studies (Fu et al., 2014; Kumar et al., 2011; C. Y. Lee et al., 2011; Mansur et al., 2008; C. T. Wang et al., 2009; Ward and Fan, 2015), the other prominent advantages of microscale systems, as opposed to their macro counterparts, may be considered as high throughput, accuracy and sensitivity, high surface-to-volume ratios, compactness, small amount of substance requirement in analyses, fast, reliable, and precise operating conditions, substantially minimized waste production, better temperature uniformity and control, minimization of

human factor in measurements, automation capabilities, and safety in case of harmful, toxic, or explosive material usage.

Major components of microfluidic platforms are generally micromixers, micropumps, microvalves, and microactuators (Gambhire et al., 2016). In these systems, while micromixers are utilized to mix two or more fluids, other components usually function to provide or regulate fluid flow. Besides, micromixers can also be employed as a stand-alone device (Nguyen and Wu, 2005), such as microreactors along with serving as a mixing element integrated in a microchip network. Micromixers are generally classified as active and passive (Gidde et al., 2017; C. Y. Lee et al., 2011) depending on the mixing strategy employed. However, fast and homogenous mixing of two or more fluids at submillimeter ranges are the main purpose of all kind of micromixers in both categories.

In active micromixers, fluid mixing is carried out by means of external disturbance fields, such as magnetic, acoustic, thermal, electrical, and pressure (Kumar et al., 2011; Nguyen, 2012a). Although active micromixers enhance mixing efficiency substantially over a short distance (i.e., reduce mixing time), these devices are inherently complicated systems. Extra component and power source requirements to generate external perturbation effects on the flow field create a complexity in terms of fabrication and integration of these units with other microchip elements (Alam et al., 2014). Furthermore, some external disturbance forces, such as heat and electrical field may not be suitable for biochemical applications due to the damaging effects of these factors on biological samples (Xu et al., 2011).

On the contrary, despite presenting relatively poor mixing performances, passive micromixers are smooth mixing platforms with several significant advantages. In passive mixing approach, fluids are mixed in microchannels utilizing the fluid flow energy within the micromixer and exploiting two well-known mixing phenomena: advection and molecular diffusion (Reyes et al., 2002). Accordingly, these systems do not require any extra components or power sources except that used to deliver fluids to the micromixer. As a result of offering a physically plain mixing configuration, passive micromixers are typically easy to fabricate, provide simple and stable operating conditions, and present better integrability with microfluidic systems (Capretto et al., 2011; Mansur et al., 2008; Nguyen and Wu, 2005). In addition, lack of additional components and harmless external effects makes these units a suitable platform for stand-alone applications and sensitive biochemical processes. Therefore, such structural and operational advantages of passive mixing approach over the active type have motivated several researchers to improve fluid mixing and reduce mixing length at microscales.

Mixing is defined as a transport process in which non-uniformity of species, phases, or temperature are diminished (Nguyen, 2012a) through various mechanisms, such as advection, molecular diffusion, and turbulent diffusion (i.e., eddy diffusion). In a mixing process, the function of these mechanisms depends strongly on the fluid flow character—laminar or turbulent—which is determined by the dimensionless Reynolds (Re) number. The Re number is characterized as the ratio of inertial forces to viscous forces and usually, $Re = 2300$ is accepted as the transition point (Tran-Minh et al., 2014; Lilin Wang et al., 2007) after which flow regime starts to change from laminar flow to turbulent flow.

In macroscopic mixing systems, mixing mainly develops based on effective turbulent flow dynamics by which liquids are naturally stirred, and the impact of molecular diffusion in turbulent flow regimes can be ignored since the turbulent diffusivity is the dominant mixing parameter (Demirel and Aral, 2016). In microscale mixing structures, however, Re number can hardly exceed 2000 in a pressure range of 1–10 bars (Wong et al., 2004) and even going beyond $Re > 1000$ is impractical (Jian Chen et al., 2011) due to operational difficulties and high energy requirement to overcome viscous effects in the flow. Accordingly, turbulent flow cannot be created at microscales and mixing needs to be carried out under laminar flow conditions utilizing the transport processes such as advection and molecular diffusion.

In passive micromixers, fluid mixing arises as a challenging task because of advection-dominant transport developed in microchannels. Strictly laminar fluid flow—usually $Re < 100$ (Le The et al., 2015)—and very low molecular diffusion coefficients of several large molecules and electrolytes in chemical and biological solutions—typically in the range of 10^{-11} – 10^{-9} m^2/s (Bhopte et al., 2010; Nguyen, 2012a)—inherently create difficult mixing conditions. Namely, at low Re numbers advection cannot be utilized as a mixing mechanism effectively due to straight microchannels in which unidirectional flow is developed. Thus, mixing process only depends on molecular diffusion which is a slow process. Under these conditions, mixing length increases substantially to obtain an adequate mixing efficiency, and hence a very long mixing channel is required which is not desirable. The length of mixing channel required may rise even to the order of a meter depending on micromixer configuration, flow velocity, and the magnitude of diffusion coefficient. Consequently, increasing mixing distance leads three fundamental problems in

microfluidic systems: (i) integration of the micromixer into a microfluidic scheme; (ii) high energy requirement due to the increased pressure drop; and, (iii) long mixing time.

In passive micromixers, these problems can be dealt with the effective utilization of advection mechanism by which secondary flows or transversal velocity components are generated in microchannels—also referred as chaotic advection (Bhopte et al., 2010; Nguyen, 2012a). Correspondingly, contact surface area or in other words, contact time between fluids is enhanced and diffusive mixing is accelerated which in turn helps to improve mixing efficiency and reduce the mixing length. On the other hand, fluid mixing can be accomplished in virtue of the advection process alone. In this case, molecular diffusion effects are substantially minimized with increasing flow velocity and fluids are mixed based on complex flow patterns, formed by the chaotic advection in microchannels. Considering the limited variable options in passive mixing approach, a complex flow pattern can be achieved only by alternative flow manipulations and microchannel configurations. Therefore, developing special design topologies in passive micromixers is essential to improve mixing efficiency and reduce mixing length.

1.2 Motivation and Objectives

In previous studies, it was pointed that micromixers are typically essential and one of the most important components of microfluidic systems (Alam et al., 2014; Alam and Kim, 2012; Mansur et al., 2008). This is primarily because in the majority of biological and chemical applications, mixing of fluids is usually an integral part of a process. Therefore, in these practices several factors, such as accuracy, speed, and efficiency of a reaction or analysis, microchip dimensions, and chip operating time are determined directly

by the characteristics of mixing activity (Fujii et al., 2003; C. Y. Lee et al., 2011; Sadegh Cheri et al., 2013).

In his extensive book on micromixers, Nguyen (Nguyen, 2012a) stated that content and distribution of products and reaction rate in a chemical reaction at microscales are affected by mixing time. For instance, in a chemical reaction if a product desired tends to react with one of the reactants, a slow mixing time can inhibit the process yielding an unwanted by-product (Shah et al., 2012). Rapid and efficient mixing of reagents in several chemical and biological applications are also essential to obtain quick and accurate diagnosis results. Typical examples are enzyme reactions, protein folding, cell activation, nucleic acid synthesis or sequencing, complex chemical reactions and drug delivery applications (Bhopte et al., 2010; Nguyen and Wu, 2005).

In addition to the important effects of mixing characteristics on several processes, an excessive mixing distance may radically affect the physical integration of a micromixer into a microfluidic scheme. A micromixer unit with a centimeter-long mixing channel becomes impractical to integrate on a microfluidic chip (Le The et al., 2015) which overall has a few square centimeters footprint. The development of micromixers to yield high mixing efficiencies over a short distance is also essential for further progress of microfluidic chip technology. Thus, the fabrication of much smaller, cost- and energy-efficient, and versatile microfluidic devices may be enabled for various practices.

In view of the above arguments and the previous section, the following points constitute the main motivation of this study to improve fluid mixing and reduce mixing length in passive micromixers: (i) the importance of micromixers in microfluidic systems;

(ii) several key advantages of passive mixing method over active micromixers; (iii) the urgency of fast and through mixing in several chemical and biological applications; (iv) integration problems of micromixers with microfluidic systems; and, (v) further improvement of microfluidic technology.

To date, numerous micromixer designs have been proposed to improve fluid mixing based on passive mixing approach. In most of these numerical and experimental efforts, mixing enhancement generally takes place as a trade-off between energy needed, mixing length (or mixing time) required, operational challenges, and the complexity of design structure in terms of fabrication. For instance, although injection-based flow manipulating passive micromixer designs help to increase mixing performances, this is typically achieved over a long distance with a high pressure drop in the system as may be seen in several previous studies (Mubashshir A. Ansari et al., 2012; Bothe et al., 2006; Izadpanah et al., 2018; Wong et al., 2004). Besides, mixing efficiencies obtained are far behind an adequate level, which is commonly accepted as 80 % (Tran-Minh et al., 2014), for several chemical and biological practices.

Similar problems are also seen in other passive micromixer designs studied. For example, although lamination passive micromixers enhance fluid mixing at low Re numbers, these devices present fabrication complexities (Alam et al., 2014) to transform main flow into multiple sub-streams. Planar micromixers are easy to fabricate, but usually need to be operated at high Re numbers to improve fluid mixing (Alam et al., 2014; Gidde et al., 2017) or require long mixing channels when operated at low Re numbers (Bhagat et al., 2007). Passive micromixers with grooved mixing channels (Mubashshir Ahmad Ansari and Kim, 2007; D. Wang et al., 2017; Lei Wang et al., 2012) usually offer a long mixing

distance which may increase up to a few centimeters. Despite providing high mixing efficiencies, passive micromixer designs with a mixing channel obstructed (Alam et al., 2014; Gidde and Pawar, 2019) or constrained (Hossain and Kim, 2014; Shih and Chung, 2007) typically suffer from high pressure drops.

Therefore, the main objective of this study is to develop passive micromixers in which all the aforementioned factors are substantially minimized. In this regard, this study introduces two novel passive micromixer designs to the literature. The designs improve mixing efficiency and reduce mixing length considerably under reasonable pressure drops as well as presenting fabrication ease.

Numerical investigation of passive micromixer designs plays a significant role to reduce the time, effort, and cost in experimental studies. The effect of several variables in a design geometry may be studied, evaluated, and optimized utilizing numerical simulation outcomes before the fabrication of ultimate design. For this purpose, Computational Fluid Dynamics (CFD) simulations are usually employed to investigate fluid flow and solute transport at microscale (Okuducu and Aral, 2018). However, in numerical passive micromixer studies advection-dominant transport creates serious complications in terms of accurate evaluation of mixing efficiency (Bailey, 2017; M. Liu, 2011). In the numerical solution of advection-dominant systems, numerical problems usually occur as oscillations and unphysical diffusion (i.e., numerical diffusion, false diffusion, or artificial diffusion). Most common numerical methods, such as Finite Volume Method (FVM) and Finite Element Method (FEM), that are employed in CFD applications usually suffer from similar numerical error outcomes. In several numerical passive micromixer studies, numerical

diffusion effects have been usually overlooked and erroneous mixing performance results have been reported.

Therefore, another objective of this study is to comprehensively characterize and quantify the false diffusion effects in numerical passive micromixer simulations to provide physically reliable mixing outcomes. For this purpose, several flow, transport, grid, and micromixer configurations are considered when both FVM and FEM is used in solution. Nonetheless, the main emphasis is given on FVM since this technique is mainly utilized in this study and widely used in numerical passive micromixer investigations in the literature.

1.3 Thesis Scheme

In Chapter 2, a literature review of passive micromixers is presented. Typical passive mixing approaches, employed in micromixers, are identified. Several examples of passive micromixer designs are discussed in terms of mixing characteristics and numerical diffusion effects, and the outcomes reported are summarized. Lastly, the most common fabrication materials and techniques, utilized to produce passive micromixers, are reviewed.

Chapter 3 presents the fundamental mathematical equations that are employed in this study. In this chapter, governing equations, which are used to resolve fluid flow and scalar transport domains, are described under the assumptions considered in this study. Dimensionless numbers, used to determine flow and transport characteristics, and approaches for quantitative evaluation of mixing outcomes are identified. Mathematical methods, used in grid studies and quantification of numerical diffusion errors, are explained. The CFD solver settings are summarized, and a validation study is conducted.

Chapter 4 is dedicated to characterization of numerical errors in CFD simulations of different passive micromixer designs. First, numerical errors are examined in a classical T-shaped design in terms of various grid types, numerical methods, discretization schemes, flowrates, and transport scenarios. Second, numerical errors are investigated in two- and four-inlet swirl-generating micromixer designs based on hexahedron-type mesh elements.

In Chapter 5, convex semi-circular-ridge (CSCR) passive micromixer design is presented. The design developed is evaluated for different injection, flow, and transport conditions. The outcomes obtained are comparatively discussed with the results of a classical-T micromixer. Alternative designs are investigated, and the mixing characteristics are compared with the CSCR micromixer.

A novel diffusion-based fluid overlapping mixing approach is presented in Chapter 6. The design of nested-type inlets is introduced, and alternative nested inlet geometries are evaluated. The mixing of fluids is investigated in a circular-shaped fluid overlapping (CSFO) passive micromixer design for various injection, flowrate, and transport conditions. The mixing results obtained are discussed comparatively with that of reported in the literature as well as a classical T-shaped passive micromixer.

In Chapter 7, the overall study is summarized, key findings are highlighted, and several remarks are presented for future studies.

CHAPTER 2. LITERATURE REVIEW

2.1 Introduction

As mentioned in the previous chapter, unlike the active micromixers in which fluids are mixed based on external disturbance forces, passive mixing platforms perform the mixing task exploiting internal flow dynamics in microscale channels. Despite exhibiting relatively low mixing performances and requiring special design efforts, passive micromixers have been at the forefront of the active types (Y. Z. Liu et al., 2004; Viktorov and Nimafar, 2013). Structural and operational benefits of passive mixing approach have attracted several researchers to improve fluid mixing at microscales. To that end, numerous passive micromixer designs have been proposed over decades. In this chapter, passive mixing approaches and various passive micromixer examples, designed based on these approaches, are reviewed in terms of fluid mixing characteristics. In addition, several numerical passive micromixer studies are assessed with respect to numerical diffusion errors. Lastly, materials that are used to fabricate micromixers and fabrication methods are summarized.

2.2 Passive Mixing and Micromixer Designs

In passive mixing technique, fluids are mixed relying on two mixing phenomena—advection and molecular diffusion—utilizing the flow energy in microchannels of which width and height typically range from a few tens to hundreds of micrometers. While advection describes the transport process through the bulk motion of fluids, molecular diffusion occurs due to the movement of particles from high concentration to low

concentration based on the random motion of particles (Nguyen, 2012a). In microchannels, effective utilization of advection becomes rather difficult due to strong viscous effects and fluids typically form segregated flow patterns as a result of very low flow velocities in which laminar flow conditions exist. In this case, fluid mixing is predominantly controlled by molecular diffusion (Rasouli et al., 2018) over the contact surface of fluid bodies. However, very low diffusion constants and limited contact surface area yield inefficient mixing results. In several studies (Alam and Kim, 2013; Tran-Minh et al., 2014), it was reported that this problem may be overcome by increasing the contact surface area between fluids which in turn reduces diffusion path, increases effective diffusion domain and accelerates the diffusive mixing. For this purpose, several passive micromixer designs have been proposed based on two passive mixing principles: chaotic advection and molecular diffusion.

In molecular diffusion-based designs, main flows are divided into several sub-streams or layers of fluid segments which are aligned in microchannels to be in serial or parallel flow regions as shown schematically in Figure 2.1. Therefore, in these flow domains contact surface between fluids is increased systematically and diffusive mixing is promoted. Typical design examples include segmentation (Fujii et al., 2003; Nguyen and Huang, 2006), pulse injection (Glasgow and Aubry, 2005; Silva et al., 2017), and laminating passive micromixers (Branebjerg et al., 1996; Gray et al., 1999). The segmentation and pulse injection passive micromixers offer a simple design topology and function exploiting the operational features of micropumps that are used to deliver fluids to the micromixer (e.g., square wave (Glasgow et al., 2004; Nguyen and Huang, 2006) or sinusoidal (C. Cortes-Quiroz et al., 2014; Glasgow and Aubry, 2005) fluid injection). In

contrast, laminating designs are operated with a constant flowrate or pressure and require a complex channel network to align fluid domains in microchannels. In this regard, while the segmentation and pulse injection passive micromixers may require extra operational effort to control fluid injection, laminating designs often require a complex fabrication process (Alam et al., 2014) since several junctions need to be connected properly.

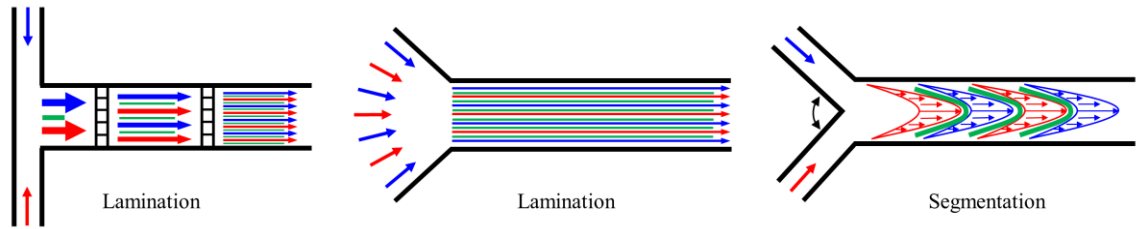


Figure 2.1 Enhancement of contact surface area in molecular diffusion-based passive micromixer designs. Red and blue line arrows represent different fluids. Green color shows the contact surface and diffusive interaction between different fluids.

In chaotic advection-based designs, fluids are manipulated to generate secondary flows or transversal velocity components in microchannels by which interfacial area between fluid bodies is increased. In this sense, the chaotic advection involves the processes in which fluids are subjected to split, stretch, twist, break or fold flow configurations (Castelain et al., 2001; Okuducu and Aral, 2019; Xia et al., 2005). While chaotic advection-based passive micromixers enhance diffusive mixing at low Re numbers (e.g., typically $Re < 10-20$), molecular diffusion effects are minimized with increasing Re number and fluids are mixed based on complex flow profiles. Therefore, unlike the molecular diffusion-based passive micromixers, which are typically operated at low Re numbers to enhance diffusive mixing, chaotic advection-based passive micromixers may be designed for a wide range of flow conditions. The desired flow rate in microchannels is

generally obtained by applying a constant flowrate or pressure gradient through inlet-outlet boundaries. The use of the latter is also known as pressure-driven flow.

In the current passive micromixer literature, numerous 3-D chaotic advection-based passive micromixer designs are proposed to improve fluid mixing at microscales. Typical geometries are shown schematically in Figure 2.2. These configurations mostly include serpentine channel designs (Mubashshir Ahmad Ansari and kim, 2009; Clark et al., 2018; Nonino et al., 2009), simple channel modifications (Bhopte et al., 2008; C. A. Cortes-Quiroz et al., 2014; Fang et al., 2012), curved channels (Alam et al., 2014; Yang et al., 2013), obstructed channels (Afzal and Kim, 2012; Shih and Chung, 2007), split-and-recombination (SAR) type designs (Mubashshir Ahmad Ansari et al., 2010; Raza et al., 2018), planar geometries (Alam and Kim, 2013; Gidde et al., 2017), grooved channels (Hossain and Kim, 2010; Jian Chen et al., 2011), injection-based designs to manipulate flow in plain microchannels (Izadpanah et al., 2018; Roudgar et al., 2012; Soleymani et al., 2008), and microchannels with baffles (Fang et al., 2012; Shih and Chung, 2007). Although this classification is done based on the channel geometries, in several passive micromixer studies different geometric features are employed in a single design. For example, Liu et al. (K. Liu et al., 2015) utilized both curved channel and SAR features in a helical shape passive micromixer, Sheu et al. (Sheu et al., 2012) proposed a parallel laminar SAR micromixer with tapered curved microchannels, and Rasouli et al. (Rasouli et al., 2018) surveyed a micromixer design with curved and baffle-embedded microchannels.

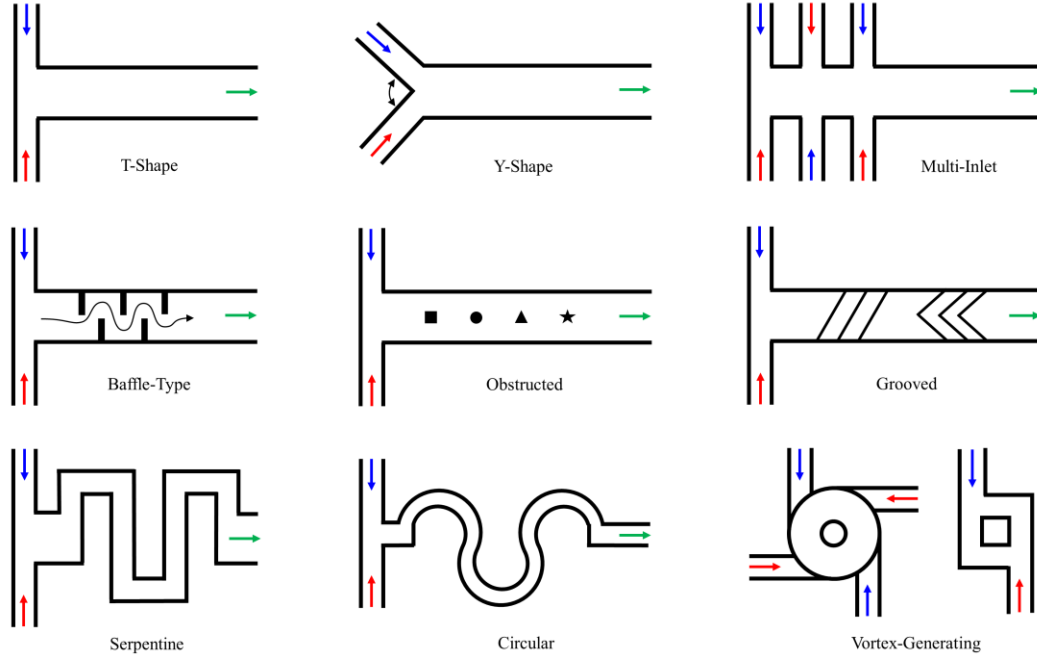


Figure 2.2 Typical passive micromixer designs. All designs have a height perpendicular to the plane. Red and blue line arrows represent different fluids in the inlet channels. Green line arrows represent mixed fluids at the outlet.

In passive micromixer researches, usually a wide range of fluid flow and transport conditions are tested to determine the effective functioning limits of the design developed. These conditions are represented by various dimensionless numbers, such as Reynolds (Re), Peclet (Pe), and Schmidt (Sc). While Re and Pe numbers are used to determine the characteristics of fluid flow (e.g., laminar or turbulent) and transport (e.g., advection– or diffusion–dominant) in a micromixer, respectively, Sc number indicates mass transfer character due to momentum or molecular diffusion. Detailed descriptions along with mathematical formulations of Re, Pe, and Sc numbers are presented in Chapter 3. In addition, molecular diffusion coefficient is typically selected to be in a range of 10^{-11} – 10^{-9} m^2/s to simulate advection-dominant transport conditions in microchannels. Although passive micromixers can be operated with several bars of pressure drop between inlets and outlet, examples are limited to a few experimental studies (Böhm et al., 2001; Wong et al.,

2004) in the literature. Generally, high pressure drops are not desired due to bonding complexities and energy supply concern (Nguyen and Wu, 2005). Therefore, passive micromixer design studies usually aim to enhance fluid mixing under a reasonable pressure drop condition which is typically expected to be much less than a bar.

Due to smooth design architecture and strong mixing capabilities, 3-D micromixer geometries consisting of inlet and mixing channels (e.g., Y-, and T-shape) are broadly examined under various injection strategies and channel modifications. For example, Fang et al. (Fang et al., 2012) examined a T-shape passive micromixer with several baffle-embedded mixing units along the mixing channel. Numerical and experimental results showed that the design proposed induced chaotic advection in the mixing units at $Re = 0.29$ and increased mixing performance. Authors reported that 28-period mixing unit is required (i.e., ~ 1.7 cm axial distance) to mix fluids completely.

Ortega-Casanova and Lai (Ortega-Casanova and Lai, 2018) surveyed the effects of multiple inlets in a passive micromixer design with a single mixing unit like the one used in the study above (Fang et al., 2012). In this study, authors tested three transport scenarios (i.e., $Sc = 2 \times 10^3$, 4×10^3 , and 10×10^3) for two flow conditions (i.e., $Re = 0.1$ and 0.29). Numerical simulation results show that increasing the inlet numbers is more effective for the highest flow condition and Sc number, tested in the study. When the effect of seven- and two-inlet configurations are compared for the most challenging mixing condition (i.e., $Sc = 10 \times 10^3$), seven-inlet configuration increase mixing efficiency approximately 5.5 and 3.5 times for $Re = 0.29$ and 0.1 respectively. For the highest Sc number and seven-inlet configuration, authors achieved around 90% and 80% mixing efficiency at the exit of the micromixer (i.e., ~ 5000 μm axial distance) for $Re = 0.1$ and 0.29 respectively.

Gidde et al. (Gidde et al., 2017) proposed a planar passive micromixer with circular and square mixing chambers. Authors performed a wide range of Re scenarios between 0.1 and 75 and showed that micromixers increase mixing efficiency based on the development of chaotic advection. While both micromixer designs produce rather similar mixing outcomes for $Re = 0.1, 1, \text{ and } 5$, square chamber configuration result in lower pressure drop over the circular design. In both designs, mixing efficiency is significantly enhanced when the flowrate was increased, and the highest mixing efficiency values are achieved when $Re = 75$. The maximum pressure drop is quantified around 11 kPa when constriction channel width is selected as 200 μm in circular chamber design. The mixing distance to reach 80% mixing efficiency is reported as approximately 10000 and 5000 μm for $Re = 5$ and 75 respectively.

Afzal and Kim (Afzal and Kim, 2012) investigated a split-and-recombination (SAR) type micromixer for a Re range 10–70. The design proposed enhance mixing by generating secondary flows in sub-channels. More than 80% mixing efficiency is obtained at the exit of the micromixer (i.e., $\sim 10000 \mu\text{m}$ axial distance) in cases where Re is greater than 30. The range of pressure drops reported is around 3–10 kPa for corresponding Re numbers 30–70 in the best-case scenario tested.

Yang et al. (Yang et al., 2013) designed a two-layer passive micromixer using spiral channels, consisting of semi-circles. Authors connected two spiral channels via an erect channel employing multi-layer fabrication techniques. Numerical and experimental results show that the design create chaotic advection based on Dean effects (i.e., Dean flow in curved channels (S A Berger et al., 1983)). Transverse flows, generated in the curved channels, improve fluid mixing with increasing flow velocities. The design developed

provides around 90% mixing efficiency in a total length of 2340 μm when $\text{Re} > 40$. For lower flow velocities, e.g., $\text{Re} = 32, 24, 16$, and 8 mixing efficiencies reported are around 80, 65, 50, and 35% respectively. It is also reported that complete fluid mixing can be obtained with further increase of Re number, but this will cause a higher pressure in the micromixer and negatively affect channel connections. Instead, authors extended the spirals in each layer by adding another semi-circular channel with a diameter of 200 μm and reached 99% mixing efficiency at $\text{Re} = 40$.

Alam et al. (Alam et al., 2014) studied the effects of obstructions in curved and straight channels for various flowrates (e.g., $0.1 \leq \text{Re} \leq 60$). It is shown that compared to the plain curved channel, adding obstacles significantly increases mixing efficiency at low Re numbers tested. While hexagonal and circular mixing elements perform similarly, the effect of diamond obstacles is less than other two shapes until $\text{Re} = 50$ is reached. Employing the circular obstacles, authors obtained mixing efficiency values around 88% on the outlet plane (i.e., $\sim 5000 \mu\text{m}$ axial distance) for $\text{Re} = 0.1$ and $\text{Re} > 15$ flow scenarios. Pressure drops are reported as 10 kPa and 23 kPa at $\text{Re} = 60$ for straight and curved channels respectively.

Gidde and Pawar (Gidde and Pawar, 2019) surveyed a three-inlet passive micromixer with rectangular and elliptic baffles for Re numbers between 0.1 and 50. The micromixers examined activate vortex generation and provide over 85% mixing efficiency for $\text{Re} \geq 10$. Pressure drops, obtained at $\text{Re} = 50$, are nearly 40 kPa and 30 kPa for rectangular- and elliptic-baffle configurations respectively.

Ritter et al. (Ritter et al., 2016) proposed passive micromixer with nozzle-diffuser-type obstacles, aligned in the mixing channel. Numerical simulations show that obstructed design perform better than the plain form in a Peclet (Pe) range between 100 and 5000. This is observed as a result of transition from diffusive mixing to advective mixing in this Pe range. When $Pe < 100$, however, both design configurations yield quite similar mixing outcomes as a result of dominant diffusive effects in the mixing channel. Although the obstructed design considerably increases mixing efficiency for higher flowrates, this is achieved at a cost of high pressure drops in the micromixer. Authors quantified the mixing efficiency to be around 50% at the center of the micromixer (i.e., 1600 μm axial distance) when $Pe = 5000$ and $Re = 100$. The corresponding pressure drop for this case is reported as around 55 kPa.

Chen et al. (Jian Chen et al., 2011) performed a numerical and experimental study on a passive micromixer with crosswise ridges positioned in the mixing channel. It is shown that the generation of rotational flows along the mixing channel promotes fluid mixing. Mixing lengths, predicted to reach 90% efficiency, are reported as 4.86 cm and 3.65 cm for Re numbers 0.05 and 50 respectively.

Wang et al. (Lei Wang et al., 2012) attached cylindrical grooves on lateral walls of a rectangular duct. Results indicate that creation of transversal velocities inside the grooves considerably improve mixing efficiency in a distance less than 20000 μm for a Re number range 1–100. Authors obtained the lowest pressure drop around 9.3 kPa for $Re = 100$ scenario.

Ansari et al. (Mubashshir A. Ansari et al., 2012) proposed a T-shaped mixer that favors vortex formation in the mixing channel. Experimental results show that non-aligned injection strategy enhances mixing efficiency over a simple T-shaped micromixer when $Re \geq 10$. This is achieved because non-aligned inlet channels enable vortex flow at low flowrates. The mixing efficiencies—which are quantified at a 7000 μm axial distance in the mixing channel—are found to be approximately between 15% and 50% for a Re range 10 to 70.

Roudgar et al. (Roudgar et al., 2012) examined a plain T-shaped micromixer with inlets, split horizontally and vertically. It is shown that using split inlets with an unequal injection strategy substantially increases mixing efficiency. The maximum mixing efficiencies are reported as 37% and 58.5% at the exit (i.e., 600 μm axial distance) for $Re = 1$ and 100 flow cases respectively.

In their detailed work, Galletti et al. (Galletti et al., 2012) studied vortex and engulfment flow regimes in a plain T-mixer. Authors investigated a wide range of Re scenarios between 96 and 527. The highest mixing efficiency is reported as around 45% at the outlet of the micromixer, i.e., 3000 μm axial distance.

2.3 False Diffusion Effects in Numerical Passive Micromixer Studies

In passive micromixer studies, advection dominance in microchannels create numerical challenges as well as mixing difficulty. The resolution of sharp concentration gradients in a transport domain is a challenging task for the most common numerical techniques, such as FVM and FEM (Carroll et al., 2010). Both methods suffer from numerical diffusion and numerical dispersion effects when $Pe \gg 1$. While numerical

diffusion error manifests itself as extra diffusion (i.e., unphysical diffusion) in the transport system, numerical dispersion error cause oscillations on the concentration front and back (Okuducu and Aral, 2018). The magnitude of these problems strongly depends on discretization techniques, grid properties, flow velocity, and molecular diffusion coefficient (or viscosity for fluid flow). For example, while the first-order discretization schemes are more prone produce numerical diffusion than second order schemes (M. Liu, 2011), first order schemes provide stable solutions without oscillations (Godunov and Ryaben'kii, 1963).

In FVM, orthogonal alignment of flow with grid boundaries plays a significant role to control the amount of numerical diffusion (Patankar, 1980). Therefore, while the use of hexahedron type elements helps to reduce numerical diffusion errors in the numerical solution, the use other element types, such as tetrahedron and prism may yield high numerical diffusion errors. For numerical solution of advection-dominant transport systems, FEM requires certain stabilization techniques to suppress the oscillations in the solution when $Pe \gg 1$ (Gresho and Lee, 1981). In some of these techniques, Pe number is reduced by artificially increasing molecular diffusion constant. Although this method may help to provide acceptable results in macroscale applications where molecular diffusion effects may be ignored, the use of this approach may cause additional unphysical diffusive mixing in microscale mixing systems where molecular diffusion predominantly controls fluid mixing.

In numerical micromixer investigations, mesh characterization is a critical step to identify and control numerical errors. In the current micromixer literature, there is no standard and accepted procedure for grid studies. Generally, mesh properties tested (e.g.,

grid size, grid type, mesh density, and element positioning etc.) are chosen as a rule of thumb or based on computational limits. However, these properties need to be considered and used appropriately depending on the type of physical problem to avoid reporting unphysical mixing results in numerical simulations as reported in References (Bailey, 2017; M. Liu, 2011; Okuducu and Aral, 2018).

For instance, the selected mesh level in References (Galletti et al., 2012; Roudgar et al., 2012) was primarily considered to resolve the flow field instead of solute transport although quite high Peclet numbers (e.g., on the order 10^4 – 10^6) were examined. In several papers (Afzal and Kim, 2012; Alam et al., 2014; Gidde et al., 2017; Izadpanah et al., 2018; Javaid et al., 2018; Raza et al., 2018; J. Zhang and Luo, 2018), very close mesh densities (i.e., total mesh element numbers) were employed for grid studies which implies that the effects of numerical diffusion cannot be revealed clearly. In these applications, numerical simulations may be considered as grid-independent with a minimal error percentage even though a serious amount of error remains in the reported results. On the other hand, in some studies (Afzal and Kim, 2012; C. A. Cortes-Quiroz et al., 2014; Gidde et al., 2017; Izadpanah et al., 2018; J. Zhang and Luo, 2018), low or moderate Re or Pe cases were used to determine a grid level, but higher Re or Pe case results were reported in these studies which are inconsistent.

In the current literature, only a few papers (Bailey, 2017; Carroll et al., 2010; M. Liu, 2011) have examined the influence and extent of numerical problems in the estimation of mixing performance in passive micromixers. For instance, Liu (M. Liu, 2011) investigated several micromixer studies and extensively discussed the extent of numerical diffusion problems in the micromixer literature. It was reported that numerical diffusion effects of

high-order schemes were rarely discussed in the literature. In the study, several tests are conducted using different numerical schemes under various grid size, flow, and transport conditions for a three-dimensional microchannel mixer. Hexahedron type mesh elements are utilized in FVM and a set of equations is proposed to quantify average numerical diffusion error which results from both flow and scalar transport solutions. Tetrahedron type mesh elements are also studied, and it is advised that the use of this type element should be avoided especially for scalar transport solution since the amount of false diffusion and computational cost is higher than that of hexahedral mesh type. Various high order schemes are examined (e.g., Second-Order Upwind, QUICK (Leonard, 1979), MUSCL (van Leer, 1979)) and it is reported that false diffusion can be significantly reduced if higher order schemes are used instead of first order upwind schemes.

Bailey (Bailey, 2017) examined false diffusion effects using FVM in a two-dimensional test problem for both structured and unstructured grids. First and second-order upwind methods were applied, and the amount of false diffusion generated was quantified. Author developed a set of procedures to estimate and manage the required grid size by which false diffusion can be reduced in steady microscale mixing simulations.

Soleymani et al. (Soleymani et al., 2008) studied flow dynamics and mixing in a T-shape micromixer using FVM and discussed several approaches to diminish numerical diffusion effects at moderate cell Pe numbers. Authors performed a spatial discretization using high-order QUICK scheme, locally refined the mesh and increased the molecular diffusion constant artificially to overcome high computation cost. In the study, it was reported that numerical simulation results were used for optimization purposes rather than the physical mixing evaluation of the micromixer.

In several numerical passive micromixer studies, it is mentioned that using a second-order discretization scheme substantially minimizes numerical diffusion errors (C. Cortes-Quiroz et al., 2014; Hossain and Kim, 2016; Raza et al., 2018). Although this statement is conceptually correct, second-order discretization schemes may still produce serious amount of unphysical diffusion depending on other factors mentioned previously. Accordingly, in numerous studies unphysical mixing effects of the numerical diffusion errors have been overlooked and erroneous mixing results have been reported.

For example, Cortes–Quiroz et al. (C. A. Cortes-Quiroz et al., 2014) numerically investigated fluid mixing in a swirl-generating 3-D passive T-mixer with a 2000 μm long mixing channel. Authors tested several flow conditions for a Re number range between 100 and 500 using the FVM and second-order upwind discretization. To examine the grid sensitivity at $\text{Re} = 250$, authors employed six different mesh levels consisting of structured brick elements with mesh densities between 3 million and slightly over 5 million. In the study, 4.3 million elements were used for all simulations. Although very high Peclet numbers (e.g., on the order of 10^5) were studied, numerical diffusion effects on mixing were not reported.

Modifying the inlets and constricting the mixing channel, Zhang and Luo (J. Zhang and Luo, 2018) studied a similar 3-D swirl-induced T-mixer in (C. A. Cortes-Quiroz et al., 2014) for various Reynolds numbers between 10 and 70 using FEM. All simulations were conducted using a mesh density around 277,000 with structured and unstructured elements. The numerical results of the original 3-D micro T-mixer (OTM) in this study were compared with an experimental study (Mubashshir A. Ansari et al., 2012). While using a 5000 μm shorter mixing channel in numerical simulations, approximately 20% higher

mixing efficiency was reported when compared with the experimental result at $Re = 70$. Such a large discrepancy was more likely to have emerged due to high numerical diffusion errors in the solution, which was due to the use of a rather coarse mesh in simulations.

Raza et al. (Raza et al., 2018) examined a serpentine SAR micromixer for a Re number range between 0.1 and 120 using the FVM and a second-order scheme. Authors discretized the computational domain using an unstructured hybrid mesh consisting of both hexahedron and tetrahedron mesh elements. Although tetrahedron-type mesh elements were employed and very high Peclet numbers (e.g., on the order of 10^4) were simulated, numerical diffusion effects were not reported in the study. In addition, a quite coarse mesh density was selected for the entire simulations as a result of performing a misleading grid study in which very close mesh densities were tested.

Ansari et al. (M. A. Ansari et al., 2018) surveyed a comparative analysis of classical T-mixer and vortex T-mixer both numerically and experimentally for Re numbers between 1 and 80. In this study, numerical simulations were conducted using a structured hexahedral mesh with a grid size of $4\ \mu\text{m}$ at the T junction and larger elements were used at the downstream end with a total element number of approximately 1.3 million. In this numerical solution, FVM was used. Even though it was realized that numerical simulations were not free of numerical diffusion, this was not examined and reported.

Izadpanah et al. (Izadpanah et al., 2018) studied fluid mixing for Re cases 75–400 in a T-shaped and double T-shaped micromixer geometry and investigated the effects of vortex and engulfment flow regimes on mixing using FVM. For a mesh independence study at $Re = 260$, four different mesh densities consisting of hexahedral elements ranging

from 0.24 million to 1.3 million were tested and a mesh density close to 1 million elements was selected for simulations. At such a low mesh density and high Re cases, numerical solutions will be exposed to high false diffusion, but authors evaluate the mixing performance without mentioning the contribution of numerical diffusion effects.

Chen et al. (J. J. Chen and Chen, 2011) investigated mixing using swirl-generating designs for several inlet and mixing box configurations up to $Re = 100$. Authors employed a structured mesh with hexahedron elements and discretized the computational domain using FVM. It was reported that to reduce numerical diffusion effects, mesh refinement was maintained until the mixing index difference was below 5% between mesh levels, but the grid sizes and mesh density levels employed in simulations were not reported in the study.

On the other hand, in several micromixer studies (Gidde et al., 2017; Jain et al., 2013; Le The et al., 2015; T. Li and Chen, 2017; VIRK and HOLDØ, 2016; Lei Wang et al., 2012) where the FEM was employed, the authors did not report the instability and false diffusion effects although they have studied advection dominant systems. In these applications, depending on the stabilization method applied, mixing performance results reported may show significant variations depending on the degree of numerical treatment applied.

Consequently, it should be noted that considerable effort is necessary in reporting the outcome of the mixing performance in numerical studies. As stated earlier, in micromixers, molecular diffusion is typically the dominant mixing mechanism. The mixing effects of physical molecular diffusion may be acutely masked by numerical diffusion

errors. Since complete elimination of numerical errors is not possible, quantifying the presence of these errors are necessary to provide reliable and unsusceptible results in the evaluation of mixing performance of micromixers. In this thesis special attention is paid to this problem for which a chapter is devoted to this analysis.

2.4 Materials and Fabrication

Micromixers may be made using various materials, such as silicon (Böhm et al., 2001; Wong et al., 2004), glass (G. Bessoth et al., 1999), polymers (X. Chen, 2018), ceramic (Wong et al., 2003), and metals (Nguyen, 2012b). While polymer-based micromixers offer relatively lower cost and fast production periods, silicon-based micromixers are expensive due to very clean room requirement for fabrication (Nguyen and Wu, 2005). Polydimethylsiloxane (PDMS) and thermoplastic (e.g., Polymethyl methacrylate (PMMA) (X. Chen, 2018)) polymers are widely used to fabricate complex 3-D microscale structures based on various multi-layer fabrication techniques as described in Reference (M. Zhang et al., 2010). From a general point of view, micromixers may be fabricated employing various technologies, such as polymeric (e.g., soft lithography, hot embossing, injection molding, and roller imprinting), silicon-based (e.g., photolithography, wet and dry etching, silicon surface micromachining etc.), and metallic. In addition, although the use of 3-D printing technology presents some difficulties currently, the potentials of this approach is expected to change the fabrication routine of microfluidic system in the future (Gale et al., 2018). While the conventional techniques may be used to fabricate very small sizes (e.g., $\sim 1 \mu\text{m}$), the smallest channel size that can be created by 3-D printers is reported as $25 \mu\text{m}$ (Waheed et al., 2016). In this thesis the main emphasis is

on mixing performance analysis and design rather than the fabrication techniques used in micromixers.

CHAPTER 3. MATHEMATICAL-NUMERICAL METHODS AND SIMULATION DEFINITIONS USED

3.1 Introduction

In this chapter, mathematical models that are used to describe fluid flow and passive scalar transport processes at microscales are defined based on the assumptions made in the construction of the problem. Several dimensionless numbers are defined to characterize fluid flow and scalar transport dynamics in microchannels. The physical properties of mixing fluids are presented. To solve the governing equations, appropriate initial and boundary conditions are designated in accordance with the type of the physical problems examined. The numerical simulation packages and the tools which are employed in pre- and post-processing steps are introduced. The methods that are utilized to evaluate the mixing performance of micromixer designs are determined. To quantify average numerical diffusion errors in numerical simulations, systematic grid study approach is described. Lastly, the mathematical model and numerical methods presented are validated against the outcomes of two different experimental passive micromixer studies in the literature.

3.2 Mathematical Modelling of Fluid Flow and Passive Scalar Transport in Microchannels

In miniaturized flow systems, small dimensions can create key differences compared to the macroscopic equivalents. For instance, capillary forces, surface tension and molecular diffusion are important physical effects at submillimeter scales (Sackmann et al., 2014) whereas these effects are hardly considered in largescale systems. On the

contrary, while macroscale flow systems are strongly affected by the gravity force (Nguyen, 2012b), gravitational impacts are insignificant at microscales. At submillimeter levels, the basic principles of fluid mechanics are pertinent to describe the physical behavior of fluid flow (Nguyen, 2012a) which is described based on two models—molecular and continuum—depending on the length scale studied. Due to dominant intermolecular forces and electrostatic interactions, molecular properties of fluids are of great importance in nanofluidic discipline, which deals with the manipulation and control of fluids in nanometer-level confined channels (e.g., typically $\sim 1\text{--}100$ nanometer length (Ali et al., 2016; Pérez-Mitta et al., 2017)). Therefore, as the molecular models are exploited to define transport phenomena (e.g., mass, momentum, and energy) at nanoscales, the continuum model is used to characterize transport dynamics in the range of micrometers to centimeters.

In micromixers, fluid flow and passive scalar transport are defined at continuum level using a set of partial differential equations which are derived from the well-known mass, momentum, and energy conservation principles (Kirby, 2010; Nguyen, 2012c). In this dissertation, the main concentration is given to the investigation of single-phase liquid mixing in microchannels under isothermal fluid flow and passive scalar transport conditions. Here, we will assume that the fluids to be mixed are of constant density and viscosity, miscible and non-reactive with identical physical properties, which are presented in section 3.4. As mentioned above, gravitational effects are insignificant at microscales. These effects which are not considered in the mathematical model are treated the same way in other numerical passive micromixer studies (Galletti et al., 2012; Lin et al., 2005; Roudgar et al., 2012). In addition, it is assumed that there are no external body forces, such

as electrical and magnetic acting on the fluid flow in micromixer designs studied. Based on the assumptions above, the flow of an incompressible Newtonian fluid in a 3-D domain is described by the Navier-Stokes (NS) and continuity equations as given in Eq. (1) and Eq. (2), respectively.

$$\rho \left[\frac{\partial \mathbf{u}}{\partial t} + \mathbf{u} \cdot \nabla \mathbf{u} \right] = -\nabla p + \mu \nabla^2 \mathbf{u} \quad (1)$$

$$\nabla \cdot \mathbf{u} = 0 \quad (2)$$

Where μ is the dynamic viscosity (Pa·s), p is pressure (Pa), ρ is the fluid density (kg/m³), $\mathbf{u} = (u_x, u_y, u_z)$ is the velocity vector and $\nabla = \left(\frac{\partial}{\partial x}, \frac{\partial}{\partial y}, \frac{\partial}{\partial z} \right)$ is the del operator.

To investigate fluid mixing in the micromixer designs studied, advection–diffusion (AD) equation is used as given in Eq. (3), in which C and D denote scalar concentration and molecular diffusion constant (m²/s), respectively. The AD equation basically describes the transport of a passive scalar (i.e., an ideal non-reactive material (Ouro et al., 2018)) in the micromixer by advection and diffusion processes. While the former occurs due to bulk motion of fluids in microchannels, the latter is driven by the gradient of scalar concentration and is defined as the net movement of particles from a higher concentration domain to a lower concentration domain by Brownian motion (Rasouli et al., 2018). In this sense, the term, passive, implies that the fluid flow within which the scalar is transported is not affected by that scalar.

$$\frac{\partial C}{\partial t} + \mathbf{u} \cdot \nabla C = D \nabla^2 C \quad (3)$$

3.3 Dimensionless Numbers

In micromixer studies, several dimensionless numbers, such as Reynolds (Re), Schmidt (Sc) and Peclet (Pe) number are typically used to determine the fluid flow and scalar transport characteristics as given in Eq. (4), Eq. (5) and Eq. (6), respectively. In a flow system, laminar or turbulent character of the flow is identified by the magnitude of the Re number which denotes the ratio of inertial forces to viscous forces. In CFD studies, $Re = 2300$ is usually accepted as the critical point (Nguyen and Wu, 2005; Tran-Minh et al., 2014) after which flow regime begins to shift from laminar flow to turbulent flow. In microchannels, Re number is typically far below than this transition point, and therefore dominant viscous effects inherently create strict laminar flow conditions.

$$Re = \frac{\bar{u}D_h}{\nu} \quad (4)$$

$$Sc = \frac{\nu}{D} \quad (5)$$

$$Pe = \frac{\bar{u}D_h}{D} = ReSc \quad (6)$$

Where \bar{u} is the average flow velocity (m/s) on a given cross-section, ν is the kinematic viscosity (m^2/s) which is defined as the ratio of dynamic viscosity to fluid density as given in Eq. (7), D_h is the characteristic length which is assumed to be hydraulic diameter of a duct (m) as defined in Eq. (8) in which A is the area (m^2) and P_w is the wetted perimeter of the duct (m).

$$\nu = \frac{\mu}{\rho} \quad (7)$$

$$D_h = \frac{4A}{P_w} \quad (8)$$

The Sc number is defined as the ratio of momentum diffusivity to mass diffusivity and is mainly used to quantify the character of mass transfer due to momentum or molecular diffusion (Bergman et al., 2011). In laminar flows, a high Sc number indicate difficult fluid mixing conditions since dominant momentum diffusion will create a thick hydrodynamic layer relative to the boundary layer of molecular diffusion.

The Pe number represents the ratio of species transport rate due to advection and diffusion. High Pe numbers indicate challenging mixing conditions where species transport dominantly takes place due to advection rather than diffusion. Meanwhile, the Pe number can also be defined as the product of the Re number and Sc number as formulized in Eq. (6). In this dissertation, Re and Pe numbers are computed in the exit channel of the micromixers examined.

In addition to the above characteristic numbers, cell Reynolds (Re_Δ) and cell Peclet (Pe_Δ) numbers, which are presented in Eq. (9) and Eq. (10), respectively, are also used observe the accuracy and stability of a numerical solution. For instance, when Re_Δ or Pe_Δ number is greater than 1 in FEM, oscillatory numerical solutions are yielded due to inadequate resolution of large gradients in flow and scalar transport domains. Similar numerical problems also occur in FVM depending on the magnitude of Re_Δ and Pe_Δ as will be examined thoroughly in Chapter 4.

$$Re_{\Delta} = \frac{\bar{u}\Delta x}{\nu} \quad (9)$$

$$Pe_{\Delta} = \frac{\bar{u}\Delta x}{D} \quad (10)$$

Where Δx is the average grid size on a given cross-section and the subscript delta implies cell Reynolds and Peclet numbers. In this study, Re_{Δ} and Pe_{Δ} are calculated as an average value as defined and practiced in Reference (M. Liu, 2011) since the magnitude of velocity differs locally across a given cross-section in the computational domain.

3.4 Simulation Setup and Numerical Solution of Governing Equations

In this research, Computational Fluid Dynamics (CFD) simulations are utilized to resolve fluid flow and scalar transport fields in the passive micromixers examined. Numerical simulations are conducted as steady-state or time-dependent depending on the feeding type of the micromixers with the mixing fluids. While the former is used in cases where the fluid injection is constant over time that is the case in the majority of the research, the latter is used only in Chapter 6 where sequential (or pulse) fluid injection is applied. To investigate fluid mixing under steady-state conditions, numerical simulations are conducted in two stages as follows. First, a steady-state flow domain is obtained from the simultaneous solution of Eq. (1) and Eq. (2). Second, a steady-state passive scalar transport simulation is carried out by solving Eq. (3) utilizing the stationary flow domain obtained. In unsteady fluid injection conditions, a single, time-dependent simulation is performed for the coupled fluid flow and scalar transport equations given in Eq. (1)–(3).

To solve the governing fluid flow equations, the following boundary conditions are prescribed in the numerical simulations: a uniform velocity profile at the inlets, zero-gauge pressure at the outlet, and zero fluid velocity, i.e., no-slip condition, on the walls of the micromixers. In addition, zero gradient boundary condition is imposed for the velocity at outlet boundaries. Meaning that the velocity is developed at the exit of the micromixers, and therefore its gradient is equal to zero in the direction perpendicular to the exit surface. As an initial condition, the flow domain is filled with the mixing fluid and the medium is stagnant. In all scenarios, an equal amount of fluid is injected from the inlets of micromixers depending on the flow condition, i.e., Re number, simulated. In numerical solution of the AD equation, the gradient of scalar concentration is set to zero at the outlet and wall surfaces of the micromixers. The zero gradient boundary condition is applied to prevent the scalar undergo diffusion over the above boundaries. In all micromixer designs examined, fluid mixing is investigated by imposing relative scalar concentrations, 0 and 1, from the inlets of micromixers as described schematically in each chapter. The initial value of scalar concentration is set to be zero in the computational domain of the micromixer designs examined. All the boundary conditions, designated to solve the governing fluid flow and passive scalar transport equations, are tabulated in Table 3.1.

Table 3.1 Boundary conditions and physical fluid properties.

Simulation	Fluid Properties	Boundary	Boundary Condition
Laminar Fluid Flow	$\rho = 1.0 \times 10^3 \text{ kg/m}^3$ $\mu = 1.0 \times 10^{-3} \text{ Pa}\cdot\text{s}$	Inlet Outlet Wall	Uniform Inflow $p = 0, \partial u / \partial \mathbf{n} = 0$ No-Slip
Passive Scalar Transport	$D_1 = 3.0 \times 10^{-10} \text{ m}^2/\text{s}$ $D_2 = 1.5 \times 10^{-9} \text{ m}^2/\text{s}$ $D_3 = 3.0 \times 10^{-9} \text{ m}^2/\text{s}$	Inlet Outlet Wall	$C = 1 \text{ or } C = 0$ $\partial C / \partial \mathbf{n} = 0$ $\partial C / \partial \mathbf{n} = 0$

Throughout the research, identical fluids are employed to investigate the mixing performance of micromixer designs studied. The physical properties of mixing fluids are chosen close to that of water at 20 °C (Mubashshir Ahmad Ansari et al., 2010; Izadpanah et al., 2018) with a density (ρ) and viscosity (μ) of $1 \times 10^3 \text{ kg/m}^3$ and $1 \times 10^{-3} \text{ Pa}\cdot\text{s}$, respectively. It is worth noting that water is usually preferred as a carrying fluid in most numerical and experimental micromixer studies as can be seen in References (Roudgar et al., 2012; Silva et al., 2017; Soleymani et al., 2008). This is due to the fact that water is the most common solvent that is utilized in several chemical and biological processes. To investigate the numerical diffusion errors and mixing characteristics of micromixers in different advection dominance conditions, three different molecular diffusion constants are determined as given in Table 3.1. The magnitudes of molecular diffusion coefficients chosen are small enough to cover several large molecules and electrolytes in chemical and

biological solutions (Nguyen, 2012b) as typically employed in several passive micromixer studies (Bhopte et al., 2010; Gidde et al., 2017; Roudgar et al., 2012).

In this dissertation, numerical solution of the governing partial differential equations is carried out using both Finite Volume Method (FVM) and Finite Element Method (FEM) with two different CFD tools. These are OpenFOAM (v5.0, OpenFOAM Foundation, OpenCFD Ltd., Bracknell, UK) and COMSOL Multiphysics® (v5.3a, COMSOL AB, Stockholm, Sweden), respectively. However, it should be noted that while the FVM was employed as the main solver throughout the research to investigate both numerical diffusion errors and fluid mixing in the micromixer designs, the FEM is only utilized in the Chapter 4 to examine the effects of artificial diffusion stabilization technique in numerical micromixer studies.

OpenFOAM is a non-commercial, open-source CFD software based on the FVM application, in which both structured and unstructured meshes can be used. In all numerical simulations, the following solvers provided in OpenFOAM library are employed. To solve the governing equations for steady-state, incompressible and laminar fluid flow, the simpleFOAM solver is utilized in which the SIMPLEC (semi-implicit method for pressure linked equations-consistent) (Van Doormaal and Raithby, 1984) algorithm is used to solve pressure-velocity coupling. In the flow equation, convection and diffusion terms are discretized using the second-order upwind (Warming and Beam, 1976) (i.e., Gauss linearUpwind) and second-order central difference (Moukalled et al., 2015) (i.e., Gauss linear) schemes, respectively. The AD equation is solved utilizing the scalarTransportFoam solver in which, while the second-order central difference scheme (i.e., Gauss linear) is used to treat the diffusion terms, various numerical algorithms (e.g., first-order upwind,

second-order upwind, QUICK, MUSCL, limitedLinear (Sweby, 1984)) are tested to discretize the advection terms. The outcomes of the test simulations are presented comparatively in Chapter 4. It should be noted that while the second-order upwind scheme (i.e., Gauss linearUpwind) is chosen as a standard numerical scheme to discretize advection terms in the AD equation, other numerical schemes are used only in Chapter 4 to observe and ensure the boundedness of scalar concentrations in both structured and unstructured meshes. To improve stability in steady-state computations, under-relaxation technique (Moukalled et al., 2015) is exploited with a relaxation factor of 0.9 for the velocity and scalar variables. In all steady-state simulations, iterations are continued until the initial residuals of pressure, velocity, and scalar transport equations fall below 10^{-6} which is assumed to yield converged solutions as typically practiced in the numerical passive micromixer literature (Mubashshir Ahmad Ansari and kim, 2009; J. Li et al., 2013; Roudgar et al., 2012). The threshold of convergence criterion is reduced to 1×10^{-12} in cases where engulfment flow profile is expected in a classical T-shaped micromixer (i.e., $Re > 140$). Further information about the numerical simulation of engulfment flows can be found in Reference (Galletti et al., 2012). In time-dependent simulations, a modified form icoFOAM solver is exploited to solve coupled fluid flow and scalar transport equations. While second-order upwind and central difference schemes are utilized to discretize advection and diffusion terms, respectively, temporal terms are discretized using the Crank-Nicolson scheme with an off-centering coefficient of 0.9 (OpenFOAM.). In transient simulations, time steps are chosen small-enough to meet Courant–Friedrichs–Lewy (CFL) stability condition that is $CFL \leq 1$ (Moukalled et al., 2015). Note that in this dissertation, time-dependent solutions are obtained with a maximum CFL number of 0.5.

In cases where the FVM is employed, non-commercial Gmsh (Geuzaine and Remacle, 2009) and Paraview (Ahrens et al., 2005) packages are used in pre– and post–processing steps to generate micromixer designs and visualize simulations outcomes, respectively. Matlab software (v2016a, MATLAB, Natick, Massachusetts, US) is employed to process the data throughout the research.

COMSOL Multiphysics®, which is a commercial CFD software, was employed to analyze the artificial diffusion effects in numerical solutions where FEM is employed to simulate advection-dominant transport systems. In COMSOL Multiphysics® package, standard simulation modules, laminar flow and transport of diluted species, are utilized to resolve fluid flow and scalar transport domains, respectively. The built-in geometry interface in the software was used to generate the micromixer geometry and discretize the computational domain. For the purpose of uniformity between FVM and FEM solutions, second-order discretization accuracy is also maintained in FEM simulations. In addition, the convergence level of steady-state fluid flow and scalar transport equations were set equivalent to that of FVM simulations. To dampen the oscillation effects during the solution of governing fluid flow and passive scalar transport equations, COMSOL Multiphysics® provides two stabilization options which are referred as consistent and inconsistent (or isotropic diffusion) methods. In the consistent method, directions and gradients of variables are evaluated by the solver and appropriate corrections are made in both streamwise and cross-wind directions. In the inconsistent stabilization, physical diffusivity (momentum or molecular) is increased artificially to reduce Re_{Δ} or Pe_{Δ} number—depending on the physical problem type—in the simulation and obtain a stable solution. In this research, simulations are conducted for both correction methods to show

artificial diffusion effects in numerical solutions. Here, it should be noted that artificial diffusion stabilization in FEM applications is a well-documented method in the current literature (Kuzmin, 2010; Patankar, 1980). Thus, the implementation of this method in FEM is exhaustively explained in Chapter 4. On the other hand, the consistent stabilization technique is offered as a black box in the software, and hence the numerical details of this correction approach could not be obtained. The overall information about stabilization methods can be found in the laminar flow and transport of diluted species modules user's guide in COMSOL Multiphysics® package (v5.3a, COMSOL AB, Stockholm, Sweden). Therefore, the performance of both stabilization approaches is evaluated comparatively based on the simulation outcomes.

In this dissertation, FEM and FVM simulations were performed on a personal computer with an Intel Core i7-6900K processor (Intel Corporation, Santa Clara, CA, USA), which was overclocked to run at 4.2 GHz, and 64 GB 3200 MHz random-access memory (RAM).

3.5 Quantification of The Degree of Mixing in Micromixers

In numerical passive micromixer studies, mixing efficiency on a given cross-section is typically measured using the mixing index (MI) approach, which is computed based on the standard deviation of scalar concentration from the mean concentration on the cross-section, as formulated in Eq. (11)–(12) (Cai et al., 2017; Gidde et al., 2017; Ortega-Casanova and Lai, 2018).

$$MI = 1 - \sqrt{\frac{\sigma^2}{\sigma_{\max}^2}} \quad (11)$$

$$\sigma^2 = \frac{1}{N} \sum_{i=1}^N (C_i - C_m)^2 \quad (12)$$

Where σ and σ_{\max} are the standard deviation and maximum standard deviation of scalar concentration on the cross-section respectively, C_i is the concentration at i_{th} sampling point, C_m is mean concentration and N is the total number of sampling points on the cross-section. Nonetheless, it should be noted that the use of Eq. (11)–(12) to quantify the degree of mixing on a certain plane is limited to the cases where the distribution of scalar concentration is uniform on that plane. When scalar concentration is not distributed uniformly across a flow profile and concentrated at a specific region in that profile as shown schematically in Figure 3.1, employing a method based on only the standard deviation of scalar concentration may cause inaccurate evaluation of mixing efficiency. As may be seen in Figure 3.1, the amount of fluid carried at the center of a parabolic velocity profile is higher than that of carried in the regions close to the channel walls. In such circumstances, it is important to involve the effect of flowrate to avoid over- or underestimate the mixing value on the cross-section examined. For this purpose, the modified version of MI should be used as formulated through Eq. (13)–(15), which is also known as flowrate-averaged mixing concept (i.e., cup mixing) in the literature (Roudgar et al., 2012). Furthermore, it is worth noting that in the case of symmetrical flow profile and uniform concentration distribution on a cross-section, both MI approaches yield the same mixing value.

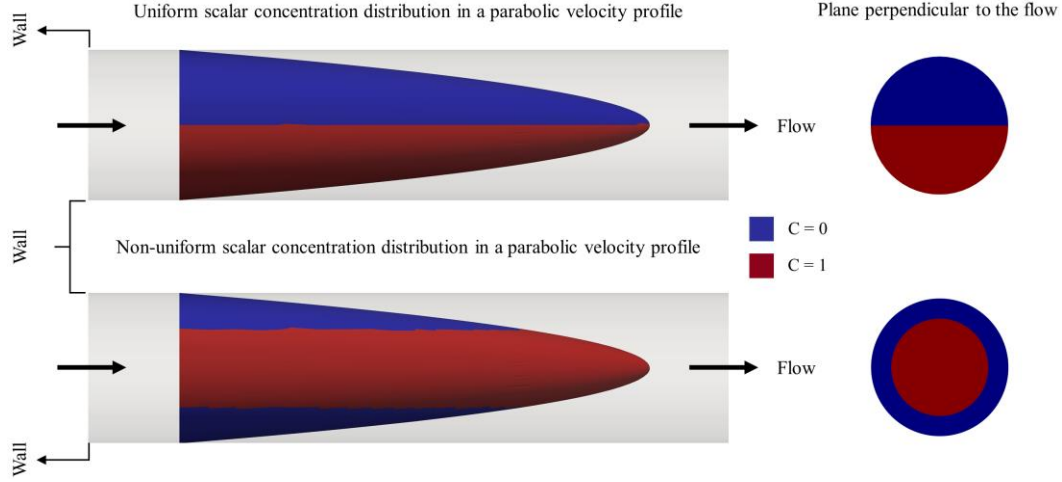


Figure 3.1 Uniform and non-uniform distribution of scalar concentration in a parabolic velocity profile.

$$MI = 1 - \sqrt{\frac{\sigma^2}{\sigma_{\max}^2}} \quad (13)$$

$$\sigma^2 = \frac{\int_A (C_i - \bar{C})^2 \cdot u_i dA}{\int_A u_i dA} \quad (14)$$

$$\bar{C} = \frac{\int_A C_i \cdot u_i dA}{\int_A u_i dA} \quad (15)$$

Where \bar{C} , u_i , and A are flowrate-averaged scalar concentration on the cross-section, velocity at i_{th} sampling point and cross-section area, respectively.

The range of MI changes between 0 and 1 which correspond unmixed (0%) and complete mixed (100%) mixing states, respectively. To maintain consistency in the dissertation, the same notation, i.e., MI, is used for both mixing efficiency quantification approaches given above. However, it should be noted that while Eq. (11)–(12) are used

only in Chapter 4 due to uniform scalar distribution in all micromixer designs studied, Eq. (13)–(15) are used in Chapter 5 and Chapter 6 since some injection scenarios cause scalar concentration to be centralized at specific regions of the flow profile. Meanwhile, in this study, mixing quality (MQ) of a micromixer is defined as outlet mixing index (MI_{Outlet}) per kPa pressure drop (Δp) in the micromixer as given in Eq. (16). As the Δp is considered to be the pressure loss between inlet (p_{in}) and outlet (p_{out}) of the micromixer as given in Eq. (17), pressure value on a given plane is computed using Eq. (18), in which A denotes the surface area.

$$MQ = \frac{MI_{Outlet}}{\Delta p} \quad (16)$$

$$\Delta p = p_{in} - p_{out} \quad (17)$$

$$p = \frac{\int_A p dA}{\int_A dA} \quad (18)$$

3.6 Mesh Refinement Study and Quantification of Numerical Diffusion Errors

In CFD applications, mesh generation is a pivotal stage since spatial discretization errors will inherently affect the numerical solution. Theoretically, it is known that temporal and spatial discretization errors asymptotically approach zero by reducing the time step and mesh element size. Nonetheless, as the mesh is refined, computational cost and the solution time increases in parallel. Accordingly, an optimized solution in terms of accuracy, computational cost and solution time becomes essential. The aim of systematic grid studies in CFD applications is to manage spatial discretization errors and choose an appropriate

mesh density that is computationally feasible (Freitas, 2002). In this dissertation, a systematic mesh study is conducted before the numerical simulations of all micromixer designs examined. For this purpose, several mesh levels are determined to observe and quantify the evolution of spatial discretization errors with reducing grid sizes. Eq (19) is used to measure the discrepancy between a certain mesh level and the finest mesh for a given parameter.

$$\Delta D(P)_{L(F)-L} = \left| \frac{P_L - P_{L(F)}}{P_{L(F)}} \right| \times 100 \quad (19)$$

Where $P_{L(F)}$ and P_L denote the parameter values, obtained from the numerical solutions of the finest and a certain mesh level, respectively. $\Delta D(P)_{L(F)-L}$ shows the difference, as a percentage, between a mesh level and the finest mesh with respect to the parameter employed. To determine a grid level properly, mesh studies are performed for the worst-case scenario of both fluid flow and scalar transport, i.e., the highest Re and Pe conditions, in all micromixer designs examined. While pressure drop and average velocity values are employed as flow parameters, MI is used as a scalar transport parameter. When the difference between a certain mesh level and the finest mesh is less than 5% for the parameters tested, further refinement is not considered. In this case, the coarser mesh level is selected for the rest of the simulations since a substantial increase in computational cost will provide a trivial accuracy gain.

In this study, average numerical diffusion in a passive scalar transport simulation, where FVM is used to discretize the governing equations, is quantified utilizing the procedure proposed in Reference (M. Liu, 2011). In this approach, effective diffusion

coefficient (D_E) is defined to represent the actual diffusivity in the numerical solution, which is approximately sum of the molecular and numerical diffusion coefficients as given in Eq. (20), in which D_M and D_N denote the molecular (or physical) and numerical diffusion coefficients, respectively.

$$D_E \approx D_M + D_N \quad (20)$$

The effective diffusivity in Eq. (20) is computed using the numerical solution of a passive scalar transport as formulated in Eq. (21).

$$D_E = \frac{\overline{C_{inlet}^2} - \overline{C_{outlet}^2}}{2\tau(\nabla C)_{\forall}^2} \quad (21)$$

Where

$$\overline{C_{inlet}^2} = \frac{1}{Q} \int_{A_{inlet}} \mathbf{n} \cdot \mathbf{u} C^2 dA \quad (22)$$

$$\overline{C_{outlet}^2} = \frac{1}{Q} \int_{A_{outlet}} \mathbf{n} \cdot \mathbf{u} C^2 dA \quad (23)$$

$$\overline{(\nabla C)_{\forall}^2} = \frac{1}{V} \int_V (\nabla C) \cdot (\nabla C) dV \quad (24)$$

$$\tau = \frac{V}{Q} \quad (25)$$

In these equations, C is the scalar concentration, \mathbf{n} is the unit normal of a surface, V is the micromixer volume, Q is the volumetric flow rate, $\overline{C_{inlet}^2}$ and $\overline{C_{outlet}^2}$ are the flow rate

weighted average mass fractions of the transported scalar at the inlet and outlet, respectively, $\overline{(\nabla C)_V}^2$ is the volume-averaged scalar concentration gradient in the transport domain, A_{inlet} and A_{outlet} are the area of inlet and outlet surfaces of a micromixer respectively and is the theoretical mean fluid residence time in the micromixer.

Given Eq. (20), average numerical diffusion can be calculated by setting the molecular diffusion constant to zero in a passive scalar transport simulation and the effective diffusivity calculated will represent the average value of numerical diffusion expected in the numerical solution of the AD equation. Therefore, to quantify an average numerical diffusion value in passive scalar transport simulations, the following steps are practiced. Initially, a steady-state flow field of a flow condition examined is obtained as described in section 3.4. Later, using this constant flow domain, two different steady-state passive scalar transport simulations are performed as follows:

In the first simulation, the AD equation is solved by setting the molecular diffusion constant to zero (i.e., $D = D_M = 0 \text{ m}^2/\text{s}$, pure advection case) and this numerical solution is used to compute an effective diffusion constant using Eq. (21). In this case, the amount of effective diffusion computed represents the average numerical diffusion in the numerical solution (i.e., $D_E \approx D_N$) as stated before. The same numerical solution of the AD equation, i.e., pure advection case where $D = D_M = 0 \text{ m}^2/\text{s}$, is also exploited to calculate a mixing efficiency at the outlet of the micromixer using Eq. (11)–(12). For convenience, the mixing efficiency, obtained from the pure advection solution, is defined as “false mixing” since it is created by the numerical diffusion errors in the numerical solution of the AD equation. At this point, it should be noted that equating the molecular diffusion constant to zero

makes the AD equation mathematically stiff as also reported in Reference (M. Liu, 2011). In this case, numerical solution of the AD equation may be quite difficult to obtain a stable solution. However, all numerical schemes employed in this study have provided a converged solution without causing any significant instability problem.

In the second simulation, the AD equation is solved again, but this time the molecular diffusion constant in the equation is set to its actual value (i.e., $D = D_M$). The numerical solution of the AD equation is utilized to calculate another effective diffusion constant which, in this case, reflects the collective effects of both false and physical diffusion in the numerical simulation (i.e., $D_E \approx D_N + D_M$). Therefore, a comparison of these two effective diffusion values, obtained from two different scalar transport simulations, reveals the predominant diffusion constant (i.e., D_N or D_M) in the numerical solution. Namely, when the ratio of D_E/D_M is approaching 1, the representation of molecular diffusion by the effective diffusion constant computed increases. In other words, molecular diffusion constant of the scalar is recovered from the numerical solution. When this ratio is exactly 1, it shows that the magnitude of numerical diffusion constant is several orders lower than that of molecular diffusion constant. Similarly, the ratio of D_E/D_N may also be used to show numerical diffusion effects. However, in this case, the ratio of 1 indicates that numerical diffusion errors are dominant in the numerical solution and effective diffusion constant completely represent these errors. In this dissertation, the maximum threshold of D_E/D_M ratio allowed in a numerical solution is determined to be 1.5 based on the outcomes reported in Reference (M. Liu, 2011). Thus, when the ratio of D_E/D_M is equal or less than 1.5, it is assumed that a numerical solution contains an insignificant amount of false diffusion and MI values mostly represent the physical or true performance of the

micromixers examined. When the D_E/D_M ratio exceeds this maximum threshold, mesh refinement is continued until yielding a D_E/D_M ratio of less than 1.5.

Consequently, the selection of an optimum mesh density for numerical simulations of a micromixer design is made based on the following criteria. Further refinement of a certain mesh level will change the numerical solution less than 5% for both flow and scalar transport parameters and the ratio of D_E/D_M in that mesh level will be equal or less than 1.5.

3.7 Validation Studies

The OpenFOAM package is employed to validate the numerical method against the experimental data of two different classical T-shaped (CT) passive micromixer studies that are entitled as Study A (Silva et al., 2017) and Study B (Mubashshir A. Ansari et al., 2012) in this section. The CT micromixer geometry consists of two identical inlet channels and a mixing channel as shown in Figure 3.2. In both experimental studies, authors utilized water as working fluids and investigated the mixing of equal amount fluids in each flow condition tested. The dimensions of the CT passive micromixers and physical properties of working fluids are presented in Table 3.2. In numerical simulations, computational domain is discretized using hexahedron mesh elements. Appropriate mesh densities are determined based on the highest flow condition examined in the experimental studies. The overall mesh densities, which are employed in the computational domain of the CT micromixers, are 3.2×10^6 and 1.063×10^6 elements for Study A and Study B, respectively. Steady-state scalar transport domain is obtained using the same boundary conditions and numerical settings described in section 3.4. To investigate fluid mixing in the CT micromixers,

relative scalar concentrations, 0 and 1, are injected as shown in Figure 3.2. The degree of mixing is calculated on the exit cross-section of the micromixers using Eq. (11)–(12).

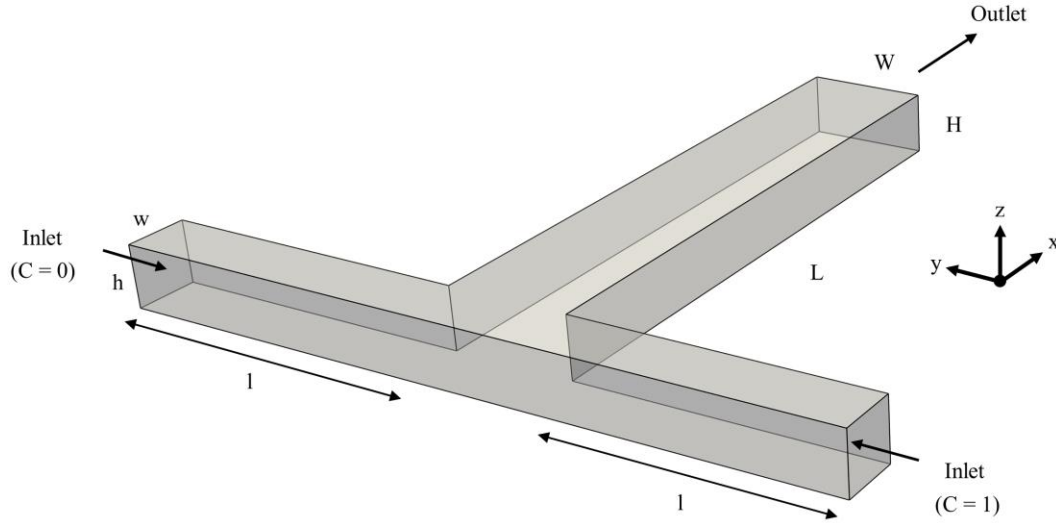


Figure 3.2 Classical T-shaped (CT) passive micromixer design.

Table 3.2 Simulation parameters employed in CFD solver validation.

CT Micromixer (units in μm)	Study A (Silva et al., 2017)	Study B (Ansari et al., 2012)
Mixing channel width (W)	200.6	200
Mixing channel height (H)	100.9	90
Micromixer length (L)	1057	7000
Inlet channel width (w)	100.3	100
Inlet channel height (h)	100.9	90
Inlet channel length (l)	500	500
Fluid Properties		
ρ (kg/m^3)	1.0×10^3	9.97×10^2
μ ($\text{kg/m}\cdot\text{s}$)	1.0×10^{-3}	9.0×10^{-4}
D (m^2/s)	2.025×10^{-9}	1.2×10^{-9}

To measure the fit of the numerical simulation outcomes to the experimental data, root mean square error (RMSE) (Neill and Hashemi, 2018) method is employed as given

in Eq. (26), in which P, E and N denote predicted value, experiment outcome and the number of experiments, respectively. The RMSE values are computed to be 0.032 and 0.02 for Study A and Study B, respectively. The mixing efficiency outcomes, which are obtained from experimental studies and numerical simulations, are plotted in Figure 3.3.

$$RMSE = \sqrt{\frac{1}{N} \sum_{i=1}^N (P_i - E_i)^2} \quad (26)$$

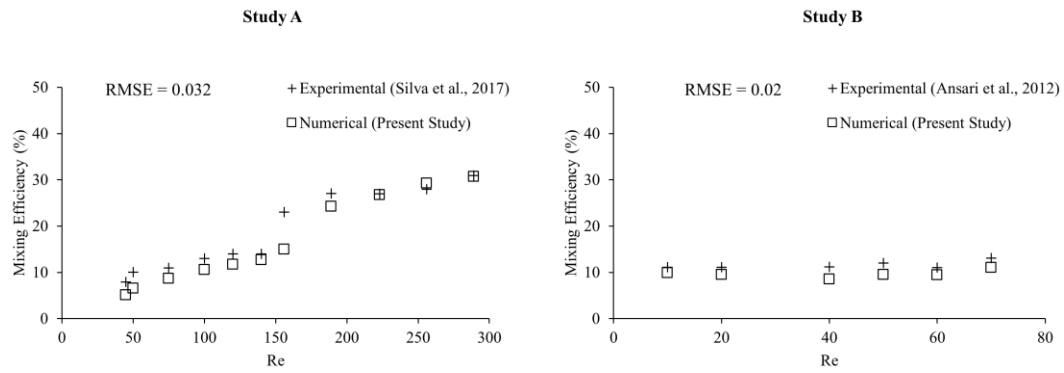


Figure 3.3 Outlet mixing efficiency vs. Re number, obtained from the experimental studies and numerical simulations.

Figure 3.3 and the small RMSE values evidently indicate that numerical simulation results are in a good agreement with the experimental data in both Study A and Study B. The numerical method presented can predict the degree of fluid mixing in micromixer designs developed in this dissertation. The overall discrepancy between the numerical and experimental mixing outcomes may be explained with the following reasons as reported in Reference (J. Zhang and Luo, 2018): the use of different techniques to measure the micromixer performance, experimental errors and complications during the fabrication process. Meanwhile, scalar concentration distributions on the exit cross-section of the

micromixers are presented in Figure 3.4 as a visual reference of the numerical mixing efficiency values plotted in Figure 3.3.

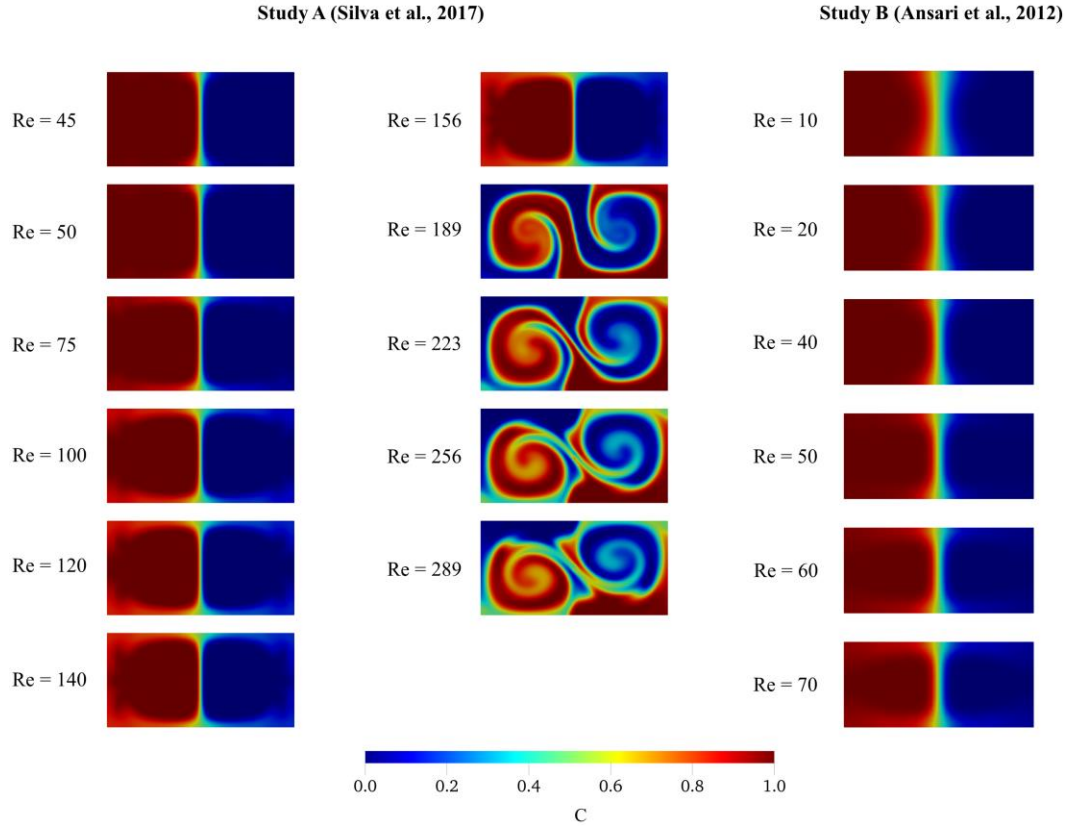


Figure 3.4 The distribution of scalar concentration at the outlet of the CT passive micromixers obtained from numerical simulations.

3.8 Summary

In this dissertation, CFD instrument is utilized to examine single-phase liquid mixing in passive micromixers. Navier–Stokes and continuity equations are employed to simulate incompressible fluid flow in microchannels. The advection-diffusion equation is used to resolve scalar transport field in the micromixers. The mixing performance of the micromixer designs is studied by employing water as working fluid in the numerical simulations. Dimensionless Reynolds, Peclet and Schmidt numbers are identified to

characterize fluid flow and scalar transport dynamics in the micromixers. While a small Reynolds number (e.g., $Re \ll 100$) defines strict laminar flow conditions in microchannels, increasing Peclet and Schmidt numbers (e.g., Pe or $Sc \gg 10^3$) indicate the difficulty of fluid mixing in the mixing domain. Two different MI approaches are presented to quantify the mixing efficiency of the micromixers. The standard or flowrate-averaged MI formulations are employed depending on the uniform or non-uniform distribution of scalar concentration in a flow profile, respectively. The numerical methods and CFD packages are introduced that is used to solve the governing fluid flow and scalar transport equations. While FVM-based OpenFOAM software is employed as the main solver throughout the research, FEM-based COMSOL Multiphysics® solver is used to investigate artificial diffusion effects in advection-dominant mixing systems. In all numerical simulations, the use of second-order accurate discretization schemes is maintained to treat spatial and temporal terms in the governing equations. The process of a systematic grid study is explained to select an appropriate mesh density in numerical simulations. The mathematical model and numerical methods presented are validated using different experimental studies in the literature. It is shown that numerical and experimental outcomes are in a good agreement. Therefore, numerical simulations can be used to investigate fluid mixing in the micromixer designs that are developed in the following chapters of this thesis.

CHAPTER 4. NUMERICAL DIFFUSION ERROR ANALYSIS IN NUMERICAL SIMULATIONS OF PASSIVE MICROMIXERS

4.1 Introduction

CFD simulations may be employed to investigate fluid flow and scalar transport at microscales. FVM and FEM are the two numerical techniques that are commonly used in these applications. In passive micromixers, advection dominant transport conditions that is Pe number is in the order of 10^4 - 10^6 range, inherently result in sharp concentration gradients for which numerical approximation is problematic in terms of controlling the numerical errors. In the current literature on micromixer studies, the extent of numerical errors is generally either overlooked or underestimated as stated in the previous chapters. Several passive micromixer studies have investigated fluid mixing employing FVM- and FEM-based CFD solvers in which the numerical diffusion and dispersion problems that appear in the solutions have not been evaluated and reported in detail. Relying on inappropriate mesh independence studies, mixing outcomes obtained are usually accepted to reflect the actual mixing performance of micromixers with insignificant errors. However, in CFD studies of passive micromixers, numerical simulation parameters need to be evaluated and chosen carefully due to special transport conditions that appear in these systems. As will be shown in this chapter, the magnitude of numerical errors in a numerical solution may even mask the physical mixing entirely depending on the characteristics of several simulation factors. From a general perspective, the components that are of great importance in numerical simulation of advection dominant transport systems are numerical algorithms, numerical stabilization techniques, discretization schemes, and the properties

of the mesh used. In aggregate, these choices may prevent the proper representation of fluid flow and mixing processes in numerical analysis of passive micromixer applications. Thus, there is a need to characterize and report these errors establish the reliability of the results.

It should be emphasized that the focus of this chapter is not on improving the mixing efficiency of a passive micromixer design examples that are examined in this chapter. Instead, depending on the aforementioned factors, the focus of this chapter is on investigation and characterization of numerical errors in passive micromixer simulations. In reference to this objective, the following two sections are handled in detail in Chapter 4.

In Section 4.4, a classical 3-D T-shape passive micromixer design is used to characterize numerical diffusion errors in mostly unidirectional flow systems. The effect of several grid types and grid sizes are examined under various flow conditions. False diffusion levels that are generated in numerical solutions are quantified and mesh densities that are required to minimize false diffusion levels are determined depending on the simulation results obtained. Also, the effect of artificial diffusion stabilization technique used in the FEM is discussed and the outcomes are compared with that of the FVM.

In Section 4.5, 3-D swirl-generating passive micromixer configurations are employed to investigate numerical diffusion errors in advection dominant scalar transport systems where secondary flows are dominant and grid-flow alignment is continuously violated. Several mesh densities, flow conditions and scalar transport scenarios are evaluated to characterize the limits of the numerical diffusion produced in the micromixer that is studied. Simulations are conducted utilizing hexahedron-type mesh elements in all

computational domains for consistency. The governing equations and boundary conditions were reviewed in Chapter 3.

4.2 Background

The two important numerical complications in the CFD studies of passive micromixers are the numerical diffusion errors (i.e., false, artificial, or unphysical diffusion) and the numerical dispersion effects. While numerical diffusion arises from the numerical approximation of the advection term in the AD equation (Bailey, 2017) which cause smearing of the sharp gradients of the concentration front in the solution, numerical dispersion occurs as the instability problems (i.e., oscillations) due to inaccurate numerical resolution of the sharp gradient locations in terms of the algorithms used in the solution of the AD equation (Moukalled et al., 2015). Both of these errors are described schematically on a classical T-shape micromixer as shown in Figure 4.1. It should be noted that both numerical complications also occur in the numerical approximation of the momentum transport equation. For that case, relatively higher kinematic viscosity values of fluids (e.g., 10^{-3} – 10^{-7} m²/s (Bailey, 2017)) against very low molecular diffusion constants (e.g., 10^{-11} – 10^{-9} m²/s) reduce the numerical viscosity (i.e., false, artificial, or unphysical viscosity) and thus numerical dispersion errors substantially. Therefore, these errors are more pronounced especially in numerical simulations of advection dominant scalar transport systems where AD equation is used.

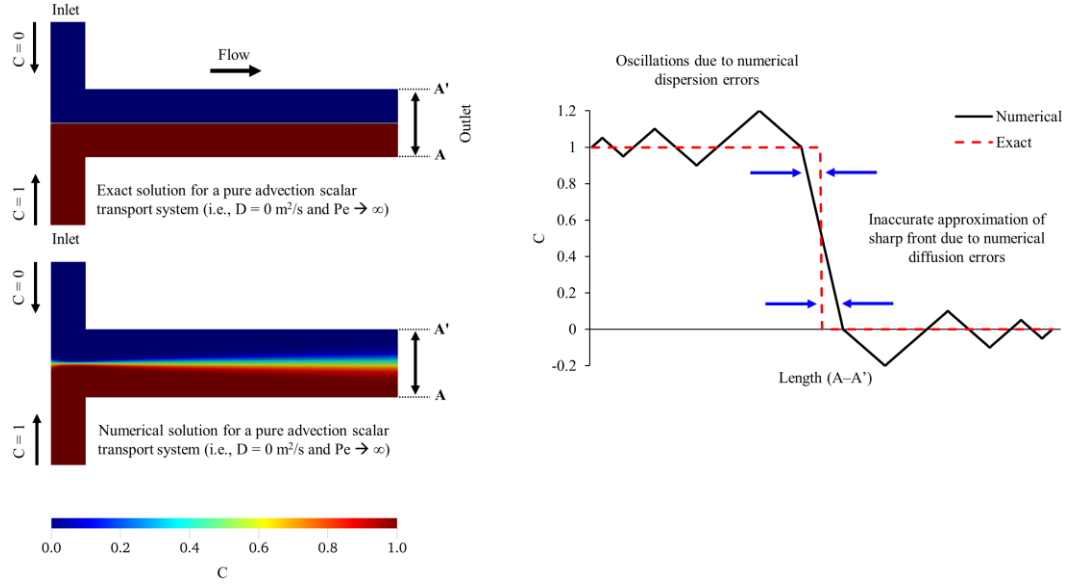


Figure 4.1 Schematic description of numerical diffusion and dispersion errors for a pure advection scalar transport in a classical T-shape passive micromixer.

The degree of numerical diffusion and dispersion errors changes with the numerical scheme that is utilized to discretize the advection terms in the governing equations. For instance, first-order accurate discretization schemes (e.g., upwind, power law, and hybrid schemes) are known to be more diffusive algorithms, yet they are also the most stable schemes when they are compared with higher order algorithms (i.e., second-order and higher). Godunov and Ryaben'kii (Godunov and Ryaben'kii, 1963) showed that a linear monotone scheme which does not create over- and under-shoots (e.g., as shown on the plot in Figure 4.1) can be at most first-order accurate. Therefore, although high order numerical schemes may present instability problems in numerical approximation of sharp gradients, relatively much lower numerical diffusion generation characteristics make high order schemes a preferred option in numerical simulations of advection dominant transport systems.

In CFD applications, particularly for advection dominant problems, FVM is more advantageous and provide relatively more consistent results (Idelsohn and Oñate, 1994) due to its conservative solution structure for mass, momentum and energy transport. In addition, in this method, it is also shown that if the flow direction is orthogonal to the grid lines or in other words, flow direction and grid lines are aligned in the computational domain, the numerical solution does not produce false diffusion (Patankar, 1980). The amount of false diffusion increases when the angle between streamlines and gridlines approaches to 45° . However, for most micromixer geometries maintaining a good mesh–flow alignment in the computational domain may be rather difficult and numerical solution inevitably exhibits the negative effects of false diffusion.

Meanwhile, although numerical diffusion is also a problem for FEM, this method mostly suffers from instability issues especially when working with advection dominant systems (Gresho and Lee, 1981). In this technique, while it is possible to avoid unwanted node-to-node oscillations by grid refinements, this approach is generally not practical because of high computational costs at fine grids. A practical approach to stabilize oscillations in FEM is known as artificial diffusion (or artificial viscosity for fluid flow) stabilization (Kuzmin, 2010) in which molecular diffusion constant (or fluid viscosity) is increased artificially at the cost of excess diffusion (or viscosity) that is added to the system. Although this method may be suitable for macroscale mixing systems where the effect of molecular diffusion is negligible, the use of this approach in passive micromixer applications will create confusion in the evaluation of the mixing performance. An accurate evaluation of fluid mixing in these systems becomes impossible since numerically added artificial diffusion and the physical molecular diffusion will both contribute to the mixing

outcome at different proportions which cannot be distinguished from one another. Therefore, artificial diffusion stabilization approach may seriously affect the interpretation of the mixing outcome of micromixer designs since excess diffusion added will entirely change the physics of the problem that is examined.

Considering the special mixing conditions that appear at micro scales, the accurate prediction and evaluation of mixing characteristics are crucial in reporting the reliability of physical mixing results. In CFD applications researchers have introduced several techniques for both FVM and FEM in the solution of fluid flow and scalar transport equations more accurately. This is done by suppressing the negative effects of numerical diffusion and dispersion errors. The most popular techniques used in stabilization of FEM and high-resolution schemes applied in FVM can be found in References (Oñate and Manzan, 2000) and (Moukalled et al., 2015) respectively with evidence of deficiencies in both techniques. Unfortunately, none of these methods are problem-free. In most cases, complete elimination of numerical errors is not possible, but quantifying the presence of these errors are necessary to provide physically reliable and unsusceptible results in the evaluation of mixing performance of micromixer designs.

4.3 Qualitative Description of The Numerical Diffusion Problem in FVM

In FVM, numerical diffusion develops in the discretization of the advection terms of the AD equation. The magnitude of this error changes depending on the accuracy of the numerical solution scheme employed, flow velocity, grid size, and the angle between flow velocity and grid boundaries (M. Liu, 2011). In Figure 4.2, the extent of false diffusion effects in FVM are qualitatively shown for various discretization schemes, grid sizes, and

mesh-flow alignment scenarios. In the literature, this is also known as the standard test as described and used in Reference (Bailey, 2017). In a 2-D square domain with an edge size of $1000\text{ }\mu\text{m}$, a constant flow field is set across the domain for three different cases and each case was also tested for two different mesh levels, L1 (400 elements) and L2 (10,000 elements), using first-order and second-order accurate upwind numerical schemes. While Figure 4.2a and Figure 4.2b show 45° and 0° flow-grid alignment for equally spaced square grid type respectively, Figure 4.2c shows randomly changing flow orientation for a triangular mesh system. The constant flow fields applied for scenario (b) and scenarios (a) and (c) are $(u, v) = (0.01\text{ m/s}, 0)$ and $(0.01\text{ m/s}, 0.01\text{ m/s})$ respectively, which corresponds to $\text{Re} = 10$ as calculated in (Bailey, 2017). Thus, Figure 4.2 shows a steady-state scalar transport solution of a pure advection system (i.e., $D = 0\text{ m}^2/\text{s}$, $\text{Pe} \rightarrow \infty$) with the imposed scalar values of 0 and 1 in inflow boundaries as shown in Figure 4.2a–c. The gradient of transported scalar at all other boundaries are set to zero.

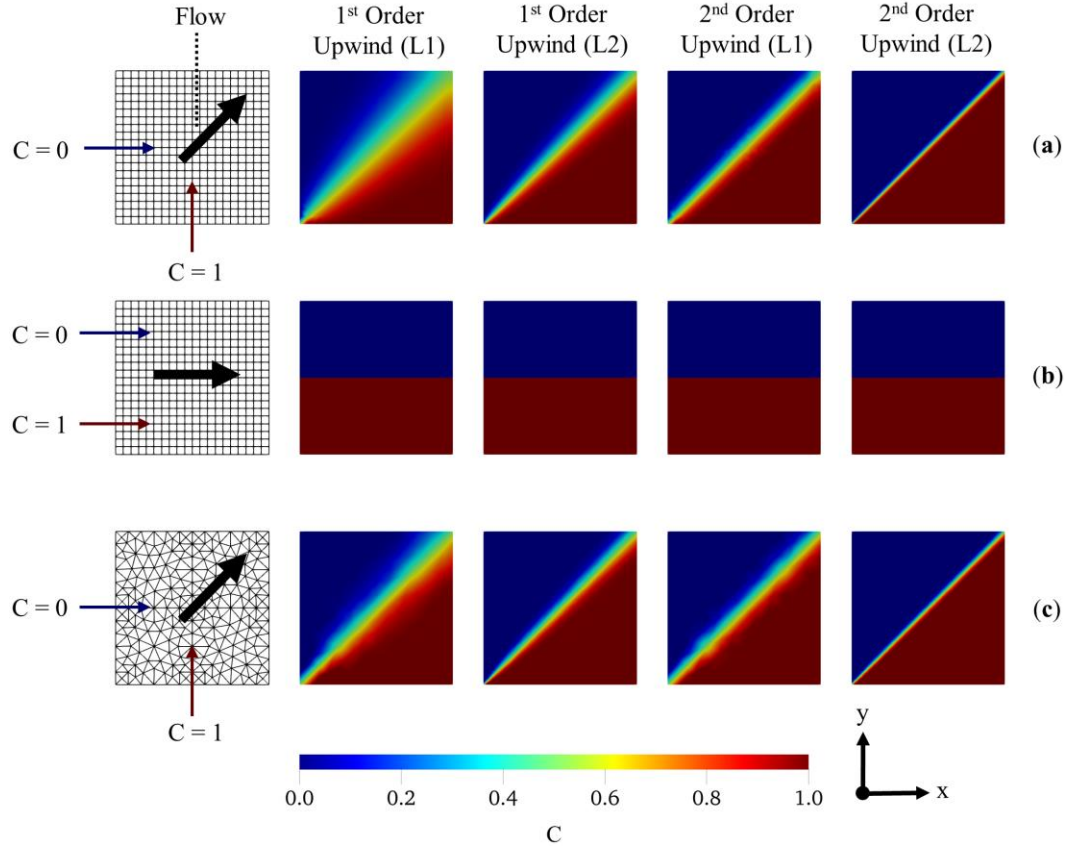


Figure 4.2 Transported scalar distributions in different grid-flow alignment conditions of the 2-D test: (a) square elements with 45° flow angle; (b) square elements with 0° flow angle (orthogonal); and (c) triangular elements with randomly changing flow-boundary angle.

As can be seen from Figure 4.2b, numerical diffusion does not exist when fluid flow is orthogonal to the grid boundaries even if the first-order accurate upwind scheme and coarser grid elements are used. In contrast, when flow is oblique to the grid lines, the solution creates numerical diffusion depending on the angle between flow and grid lines. As shown in Figure 4.2a, when this angle is constant at 45°, the numerical solution creates the maximum amount of false diffusion on the coarser grid, L1. When triangular elements are employed, the amount of false diffusion produced is less than the worst-case scenario (a) at L1, but the solution still contains a substantial amount of false diffusion as a result of randomly changing flow and grid alignment as shown in Figure 4.2c. Thus, less

numerical diffusion with the use of triangular elements is due to relatively less obliqueness between flow direction and element boundary as a result of random orientation of the boundaries which may yield orthogonality for some elements throughout the domain. On the other hand, it is notable that using a second-order accurate scheme for discretization of the advection term and grid refinement significantly reduces the amount of numerical diffusion generated for scenarios (a) and (c). However, it should be pointed that using a very fine mesh in passive micromixer studies may not be practical and possible due to a high computational cost.

In Figure 4.3, the same 2-D standard test is extended to a four-inlet case. In this case, the numerical diffusion generated is increased as a result of enlarged contact surfaces between fluid bodies. It may be seen in Figure 4.3d that the first-order accurate upwind scheme along with a relatively coarse mesh yield a completely different result than the physical problem. Like the case in Figure 4.2a, constantly maintained 45° grid-flow angle creates the maximum false diffusion along the contact surface of the fluid pairs in the streamwise direction. However, in this scenario the expanded contact surface between fluid pairs makes the outcome worse by generating more false diffusion in the solution. When Figure 4.3d is compared with Figure 4.3f and Figure 4.3g, the use of triangular elements results in less false diffusion because of reduced inclination between the flow and grid boundaries. Moreover, applying a unidirectional flow slightly diminishes the false diffusion production as depicted in Figure 4.3g. This occurs because of improved mesh-flow orthogonality within the transport domain. The four-inlet numerical simulations produce higher amounts of numerical errors than the two-inlet solutions under the same flow conditions in this problem. The use of the second-order discretization scheme and

smaller grid elements significantly reduce the numerical errors in scenarios (d), (f), and (g).

Consequently, numerical diffusion, generated in numerical simulations of a pure advection scalar transport system, depends on several parameters as shown qualitatively in the 2-D standard test cases. All these factors need to be considered together to control and evaluate the amount of numerical diffusion generated. It should also be pointed that the 3-D systems create relatively much complicated numerical diffusion patterns due to the contribution of additional dimensions and secondary flows. Although grid refinement may be a unique solution to eliminate numerical diffusion errors since maintaining a constant mesh-flow orthogonality is not possible for most problem types, drastically increased computational requirement often prevents this approach as will be discussed extensively in the rest of this chapter. Thus, quantification of numerical diffusion is essential when analyzing and reporting the mixing performance of micromixer designs.

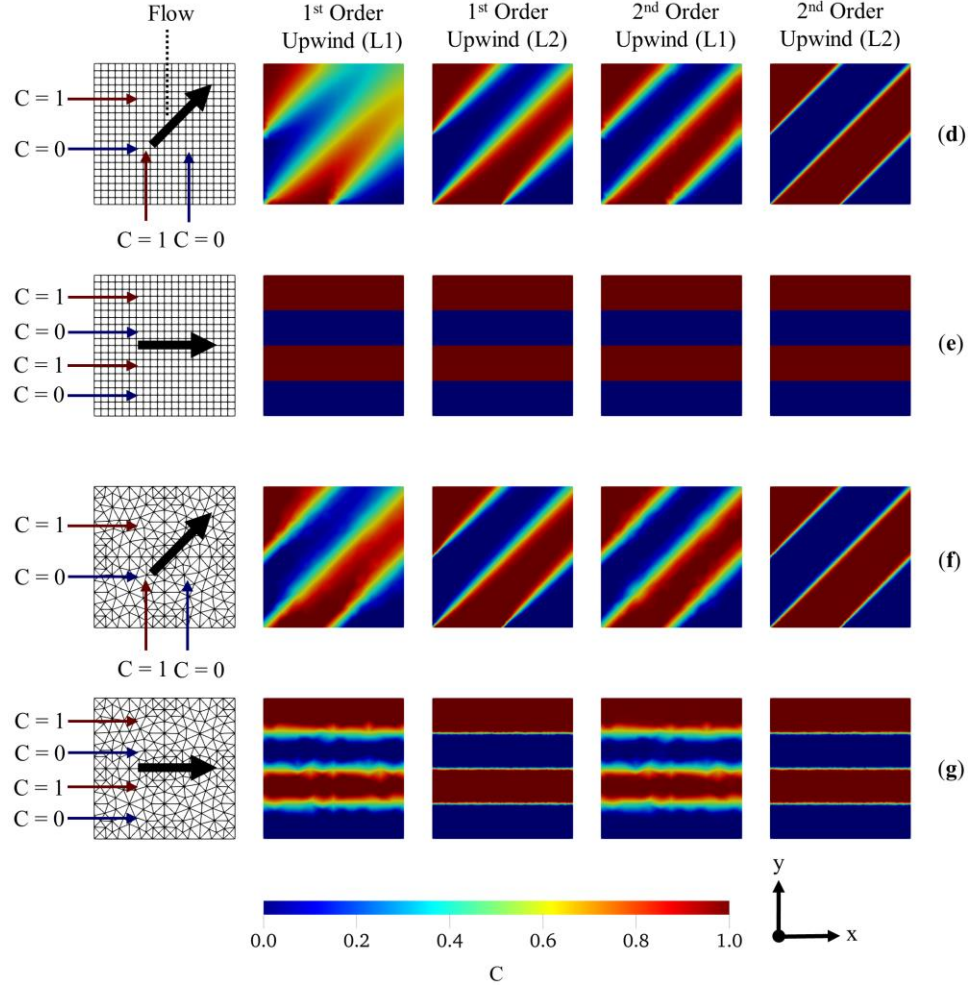


Figure 4.3 Transported scalar distributions in different grid-flow alignment conditions of the extended 2-D test case for multi-inlet scenarios: (d) square elements with 45° flow angle; (e) square elements with 0° flow angle (orthogonal); (f) and (g) triangular elements with randomly changing flow-boundary angle with imposed flow fields $(u, v) = (0.01 \text{ m/s}, 0.01 \text{ m/s})$ and $(0.01 \text{ m/s}, 0)$ respectively.

4.4 Computational Evaluation of Numerical Diffusion Errors for Different Mesh Types, Discretization Schemes and Numerical Techniques in A 3-D T-Shape Passive Micromixer

4.4.1 Micromixer design and case setup

In this section, a classical T-shape passive micromixer design is employed to investigate the behaviour of numerical errors in a 3-D mixing system. The T-shape micromixer geometry consists of two identical inlet channels and a mixing channel as shown schematically in Figure 4.4. The inlet channels have a length and a square cross section of $500\text{ }\mu\text{m}$ and $100\text{ }\mu\text{m} \times 100\text{ }\mu\text{m}$ respectively. It should be noted that the length of the inlet channels is chosen long enough to allow flow development before entering the mixing channel and to prevent numerical solutions from possible boundary effects during the numerical simulations of test cases. The mixing channel length (L) has a length of $1000\text{ }\mu\text{m}$ with a width (W) and height (H) of $200\text{ }\mu\text{m}$ and $100\text{ }\mu\text{m}$ respectively. The dimensions of the T-shape micromixer chosen are consistent with T-shape geometries that are widely studied in the passive micromixer literature as may be seen in References (Bothe et al., 2006; Roudgar et al., 2012; VIRK and HOLDØ, 2016).

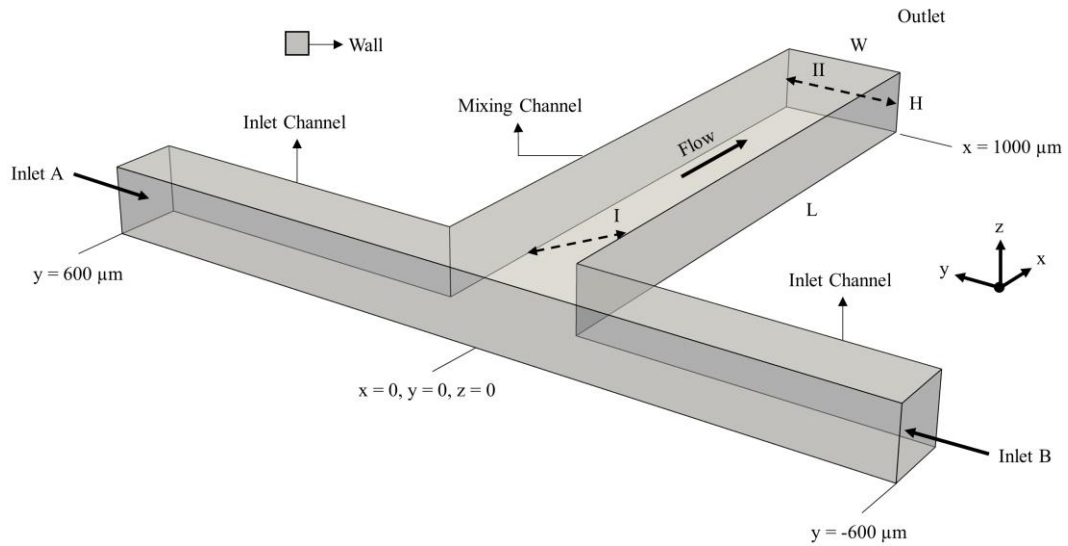


Figure 4.4 3-D view of T-shape passive micromixer.

To examine the behaviour of numerical errors for various mesh configurations and flow conditions in the T-shape passive micromixer, several test cases are designed.

Simulations are setup for five different flow scenarios (i.e., $Re = 0.1, 1, 10, 50$, and 100) and three different mesh structures (i.e., structured hexahedral, structured prism, and unstructured tetrahedral), which are generated using the elements shown in Figure 4.5. In all simulations, molecular diffusion constant of the transported scalar is set to be $D_M = 3 \times 10^{-10} \text{ m}^2/\text{s}$ which is rather small to create advection dominant transport conditions in the T-shape micromixer. All test cases planned and simulation parameters are given in Table 4.1.

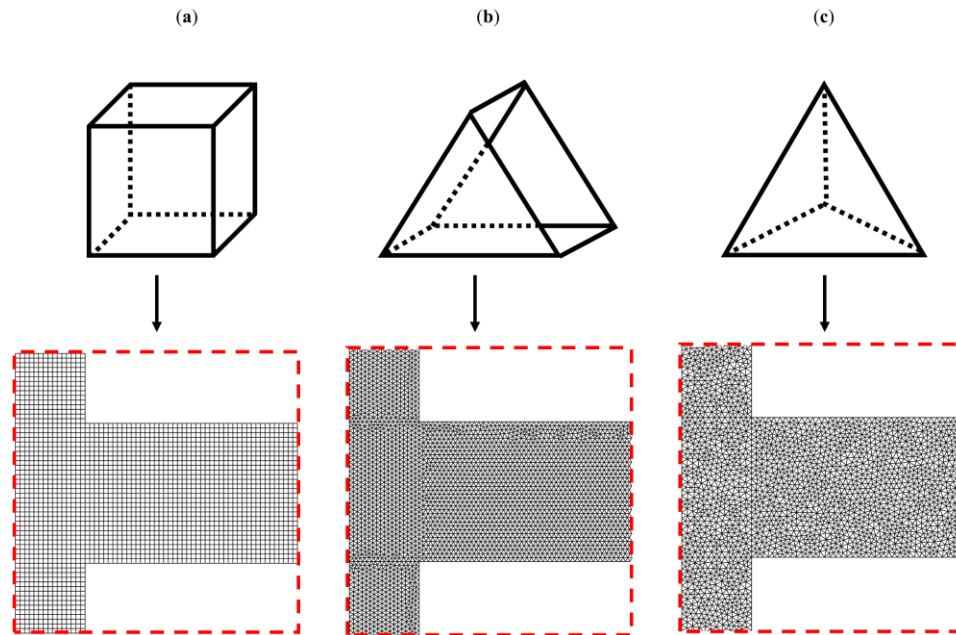


Figure 4.5 3-D mesh element types and orientations in the computational domains: (a) Hexahedron; (b) Prism; (c) Tetrahedron.

Table 4.1 Test cases and simulation parameters for hexahedral, prism, and tetrahedral mesh configurations.

Inlet Velocity (m/s)	Mixing Channel	
	Re	Pe
0.00075	0.1	3.33×10^2
0.0075	1	3.33×10^3
0.075	10	3.33×10^4
0.375	50	1.67×10^5
0.75	100	3.33×10^5
Mesh Level	Constant Flow, Re = 100	
	Re _Δ *	Pe _Δ *
L1: $\Delta x = 2.0 \mu\text{m}$	1.50	5000
L2: $\Delta x = 3.0 \mu\text{m}$	2.25	7500
L3: $\Delta x = 4.5 \mu\text{m}$	3.38	11250
L4: $\Delta x = 6.6 \mu\text{m}$	4.95	16500
Re	Constant Grid Level, L1	
	Re _Δ	Pe _Δ
0.1	0.0015	5
1	0.015	50
10	0.15	500
50	0.75	2500
100	1.5	5000

* Re_Δ and Pe_Δ numbers are calculated for the structured hexahedral mesh.

It should be mentioned that if the flow profiles in the inlet channels are not fully developed before entering the mixing channel, stratified (or separated) flow regions may occur in the confluence region. That is the liquids which approach to the mixing channel from two different inlet streams travel side-by-side along the mixing channel without rotation in the z-direction for all Re scenarios. If, however, the flow in the inlet channels are fully developed, periodic (or vortex) flow type is observed in the confluence region for cases where $\text{Re} \geq 50$. As described earlier, the length of the inlet channels of the micromixer is selected long enough to create fully developed flow profile for the highest flow condition studied, i.e., $\text{Re} = 100$. The flow regimes observed in the micromixer are shown in Figure 4.6 for $\text{Re} = 0.1$ and 100 cases. In addition, velocity profiles at different cross-sections in

the mixing channel are shown in Figure 4.7. As shown in Figure 4.7, the most non-uniform flow in the mixing channel occurs at $x = 200 \mu\text{m}$ as a result of vortex flow at $\text{Re} = 100$. However, rotational effect of fluids is dissipated after this point and parabolic velocity profile is developed towards the outlet of the micromixer. Investigation of the fully developed flow effects in the inlet channels on mixing efficiency is not the scope of this chapter and this point will not be discussed further. The outcomes of the fluid flow, obtained in this study, agree well with the findings of other T-shape micromixer studies (Galletti et al., 2012; Soleymani et al., 2008) that are reported in the literature.

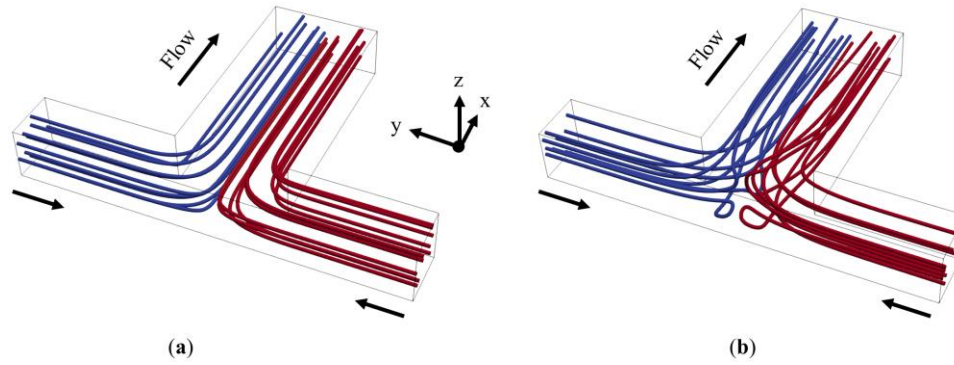


Figure 4.6 Flow profile at the beginning of mixing channel (Figures show the region between $x = 0$ and $500 \mu\text{m}$ and $y = 250$ and $-250 \mu\text{m}$): (a) Separated (or stratified) flow at $\text{Re} = 0.1$; (b) Periodic (or Vortex) flow at $\text{Re} = 100$.

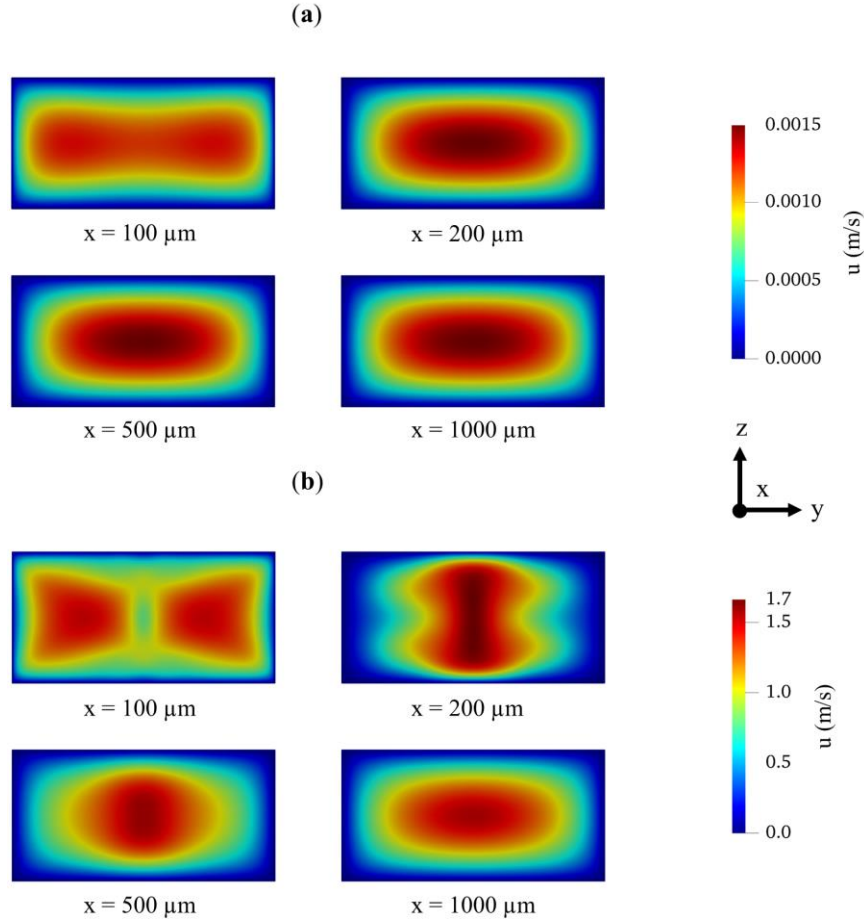


Figure 4.7 Velocity profile at four different cross-sections in the mixing channel (i.e., $x = 100, 200, 500$, and $1000 \mu m$). All planes are normal to the x-direction and color ranges were set to that of $x = 200 \mu m$ plane: (a) $Re = 0.1$; (b) $Re = 100$.

4.4.2 Results and discussion

4.4.2.1 Grid study

A grid study was conducted using FVM to observe the behaviour of the numerical errors in terms of different mesh configurations. For this purpose, four different grid levels (i.e., L1, L2, L3, and L4) were prepared for each of the three different mesh structures (i.e., structured hexahedral, structured prism, and unstructured tetrahedral). The total element numbers of mesh configurations are listed in Table 4.2. For hexahedral and prism mesh

structures, four different grid levels were created with a refinement ratio of approximately 1.5 in x, y, and z directions. However, for the tetrahedral grid type the total element number was fixed around the mesh density of prism type. As the worst-case scenario in terms of numerical error production, the highest flow condition (i.e., $Re = 100$) was chosen for the grid study. To quantify the discrepancy between mesh levels, following fluid flow and scalar transport parameters were employed. Pressure drop in the micromixer (Δp), maximum velocity magnitude (u_{max}) on the yz-plane at $x = 200 \mu m$ (on the dashed line arrow I in Figure 4.4), and mixing index at the outlet. The maximum velocity magnitude at $x = 200 \mu m$ was selected as a flow parameter since the most complex flow was observed at this point in the mixing channel (see the Figure 4.7b). Therefore, it was expected that the highest discrepancy between grid levels will occur on the yz-plane at $x = 200 \mu m$. Additionally, crosswise velocity distributions on the yz-plane at $x = 200 \mu m$ (on the dashed line arrow I in Figure 4.4) are shown in Figure 4.8 for all mesh configurations.

Table 4.2 Mesh properties and grid study results for Re = 100 case.

Mesh Level	Grid Size, Δx (μm)	Number of Cells in Computational Domain		
		Hexahedral	Prism	Tetrahedral
L1	2	3.75×10^6	8.70×10^6	8.70×10^6
L2	3	1.09×10^6	2.57×10^6	2.57×10^6
L3	4.5	3.22×10^5	7.72×10^5	7.74×10^5
L4	6.6	1.02×10^5	2.46×10^5	2.44×10^5
Mesh Level		Max Velocity, u_{max} at $x = 200 \mu\text{m}$ Plane (m/s)		
		Hexahedral	Prism	Tetrahedral
L1		1.65617	1.65691	1.65900
L2		1.65242	1.65175	1.65398
L3		1.64624	1.64361	1.64049
L4		1.63322	1.62657	1.61615
Mesh Level		Pressure Drop, Δp (kPa)		
		Hexahedral	Prism	Tetrahedral
L1		3.32141	3.35006	3.42241
L2		3.30665	3.33550	3.38129
L3		3.26461	3.29451	3.34563
L4		3.22871	3.24648	3.30822
Mesh Level		Outlet Mixing Index, MI		
		Hexahedral	Prism	Tetrahedral
L1		0.01104	0.09671	0.13965
L2		0.01129	0.10677	0.16978
L3		0.01341	0.11864	0.19725
L4		0.01755	0.15015	0.22929

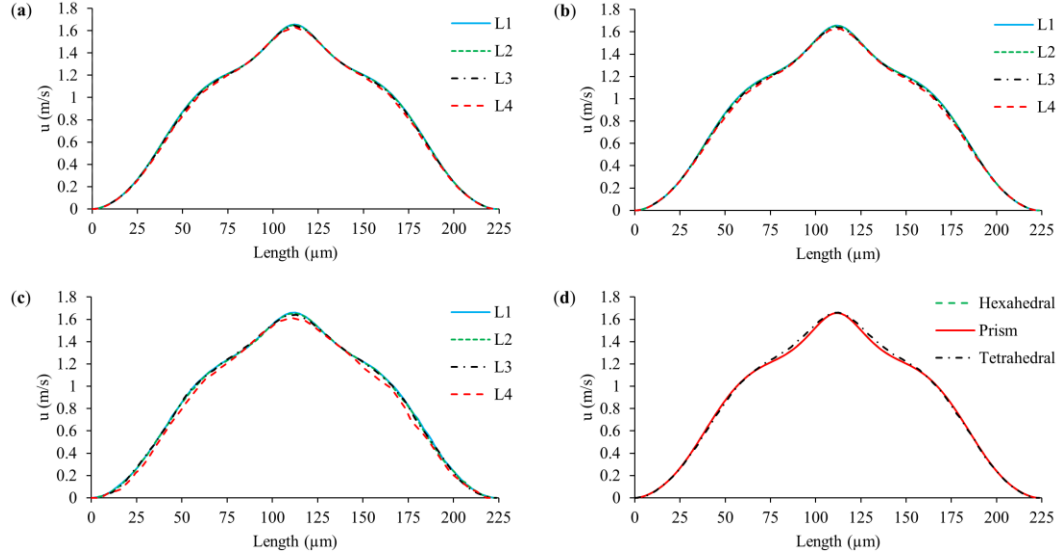


Figure 4.8 Velocity distribution on the yz-plane at $x = 200 \mu\text{m}$ (on the dashed line arrow I in Figure 4.4) from L1, L2, L3, and L4 mesh level simulations: (a) Hexahedral; (b) Prism; (c) Tetrahedral; (d) Hexahedral vs. Prism vs. Tetrahedral solutions at L1 mesh level.

As may be seen in Figure 4.8 and Figure 4.9, grid study results indicate that the flow field at $\text{Re} = 100$ is resolved consistently for all mesh configurations. The numerical solutions of different mesh structures yield almost identical values for the flow parameters tested, i.e., ΔP and u_{max} , as shown in Figure 4.9a and Figure 4.9b. In addition, even the coarsest grid size, used in each mesh structure, resolve the flow field quite accurately with an insignificant relative error with respect to the finest grid level as presented in Figure 4.9c and Figure 4.9d. The maximum discrepancy, occurred between the L1 and L4 mesh levels of the tetrahedral mesh structure, is quantified as 2.6% and 3.3% for the u_{max} and ΔP , respectively. These values are computed as 1.4% and 2.8% respectively for the structured hexahedral mesh configuration. It should be noted that although grid-flow alignment is not maintained in prism and tetrahedral meshes, flow solution is not affected from numerical errors significantly as a result of quite low Re_Δ number in the computational domain. As presented in Table 4.1, the minimum and maximum Re_Δ

numbers are 1.50 and 4.95 respectively for the hexahedral mesh (assuming Re_Δ number in prism and tetrahedral domain is close to that of hexahedral). These moderate numbers indicate a rather low advection dominance in the flow domain. In other words, inertial and viscous effects in the flow equation feed the numerical solution almost equally which reduce numerical instability and numerical viscosity in the system.

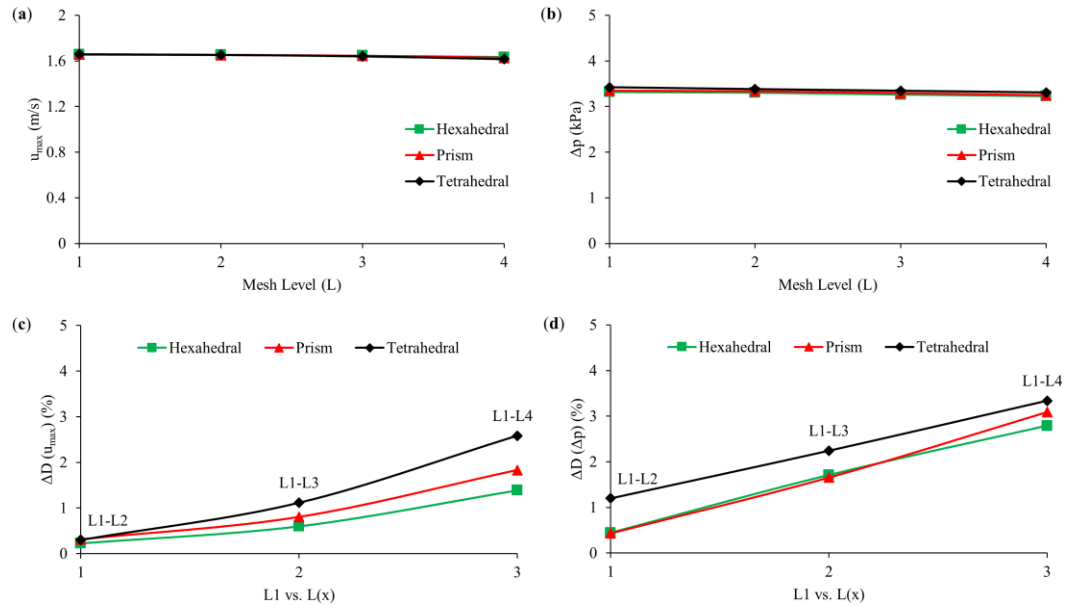


Figure 4.9 Grid study results for different mesh structures (i.e., hexahedral, prism, and tetrahedral) and grid levels (i.e., L1, L2, L3, and L4): (a) maximum velocity magnitude (u_{max}) on the yz-plane at $x = 200 \mu m$; (b) pressure drop (Δp) in the micromixer; (c) and (d) difference between mesh levels when u_{max} and Δp are employed as the flow parameters respectively.

As shown in Figure 4.8d, while the velocity profile can be resolved quite accurately for all mesh structures at L1, prism and tetrahedral mesh densities are about 2.3 times higher than that of hexahedral mesh type which is significant in terms of computational cost. The maximum difference in solutions is observed to be 2.6% between L1 and L4 of tetrahedral mesh with a mesh density difference of around 8.5 million. Also, for this type of idealization, while the difference between solutions at L1 and L2 is only 0.3 %, L1

simulations are performed using almost 6.1 million more mesh elements. When u_{\max} is employed as the parameter, the difference between the grid levels with respect to the finest grid and mesh density differences between these levels are shown in Figure 4.10.

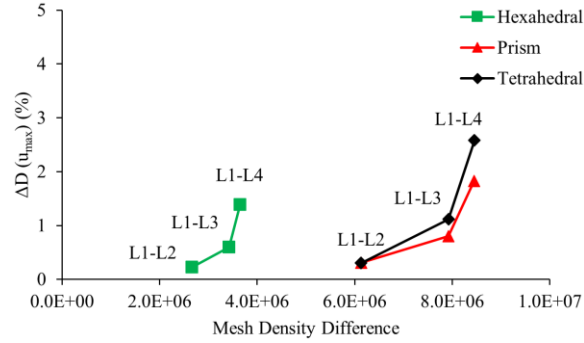


Figure 4.10 Difference between mesh levels (L2, L3, and L4) with respect to the finest mesh level (L1) when u_{\max} is the parameter vs. total mesh element number difference between mesh levels compared.

As can be seen in Figure 4.10, the structured hexahedral mesh configuration provides the best results in terms of both low numerical error production and computational cost. Even the coarsest level of this mesh type resolves the flow domain quite accurately using the lowest total element number in the computational domain. Although ~ 3.65 million lower mesh elements are used at L4, u_{\max} is estimated with a 1.4% difference compared to the finest grid level. As mentioned earlier, this is essentially observed as a result of a quite small Re_{Δ} number (e.g., $Re_{\Delta} \approx 5$) and a good grid-flow alignment, maintained throughout the mixing channel.

On the other hand, while the discrepancy between L1 and L4 levels of tetrahedral mesh is quantified as 2.6% for the u_{\max} parameter, the total element number, used in L1 level, is approximately 36 times than that of L4. In this case, employing the finest mesh level for the numerical solution of flow domain will increase the computational cost sharply

against to an insignificant numerical error reduction. Although the tetrahedral mesh presents slightly higher numerical errors than other two mesh configurations, even the coarsest level of this mesh configuration may be used to resolve the flow field for practical purposes considering the extra effort to construct structured hexahedral and prism meshes in the computational domain.

For all mesh structures, further grid refinement after L4 level does not contribute to numerical accuracy significantly, but it increases the computational cost unreasonably. However, if the relative difference limit is determined as 1%, all flow simulations can be done at L2 level for all mesh structures. In this section of Chapter 4, L1 mesh density is employed for all test cases and mesh types to investigate the magnitude of numerical diffusion errors in scalar transport solution more accurately. The reason for the selection of the finest grid in all flow scenarios (i.e., $Re = 0.1-100$) is that each case provides a different Re_{Δ} number by which the extent of numerical errors may be characterized. Likewise, increasing the grid size will also increase Pe_{Δ} number. Accordingly, instead of conducting additional simulations for different grid levels, all simulations were conducted at the finest grid size and the amount of numerical diffusion was evaluated for various Pe_{Δ} numbers, which range between 5 and 5000 for $Re = 0.1$ and 100 scenarios, respectively, as given in Table 4.1.

When outlet MI is employed as the parameter in the grid study, important discrepancies are observed between mesh levels especially for prism and tetrahedral mesh types. At this point it should be noted that, MI at the outlet of the T-shape micromixer is expected to be close to zero due to predominantly unidirectional fluid flow in the mixing channel. Meaning that chaotic advection cannot be developed in the mixing channel and

mixing is mainly controlled by the diffusive interaction across the contact surface of fluids, which is formed at the center of the mixing channel. High advection dominance in the system (e.g., $Pe = 3.33 \times 10^5$), however, substantially suppresses this diffusive interaction, and thus the development of mixing is expected to be very limited since the function of both mixing mechanisms is blocked.

Although mesh refinement reduces numerical diffusion errors in the scalar transport simulations as shown in Figure 4.11a, MI values differ substantially from one another for different mesh types. Such a high difference of MI between mesh types arises based on the amount of numerical diffusion errors, produced during the solution of scalar transport equation. Outlet mixing efficiencies, estimated from the numerical solutions of prism and tetrahedral mesh structures, are much higher than that of hexahedral type whereas the mesh densities are significantly high in these configurations. Considering that the simulation parameters are same for all mesh configurations, a high discrepancy develops between mesh types as a response of altering grid-flow alignment in the computational domains. Combined effects of mostly unidirectional fluid flow in the mixing channel and the structured hexahedral mesh create an orthogonality between flow vectors and grid boundaries. Hence, mesh-flow alignment is maintained well throughout the mixing channel and numerical diffusion errors are minimized substantially compared to the other two mesh structures. In the numerical simulations, where computational domain is discretized using tetrahedron mesh elements, the highest MI values are obtained due to randomly changing angle between flow and grid boundaries. Despite the unidirectional smooth flow pattern in the mixing channel and using 2.3 times more mesh elements at L1, tetrahedral mesh type estimates the MI ~13 times more than the structured hexahedral configuration. This factor

reduces to ~ 8.8 when the structured prism type mesh is applied in the computational domain. MI values, obtained from structured prism mesh solutions, follow a trend between the outcomes of hexahedral and tetrahedral mesh simulations. Like the structured hexahedral mesh case, unidirectional fluid flow and structured prism mesh pattern form a constant grid-flow alignment through the mixing channel. However, depending on the MI estimations of prism mesh in Figure 4.11a, it may be asserted that the angle between flow vectors and grid boundaries is much higher than 0° at which false diffusion is not generated.

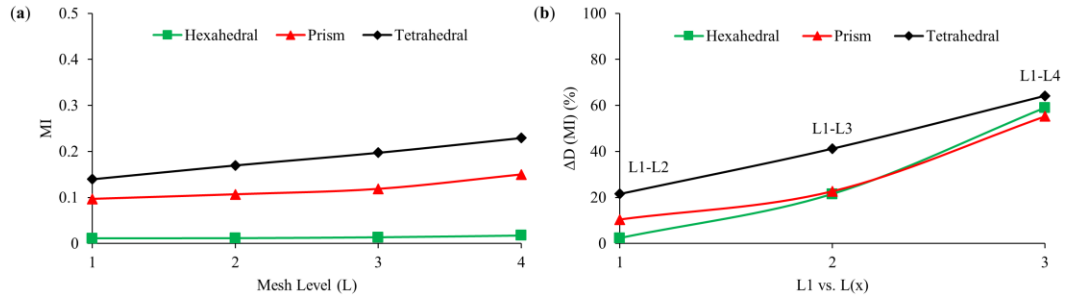


Figure 4.11 Grid study results when outlet mixing efficiency is the parameter: (a) outlet MI of hexahedral, prism, and tetrahedral mesh types at L1, L2, L3, and L4 mesh levels; (b) Difference between mesh levels (L2, L3, and L4) with respect to the finest mesh level (L1) when MI is the parameter.

Figure 4.11b shows that while hexahedral mesh type predicts outlet mixing efficiency with a 2.33% difference between L1 and L2, this amount sharply increases to a value around 10.4% and 21.6% for the same mesh levels of prism and tetrahedral configurations respectively. Besides, the variation between L1 and L4 levels of all three mesh types changes between 55% and 64%. The discrepancy between grid levels of different mesh types can also be seen from the scalar distributions at the outlet as displayed in Figure 4.12. Compared to the insignificant variations between all mesh configurations when the flow parameters, i.e., ΔP and u_{\max} , are employed in the grid study, the use of MI as a parameter shows a high difference between mesh levels of an element type and all

three mesh structures. Such a high inconsistency between fluid flow and scalar transport solutions occurs as a natural consequence of highly different momentum and scalar transport conditions in the micromixer. Although the same mesh configuration and second-order accurate discretization scheme is applied for the simulations of both problems, system dynamics are substantially different than each other. Namely, whereas the ratio of inertial forces to viscous forces is only on the order of 10^2 for fluid flow in the micromixer, the ratio between advective and diffusive scalar transport is on the order 3.33×10^5 . These ratios clearly indicate the formation of smooth velocity gradients in the flow field against steep scalar gradients in the transport domain. Consequently, numerical simulations of fluid flow and scalar transport exhibit quite different numerical error production tendency.

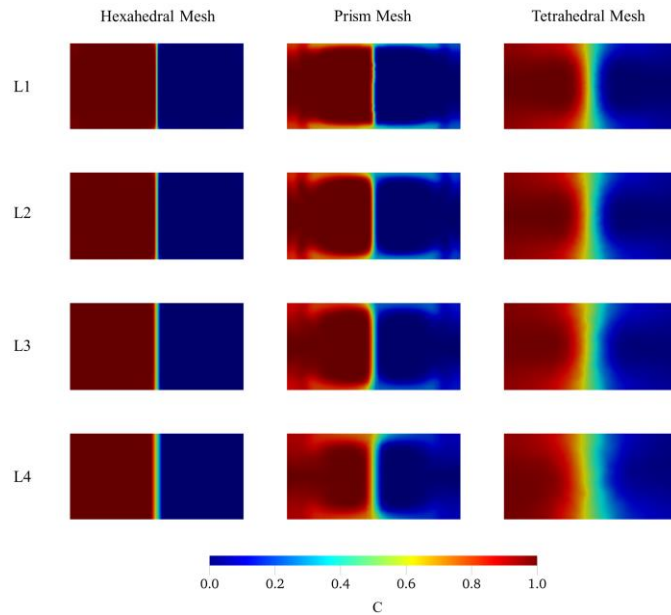


Figure 4.12 Transported scalar distributions at the outlet of the T-shape micromixer for all mesh configurations ($Re = 100$).

The comparison of Figure 4.10 and Figure 4.13 also shows the extent of numerical diffusion errors clearly for both fluid flow and scalar transport. For instance, the difference

between L1 and L4 is observed as ~2.6% for the tetrahedral type when u_{\max} is used as the parameter, yet this difference increases to ~64% when the grid study is conducted based on MI at the outlet. Even in the best-case scenario, which is the structured hexahedral mesh solution, there is a considerable disagreement between the grid study results of two different parameter sets. While the difference between L1 and L2 is ~0.23% when u_{\max} is the parameter, the degree of discrepancy increases to 2.33% for the outlet mixing efficiency. Based on these observations, parameter selection in a grid study is critical and needs to be evaluated very cautiously. Although the same mesh configuration is used to resolve fluid flow and scalar transport fields, grid tests reflect highly varied results depending on the parameter selection. Therefore, understanding the effect of error generation in numerical solutions is critical to select appropriate mesh properties based on the physical problem to be simulated. It must be emphasized that in numerical passive micromixer investigations grid type and mesh density should be selected based on scalar transport simulations. In most cases, if the scalar transport domain may be resolved with an accurate error percentage, this will also ensure the resolution of flow field with a substantially less error percentage. However, the opposite may only be true in very rare cases where Pe number is very low (e.g., $Pe < 100$).

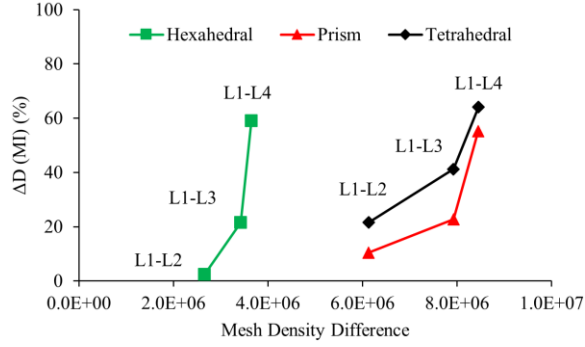


Figure 4.13 Grid study results between grid levels (L4, L3, and L2) with respect to the finest grid (i.e., L1) for MI vs. total mesh element number difference between grid levels and the finest grid.

Although very high mesh density is used in L1 level of prism and tetrahedral mesh structures, disorientation of flow and grid boundaries throughout the mixing channel cause yielding a significant amount of unphysical fluid mixing at the outlet. While the degree of mixing is computed as ~1.1% from the L1 level of hexahedral mesh solution, this value is found to be ~10% and ~14% from the same mesh level of prism and tetrahedral simulations respectively. Therefore, depending on the grid study results in Figure 4.11a, it should be noted that the use of prism and tetrahedral mesh elements in scalar transport simulations should be avoided to reduce numerical diffusion errors significantly. In several passive micromixer designs, however, discretization of a computational domain with hexahedron elements may be quite challenging due to complex micromixer topologies. In these geometries, grid-flow alignment may be improved following a hybrid meshing strategy in which while tetrahedron or prism elements are mostly employed only in the complex regions, hexahedron elements are positioned in the rest of the geometry.

In addition to the parameter and grid type effects, other key points that need to be considered in a grid study are the selection of mesh densities and conducting the grid study for the worst-case scenario in terms of numerical error generation. As mentioned in Chapter

2, in several numerical passive micromixer studies grid tests are usually performed employing very close mesh densities to observe and quantify numerical diffusion error in simulations. Nonetheless, if mesh densities are chosen very close to each other, the change of numerical errors between mesh densities may become highly deceptive. Although numerical results may contain important effects of numerical diffusion, and thus erroneous mixing efficiency values, these effects remain hidden in numerical solutions. For instance, the 21.6% difference between L1 and L2 levels of tetrahedral mesh configuration (see Figure 4.13b) could only be uncovered due to more than 6 million element difference between these two levels. It is obvious that if the total element number in L1 level is selected to yield a much less density difference with L2 level (e.g., $L1-L2 = 1$ million elements), the discrepancy (i.e., the amount of numerical diffusion errors) between these two levels will become much lower than 21.6%. Thus, although L2 mesh level resolves the scalar transport field with serious amount of numerical diffusion errors, these unphysical effects can be easily obscured depending on the density of the L1 mesh level. Besides, another problem that is frequently seen in grid test studies is the improper choice of a test case for the characterization of numerical diffusion errors. As discussed earlier, in numerical examinations of passive micromixers, grid properties should be determined based on scalar transport conditions due to high numerical diffusion production inclination of high Pe transport systems. In the meantime, grid tests should be performed for the worst-case condition of scalar transport simulations. For example, if fluid mixing is examined under several flow conditions, the highest flow scenario should be employed in a grid test to determine mesh properties based on the maximum numerical diffusion generation in overall simulations. By this way, it is ensured that the numerical solutions of all other flow

scenarios will result in less numerical diffusion errors than that of the highest flow condition. Similarly, this approach needs to be followed for different scalar transport conditions as well. If the fluid mixing performance of a passive micromixer design is investigated for various molecular diffusivity conditions, then the lowest molecular diffusion constant should be employed in the grid study. In addition, the location of the observation points in a computational domain plays a significant role to characterize numerical errors accurately. Namely, false diffusion errors, which are produced during the numerical solution, are transported and averaged in the streamwise direction. Therefore, the selection of grid study parameters from upstream and downstream locations may affect the grid test results significantly. In scalar transport simulations, MI parameter should be obtained based on the mixing dynamics of a micromixer. The effect of parameter observation locations in grid studies are extensively discussed in the Section 4.5 of the present chapter.

4.4.2.2 Analysis of numerical diffusion in FVM solutions

To minimize false diffusion in numerical solution of advection dominant systems, several high order numerical schemes have been proposed in the current literature. Unfortunately, a problem-free solution to entirely overcome this numerical complexity is not possible. Although second or higher order discretization algorithms provide more accurate solutions and may resolve steep gradients by resulting in much lower numerical diffusion than first-order schemes, they usually suffer from numerical instabilities which may affect the reliability of the numerical solution. In FVM analysis, several preliminary test simulations were conducted to observe possible instability problems in numerical solutions. First-order upwind scheme and several second-order accurate numerical

schemes (e.g., QUICK, MUSCL, second-order upwind, and limitedLinear) were tested to discretize advection terms in the scalar transport equation. In these test simulations, it was observed that prism and tetrahedral mesh configurations provide oscillatory solutions (i.e., scalar value exceeds the bounds, see Figure 4.1) when QUICK, MUSCL, and second-order upwind schemes were utilized. Although numerical solutions remained bounded during the simulations, the amplitude of oscillations varied depending on the flow condition, grid size, and regions in the computational domains. The amount of scalar value fluctuations in solutions was escalated when the flowrate was increased and/or grid size was coarsened. Besides, the maximum peaks that exceed the bounds of the scalar value were seen along center of the mixing channel ($y = 0$) since the sharp scalar gradients between fluids are formed in this region. It was also observed that the degree of oscillations was dampened significantly when the above discretization schemes are used with the hexahedral mesh structure. Nonetheless, the most stable solutions were obtained for all mesh configurations and Re scenarios when the first-order upwind and limitedLinear schemes were employed. The distributions of scalar concentration at the outlet (on the dashed line arrow II in Figure 4.4) are presented in Figure 4.14 for L1 level of all mesh types at $Re = 100$ when first-order upwind and limitedLinear numerical schemes are utilized. Meanwhile, it should be mentioned that the limitedLinear is a type of high-resolution total variation diminishing scheme (TVD) (Moukalled et al., 2015) in FVM and is mainly used to ensure the boundedness in numerical simulations of advection dominant systems. Much detailed information about high-resolution discretization schemes may be seen in Reference (Moukalled et al., 2015).

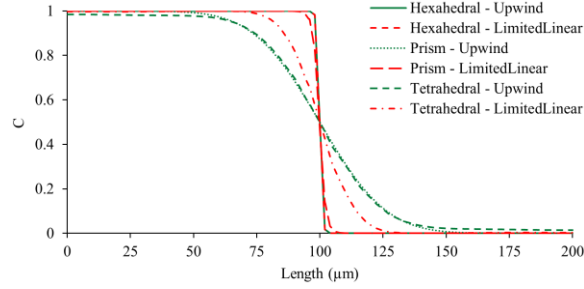


Figure 4.14 Outlet scalar distributions along the width of the mixing channel at $z = 50 \mu\text{m}$ (on the dashed line arrow II in Figure 4.4) for L1 level of all mesh types at $\text{Re} = 100$ scenario.

Figure 4.14 shows that the first-order upwind and limitedLinear schemes provide stable solutions without producing any over- and under-shoots before and after the front, advected in the mixing channel of the T-shaped micromixer. In addition, the amount of numerical diffusion, produced by the first-order upwind scheme, is very close to that of limitedLinear scheme when hexahedral mesh type is used in the computational domain. Therefore, when orthogonality between flow and grid boundaries is sustained in the streamwise direction as existed in hexahedral mesh type, the amount of numerical diffusion, produced by first-order upwind scheme, is insignificant. For other mesh groups, however, there is a significant discrepancy between scalar concentration distributions of the two different discretization algorithms since numerical diffusion effects are predominant in the first-order upwind solutions. The smearing of sharp gradients is at the maximum when prism and tetrahedral mesh types are combined with first-order upwind discretization scheme. Besides, hexahedral and prism mesh structures render similar outcomes when limitedLinear scheme is employed whereas the tetrahedral mesh solution diverges from the sharp front. At this point, however, it should be noted that although hexahedral and prism mesh solutions provide quite similar outcomes, this is observed because Figure 4.14 reflects only some portion of the numerical diffusion, produced in the

prism mesh solution. This point may also be seen evidently when Figure 4.11a, Figure 4.12, and Figure 4.14 are evaluated together. To be clear, while the MI values in Figure 4.11a include all the false diffusion errors on the outlet cross-section, Figure 4.14 shows the scalar distribution on a line along the width of the mixing channel at the outlet. Hence, Figure 4.14 can only represent some part of the numerical diffusion errors due to asymmetric scalar distribution on the outlet cross-section. If, however, the distribution of a scalar is symmetric on a given plane as will be examined in the Section 4.5, the overall discrepancy between different solutions may be represented precisely using the data between two points.

It should be noted that in all FVM simulations, advection terms in the scalar transport equation are discretized using the second order accurate limitedLinear scheme to ensure stability for all mesh configurations, tested in the present section. As it can be seen in Figure 4.15a, in which horizontal axis shows the average numerical diffusion constant, i.e., D_N , in a logarithmic scale and vertical axis shows false mixing for each mesh type and grid size at $Re = 100$, hexahedral mesh produce considerably lower numerical diffusion and accordingly less false mixing in contrast to prism and tetrahedral mesh structures. While the order of numerical diffusion constant is around 10^{-13} and false mixing is 0.5% at L1 level of hexahedral mesh, these numbers sharply increase to 10^{-9} and 10% for prism and 10^{-8} and 14% for tetrahedral mesh types. Scalar transport simulations which are conducted using tetrahedral and prism mesh types produce a numerical diffusion around five and four orders of magnitude higher than that of hexahedral mesh, respectively. As shown in Figure 4.15a, the magnitudes of these errors manifest themselves as unphysical mixing at the outlet. It is obvious that high amount of numerical diffusion that has occurred in solutions

is mainly due to non-orthogonal alignment of velocity and grid boundaries in the computational domain since other simulation parameters are all nearly constant. In tetrahedral mesh type, mesh-flow disorientation creates a significant amount of false diffusion in the numerical solution even in the finest mesh level. In prism mesh solutions, however, although mesh-flow alignment (i.e., mesh-flow orthogonality) is also not maintained in the computational domain, the amounts of numerical diffusion and false mixing are noticeably lower than that of tetrahedral type. This is essentially because structured prism mesh configuration helps to sustain a constant mesh-flow alignment in the computational domain which is not possible in tetrahedral mesh type due to randomly changing angle between flow and grid boundaries. Additionally, numerical diffusion and false mixing increases when the grid is coarsened in all mesh categories. Grid coarsening, however, show different behavior in terms of numerical diffusion and false mixing production in each mesh category. Namely, while hexahedral mesh responds the grid coarsening with a minimal numerical error increase, as it may be seen from the mild slope between mesh levels, sharply increasing slopes in the prism and tetrahedral mesh structures are the evidence of high growth rate of numerical diffusion errors in solutions.

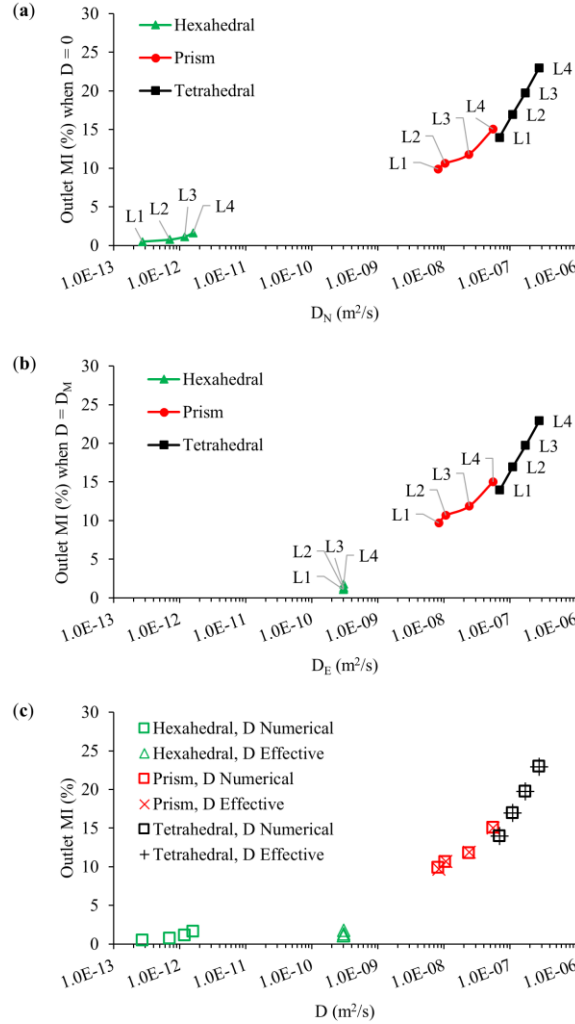


Figure 4.15 Numerical and effective diffusions in L1, L2, L3, and L4 mesh levels of hexahedral, prism, and tetrahedral mesh structures: (a) numerical diffusion vs. MI; (b) effective diffusion vs. MI; (c) physical diffusion masking.

Figure 4.15b shows the effective diffusion constant, i.e., D_E , and corresponding MI values at the outlet when the simulations are run employing the physical diffusion constant, i.e., D_M . For all the density levels of hexahedral mesh type, D_E is computed as 3×10^{-10} m²/s which clearly indicates that the physical molecular diffusion constant is completely recovered from the numerical solution of the scalar transport equation. Therefore, MI values which are obtained from hexahedral mesh solutions reflect the physical effects of the molecular diffusion constant tested. For prism and tetrahedral mesh structures,

however, the magnitude of D_E and false mixing changes depending on the mesh levels and the outcomes are almost identical with that of pure advection simulations. This is evident when Figure 4.15a and Figure 4.15b are evaluated together. If the outcomes in these two plots are presented in a single graph as shown in Figure 4.15c, it is apparent that all physical diffusion effects are completely masked by numerical diffusion errors when the computational domain is meshed using prism or tetrahedron elements. The overlapped data points of two separate simulations explicitly reveal the severity of the numerical diffusion effects. Nevertheless, this is not the case with the hexahedral mesh type. Figure 4.15c also reveals another important point that the estimated numerical diffusion constants, i.e., D_N , are several orders of magnitude lower than the physical molecular diffusion constant even for the L4 level of hexahedral mesh. Therefore, considering Pe_Δ numbers at different grid levels of this mesh type (see Table 4.1), it is possible to obtain a solution with a negligible amount of numerical diffusion even at high Pe_Δ numbers. This is essentially achieved due to mostly unidirectional fluid flow in the micromixer which ensures a good grid-flow alignment in the computational domain. However, this statement may not be correct when secondary flow patterns are created in the mixing channel. As will be discussed in the section 4.5 of the present chapter, continuous violation of grid-flow alignment may produce significant amount of numerical diffusion even the computational domain is discretized using a structured hexahedral mesh.

Figure 4.16a-c shows the change of false mixing and numerical diffusion with the density of hexahedral, prism, and tetrahedral mesh configurations respectively. In all graphs, while the horizontal axes show the mesh density, the left and right vertical axes show false mixing and numerical diffusion respectively. As may be seen in Figure 4.16a–

c, while the amount of false mixing is less than 2% even in the L4 level of hexahedral mesh solution, this amount varies in the range of 10% to 14% and 14% to 24% between L1 and L4 mesh levels solutions of prism and tetrahedral mesh configurations respectively. When these mesh structures are compared in terms of the numerical diffusion constants calculated, it may be seen that while the magnitude of numerical diffusion is around 10^{-13} – 10^{-12} range in hexahedral mesh solutions, this range sharply rises to 10^{-8} – 10^{-7} for other two mesh types. Meanwhile, using the equations in Figure 4.16b and Figure 4.16c—these equations are obtained by fitting a curve (e.g., FM and ND) to the simulation results—average mesh densities, required to obtain a negligible amount of false mixing or numerical diffusion, may be estimated for prism and tetrahedral mesh types. In Table 4.3, several average mesh density estimations are listed for predetermined false mixing and numerical diffusion values. As may be seen from the values in Table 4.3, to obtain a numerical diffusion constant equal to the actual molecular diffusion or, in other words, to yield maximum 5% false mixing at the outlet, more than 10^9 prism or tetrahedral elements need to be used in the computational domain. If these thresholds are dropped further, a more radical mesh refinement will be required. Based on these estimations, it should be noted that these mesh densities are beyond today's computational capacity even in the best-case scenario in Table 4.3. Therefore, the use of prism and tetrahedron element types should be strictly avoided to simulate advection dominant transport systems. If these element types are even employed partially in the computational domain, numerical diffusion errors need to be quantified and documented in detail to avoid reporting suspicious and erroneous mixing outcomes.

Table 4.3 Estimated prism and tetrahedron element numbers in the computational domain to reach predetermined thresholds of false mixing and numerical diffusion when $Re = 100$ and $Pe = 3.33 \times 10^5$.

False Mixing (%)	Total Mesh Element		Numerical Diffusion	Total Mesh Element	
	Prism	Tetrahedron		Prism	Tetrahedron
0.50	1.08×10^{18}	2.81×10^{17}	1.00×10^{-13}	4.37×10^{15}	1.19×10^{22}
1.00	2.61×10^{15}	1.85×10^{15}	1.00×10^{-12}	6.64×10^{13}	2.96×10^{19}
2.00	6.28×10^{12}	1.22×10^{13}	1.00×10^{-11}	1.01×10^{12}	7.37×10^{16}
5.00	2.18×10^9	1.59×10^{10}	3.00×10^{-10}	2.08×10^9	1.05×10^{13}

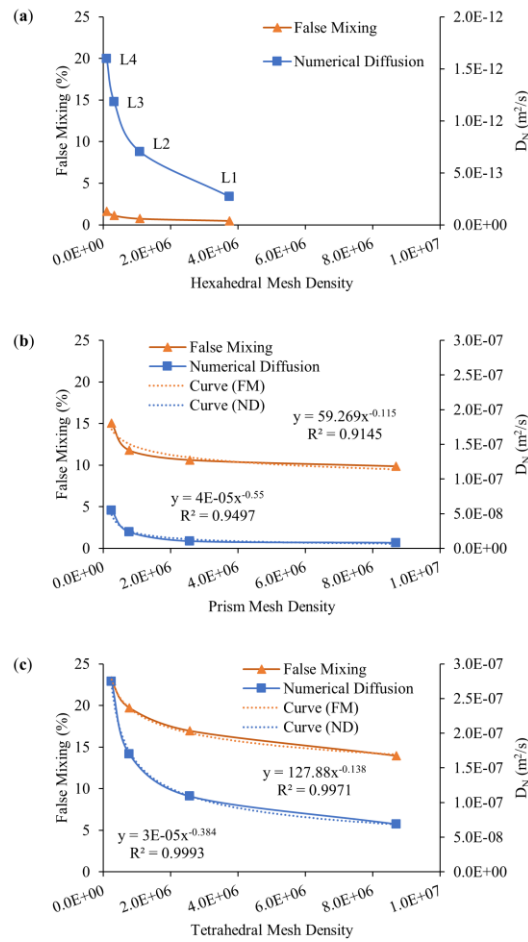


Figure 4.16 Change of numerical diffusion and false mixing with mesh density: (a) hexahedral; (b) prism; (c) tetrahedral.

The relationship between Re number and numerical diffusion constant is also investigated at L1 level of all mesh structures, as presented in Figure 4.17a. Hexahedral

mesh outcomes show that while numerical diffusion is on the order of 10^{-16} at $Re = 0.1$, the magnitude of this error rises with increasing Re number and reaches to 2.71×10^{-13} in $Re = 100$ flow scenario. Nonetheless, the level of numerical diffusion stays several orders of magnitude below the molecular diffusion constant especially in very low flow conditions. Meaning that all the MI values, obtained from hexahedral mesh solutions of different Re scenarios, reflect the physical effects of molecular diffusion completely. Figure 4.17a also shows that while prism mesh solutions yield significantly low numerical diffusion in $Re = 0.1$ and 1 cases, the amount of numerical diffusion diverges from molecular diffusion constant starting from $Re = 10$ flow case and reaches 8.08×10^{-9} value at $Re = 100$ which is nearly 27 times higher than the molecular diffusion constant simulated. Similarly, tetrahedral mesh solutions present a rising numerical diffusion trend with increasing Re numbers. For tetrahedral mesh type, while numerical diffusion is only tolerable at $Re = 0.1$, the amount numerical diffusion exceeds the molecular diffusion constant starting from $Re = 1$ scenario and continues progressively with rising flowrate in the micromixer. While the ratio between numerical diffusion and molecular diffusion (i.e., D_N/D_M) is ~ 1.7 at $Re = 1$, this ratio goes up ~ 230 at $Re = 100$ which indicates that the physical effect of molecular diffusion is severely overshadowed by numerical diffusion errors. This may also be seen clearly from Figure 4.17b which shows the change of effective diffusivity with flow scenarios tested. Also, results in Figure 4.17a and Figure 4.17b are summarized in Table 4.4 with the fractional comparisons of numerical, effective, and molecular diffusion values of all mesh types and Re scenarios that are examined in the present section.

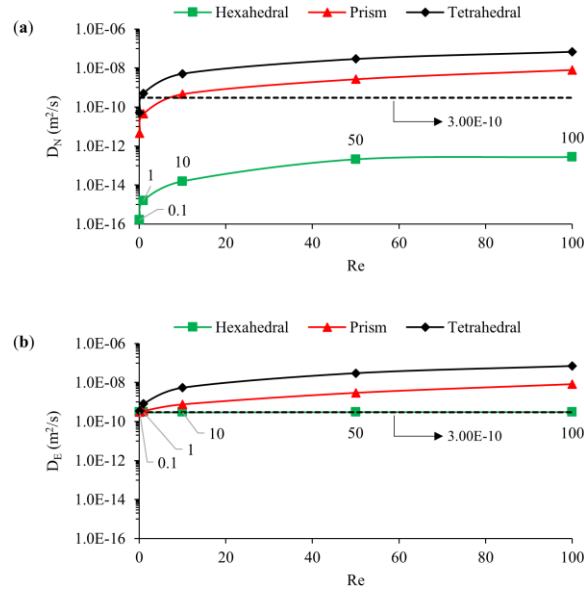


Figure 4.17 The change of numerical and effective diffusion with Re number at L1 level of hexahedral, prism, and tetrahedral mesh structures: (a) numerical diffusion vs. Re; (b) effective diffusion vs. Re.

Table 4.4 Comparisons of numerical (D_N), effective (D_E), and molecular diffusion (D_M) constants with respect to L1 level of all mesh types and Re scenarios.

Re	D_N/D_M			D_E/D_M		
	Hexahedral	Prism	Tetrahedral	Hexahedral	Prism	Tetrahedral
0.1	5.36×10^{-7}	0.01	0.17	1.00	1.01	1.17
1	5.39×10^{-6}	0.15	1.69	1.00	1.15	2.69
10	5.16×10^{-5}	1.53	17.03	1.00	2.53	18.03
50	6.91×10^{-4}	8.99	98.32	1.00	9.99	99.32
100	9.04×10^{-4}	26.94	230.01	1.00	27.94	231.01

As given in Table 4.4, the D_E/D_M ratios for hexahedral, prism, and tetrahedral mesh structures are around 1 only at $Re = 0.1$ which indicates that all mesh types can resolve the scalar field similarly only in this flow condition. In addition, prism mesh provides a solution close to that of hexahedral at $Re = 1$. Note that although prism and tetrahedral meshes provide consistent results with hexahedral mesh at $Re = 0.1$, these mesh structures

use almost 2.3 times more cells than hexahedral mesh at L1 which is important in terms of computational cost as mentioned earlier.

Figure 4.18a and Figure 4.18b show the change of outlet MI values, which are calculated from L1 level of all mesh structures and Re scenarios, in terms of numerical and effective diffusion approximations respectively. According to Figure 4.18a, although hexahedral mesh solutions produce numerical diffusion with increasing Re numbers, even the highest error magnitude is on the order of 10^{-13} which creates a negligible amount of false mixing (i.e., $\sim 0.5\%$) at the exit of the micromixer. Therefore, numerical solutions of all Re scenarios yield almost a constant MI value when hexahedral mesh structure is employed. Similar false mixing trends are also observed at different levels when prism and tetrahedral mesh structures are utilized to simulate $Re = 0.1$, 1 , and 10 flow conditions. In prism mesh solutions, although numerical diffusion is quantified around the physical molecular diffusion constant at $Re = 10$, these errors are reflected as $\sim 1.2\%$ false mixing at the outlet. The degree of false mixing grows rapidly after $Re = 10$ since the effect of numerical diffusion increases with rising flowrate. On the other hand, tetrahedral mesh solutions produce the highest unphysical mixing values among all mesh groups tested, and even the lowest flow condition produces nearly 6% false mixing at the outlet. While a mild slope is observed between $Re = 0.1$ and 10 , false mixing values continue to grow sharply beyond this range and reaches $\sim 14\%$ level in $Re = 100$ flow scenario.

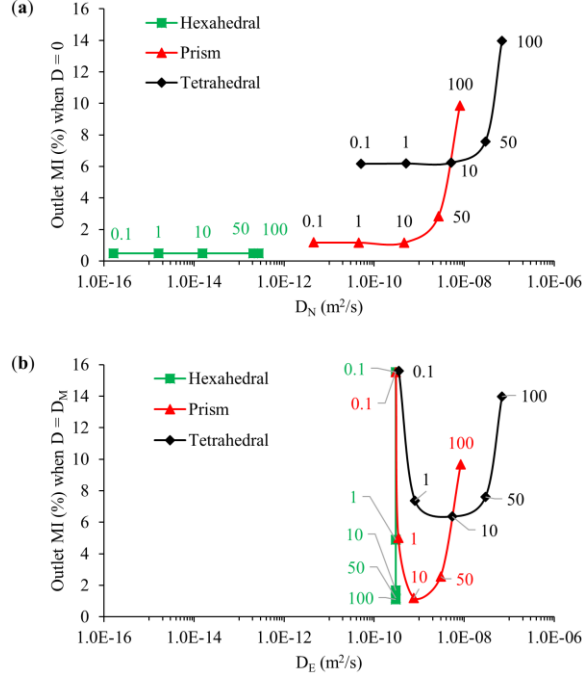


Figure 4.18 The change of outlet MI with respect to numerical and effective diffusion approximations at L1 level of all mesh structures and all Re scenarios: (a) numerical diffusion vs. MI; (b) effective diffusion vs. MI. Inserted numbers on the data points show corresponding Re numbers.

If the scalar transport simulations are performed using the physical molecular diffusion constant, all three mesh types present consistent results only at $Re = 0.1$ flow scenario as shown in Figure 4.18b. When Figure 4.18a and Figure 4.18b are evaluated together, however, there is an inconsistency between two plots which needs to be explained. In Figure 4.18a, prism and tetrahedral mesh solutions yield higher false mixing values than that of hexahedral mesh at $Re = 0.1$. This variation between mesh types is observed because while hexahedral mesh type can tolerate the pure advection transport conditions ($Pe \rightarrow \infty$) as a result of a good mesh-flow alignment in the mixing channel, other two mesh groups suffer from non-orthogonality even at low flow conditions. Nonetheless, when $Re = 0.1$ simulations are performed using the physical molecular diffusion constant, pure advection conditions are improved substantially (i.e., $Pe = 3.33 \times$

10^2) which in turn helps resulting in much lower numerical diffusion in prism and tetrahedral mesh solutions. Thus, all three mesh types estimate almost identical outlet MIs in $Re = 0.1$ simulations. This explanation is also valid for hexahedral and prism mesh structures at $Re = 1$.

As shown in Figure 4.18b, effective diffusion constants, estimated from hexahedral mesh solutions, represent the physical molecular diffusion constant in all Re scenarios. For other mesh groups, however, effective diffusion values increase with rising flowrates in the micromixer. To understand the divergence between the trendlines of hexahedral mesh and other two mesh groups, numerical diffusion effects and mixing dynamics in the T-shape micromixer need to be evaluated together. First, it should be reminded that fluid mixing mainly develops based on the diffusive interaction between fluids due to a unidirectional smooth flow profile in the mixing channel. Therefore, increasing the flowrate in the micromixer slows down diffusive mixing process since the mean residence time of the fluids is diminished in microchannels. When the hexahedral mesh outcomes are investigated in Figure 4.18b, it is obvious that the MI index values keep declining continuously with the increase of Re number in the micromixer. In addition, a vertical trendline is observed since the physical molecular diffusion constant is completely recovered from the numerical solutions of all flow conditions. In prism and tetrahedral mesh simulations, however, this situation is complicated since numerical diffusion errors contribute to unphysical fluid mixing. In prism mesh solutions, numerical diffusion effects are tolerable up to $Re = 10$ flow scenario and beyond this point MI values show an increasing trend. The outlet MI values, obtained from $Re = 50$ and 100 flow scenarios, are entirely developed by numerical diffusion errors, and hence these mixing estimates are

completely unphysical. A similar trend is also observed in tetrahedral mesh simulations, but the negative effects of numerical diffusion are at much higher levels compared to the prism mesh solutions. While these effects can be tolerated only in the lowest flow condition tested, after this point the MI results diverge from the other two mesh solutions.

4.4.2.3 Analysis of numerical diffusion in FEM solutions

In FEM analysis, simulations were only performed for hexahedral mesh type using the same simulation parameters with FVM. While L1, L2, L3, and L4 mesh levels were studied at $Re = 100$ flow condition, the finest mesh level was employed in $Re = 0.1$ simulations. These scenarios were selected to show the effects of artificial diffusion stabilization method for advection dominant systems in FEM. When Pe_Δ is greater than two, the numerical solution of AD equation gives oscillatory solution in FEM depending on the magnitude of cell Pe number. In the COMSOL software, consistent and inconsistent stabilization techniques are provided to overcome numerical instabilities during the numerical solution of scalar transport field. In the consistent stabilization approach, molecular diffusion constant is increased locally in the regions of computational domain where sharp scalar gradients exist. Therefore, the stability of the numerical solution is ensured. In the inconsistent method, however, the molecular diffusion constant is increased in the entire transport domain to reduce Pe_Δ number around two and guarantee stability during the numerical solution as described below.

$$Pe_\Delta = \frac{\bar{u}\Delta x}{D_M + D_{AD}} \quad (27)$$

To decrease the Pe_Δ number to a moderate number, molecular diffusion constant is increased by adding artificial diffusion as shown in Eq. (27). In this equation, D_{AD} describes the artificial diffusion constant and formulized as $D_{AD} = \delta \bar{u} \Delta x$, in which δ is a tuning factor, $0 < \delta < 1$. In FEM simulations, this value was selected as 0.25 and 0.50 to show artificial diffusion effects at two different magnitudes. The above tuning parameters reduce the Pe_Δ number to “4 and 2” at $Re = 100$, and “2.22 and 1.43” at $Re = 0.1$ respectively. Meanwhile, it should be stated that FEM also requires stabilization to reduce numerical viscosity and dispersion problems in numerical approximation of flow field; however, as mentioned earlier, high kinematic viscosity of the fluids reduces the Re_Δ numbers to moderate values (e.g., maximum $Re_\Delta \approx 5$ at $Re = 100$, see Table 4.1) at which numerical complications are substantially suppressed during the simulations. Figure 4.19a shows crosswise velocity distributions on the yz -plane at $x = 200 \mu\text{m}$ (on the dashed line arrow I in Figure 4.4) which are obtained from FEM solutions of hexahedral mesh levels at $Re = 100$. As may be seen from Figure 4.19a, all mesh levels can resolve the velocity profile similarly with an insignificant difference between mesh levels. Also, Figure 4.19b confirms that FVM and FEM provide almost identical results for the same velocity profile on the yz -plane at $x = 200 \mu\text{m}$.

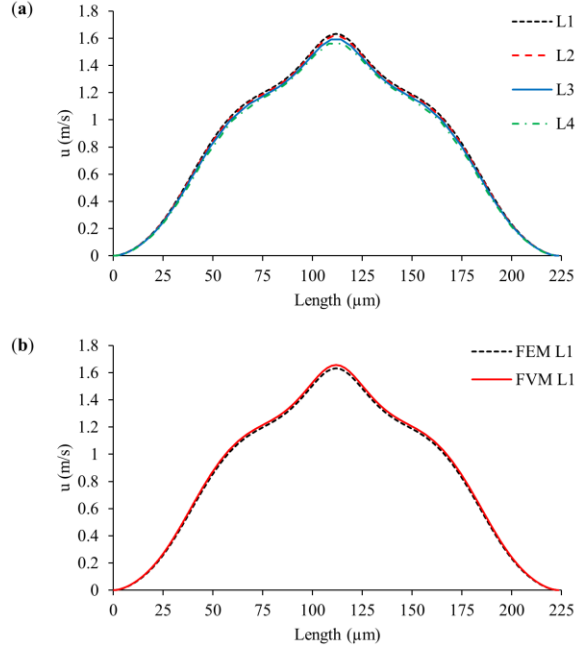


Figure 4.19 Velocity distributions on the yz-plane at $x = 200 \mu\text{m}$ (on the dashed line arrow I in Figure 4.4) in $\text{Re} = 100$ scenario: (a) FEM solutions of hexahedral mesh levels (i.e., L1, L2, L3, and L4); (b) comparison of FEM and FVM at L1 level of hexahedral mesh.

Figure 4.20a shows the outlet scalar distributions of the $\text{Re} = 100$ flow scenario (on the dashed line arrow II in Figure 4.4) which are obtained from FEM simulations with the consistent stabilization method when $\text{DM} = 3 \times 10^{-10} \text{ m}^2/\text{s}$. As reflected in Figure 4.20a, scalar transport solutions do not show an oscillatory behavior when different levels of hexahedral mesh configuration are used in the computational domain. In addition, the resolved scalar transport fields, obtained from different mesh levels, are consistent with the FVM solutions as illustrated in Figure 4.20b. An insignificant difference between the two numerical methods arises only at L4 mesh level. Nevertheless, both methods successfully captured the sharp front at the exit of the mixing channel. From Figure 4.20a and Figure 4.20b, it is apparent that consistent algorithm performs a stabilization appropriately.

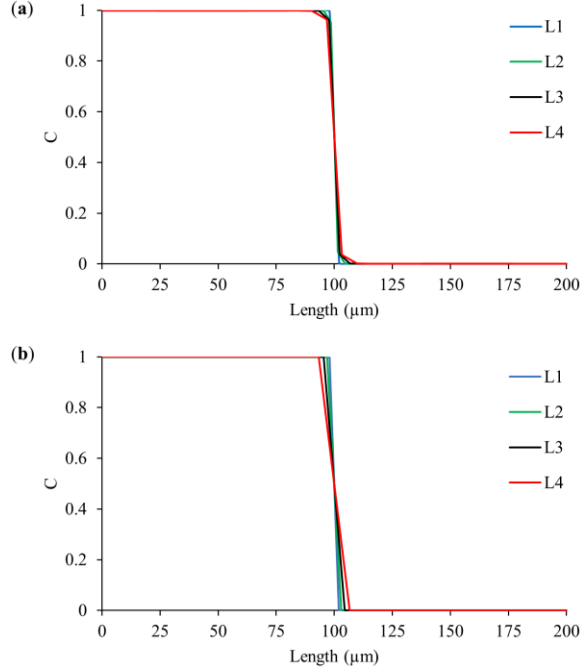


Figure 4.20 Outlet scalar distributions along the width of the outlet at $z = 50 \mu\text{m}$ (on the dashed line arrow II in Figure 4.4) for L1, L2, L3, and L4 levels of hexahedral mesh ($\text{Re} = 100$ and $\text{DM} = 3 \times 10^{-10} \text{ m}^2/\text{s}$): (a) FEM solution with consistent stabilization; (b) FVM solution.

However, when inconsistent stabilization is used in the simulations, results exhibit a considerable difference between consistent method as shown in Figure 4.21a and Figure 4.21b. If the tuning parameter is set to 0.25 ($\text{Pe}_\Delta = 4$), sharp concentration profile smears significantly. This situation is worse when the tuning parameter is increased to 0.50 ($\text{Pe}_\Delta = 2$) by which the scalar profiles are flattened noticeably. Also, the divergence in the solution increases with coarsening grid sizes. These are obviously the effects of artificially added diffusion amount. Although the solution of scalar transport equation does not show any instabilities around $\text{Pe}_\Delta = 2$, the effects of artificial diffusion in the system are not tolerable in terms of the evaluation of mixing efficiency in the micromixer. As may be figured out from Eq. (4.1), another option to reduce Pe_Δ number to 2 is using much smaller elements

in the computational domain; however, this method is not feasible since the required mesh density will increase to the order of 10^{10} .

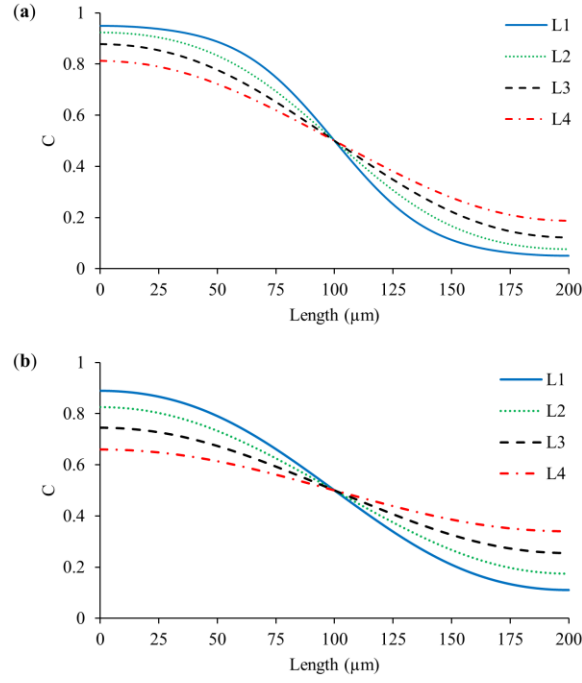


Figure 4.21 Outlet scalar distributions along the width of the outlet at $z = 50 \mu\text{m}$ (on the dashed line arrow II in Figure 4.4) for L1, L2, L3, and L4 levels of hexahedral mesh ($\text{Re} = 100$ and $D_M = 3 \times 10^{-10} \text{ m}^2/\text{s}$). FEM solutions with inconsistent stabilization: (a) $\delta = 0.25$; (b) $\delta = 0.50$.

4.4.2.4 Comparison of FVM and FEM solutions

The comparison of FVM and FEM indicates that there is a significant variation between solutions when the inconsistent stabilization method is applied in FEM as illustrated in Figure 4.22a. The inconsistent stabilization cases cannot capture the actual scalar concentration profile at the outlet of the micromixer and provide significantly altered concentration distributions depending on the size of the tuning factor. If the performance of the micromixer is evaluated using inconsistent artificial diffusion method, unphysical excess diffusivity in the system will completely mask the real mixing performance, and

thus change the mixing conditions of the physical problem investigated. As shown in Figure 4.22b, there is a negligible difference between FEM with consistent stabilization and FVM, in terms of predicted outlet mixing efficiency of the micromixer. However, when the inconsistent method is applied with a tuning parameter value of 0.5, the outlet mixing efficiency of the micromixer increases up to 75% at L4 grid size. The negative effects of the inconsistent method are still significant even for the best-case scenario, i.e., L1 mesh level and $\delta = 0.25$, in which estimated mixing efficiency is more than 30%.

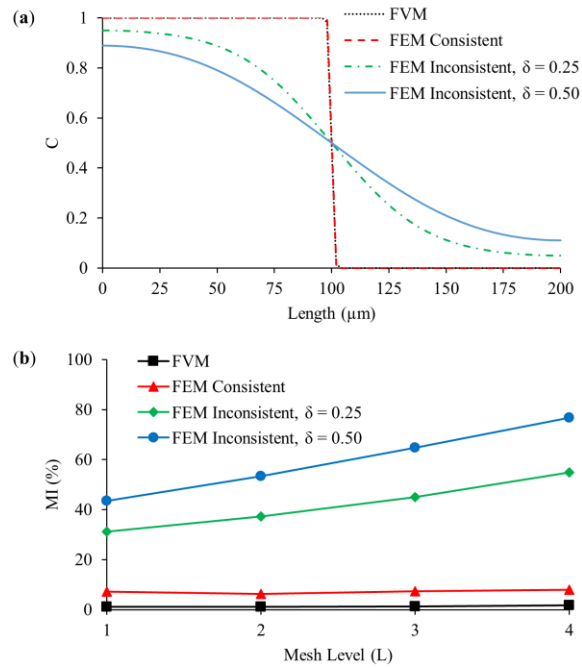


Figure 4.22 Comparison of FVM and FEM simulations at $\text{Re} = 100$ ($D_M = 3 \times 10^{-10} \text{ m}^2/\text{s}$): (a) outlet scalar distributions along the width of the outlet at $z = 50 \mu\text{m}$ (on the dashed line arrow II in Figure 4.4) for L1 level of hexahedral mesh; (b) MI at the outlet for L1, L2, L3, and L4 levels of hexahedral mesh.

The same situation is also observed in the $\text{Re} = 0.1$ simulations of hexahedral mesh type. As shown in Figure 4.23a and Figure 4.23b, FEM with consistent stabilization and FVM both render an identical concentration distribution along the mixing channel width and yield an equal mixing efficiency at the exit. Meanwhile, although the inconsistent method

captures different concentration profiles, the magnitude of smearing is decreased due to decreasing velocity magnitudes in $Re = 0.1$ flow scenario. Nevertheless, the outlet mixing efficiencies predicted are still 2 and 2.5 times more than that of FVM and FEM with consistent stabilization solutions when δ is selected 0.25 and 0.5 respectively.

In view of the above findings, the mixing performance of the micromixer may be changed artificially depending on the FEM stabilization technique employed. Using the consistent stabilization method, the results are almost uniform with FVM solutions; however, when the inconsistent correction method is employed in FEM, mixing efficiencies may increase depending on the magnitude of the tuning parameter selected. In several numerical micromixer studies, in which FEM is utilized to solve the governing equations, the effect of stabilization type employed is not discussed and reported. As evidently shown in the present section, however, the selection of an appropriate stabilization method is critical to evaluate the real mixing performance of a micromixer. Otherwise, artificial or false mixing efficiencies may be documented as physical outcomes.

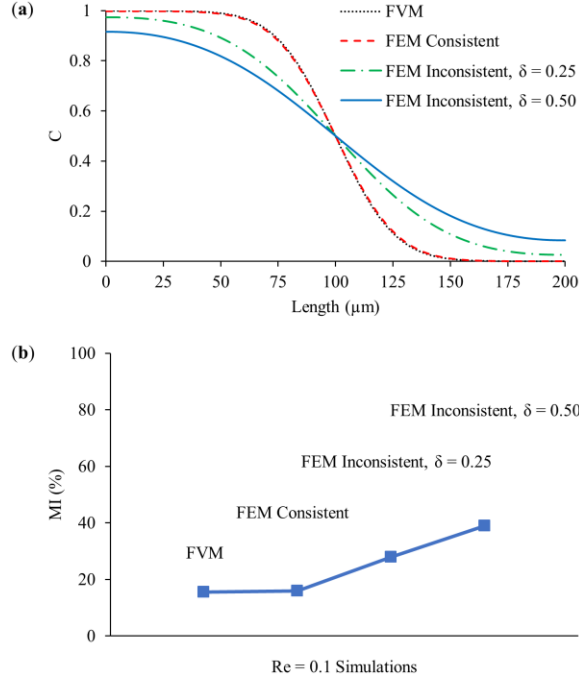


Figure 4.23 Comparison of FVM and FEM simulations at $\text{Re} = 0.1$ ($D_M = 3 \times 10^{-10} \text{ m}^2/\text{s}$): (a) outlet scalar distributions along the width of the outlet at $z = 50 \mu\text{m}$ (on the dashed line arrow II in Figure 4.4) for L1 level of hexahedral mesh; (b) MI (%) values at the outlet.

4.4.3 Conclusions

In section 4.4, the behaviour of numerical diffusion errors was examined under the conditions of mostly unidirectional fluid flow and advection dominance. For this purpose, several scenarios were setup and performed on a 3-D T-shape passive micromixer design. The effects of different flow, scalar transport, mesh properties, and numerical techniques were investigated. It was shown that grid studies should be conducted based on scalar transport simulation outcomes since the highest numerical error production occurred during the numerical solution of AD equation. In addition, outlet mixing efficiency should be preferred as a grid study parameter because the maximum discrepancy between mesh levels is observed at the outlet. It was also shown that all mesh configurations tested resolved the flow field quite similarly at the highest flow condition simulated (i.e., $\text{Re} =$

100). Thus, when flow parameters are employed in grid studies, outcomes may cause misevaluation of numerical diffusion errors and selecting inappropriate mesh configurations.

In FVM, maintaining the orthogonality between flow and grid boundaries significantly reduced the numerical diffusion in scalar transport simulations. Hence, hexahedral mesh solutions provided the most accurate mixing outcomes among all three mesh types tested. When, however, prism and tetrahedral mesh structures were used, mixing outcomes were masked by numerical diffusion errors. All three mesh configurations provided consistent mixing results for only the lowest flow condition tested (i.e., $Re = 0.1$ and $Pe = 3.33 \times 10^2$). Based on the results in this section, it should be emphasized that the use of prism and tetrahedral mesh types should be avoided or limited substantially to resolve scalar field in advection dominant transport systems.

When FEM was employed in the flow simulations, flow domain was resolved with insignificant differences between hexahedral mesh levels and almost identical flow solutions were obtained with FVM. Besides, in the scalar transport simulations, different outcomes were obtained depending on the type of stabilization technique applied. The consistent stabilization method yielded almost the same results with FVM whereas the inconsistent stabilization approach changed the physical problem examined and caused the mixing performance of the micromixer to be increased unphysically. Therefore, when FEM is used in numerical investigations of advection dominant scalar transport systems, the effect of numerical stabilization technique applied should be evaluated carefully to avoid reporting suspicious mixing outcomes.

4.5 Computational Evaluation of Numerical Diffusion Errors for Different Grid Levels of Hexahedron Element Type and Peclet Number Scenarios in 3-D Swirl-Generating Passive Micromixers

4.5.1 Micromixer design and case setup

In previous section, the impact of numerical diffusion was exhaustively examined in a simple T-shaped passive micromixer and it was found that maintaining a good mesh flow orientation is essential to decrease false diffusion in advection dominant transport systems. This was only possible when hexahedron type mesh elements were employed in the computational domain. Nonetheless, unlike the simple segregated and vortex flow profiles, developed in simple T-shaped passive micromixers, complex flow patterns are expected to generate high numerical diffusion effects due to the continuous violation of flow-grid orthogonality. Thus, it is essential to identify those effects in terms of the limits of numerical diffusion errors in CFD simulations of passive micromixers to provide reliable mixing outcomes.

In this section, numerical diffusion errors are examined in complex flow systems where flow vectors constantly form oblique angles to the cell boundaries in the computational domain. For this purpose, two different 3-D swirl-generating passive micromixers with two- and four-inlet constructions are designed as shown in Figure 4.24. Micromixers consist of three branches as follows. A square mixing channel with an edge size of $100\ \mu\text{m}$ and length (L) of $1900\ \mu\text{m}$, a $400\ \mu\text{m}$ -wide square mixing box with a $100\ \mu\text{m}$ height, and $500\ \mu\text{m}$ -long inlet channels with a cross-section of $100\ \mu\text{m} \times 100\ \mu\text{m}$.

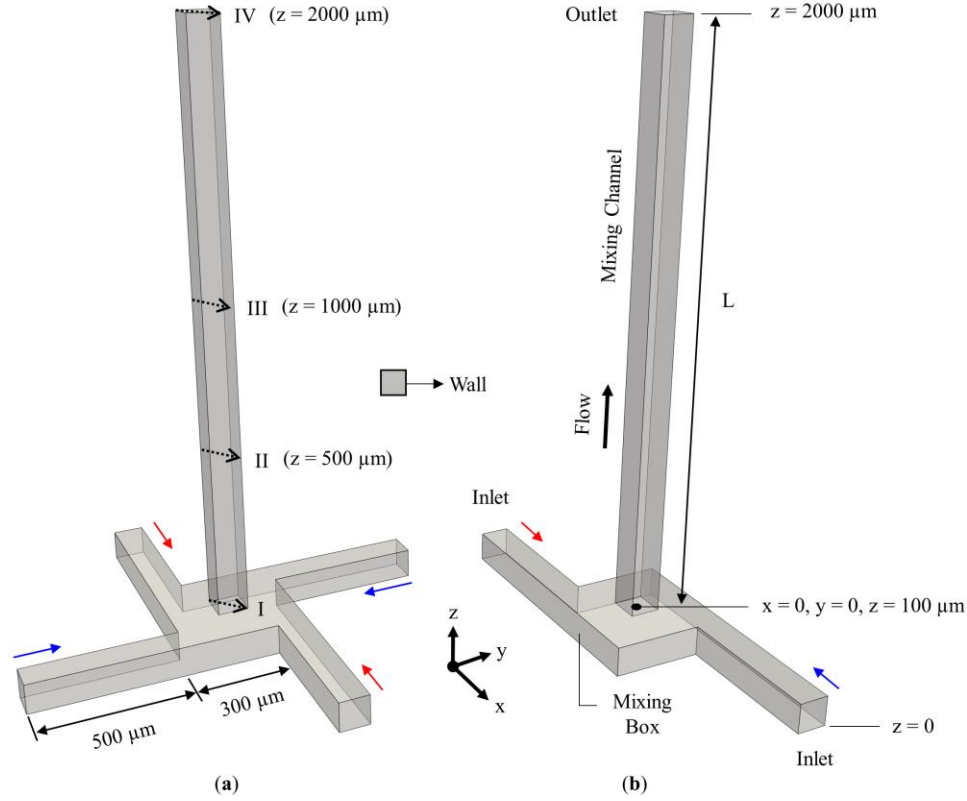


Figure 4.24 Swirl-generating passive micromixers: (a) four-inlet design and (b) two-inlet design. Dashed arrow lines I, II, III, and IV are edge-to-edge on the x-y plane at different z-heights; $z = 100, 500, 1000$, and $2000 \mu\text{m}$ respectively.

The computational domain in both four-inlet and two-inlet designs are meshed using structured hexahedron-type elements at six different mesh density levels as given in Table 4.5. As shown in Figure 4.25, while smaller grid sizes in the second column of Table 4.5 are used in the mixing channel and partially in the mixing box, since high swirl generation is expected to occur in these sections of the micromixers, larger grid sizes are positioned in the inlet channels due to the fact that flows in the inlet channels are mainly unidirectional and mesh-flow alignment is kept seamlessly in these regions. To preserve a good mesh quality in the computational domain, the maximum aspect ratio in a single hexahedron mesh element is selected as 2.

Table 4.5 Mesh properties and densities for six different levels.

Mesh Level	Δx (μm)	Total Mesh Elements (Million)	
		Four-inlet	Two-inlet
L1	1.25–2.50	16.40	15.10
L2	1.50–2.50	10.00	9.20
L3	1.75–3.00	6.30	5.70
L4	2.00–3.00	4.60	4.10
L5	2.25–3.50	3.00	2.75
L6	2.50–3.50	2.50	2.10

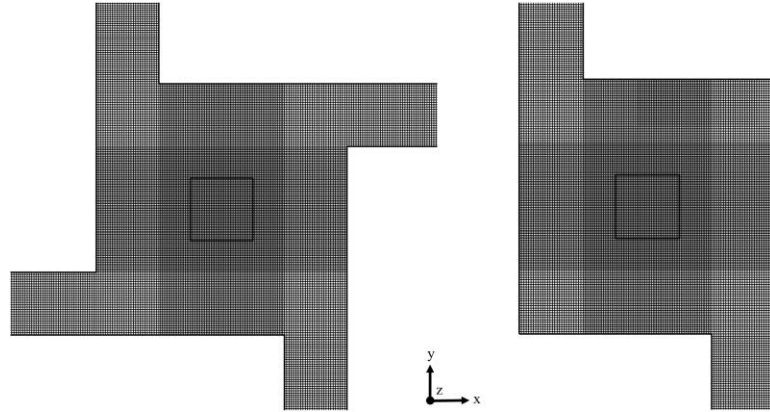


Figure 4.25 Orientation of structured hexahedron mesh elements in the computational domains.

To quantify and characterize the upper limits of the numerical diffusion effects, the transport of a passive scalar is investigated for three different molecular diffusion constants under two different swirling flow conditions, i.e., $Re = 120$ and 240 , as given in Table 4.6. In addition, the corresponding Pe and Pe_{Δ} numbers for all simulation scenarios are also presented in Table 4.6 to be able to characterize the false diffusion generation in the system. Initially, numerical diffusion analysis is conducted using the smallest molecular diffusion constant in Table 4.6 for all the mesh levels of micromixer configurations and two flow conditions. Later, the outcomes are evaluated and other molecular diffusion constants are

simulated for only mesh levels L1, L3, and L6 since the magnitude of false diffusion in passive scalar transport simulations may be well defined based on the Pe_Δ number, which carries the properties of grid size, velocity, and molecular diffusivity. Therefore, characterization of the numerical diffusion errors for three different grid sizes (or Pe_Δ number) will provide sufficient information on the evolution of the numerical diffusion trend in the system.

Table 4.6 Test cases for two-inlet and four-inlet micromixer designs.

Reynolds				120		
240						
D_M (m²/s)	3×10^{-10}	3×10^{-9}	6×10^{-8}	3×10^{-10}	3×10^{-9}	1.5×10^{-8}
Peclet	8×10^5	8×10^4	4×10^3	4×10^5	4×10^4	2×10^3

Mesh Level				Pe_Δ		
L1	10,000	1000	50	5000	500	100
L2	12,000	1200	60	6000	600	120
L3	14,000	1400	70	7000	700	140
L4	16,000	1600	80	8000	800	160
L5	18,000	1800	90	9000	900	180
L6	20,000	2000	100	10,000	1000	200

4.5.2 Results and discussion

4.5.2.1 Grid study

To observe the trend in numerical errors in fluid flow and passive scalar transport simulations, six different mesh levels are determined for the micromixers designed. The density difference between L1 and L6 levels is around 14 million and 13 million for four-inlet and two-inlet micromixers respectively. Such a big density difference between meshes is necessary to capture the numerical diffusion effects in terms of the characteristics of the

complex fluid flow in the micromixers. Figure 4.26 shows the mesh study results for fluid flow at $Re = 240$ based on two different flow parameters, the pressure drop in micromixers and velocity distribution at the exit of the mixing box (Line-I in Figure 4.24) where the most complex flow profile is observed. It is clear from Figure 4.26c and Figure 4.26d that the fluid flow in micromixers is resolved identically for all mesh levels tested. The maximum difference between L1 and L6 for both test parameters is less than 1%. As mentioned earlier, this small difference between grid levels occurred as a result of the relatively high kinematic viscosity (e.g., $\nu = 10^{-6} \text{ m}^2/\text{s}$) of the fluids which leads to a very low Re_Δ number in the computational domain (see section 4.2). At $Re = 240$, even the biggest grid size, L6, results in a Re_Δ number around 6 in the mixing channel which creates an insignificant amount of numerical viscosity in the flow solution.

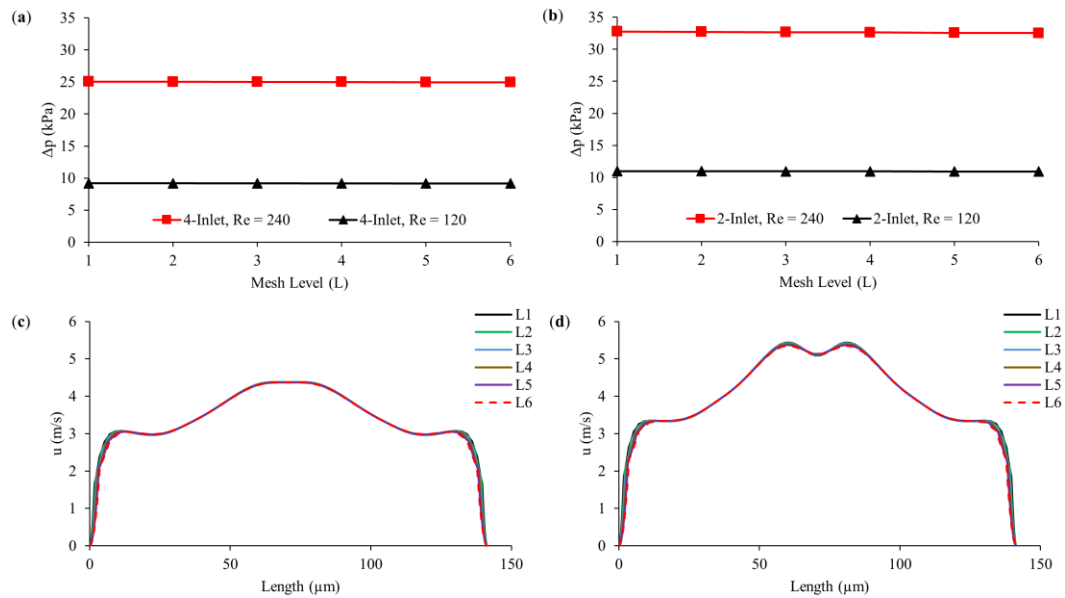


Figure 4.26 Grid study results for fluid flow: (a) and (b) pressure drop (Δp) in micromixers at $Re = 240$ and 120 for four-inlet and two-inlet designs respectively; (c)

and (d) velocity distribution on x-y plane at the exit of mixing box (Line-I in Figure 3) at $Re = 240$ for four-inlet and two-inlet designs respectively.

In contrast to the consistency between mesh levels in terms of the resolution of the flow field, passive scalar transport simulations show a high discrepancy as a result of much higher Pe_Δ numbers compared to the Re_Δ numbers in the momentum transport. Such high Pe_Δ numbers (see Table 4.6, when $D_M = 3 \times 10^{-10} \text{ m}^2/\text{s}$) essentially indicate the occurrence of sharp concentration gradients in the scalar transport domain. Figure 4.27 and Figure 4.28 show scalar transport results for different mesh levels at $Re = 240$ and 120 flow conditions respectively. In each figure, while “a and b” and “c and d” plots represent four-inlet and two-inlet micromixer configurations, “a and c” and “b and d” plots show concentration distributions on Line-I and Line-II, as positioned in Figure 4.24, respectively. In both flow scenarios, while all mesh levels in micromixer configurations exhibit relatively similar concentration distributions at the exit of the mixing box, these concentration trends differentiate at $z = 500 \text{ }\mu\text{m}$ in the mixing channel. This is because swirl motion starts in the mixing box and continually develops in the streamwise direction. Therefore, during the rotational flow of fluid pairs in the mixing channel, the transport solution starts producing numerical diffusion depending on the development of swirl profile and the magnitude of the Pe_Δ number for a specific mesh level. As a result of the difference between flow patterns, scalar concentration trends on the same sampling lines and variations between mesh levels are quite different for four-inlet and two-inlet configurations. In both micromixer configurations, however, there is a distinct difference between mesh levels L1 and L6 in terms of the resolution of the scalar field at $z = 500 \text{ }\mu\text{m}$ as shown in plots (b) and (d) of Figure 4.27 and Figure 4.28. Such a large variation emerged as a result of a doubled Pe_Δ number between mesh levels L1 and L6 which are 10,000 and 20,000 for $Re = 240$ and

5000 and 10,000 for $Re = 120$ respectively. Meanwhile, variations between all mesh levels are obviously smaller in the $Re = 120$ when compared to the $Re = 240$ case, due to smaller Pe_Δ numbers which generate relatively less numerical diffusion. On the other hand, although increasing the mesh density helps to resolve differences in scalar concentration trends, still the finest mesh may contain a substantial amount of numerical diffusion because the Pe_Δ number is still in the order of 5000 even for the best-case scenario, tested in this section (e.g., $Re = 120$, L1 mesh level, and $D_M = 3 \times 10^{-10} \text{ m}^2/\text{s}$).

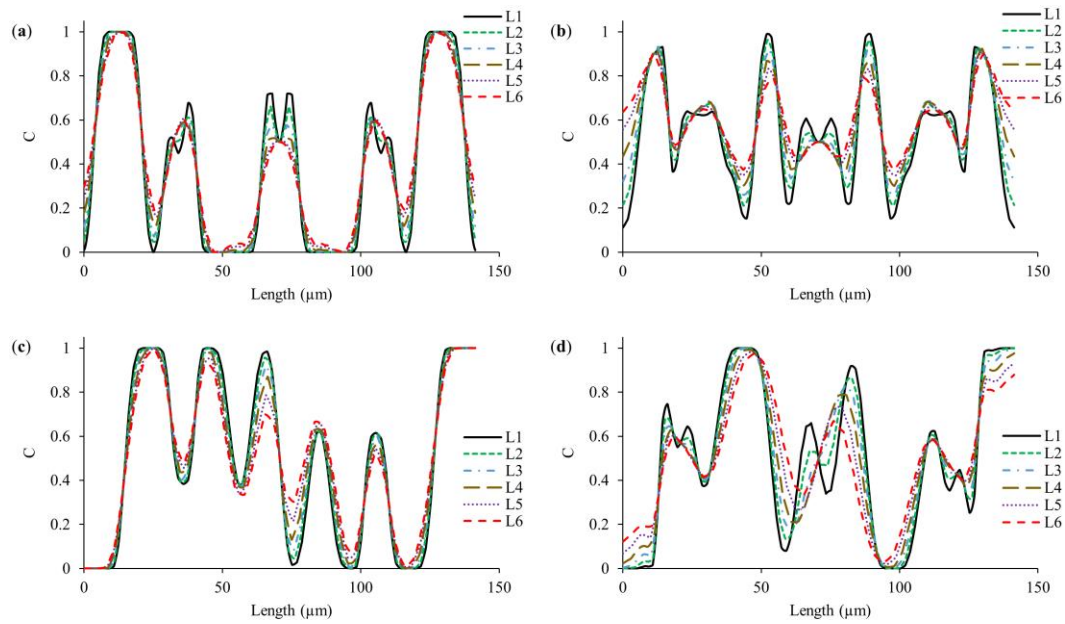


Figure 4.27 Grid study results for scalar transport at $Re = 240$: (a) and (c) concentration distribution on x-y plane at the exit of the mixing box (Line-I in Figure 4.24) for four-inlet and two-inlet designs respectively; (b) and (d) concentration distribution on x-y plane at $z = 500 \mu\text{m}$ (Line-II in Figure 4.24) for four-inlet and two-inlet designs respectively.

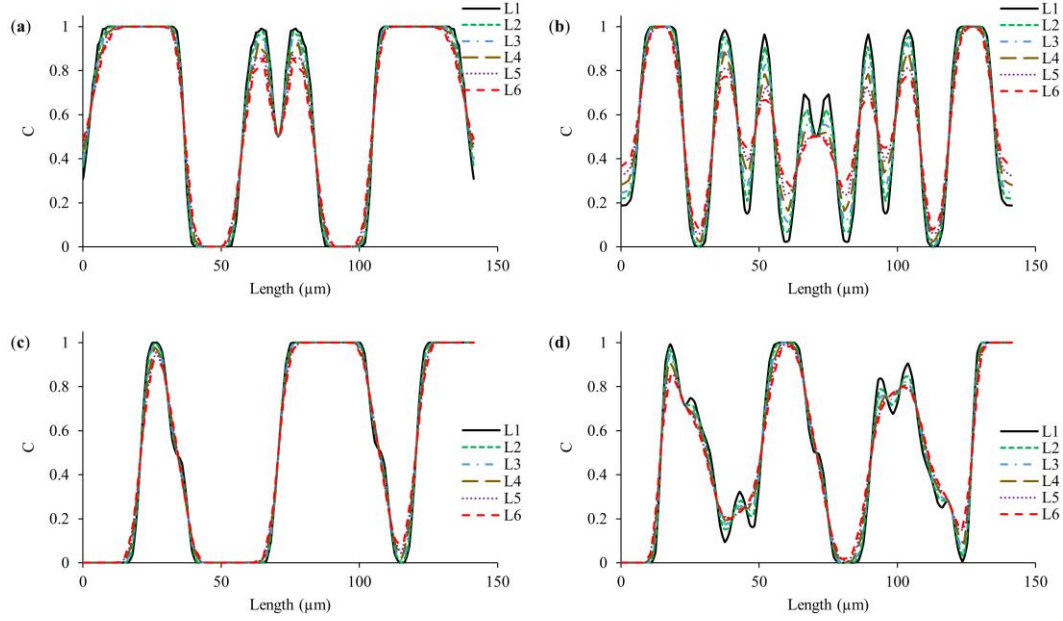


Figure 4.28 Grid study results for scalar transport at $Re = 120$: (a) and (c) concentration distribution on x-y plane at the exit of the mixing box (Line-I in Figure 4.24) for four-inlet and two-inlet designs respectively; (b) and (d) concentration distribution on x-y plane at $z = 500 \mu m$ (Line-II in Figure 4.24) for four-inlet and two-inlet designs respectively.

To further investigate the numerical diffusion development in the micromixers, mixing on different cross-sections between the entrance and outlet of the mixing channel were measured and graphed as shown in Figure 4.29 in which “a and b” and “c and d” plots show four-inlet and two-inlet micromixer configurations and “a and c” and “b and d” plots show $Re = 240$ and 120 scenarios respectively. In the $Re = 120$ case, while mesh levels predict a similar amount of mixing values at the entrance of the mixing channel, measured mixing values are different due to developing mixing in the mixing channel. These differences between mesh levels emerge as a result of numerical diffusion during the mixing process in the mixing channel since each mesh level resolves different scalar concentration profiles as previously shown in Figure 4.27 and Figure 4.28. Depending on the flow profile created and the magnitude of the swirls in the mixing channel, variation

between mesh densities increases until a certain distance in the mixing channel is reached. After this point, mesh levels exhibit a mild convergent tendency. At $Re = 240$ scenario, however, while the two-inlet design shows a similar mixing estimation trend as observed in the $Re = 120$ case, the four-inlet configuration draws quite a different profile. As the variation between mixing indexes of different mesh densities increases until the $z = 500$ μm in the mixing channel, after this point, the variation declines, and a convergence is observed at the outlet of the micromixer. Thus, it should be noted that selecting the scalar concentration sampling points for grid studies becomes important to reveal the actual contradiction between mesh levels. Figure 4.30 shows the comparison of mesh levels with the finest mesh in terms of mixing index on the x-y plane at different z-distances of the mixing channel. Similarly, while “a and b” and “c and d” plots show the results for four-inlet and two-inlet micromixer designs, “a and c” and “b and d” plots represent $Re = 240$ and 120 scenarios, respectively.

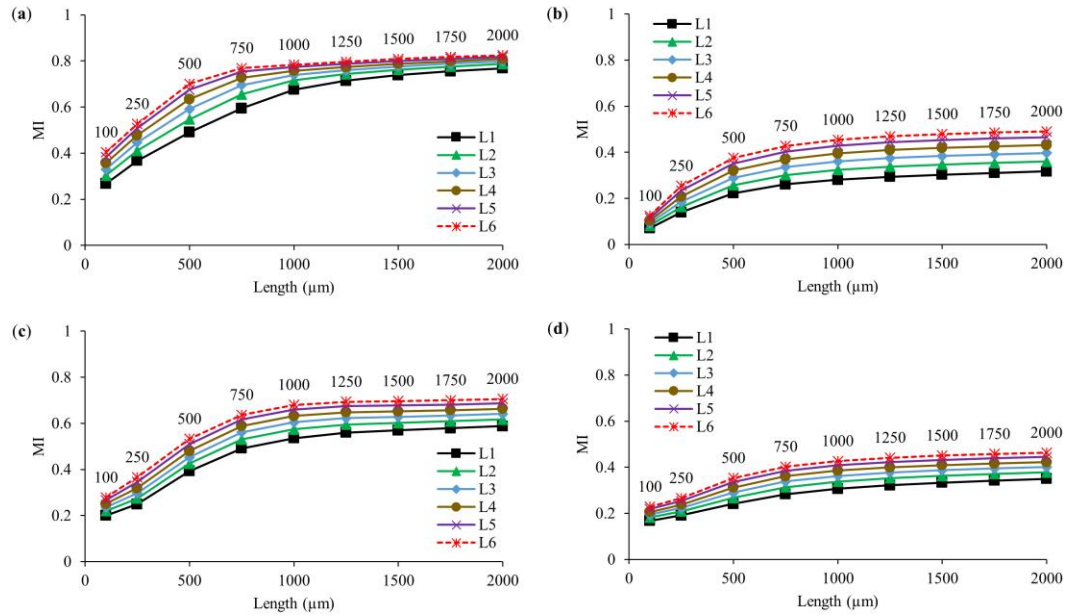


Figure 4.29 Mixing index (MI) values of different cross-sections along the mixing channel: (a) and (c) four-inlet and two-inlet designs at $Re = 240$ respectively; (b) and (d) four-inlet and two-inlet designs at $Re = 120$ respectively. Numbers above trendlines show x-axis values in plots.

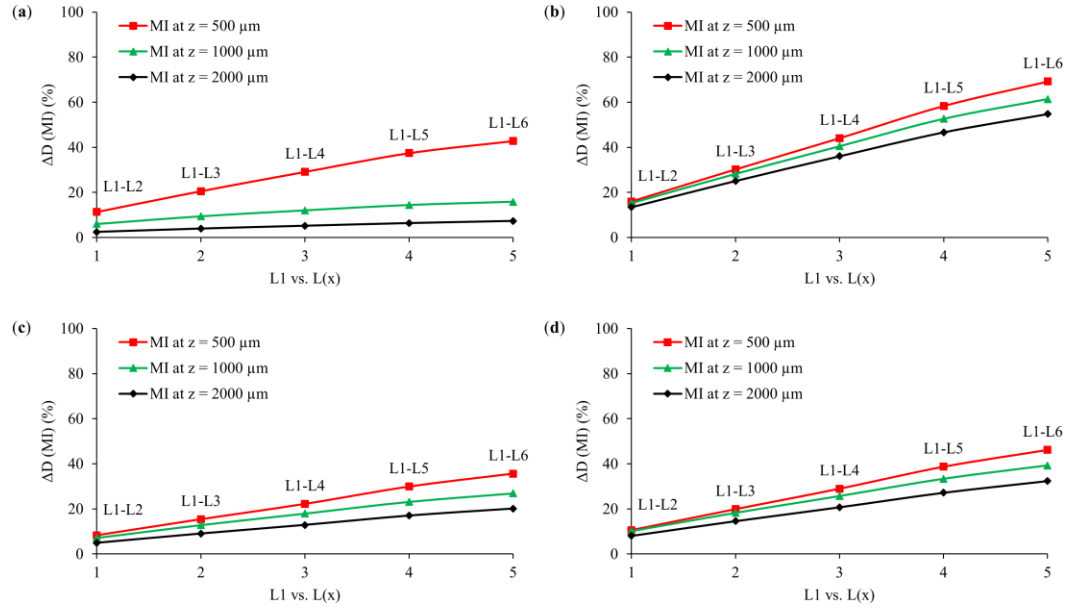


Figure 4.30 Comparison of mesh levels (L2, L3, L4, L5, and L6) with L1 using at different heights in the mixing channel ($z = 500, 1000$, and $2000 \mu m$): (a) and (c) four-inlet and two-inlet designs at $Re = 240$ respectively; (b) and (d) four-inlet and two-inlet designs at $Re = 120$ respectively.

As may be seen from Figure 4.30a–c, and d that mesh refinement considerably reduces the numerical diffusion errors in both micromixer configurations and flow cases. Besides, the maximum difference occurs between L6 and L1 meshes as expected and gradually diminishes with increasing mesh density until the level of L2 and L1 is reached, which is around 10% for all cases. On the other hand, the mixing outcomes, obtained from separate locations, result in different trends for mesh comparisons. Namely, discrepancies between meshes with the finest level reach the maximum at the $z = 500 \mu m$ sampling point and beyond this point it starts decreasing across the mixing channel. While the two-inlet

design reacts to mesh refinement and sampling regions similarly for both $Re = 240$ and 120 flow scenarios as shown in Figure 4.30c and Figure 4.30d, four-inlet configuration shows quite low differences beyond the $z = 500 \mu m$ sampling point at $Re = 240$ as shown in Figure 4.30a. For this case, therefore, the use of the outlet mixing index in the mesh study may seriously mislead the evaluation of numerical diffusion because as the difference between L6 and L1 is around 7% at the outlet, this is 42% at the $z = 500 \mu m$ point. This contradiction is also observed in all other cases at relatively lower magnitudes. The discrepancy observed at different points and the converging tendency of different mesh resolutions across the mixing channel require an explanation. Figure 4.31a and Figure 4.31b show the fluid flow and passive scalar transport domains in the mixing channel of the four-inlet design for both $Re = 240$ and 120 scenarios respectively. As evidenced in Figure 4.31a, the swirling fluid motion starts at the entrance of the mixing channel and continues strongly till the $z = 500 \mu m$. After this point, the intensity of the swirl is dampened and fluid pairs flow along the mixing channel with a relatively smoother rotational movement. Hence, the maximum amount of numerical diffusion is produced between $z = 100 \mu m$ and $500 \mu m$ depending on the grid resolution used. Beyond $z = 500 \mu m$ point, however, the numerical errors, which are already generated, are averaged and transported in the mixing channel as mixing.

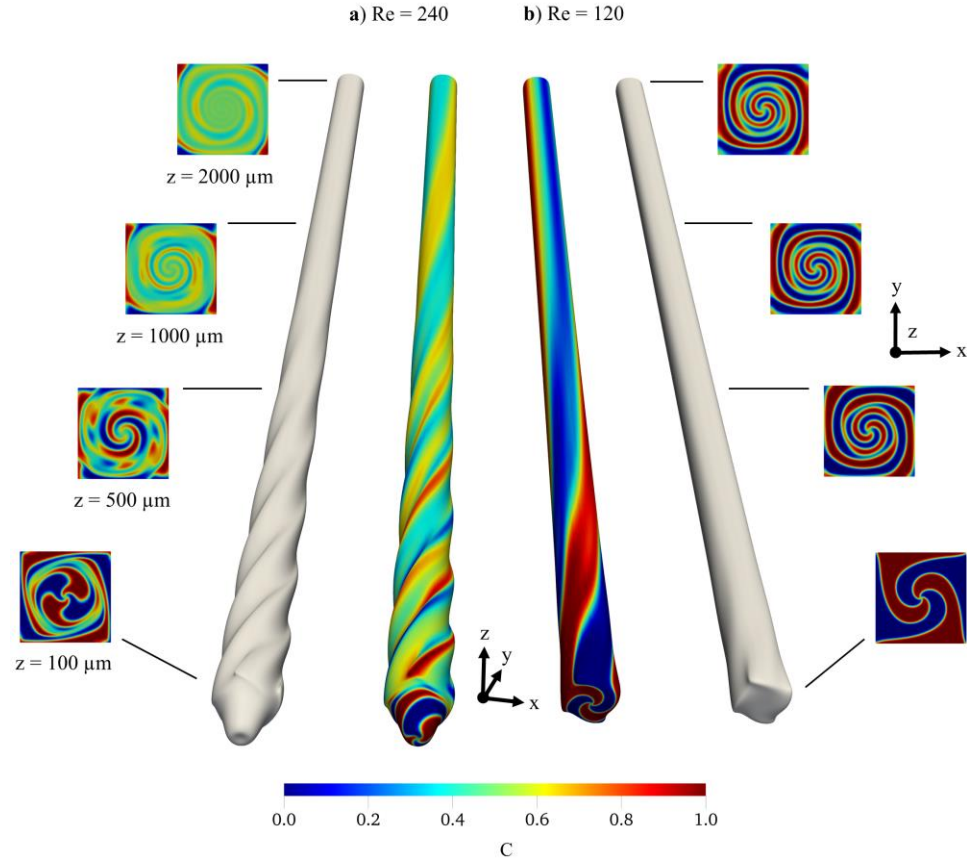


Figure 4.31 Fluid flow and scalar transport domains in the mixing channel of the four-inlet design: (a) $Re = 240$ (left two shapes) and (b) $Re = 120$ (right two shapes). Colored images show passive scalar transport solutions at the L1 mesh level.

The same explanation is also true for $Re = 120$ scenario, but the difference between results at $z = 500 \mu m$ and beyond is less than that of $Re = 240$ case. This is mainly as a result of a relatively low flow velocity and moderate swirl profile, generated in the mixing channel, as shown in Figure 4.31b. In the case of the two-inlet design, flow pattern is quite different than that of four-inlet configuration at $Re = 240$ whereas the swirl profile generated is similar to the four-inlet design at $Re = 120$ as shown in Figure 4.32a and Figure 4.32b respectively. Nevertheless, the maximum difference between mesh resolutions and the finest mesh is still observed at $z = 500 \mu m$ point for both flow scenarios. Based on the discussions in section 4.3, the two-inlet design is expected to produce less numerical

diffusion since injecting the fluids over two inlets will form a relatively small contact surface between fluid bodies compared to the four-inlet injection strategy. However, when the outcomes of the two micromixer configurations are compared qualitatively at $Re = 120$, this is not as projected in the 2-D test case in section 4.3. Although the fluids in the four-inlet micromixer create a larger contact surface at $Re = 120$ as shown in Figure 4.31b, the green regions in this figure are lower than that of the two-inlet solution as displayed in Figure 4.32b. If both figures are compared with respect to cross-sections at the entrance of the mixing channel ($z = 100 \mu\text{m}$), the two-inlet design shows much more green regions as opposed to four-inlet's distinct blue and red color pattern. This is because the uniform velocity magnitude applied from each inlet of the two-inlet micromixer is two times higher than that of the four-inlet in order to provide $Re = 240$ and 120 flow conditions. Therefore, flow patterns, generated in the mixing boxes of both micromixer configurations, are different as displayed in Figure 4.33a and Figure 4.33b, which shows the central plane of the mixing box at $z = 50 \mu\text{m}$ for both micromixer types and flow cases. It is clear from Figure 4.33a and Figure 4.33b that in contrast to a balanced four-sided fluid injection structure with lower flowrates, two-sided inlet orientation and higher flowrates generate a strong vortex inside the mixing box of the two-inlet design in both flow conditions.

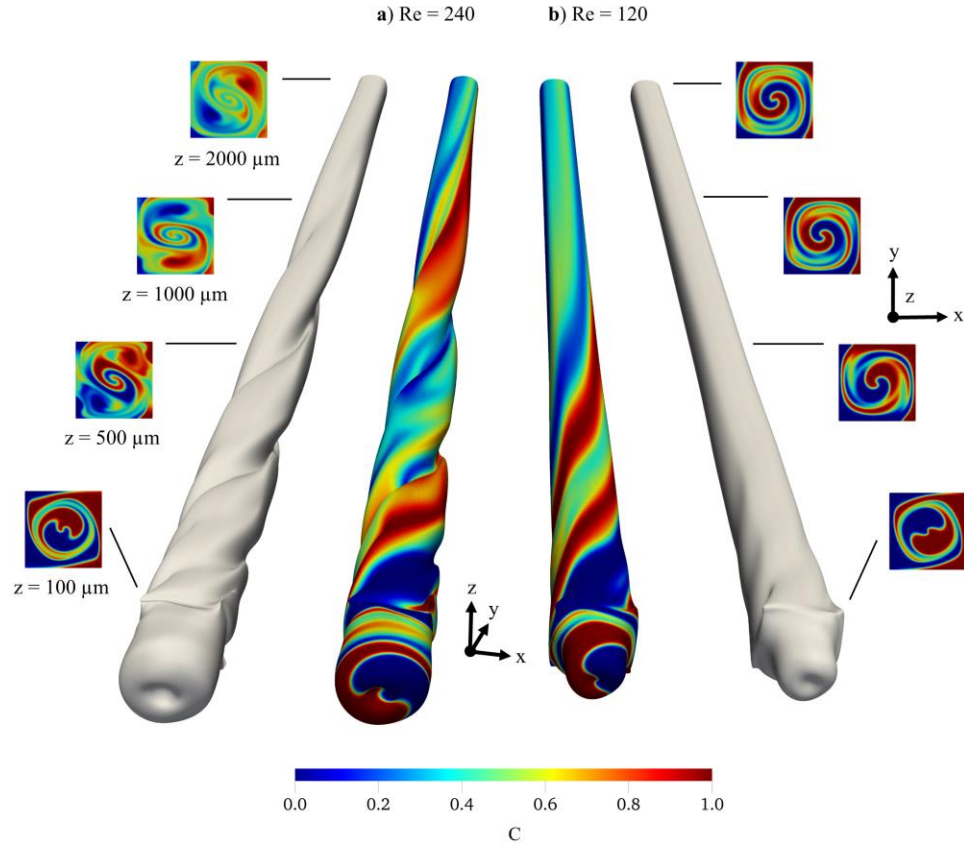


Figure 4.32 Fluid flow and scalar transport domains in the mixing channel of two-inlet design: (a) $Re = 240$ (left two shapes) and (b) $Re = 120$ (right two shapes). Colored images show passive scalar transport solutions at the L1 mesh level.

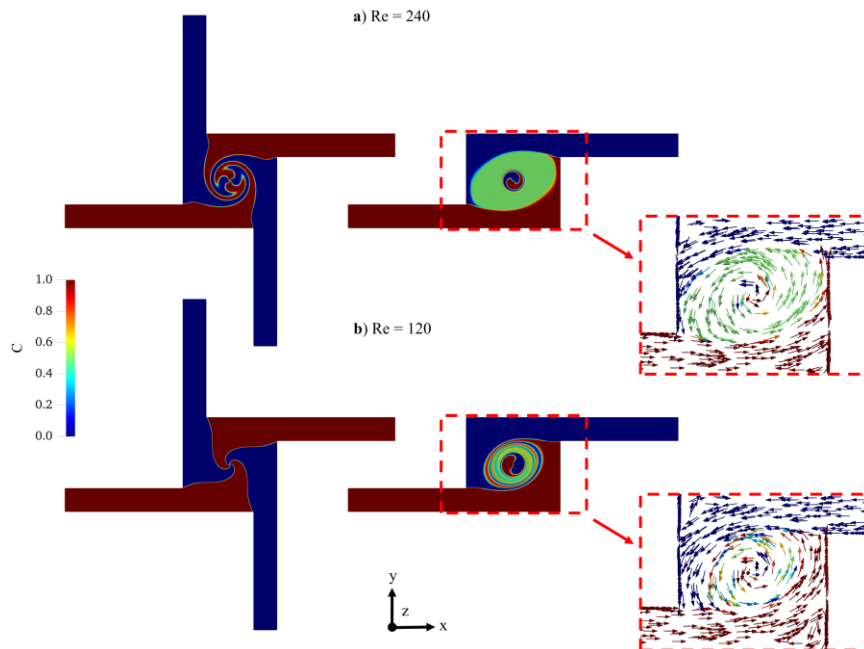


Figure 4.33 Central plane of mixing box at $z = 50 \mu\text{m}$: (a) Four- and two-inlet micromixer designs at $Re = 240$ and (b) four- and two-inlet micromixer designs at $Re = 120$. Arrows in dashed rectangles show velocity vectors on the plane colored by scalar values. Colored images show passive scalar transport solution at the L1 mesh level.

In addition, the strong vortex inside the mixing box creates two different swirls at the entrance of the mixing channel as one is at the center of the channel and the other one is around this central swirl as shown on different cross-sections of Figure 4.32a. It is obvious that while the green areas, which show a fully mixed state, on the cross-sections at $z = 100 \mu\text{m}$ are generated at the beginning of the mixing channel of the four-inlet micromixer, these green regions appear in-between the two swirls and are carried from the mixing box of the two-inlet design as shown in Figure 4.31 and Figure 4.32 respectively. This difference may also be seen when the images in Figures 4.31–4.33 are compared. As a result of higher inlet velocities in the two-inlet design, fluid bodies coming from both inlets encapsulate each other several times by rotating around the center of the mixing box as shown in Figure 4.34a and Figure 4.34b. Besides, the size of the vortex profile created inside the mixing box exceeds the dimensions of the mixing box exit, at which the finest mesh elements are used as displayed in Figure 4.25. Hence, a higher average Pe_{Δ} number around the exit section and repeated mesh-flow disorientation inside the large vortex cause a drastic increase of numerical diffusion generation in the mixing box. In view of these results, false diffusion production is mainly controlled by the mixing channel and mixing box in four-inlet and two-inlet micromixer designs respectively. Accordingly, while the grid size distribution, used inside the mixing box, is a good strategy for a four-inlet micromixer, in the case of the two-inlet configuration, smaller mesh elements need to be

positioned across the mixing box in order to control the amount of numerical diffusion produced.

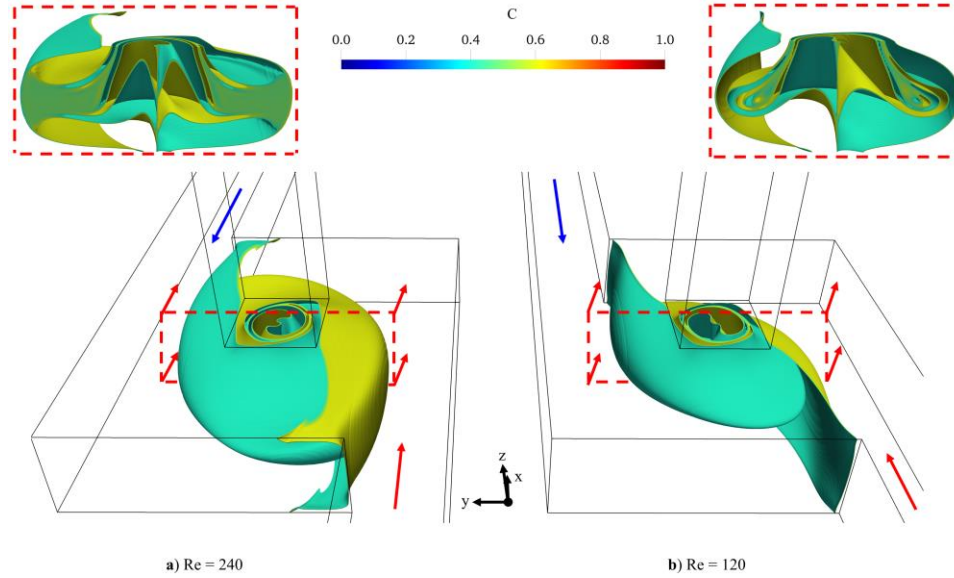


Figure 4.34 Flow profile and multi-layer mixing structure in the mixing box of two-inlet design: (a) $Re = 240$ and (b) $Re = 120$. Colored images show passive scalar transport solution at the L1 mesh level.

4.5.2.2 Analysis of numerical diffusion

In swirl-induced passive micromixers, higher flow rate requirement to create a swirling motion and very low diffusion constants inevitably lead to high Pe numbers. As it is shown in the present section, the numerical solution of high Pe transport systems is quite challenging in terms of controlling the production of numerical diffusion throughout the system. Although the total mesh element numbers used are around 16.4 and 10 million for mesh levels L1 and L2 respectively, still, the discrepancy between these mesh levels is around 10% when MI is used as the parameter. In addition, the effect of change in the numerical diffusion magnitude beyond L1 density is still not known due to the high computational cost. Thus, quantification of numerical diffusion errors is essential.

Table 4.7 shows numerical (when $D_M = 0$) and effective (when $D_M = 3 \times 10^{-10} \text{ m}^2/\text{s}$) diffusion coefficients which are computed from the numerical simulations of all micromixer designs, flow conditions, and mesh densities. As may be evidently seen in Table 4.7, the values of D_N and D_E are very close to each other in almost all scenarios tested, which indicates that the effect of molecular diffusion is severely masked by false diffusion. In both micromixer designs, D_E constants are one and two orders of magnitude higher than physical diffusion constant for $Re = 120$ and 240 flow conditions respectively. Besides, increasing the mesh density reduce the numerical diffusion generated in all scenarios simulated. The two-inlet micromixer simulations produce higher numerical diffusion than that of the four-inlet micromixer structure especially at $Re = 240$ flow scenario. This is obviously due to the strong vortex formation inside the mixing box as explained earlier. Nevertheless, all flow and mesh scenarios, tested for both micromixer designs, failed to recover the given physical diffusion constant and exposed high numerical diffusion errors.

Table 4.7 Numerical (D_N) and effective (D_E) diffusion constants for different micromixer designs, flow scenarios, and mesh densities when $D_M = 3 \times 10^{-10} \text{ m}^2/\text{s}$.

Mesh Level	Four-inlet Design				Two-inlet Design			
	Re = 240		Re = 120		Re = 240		Re = 120	
	D_N	D_E	D_N	D_E	D_N	D_E	D_N	D_E
L1	1.80×10^{-8}	1.93×10^{-8}	2.36×10^{-9}	2.93×10^{-9}	2.17×10^{-8}	2.24×10^{-8}	3.74×10^{-9}	4.41×10^{-9}
L2	2.62×10^{-8}	2.74×10^{-8}	3.64×10^{-9}	4.30×10^{-9}	3.11×10^{-8}	3.19×10^{-8}	5.44×10^{-9}	6.17×10^{-9}
L3	3.48×10^{-8}	3.60×10^{-8}	5.16×10^{-9}	5.94×10^{-9}	4.11×10^{-8}	4.18×10^{-8}	7.32×10^{-9}	8.09×10^{-9}
L4	4.41×10^{-8}	4.52×10^{-8}	7.13×10^{-9}	8.04×10^{-9}	5.21×10^{-8}	5.27×10^{-8}	9.40×10^{-9}	1.02×10^{-8}
L5	5.60×10^{-8}	5.70×10^{-8}	9.70×10^{-9}	1.07×10^{-8}	6.62×10^{-8}	6.67×10^{-8}	1.22×10^{-8}	1.29×10^{-8}
L6	6.59×10^{-8}	6.69×10^{-8}	1.24×10^{-8}	1.36×10^{-8}	7.83×10^{-8}	7.89×10^{-8}	1.47×10^{-8}	1.54×10^{-8}

For a better presentation of Table 4.7, effective diffusion values are normalized by the molecular and numerical diffusion coefficients for each mesh level as shown in Figure 4.35a and Figure 4.35b respectively. The ratio of D_E/D_M shows the performance of a passive scalar transport simulation in terms of false diffusion production in the numerical solution. Namely, if the amount of false diffusion in the numerical solution approaches to zero, the molecular diffusion coefficient will be recovered by effective diffusion coefficient, and therefore the D_E/D_M ratio will be approaching to 1. Figure 4.35a evidently shows that the amount of false diffusion, produced in $Re = 120$ flow condition, is significantly lower than that of $Re = 240$ for both micromixer types.

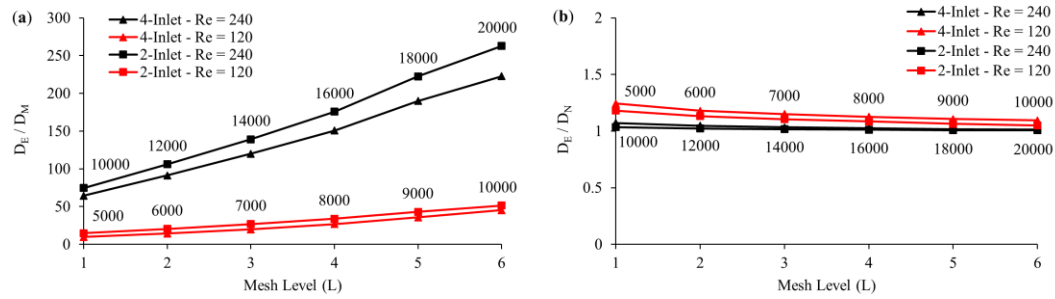


Figure 4.35 Normalized effective diffusion constant vs. mesh levels: (a) D_E/D_M and (b) D_E/D_N . The numbers above and below the trend lines show Pe_Δ numbers for corresponding mesh levels and flow conditions.

The two-inlet and four-inlet designs show a variation for the same Pe_Δ numbers which implies that the degree of grid-flow misalignment—hence the tendency of numerical diffusion generation—is quite different in the computational domains of both micromixer configurations. Accordingly, it should be noted that considering the Pe_Δ number alone in the control of false diffusion errors may mislead because it is obvious from Figure 4.35a that the two-inlet design is prone to create more numerical diffusion than the four-inlet design when $Re = 240$. This difference increases when coarser grid elements are used in

simulations. Even for the best-case scenario (e.g., $Re = 120$ and L1 mesh level), the smallest Pe_Δ number is on the order of 5000 which is a large number to control false diffusion in numerical simulations. Therefore, effective diffusion values predicted are approximately 10 and 15 times higher than the physical molecular diffusion constant for four-inlet and two-inlet designs, respectively.

Similarly, D_E/D_N ratio may also be used to evaluate the extent of false diffusion as shown in Figure 4.35b. In this case, however, when the ratio is 1, effective diffusion constant only reflects numerical diffusion, generated in the simulation. It is clear from the Figure 4.35b that even for the minimum Pe_Δ number, the ratio is around 1.25 which indicates that effective diffusivity is still close to the numerical diffusivity in the solution. In the meantime, when Figure 4.35a and Figure 4.35b are compared, there is a consistency between the ratios of D_E/D_M and D_E/D_N in each scenario tested. Such a concordance in outcomes basically indicates that average numerical diffusion generation in a passive scalar transport simulation is quantified coherently by the method employed in this dissertation. According to the outcomes given in Table 4.7, the numerical simulations contain substantial amount of false diffusion and cannot reflect the physical effects of molecular diffusion constant. Therefore, the mixing efficiencies in Figure 4.29 are still masked by the false diffusion errors in solutions. As mentioned earlier, this occurs due to the erroneous resolution of sharp concentration gradients in the computational domain which is represented by quite high Pe_Δ numbers.

To observe the effects of smaller Pe_Δ numbers, higher molecular diffusion constants are tested for mesh levels of L1, L3, and L6 keeping the same flow conditions. Initially, the original molecular diffusion constant (i.e., $D_M = 3 \times 10^{-10} \text{ m}^2/\text{s}$) is increased 10 times

for both flow conditions by which Pe_{Δ} numbers are reduced 10 times. Later, considering the false diffusion production tendency of flow conditions, 200 and 50 times higher molecular diffusion constants are tested for $Re = 240$ and 120 scenarios respectively. The increased molecular diffusion constants and the corresponding Pe_{Δ} numbers may be found in Table 4.6.

As shown in Figure 4.36, which shows the change of D_E/D_M ratio with respect to the three mesh levels and molecular diffusion constants, the recovery of physical diffusion constant from a numerical solution increases in cases where Pe_{Δ} number is small. For instance, in the $Re = 240$ scenario, reducing the average Pe_{Δ} number from 10,000 to 1000 by using the $D_M = 3 \times 10^{-9} \text{ m}^2/\text{s}$, decreases the ratio from 64 to 8 for the four-inlet design and 75 to 9 for the two-inlet design at L1 mesh level as shown in Figure 4.36a and Figure 4.36c respectively. Nonetheless, the D_E/D_M ratios of 8 and 9, observed at L1 mesh level, are still quite high to reflect the physical effects of the molecular diffusion constant employed. When $D_M = 6 \times 10^{-8} \text{ m}^2/\text{s}$ is tested for the same flow condition ($Re = 240$), the D_E/D_M ratio reduces to 1.31 and 1.36 points at the L1 mesh level ($Pe_{\Delta} = 50$) for the four-inlet and two-inlet micromixers respectively. In this case, numerical diffusion effects are mostly suppressed due to a tolerable Pe_{Δ} number, and therefore the D_E/D_M ratio approaches to one, which means that physical diffusivity is mostly reflected in numerical solutions. For coarser grids, L3 ($Pe_{\Delta} = 70$) and L6 ($Pe_{\Delta} = 100$), the D_E/D_M ratio is “1.61 and 2.13” and “1.69 and 2.32” for the four-inlet and two-inlet micromixer designs, respectively. Thus, when Pe_{Δ} number is 100, the magnitude of diffusion constant, recovered from the numerical solution, is more than two times higher than the magnitude of physical molecular diffusion constant tested.

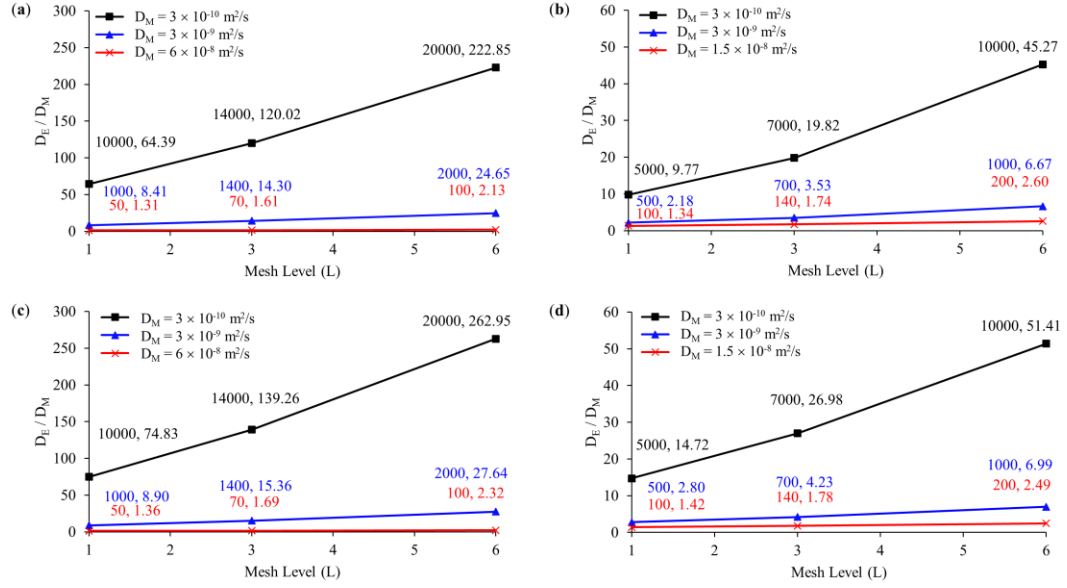


Figure 4.36 The ratio of D_E/D_M vs. mesh levels (L1, L3, and L6): (a) and (c) four-inlet and two-inlet designs at $Re = 240$ respectively; (b) and (d) four-inlet and two-inlet designs at $Re = 120$ respectively. The semicolon-separated numbers above the trend lines (corresponding to line color) show Pe_Δ numbers (left) and y-axis values (right) for mesh levels.

At $Re = 120$ flow condition, the ratios of D_E/D_M for $D_M = 3 \times 10^{-9} \text{ m}^2/\text{s}$ ($Pe_\Delta = 500$ at L1) are 2.18 and 2.80 for the four-inlet and two-inlet micromixer designs as shown in Figure 4.36b and Figure 4.36d respectively. In addition, when $D_M = 1.5 \times 10^{-8} \text{ m}^2/\text{s}$ ($Pe_\Delta = 100$ at L1) for the same flow condition, the D_E/D_M ratios for the four-inlet and two-inlet micromixers are 1.34 and 1.42 respectively. If these ratios are compared with that of the $Re = 240$ flow scenario, it is obvious that the physical diffusion recovery performance in both flow scenarios is almost equal even though the Pe_Δ is two times higher at $Re = 120$. When $Re = 120$ cases are examined, scalar transport simulations can tolerate a higher Pe_Δ number in terms of numerical diffusion production because the intensity of rotational fluid motion at $Re = 120$ is considerably lower compared to the $Re = 240$ flow scenario. Therefore, outcomes evidently show that while the magnitude of a Pe_Δ number is an important parameter to understand the extent of numerical diffusion generation in

numerical solutions, the pattern of fluid flow in a micromixer is similarly important since it will determine the degree of mesh-flow misalignment in the computational domain.

To validate the effects of estimated D_E/D_M ratios visually, the L1, L3, and L6 mesh level scalar transport solutions of four-inlet micromixer design is examined for two different molecular diffusion constants at $Re = 240$. Figure 4.37a and Figure 4.37b show scalar concentration distributions at $z = 500 \mu m$ (Line-II in Figure 4.24) for the molecular diffusion scenarios of $D_M = 3 \times 10^{-10} m^2/s$ and $D_M = 6 \times 10^{-8} m^2/s$, respectively. As shown in Figure 4.37b, indeed, variations between mesh levels are significantly decreased because L1, L3, and L6 mesh levels resolve the scalar transport domain at relatively very low Pe_Δ numbers which are 50, 70, and 100 respectively. The corresponding D_E/D_M ratios for these three Pe_Δ numbers are 1.31, 1.61, and 2.13 respectively. While L1 and L3 mesh levels follow almost an identical trend, L6 mesh level slightly diverges from these two solutions as a result of higher D_E/D_M ratio. When, however, the D_E/D_M ratios are 64, 120, and 223 for L1, L3, and L6 mesh levels respectively, there is a significant discrepancy between these mesh levels as plotted in Figure 4.37a. Because of a much higher D_E/D_M ratio, L6 mesh level resolves a quite different concentration profile from other two mesh levels. Therefore, calculated D_E/D_M ratios are valid and consistent with scalar transport solutions as reflected in Figure 4.37a and Figure 4.37b.

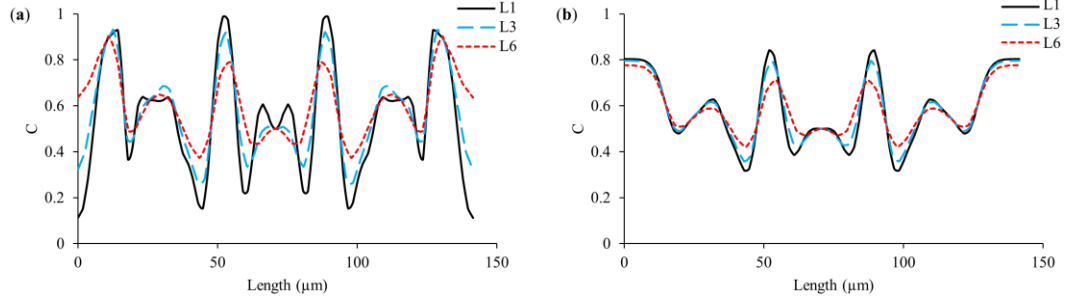


Figure 4.37 Scalar concentration distribution on the x-y plane at $z = 500 \mu\text{m}$ (Line-II in Figure 4.24) for four-inlet design at $\text{Re} = 240$: (a) $D_M = 3 \times 10^{-10} \text{ m}^2/\text{s}$ and (b) $D_M = 6 \times 10^{-8} \text{ m}^2/\text{s}$.

In Reference (M. Liu, 2011), it is noted that when fluid mixing is completed at very early stages in a micromixer, including the entire micromixer domain to compute effective diffusion constant may result a substantially averaged and imprecise value. In all scenarios tested, the maximum MI is quantified at the outlet of the four-inlet micromixer when $\text{Re} = 240$ and $D_M = 6 \times 10^{-8} \text{ m}^2/\text{s}$. The evolution of MI values at $z = 500, 1000$, and $2000 \mu\text{m}$ in the mixing channel are 73, 95, and 98%, respectively. Thus, the effective diffusion constant calculated mainly shows the actual diffusivity in the numerical solution since the development of mixing continues through the exit of the micromixer.

In this section, although numerical diffusion effects are examined in swirl-based micromixers, the findings here are also valid for high Pe scalar transport systems in which secondary flows are dominant. In grid-based numerical techniques, numerical diffusion errors can be diminished to negligible levels when mesh density is increased. However, in specific cases, such as swirling flows, where grid-flow orientation is continuously violated, this approach may become unfeasible due to a high computational power requirement. For instance, to render a Pe_Δ number of 10 in the mixing channel, approximately 10^{15} hexahedron elements are needed to be employed in the computational domain. Such a mesh

density is obviously far beyond the computational capacity of today's workstations. In that case, alternative approaches to the grid-based methods should be considered. In the literature, several researchers proposed and practiced particle-based numerical methods, which are specialized to simulate high Pe scalar transport systems yielding a negligible amount of numerical diffusion, as may be seen in References (Matsunaga and Nishino, 2013; Matsunaga et al., 2015; Vikhansky, 2004) and the references therein. The algorithms, developed in these studies, present different computational advances which are beyond the scope of this dissertation. In general, these methods require less computational power compared to the conventional grid-based numerical techniques. However, the most prominent disadvantage of particle-based numerical methods is that these methods are not presented as a standard solver in the most common CFD packages, and therefore need to be coded specifically for each problem to be solved.

4.5.3 *Conclusions*

In section 4.5, numerical diffusion errors were investigated under complex fluid flow conditions. For this purpose, two different 3-D swirl-induced passive micromixers with two- and four-inlet injection configurations were designed. In these micromixer designs, fluid flow and passive scalar transport were examined numerically in terms of numerical diffusion effects on the physical problem under different flow conditions, mesh densities, and molecular diffusion constants. In all numerical simulations, computational domains were discretized using structured hexahedron elements.

In swirl-generating micromixers, the flow domain at $Re = 240$ was resolved similarly by six different mesh densities. As a result of a small Re_{Δ} number, the maximum

difference between the finest and coarsest mesh levels was less than 1%. Different injection strategies caused yielding different flow dynamics in the micromixers. The four-inlet design generated a smooth swirl profile in the mixing channel whereas a strong vortex formation occurred in the mixing box of the two-inlet design.

In the case of the scalar transport solution at $Re = 240$ and $Pe = 8 \times 10^5$, the discrepancy between mesh levels L1 and L6 increased up to 60% at $z = 500 \mu m$ in the mixing channel. For the same flow and transport conditions, the difference between the two finest meshes, L1 and L2, was quantified around 10%. The amount of numerical diffusion in the simulations were quantified to characterize numerical diffusion limits in both micromixer types. When $Re = 240$ flow case is simulated using the finest mesh level, effective diffusion constants, recovered from numerical solutions, were 64 and 75 times higher than the physical diffusion constant in four-inlet and two-inlet micromixers respectively. In the $Re = 120$ flow case, the above numbers dropped to 10 and 15 respectively.

In all scenarios, false diffusion amount, generated in the two-inlet micromixer design, was found to be higher than that of the four-inlet configuration. When relatively small Pe_Δ numbers (e.g., $Pe_\Delta < 100$) were studied, ratio of D_E/D_M was found to be around 1.35 which indicates that numerical diffusion errors in numerical simulations were reduced considerably. Beyond $Pe_\Delta = 100$, however, physical effects of molecular diffusion were masked by numerical diffusion errors.

Consequently, it was shown that numerical diffusion generation in a 3-D scalar transport simulation depends on the magnitude of Pe_Δ number and flow pattern formed.

When Pe_Δ number is larger than a certain value and grid-flow alignment is constantly disturbed, numerical schemes cannot resolve high scalar gradients accurately and produce unphysical diffusion in the numerical solution. As shown in this section, 3-D simulations of advection dominant transport systems are prone to generate substantial amount of unphysical diffusion especially under complex flow conditions. It should be pointed that all the unphysical diffusion in numerical solutions behaves as molecular diffusion during a mixing process, and hence contributes the mixing efficiency of a micromixer. Therefore, numerical simulations of advection dominant systems need to be carried out carefully to avoid reporting unphysical mixing results.

As a conclusion, the numerical error characteristics discussed in Chapter 4 will be carefully considered and analyzed in the remaining chapters of this thesis where improved micromixer designs are developed and evaluated.

CHAPTER 5. NOVEL 3-D T-SHAPED PASSIVE MICROMIXER DESIGN WITH HELICOIDAL FLOWS

5.1 Introduction

In passive mixing micromixer design, the development of an effective chaotic flow structure is important to produce well-mixed fluids over a short distance in the micromixer. Chaotic flow involves the processes in which fluids are subjected to split, stretch, twist or fold during transport. As discussed in Chapter 2, several passive micromixer designs have been proposed to improve fluid mixing in this direction. In most of these efforts, mixing improvement usually takes place as a trade-off between the energy required to maintain the flow in the mixer, mixing length of the mixer and the complexity of design structure in terms of limitations during fabrication. For instance, although the vortex and engulfment flows in unobstructed T-shaped micromixers help to raise mixing performance, this is typically achieved over a long distance with a high pressure drop in the system. In addition, mixing efficiencies reported (e.g., see References (Bothe et al., 2006; Galletti et al., 2012; Izadpanah et al., 2018)) are still far behind an acceptable threshold value (e.g., 80% (Tran-Minh et al., 2014)). Similar consequences are also seen in grooved- and obstruction-type passive micromixer geometries (e.g., see References (Gidde and Pawar, 2019; D. Wang et al., 2017; Lei Wang et al., 2012)). In this chapter, we propose a simple, yet effective and novel micromixer design in which all the aforementioned factors are minimized substantially. The micromixer design proposed is examined under a wide range of flow, injection, and diffusivity conditions. In addition, alternative design configurations are discussed, and outcomes are presented comparatively.

5.2 Micromixer Design for Helicoidal Flow Generation

The micromixer geometry consists of two identical inlet channels and a mixing channel with lengths of 500 μm and 2000 μm , respectively. While both inlet channels have a square cross-section with an edge size of 100 μm , the width (W) and height (H) of the rectangular mixing channel are 200 μm and 100 μm , respectively. The T-shaped micromixer is fitted with semi-circular ridges which are placed on the bottom floor of the mixing channel. These are convex obstacles in the streamwise direction. In this design, overall, twelve identical ridges are used with a height (H_r), diameter (D_r), and thickness (t_r) of 50 μm , 160 μm , 20 μm , respectively. The centers of semi-circular elements are aligned with a pitch length (l_p) of 150 μm starting from the confluence region (i.e., $x = 100 \mu\text{m}$). All dimensions chosen are like the 3-D T-shaped designs, studied in the passive micromixer literature (see References (Jian Chen et al., 2011; Roudgar et al., 2012; Sabotin et al., 2013)). In the meantime, the unobstructed form of the micromixer, i.e., classical-T (CT), is used as a reference design. Both the CT and convex semi-circular-ridge (CSCR) micromixers are shown in Figure 5.1.

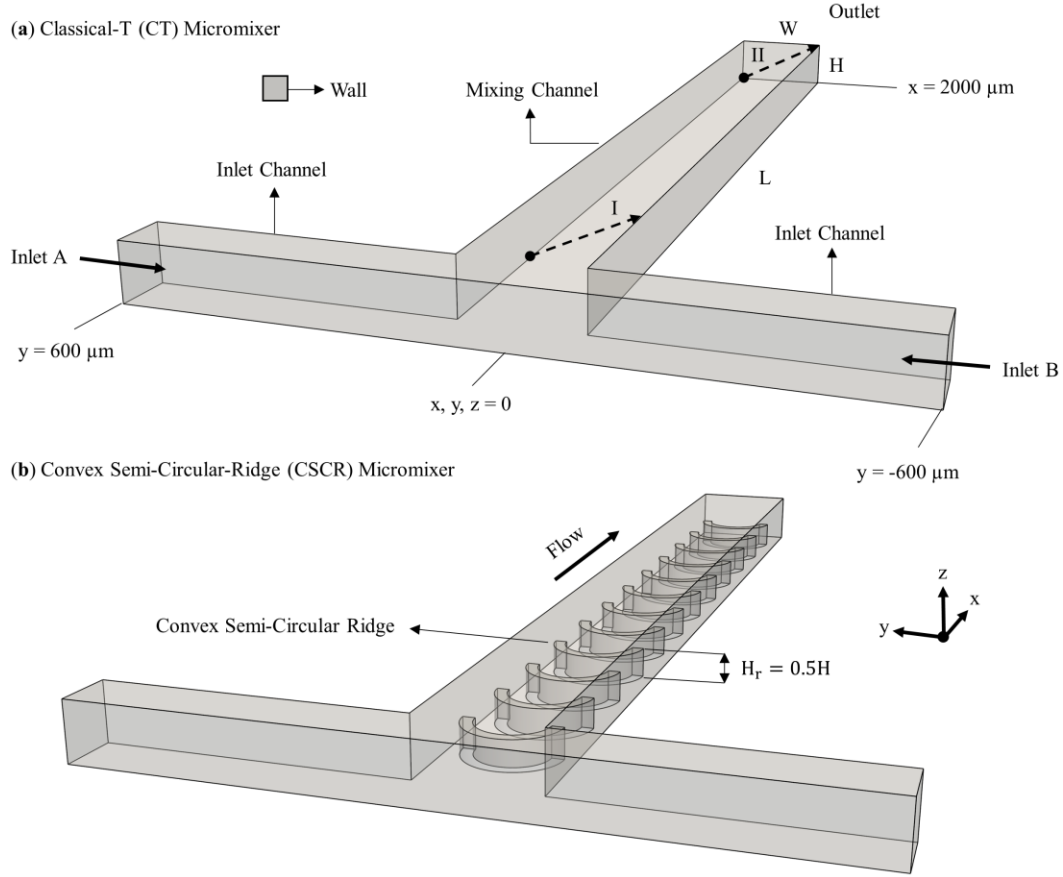


Figure 5.1 3-D micromixer geometries (a) Classical-T (CT) micromixer; (b) Convex semi-circular-ridge (CSCR) micromixer. Diagonal dashed line arrows I and II are on the y-z plane at $x = 100$ and $2000 \mu\text{m}$, respectively.

5.3 Case Setup

The mixing characteristics of these micromixers were investigated under various flow and molecular diffusion conditions. In addition, different injection strategies were examined to exploit the flow patterns generated effectively. However, the amount of the fluid injected from the inlets, were retained equal in all scenarios. Reynolds numbers with corresponding inlet velocities, molecular diffusion constants, and Schmidt numbers that are tested as tabulated in Table 5.1. It should be noted that D_1 , D_2 , and D_3 molecular diffusion cases also correspond Sc_1 , Sc_2 , and Sc_3 scenarios, respectively. To maintain

consistency throughout the present chapter, scalar transport simulations were evaluated with respect to different molecular diffusion constants instead of Schmidt numbers.

Table 5.1 Fluid flow and passive scalar transport test scenarios.

Fluid Flow		Passive Scalar Transport	
Reynolds Number	Inlet Velocity (m/s)	Molecular Diffusion Coefficient (m ² /s)	Schmidt Number
0.1	7.50×10^{-4}		
0.5	3.75×10^{-3}		
1	7.50×10^{-3}		
5	3.75×10^{-2}	$D_1 = 3.0 \times 10^{-10}$ $D_2 = 1.5 \times 10^{-9}$ $D_3 = 3.0 \times 10^{-9}$	$Sc_1 = 1/3 \times 10^4$
10	7.50×10^{-2}		$Sc_2 = 2/3 \times 10^3$
20	1.50×10^{-1}		$Sc_3 = 1/3 \times 10^3$
40	3.00×10^{-1}		
80	6.00×10^{-1}		
160	1.20×10^0		
240	1.80×10^0		

Alternative inlet types and injection modes applied are shown schematically in Figure 5.2. Note that, split inlets are obtained by dividing the inlet cross-section equally. Both split inlets and 3-D mixing elements can be fabricated using the multi-layer fabrication techniques as discussed in Chapter 2. For the sake of convenience, the test scenarios are coded in the rest of the study using the acronyms in Figure 5.1 and Figure 5.2. In three-part coding, while the first letters represent micromixer type (e.g., CT or CSCR), the middle and last letter combinations denote inlet type (e.g., FI, HS, VS) and injection method (e.g., AI, SI), respectively. For example, CT-VS-AI represents the classical-T micromixer with vertical split inlet and alternating injection. These definitions are also explained in Figure 5.2 schematically.

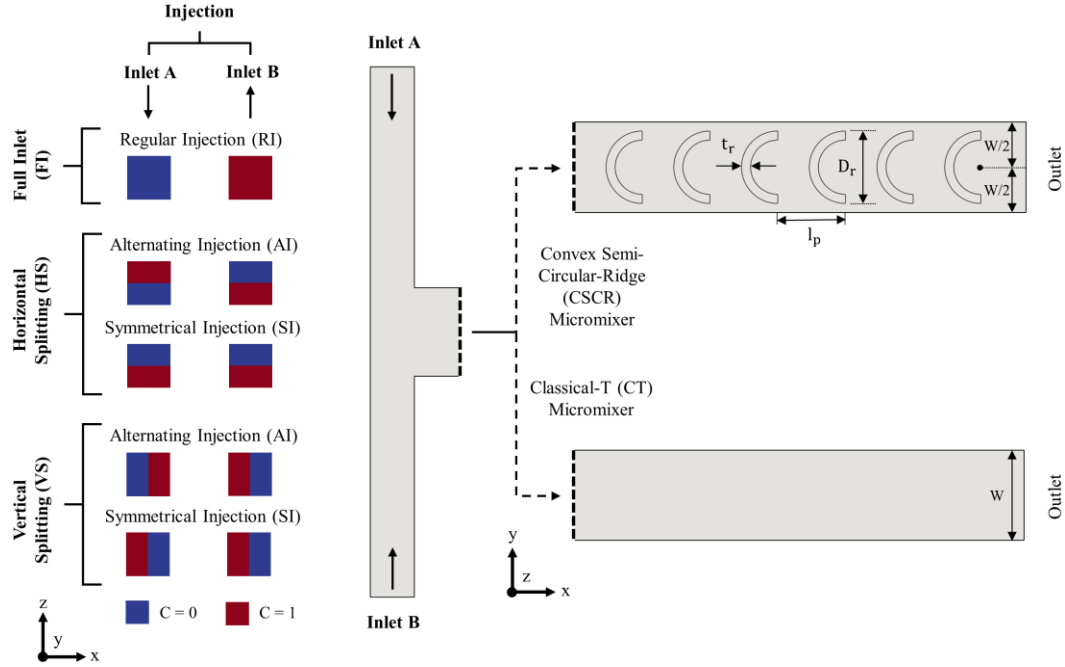


Figure 5.2 Inlet types, injection modes, and 2-D micromixer geometries.

5.4 Results and Discussion

5.4.1 Grid study

In this chapter, five different mesh levels, consisting of hexahedron elements, were employed to determine a mesh density in which spatial discretization errors are insignificant. Differences between total element numbers are chosen adequately to be able to capture relative numerical errors in simulations. The properties of mesh levels tested are given in Table 5.2. Grid study was conducted for the CT-VS-AI micromixer configuration. Numerical simulations were performed for the worst-case scenario in terms of numerical diffusion production tendency (i.e., $Re = 240$ and $D = D_1$). To quantify the discrepancy between each mesh level and the finest mesh level, following flow and transport parameters were employed. Pressure drop (Δp) in the micromixer, average velocity (u_{avr}) on the dashed line arrow I in Figure 5.1, and mixing index (MI) at the outlet.

Table 5.2 Mesh properties tested in grid study.

Mesh Level	Grid Size, Δx (μm)	Total Elements
L1	1.75	9.21×10^6
L2	2.00	5.94×10^6
L3	2.25	4.14×10^6
L4	2.50	3.20×10^6
L5	3.00	1.79×10^6

Figure 5.3a shows that the maximum difference, occurred between the L5 and L1 levels, is less than 1% for both flow parameters tested, i.e., Δp and u_{avr} . According to the trendlines, even the coarsest mesh level is enough to render the flow field quite accurately. However, in contrast to the small Re number in the flow simulation, the transport domain is resolved for a high Pe number which is on the order of 8×10^5 . When outlet MI is used as the parameter, the highest difference is observed as 22% between the L5 and L1. The peak difference is followed by the values of 11.8%, 8.3%, and 2.8% for other grid level comparisons. Such a big difference between grids emerged as a result of numerical diffusion generation in the solution. The development of mixing on several planes along the mixing channel is shown in Figure 5.3b. In addition, velocity and scalar concentration distributions at the exit (i.e., on the dashed line arrow II in Figure 5.1) are plotted in Figure 5.3c and Figure 5.3d, respectively. The graphs in Figure 5.3 evidently show that the results, obtained from different mesh levels, converge to the finest grid. When the top two mesh densities are compared, increasing the element numbers by 3.2 million cause a 2.8% change in the mixing index value. Therefore, considering the high computational expense against an insignificant accuracy gain, the L2 grid size is selected for the rest of the simulations in this chapter. To validate this selection, average numerical diffusion was

quantified using the numerical solution of the L2 mesh level. The D_E/D_M ratio was found to be 1.174 which is quite close to 1. This implies that the molecular diffusion constant simulated is mostly recovered by the effective diffusion constant computed. Thus, the amount of average numerical diffusion errors is trivial when the L2 mesh level is used. In addition, average numerical diffusion was also computed in the CSCR micromixer design due to complex flow formation, and therefore high numerical diffusion error generation tendency. For this purpose, CSCR-VS-AI micromixer configuration was employed. Scalar transport simulation was conducted for the same mesh level and molecular diffusion constant given above. However, flow condition was set to $Re = 40$, which is the highest flow condition, examined in the CSCR design configurations. The D_E/D_M ratio was found to be 1.275 which evidently shows that the CSCR design generates more numerical diffusion than that of CT micromixer. The CSCR design produced approximately 8.6% more numerical diffusion than the CT micromixer even though six times lower flow condition— $Re = 40$ in the CSCR design against $Re = 240$ in the CT micromixer—was simulated. As exhaustively studied in Chapter 4, such a disproportional numerical diffusion production difference between the CSCR and CT micromixers occurred as a result of much complex flow profile, developed at $Re = 40$ in the CSCR design. Nonetheless, the D_E/D_M ratio of 1.275 is still quite close to 1 which indicates that molecular diffusion effects are dominant in the numerical simulation. Consequently, in this chapter, when computational domains are discretized using the L2 mesh level, numerical simulations of the CT and CSCR micromixers provide reliable mixing outcomes with insignificant false diffusion production in numerical solutions even in the worst-case transport conditions.

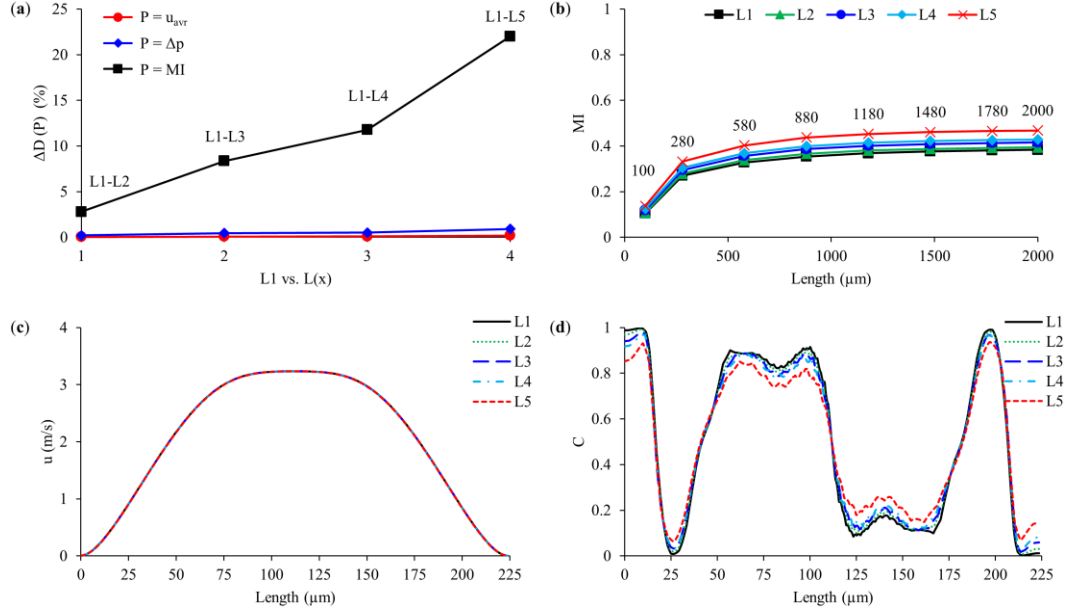


Figure 5.3 Grid study outcomes: (a) difference (%) between mesh levels for the parameters tested; (b) development of mixing on different y-z cross-sections along the mixing channel; (c) and (d) velocity and concentration distributions at the exit, respectively (dashed line arrow II in Figure 5.1).

5.4.2 Classical-T (CT) micromixer

In this section, the mixing characteristics of the CT micromixer is investigated for the entire Re scenarios and molecular diffusion constants given in Table 5.1. In addition, all inlet types and injection methods in Figure 5.2 are tested to document the mixing effects as benchmark values. In the CT micromixers, typically the following flow regimes develop depending on the flowrate imposed: separated (i.e., segregated), vortex, and engulfment. Figure 5.4 illustrates the fluid path lines in these flow types with corresponding Re numbers. In a separated flow, which is usually observed at very low Re numbers, fluids injected from inlets, travel alongside in the mixing channel. In this type of flow regime, fluid bodies create a small contact surface, and therefore mixing is completely controlled by molecular diffusion. In vortex flow, however, impingement of streams at the center of

the confluence region creates two-counter-rotating vortex pairs in each side of the mixing channel. The periodic movement of fluids relatively increases the contact surface area in comparison with segregated flows. Furthermore, flow type is described as engulfment when the inlet streams partially reach the opposite side of the mixing channel. In engulfment flow, fluid bodies can be stretched, and the contact surface is enlarged higher than that of separated and vortex flow profiles.

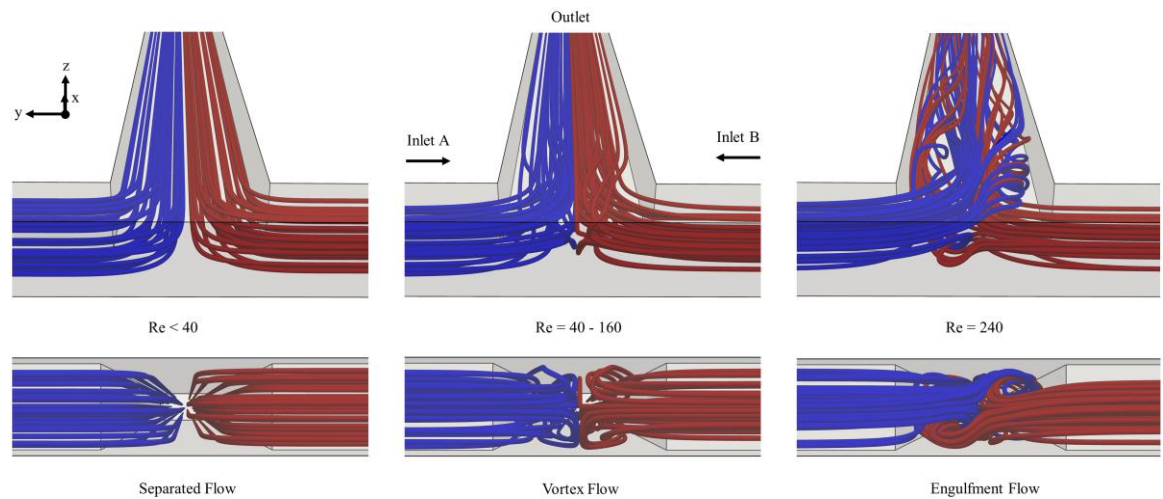


Figure 5.4 Flow regimes in the CT micromixer: separated, vortex, and engulfment. Blue and red colors are used to differentiate flow pathlines in inlet A and inlet B.

Pressure drops and outlet mixing efficiencies which are obtained from the CT-FI-RI micromixer configuration are given in Figure 5.5a Figure 5.5b, respectively. As shown in Figure 5.5a, while the pressure drop values are less than 1 kPa until $Re = 40$, the formation of complex flow patterns sharply increases the pressure difference between inlets and outlet. The maximum pressure drop is observed in the engulfment flow regime with a value of slightly over 15 kPa. On the contrary, mixing indexes follow a reverse trend with rising flowrates until the highest flowrate scenario as shown in Figure 5.5b. In very low Re conditions (e.g., $Re = 0.1$ and 0.5), relatively high mixing efficiencies are obtained due to

long residence time of fluids in the mixing channel. In this case, fluid mixing is purely characterized by diffusive mixing mechanism which is a slow process. Besides, further increase of the Re number yields advection dominant transport conditions where the effect of molecular diffusion is substantially reduced. As a result of diminishing residence times and limited contact surface area formed, mixing indexes continually drop until the Re = 240 flow scenario. Nevertheless, when the engulfment flow pattern is created in the mixing channel, mixing efficiency is mainly enhanced due to the chaotic motion of fluids. In this flow scenario, a mixing index value, around 33%, is obtained at the exit of CT-FI-RI micromixer for all molecular diffusion coefficients, simulated.

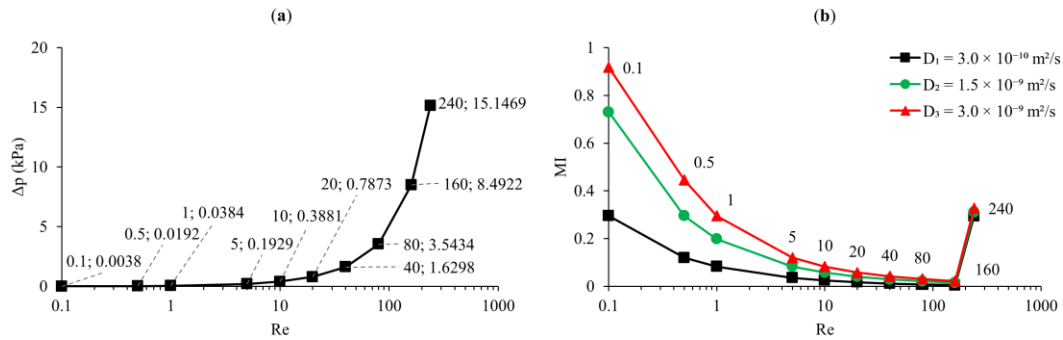


Figure 5.5 (a) Pressure drop vs. Re number in CT micromixer. The numbers before and after the semicolons represent Re number and pressure drop values, respectively; (b) MI vs. Re number for different molecular diffusion coefficients in CT-FI-RI.

The low mixing outcomes of the CT-FI-RI micromixer clearly show that secondary flows, developed in the mixing channel, cannot be exploited efficiently. For further investigation of improving the degree of mixing in the CT micromixer, alternative injection types are tested. As shown in Figure 5.6, multi-injection application contributes to the effective utilization of flow profiles generated in the CT micromixer. While the improvement in mixing is apparent in separated and vortex flows, split inlets yield quite similar outcomes with the CT-FI-RI configuration at Re = 240. In low Re cases (e.g., Re =

0.1, 0.5, and 1), horizontal and vertical split inlets improve mixing efficiency due to the formation of additional contact layer in the inlet channels. In such flow conditions, the amount mixing efficiency is fundamentally determined by the magnitude of molecular diffusion constant. In vortex flow type, however, the improvement in mixing is mainly affected from the splitting type of inlets. Namely, while the trendlines continue dropping with increasing Re number in horizontal splitting cases, vertical injection of fluids improves the degree of mixing in cases where $Re > 20$ ($D = D_1$). This is because vertically travelling fluids in the inlet channels form the upper and lower vortices jointly (see the vortex pairs in each side of the mixing channel in Figure 5.4). On the contrary, if the flows are aligned horizontally, double vortex pattern is formed separately by top and bottom streams in an inlet channel. The effect of splitting and injection types can be seen in Figure 5.7, in which outlet concentration distributions are shown. Meanwhile, in both split inlet types, alternating injection presents slightly better mixing values until the engulfment flow case. Such a gain in mixing efficiencies is achieved as a result of extra contact surface that is formed between inlet streams along the mixing channel. In engulfment region, however, all the test scenarios yield almost identical mixing efficiencies due to small residence time of fluids in the micromixer. Although the contact surface is inherently larger in alternating injection modes, this is inhibited by relatively short contact time between fluids. Thus, diffusive mixing cannot be utilized effectively, and all splitting and full inlet scenarios provide quite similar mixing results based on advective mixing.

As shown in this section, mixing of fluids in the CT micromixers is rather challenging. Despite observing mixing improvements for multiple injection strategies, the degree of mixing is still far behind the desired levels (e.g., 80%). Particularly, mixing

indexes, obtained from the lowest diffusion constant (D_1), are unacceptable for several microfluidic applications as discussed in Chapter 1 and Chapter 2.

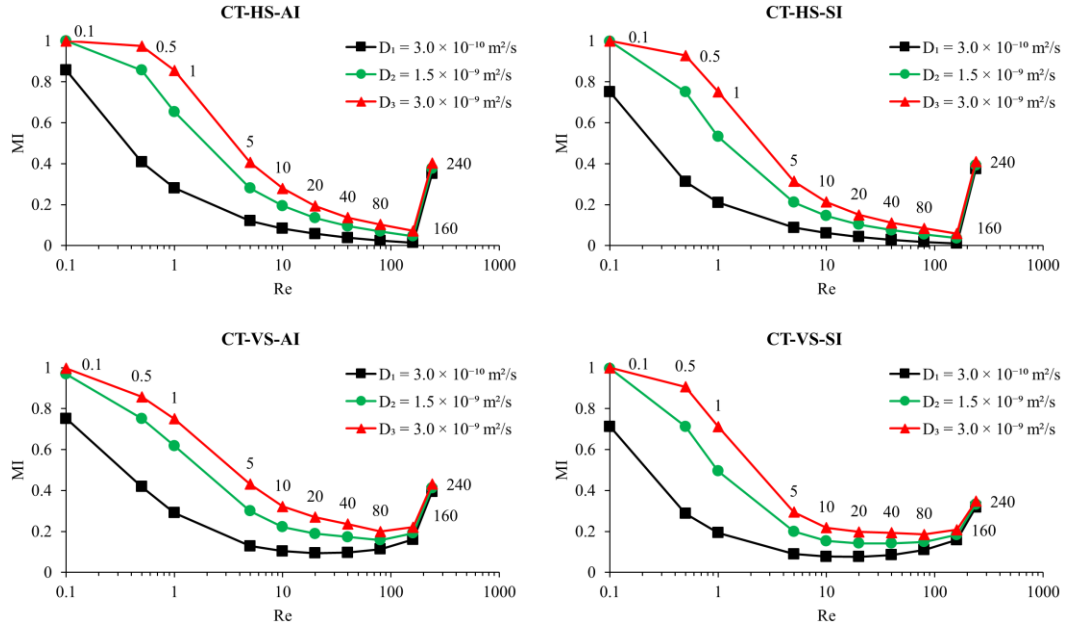


Figure 5.6 MI vs. Re for CT-HS-AI, CT-HS-SI, CT-VS-AI, and CT-VS-SI micromixer configurations and D_1 , D_2 , and D_3 molecular diffusion scenarios.

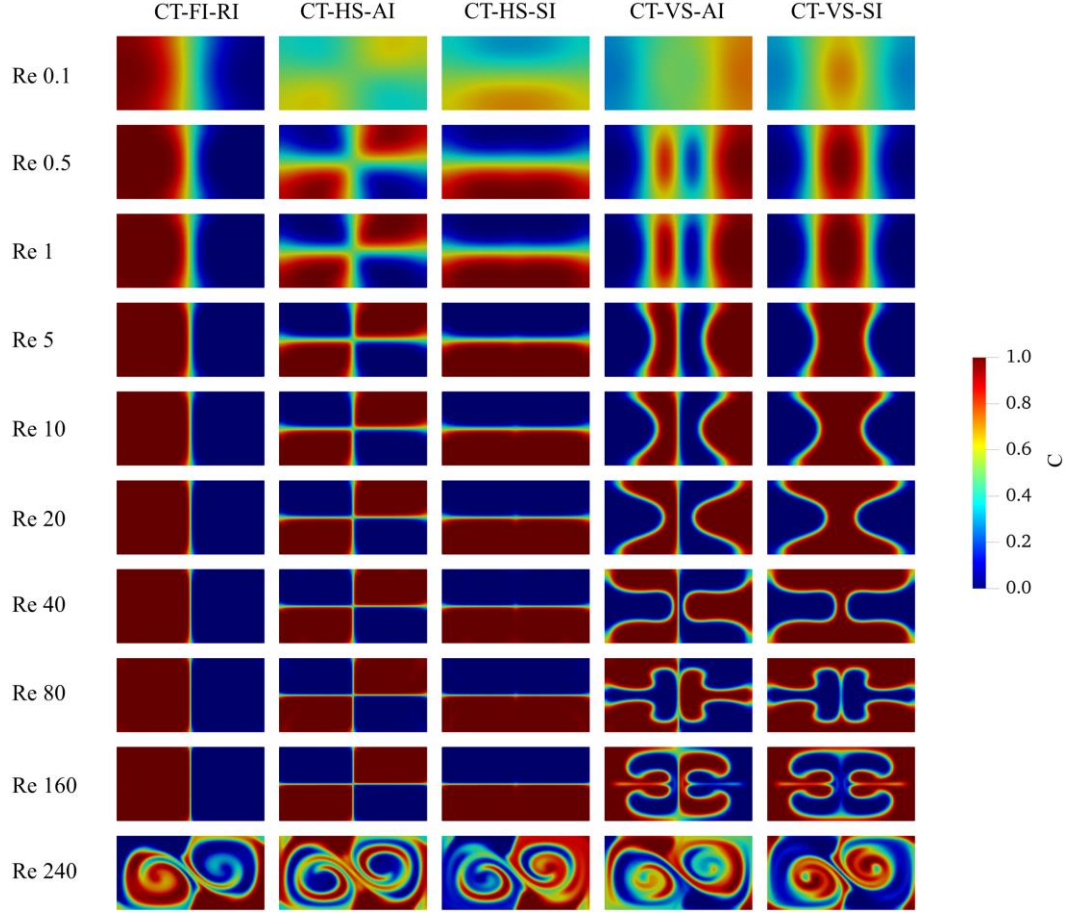


Figure 5.7 Outlet concentration distributions in CT-HS-AI, CT-HS-SI, CT-VS-AI, and CT-VS-SI micromixer configurations for D_1 molecular diffusion constant.

5.4.3 Convex Semi-Circular-Ridge (CSCR) Micromixer

As shown in the previous section, although vortex and engulfment regimes create a complex fluid flow in the CT micromixer, the deformation of fluid bodies is insufficient to substantially increase the degree of fluid mixing. Besides, pressure drops, required to form the complex flow patterns, are relatively high as presented in Figure 5.5. Therefore, preserving the same T-shaped topology, the CSCR micromixer was designed to generate an effective chaotic fluid motion under low pressure drop conditions. The novel design is tested for a Re number range between 0.1 and 40. Mixing characteristics were investigated

for the split inlet configurations with alternating and symmetrical injections. Additionally, simulations were extended for all scalar diffusion constants given in Table 5.1 to analyze the micromixer performance under different diffusivity conditions.

In the CSCR micromixer, two counter-rotating, helicoidal-shaped flow profiles are developed along the mixing channel as illustrated in Figure 5.8. The rotational fluid motion is created employing the stationary semi-circular mixing elements, aligned in the streamwise direction. As a result of effective design factor, the formation of helicoidal patterns starts right after the confluence region and continues along the mixing channel. The semi-circular ridges, which are positioned convexly on the bottom floor of the mixing channel, function to deflect and raise the flows as follows. When the incoming inlet streams reach the first mixing element, fluids, flowing at the height of ridges, i.e., $z \leq 50 \mu\text{m}$ (see the blue arrow lines in Figure 5.8), are split and diverted to the gaps, exist between the ridge and side walls of the mixing channel. In this region, the amount of fluid flow is controlled by a small gap size. Accordingly, fluid volume is raised over the gap, and flow continues with a leaning motion towards the center of the mixing channel (i.e., $y = 0$).

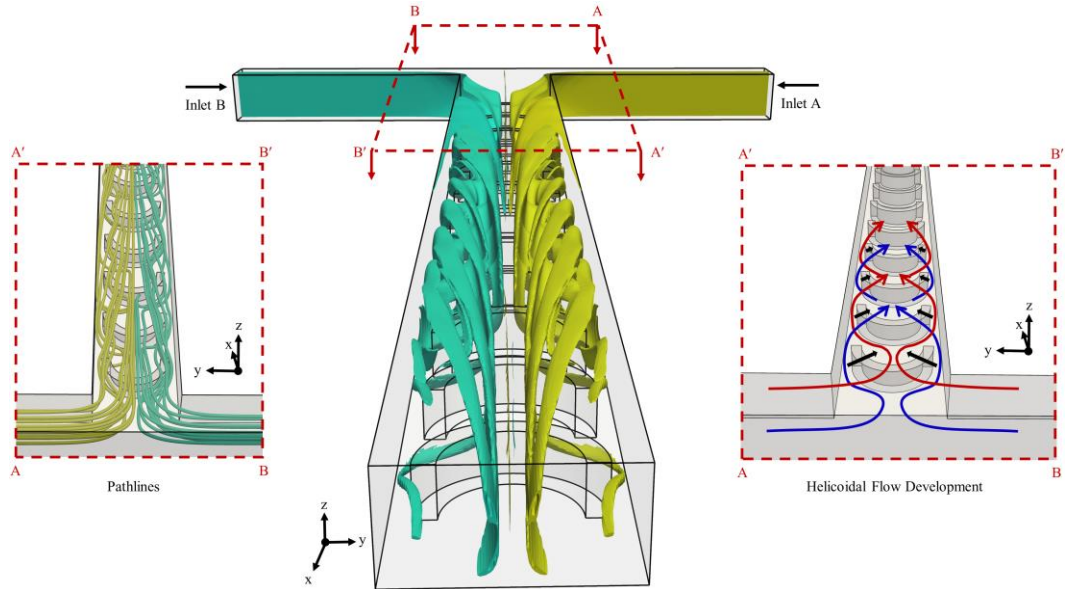


Figure 5.8 Helicoidal fluid flow in the mixing channel at $Re = 40$. Yellow and green colors show fluids, injected from inlet A and inlet B, respectively. Fluids, travelling in the lower and upper height of the inlet channel, are represented by blue and red curvy arrows, respectively.

Such an oblique fluid motion is primarily ensured by the convex curvature of the semi-circular ridge. In the meantime, the upper streams, flowing at $z > 50 \mu m$ (see the red arrow lines in Figure 5.8), are pushed inwards due to the fluid volume, increased at the edges (see the thick, black arrows). Later, these streams are split and diverted to the side walls by the following ridges in the mixing channel. It should be pointed out here that the symmetrical, leaning flows converge at the center of the mixing channel ($y = 0$) after flowing over the next several ridges (see the pathlines in Figure 5.8). By this way, straight fluid flow, above the obstructions, is blocked in the streamwise direction. So that the upper streams are intrinsically forced to use the paths between consecutive ridges. In the same way, fluids are raised over the gaps and follow the same oblique path towards the center of the mixing channel. The formation of rotational fluid flow along the mixing channel can be also tracked from Figure 5.9 which shows concentration distributions along the mixing

channel of CSCR-VS-AI configuration ($D = D_1$). Rotational fluid motion is observed even in the smallest flow scenario tested, i.e., $Re = 0.1$. In addition, the frequency of rotations is improved with increasing Re number.

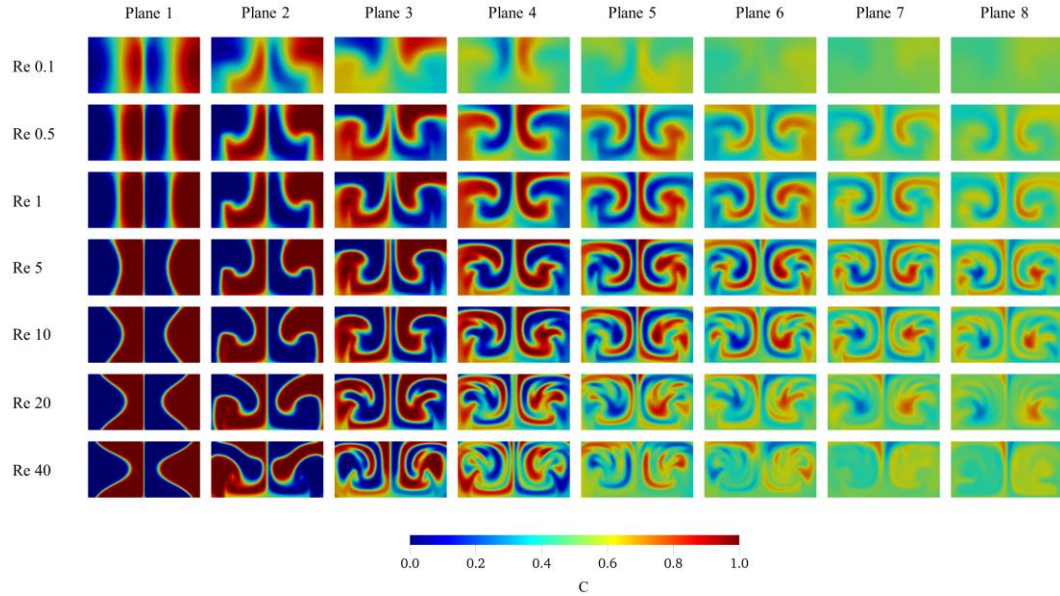


Figure 5.9 Concentration distributions in the mixing channel for the CSCR-VS-AI configuration ($D = D_1$). Plane 1 and 8 represent cross-sections at $x = 100 \mu m$ and at the outlet, respectively. Planes from 2 to 7 show the cross-sections, $30 \mu m$ after the center of odd-number semi-circular ridges starting from the confluence region. All planes are normal to the x -direction.

The maximum flow scenario was chosen as $Re = 40$ in the CSCR micromixer simulations. It is clear from the trend shown in Figure 5.9 that the chaotic behaviour of fluid flow and therefore fluid mixing improve with rising Re numbers. Further increase of Re number after 40 will increase the intensity of rotations and provide better mixing efficiencies with a cost of higher pressure drop and thus energy requirement. For the $Re = 40$ case, an effective chaotic fluid flow has yielded a mixing efficiency value greater than 80% with a feasible pressure drop. As a result of the small form factor of the semi-circular ridges, the CSCR micromixer produces the helicoidal fluid motion resulting in low pressure

drops. As shown in Figure 5.10, the pressure drops are obtained as 2.07 and 4.72 kPa at $Re = 20$ and 40 flow scenarios, respectively. When these values are compared with the outcomes of micromixer designs, reviewed in Chapter 2, the energy requirement of the CSCR micromixer is far less than that of reported in the passive micromixer literature.

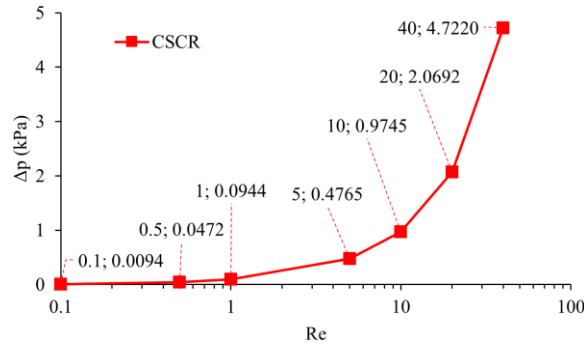


Figure 5.10 Pressure drop, Δp (kPa) vs. Re number in the CSCR micromixer. The numbers before and after the semicolons represent Re number and pressure drop values, respectively.

As presented in Figure 5.11, mixing results indicate that alternating and symmetrical injection modes provide parallel mixing outcomes. Similar mixing efficiencies are observed as a result of intermittent contact time between two flow profiles in the mixing channel. Namely, diffusive interaction between the counter-rotating, helicoidal-shaped flows is quite limited due to ongoing rotations. Therefore, the additional contact surface area, which is formed at the center of the mixing channel ($y = 0$) in alternating injection mode, cannot be utilized pointedly. However, the splitting type of flow affects the effective utilization of the chaotic flow profile as illustrated in Figure 5.12. In the mixing channel, the distribution of concentration differs with the splitting type. During the development of the helicoidal-shaped profile, the regions above ($z > 50 \mu m$) and below ($z \leq 50 \mu m$) the mixing elements are fed dissimilarly depending on the splitting type. While the horizontal split inlets deliver a different fluid ($C = 0$ or 1) to each region, the vertical

split inlets feed the upper and lower sections with a fluid pair ($C = 0$ and 1). Hence, in comparison to the horizontal type, the use of vertical split inlets forms a relatively high contact surface. Besides, the lowest mixing outcomes are obtained when the CSCR micromixer is operated in FI-RI mode. Since each of the helicoidal flows is generated separately by the fluids coming from inlet A and B as shown in Figure 5.8, the only contact surface is formed between counter-rotating fluid bodies along the center of the mixing channel ($y = 0$). In this case, the CSCR-FI-RI design is reduced to the CT-FI-RI micromixer. Both configurations yield almost identical mixing efficiencies and scalar concentration distributions as presented in Figure 5.5b and Figure 5.7, respectively (see the outcomes of the CT-FI-RI for $Re = 0.1\text{--}40$). Thus, the active utilization of the helicoidal flows is primarily controlled by the horizontal or vertical feeding type of the CSCR micromixer.

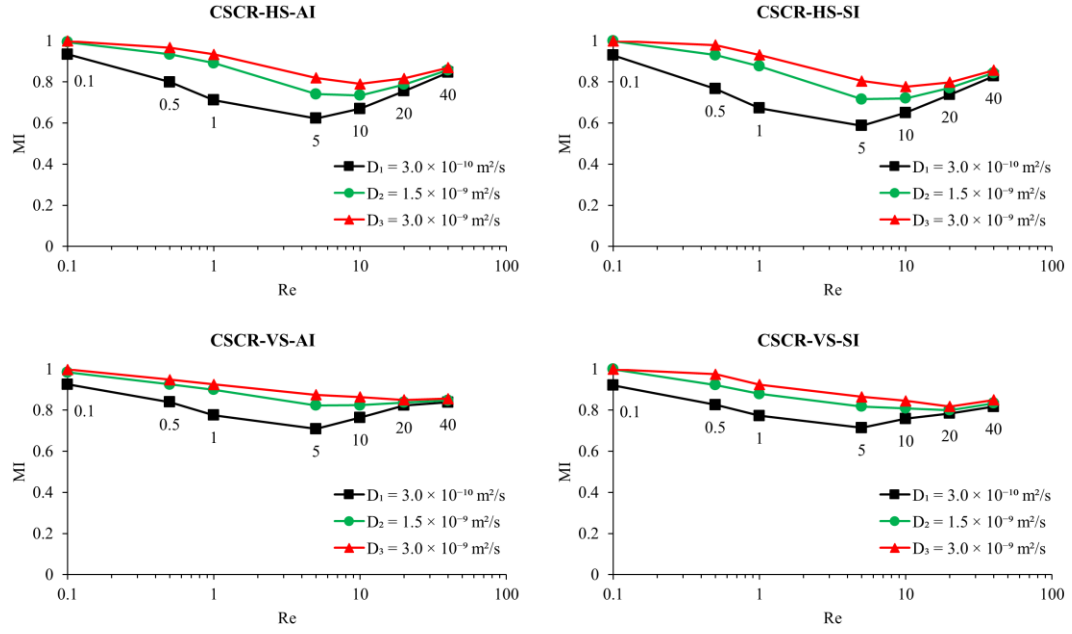


Figure 5.11 Mixing index vs. Re number for different inlet and injection configurations of the CSCR micromixer.

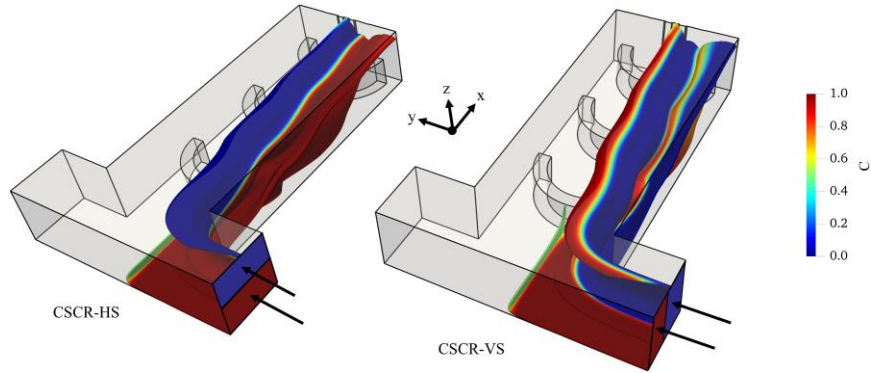


Figure 5.12 The utilization of rotational fluid flow depending on the splitting type (Re = 5 and $D = D_1$).

When the CSCR-HS-AI and CSCR-VS-AI configurations are compared, vertical split inlet provides higher mixing index values for the Re numbers between 0.5 and 20. The minimum and maximum variances are observed as 4.7% and 12.3% at Re = 0.5 and 10 flow conditions, respectively ($D = D_1$). Based on the differences calculated, the effect

of additional fluid pair is more prominent in the transition region, i.e., $Re = 1-10$. Besides, equal amount of mixing efficiency is obtained for all diffusion constants at $Re = 0.1$ and 40. In the slowest flow case, the efficiency of mixing is primarily controlled by the diffusive mixing. The extent of contact surface area in micromixer configurations is substantially suppressed by the high residence time of fluids. After $Re = 0.1$, the function of molecular diffusion diminishes with decreasing fluid residence times. This is quite evident from the deviating trendlines of the smallest diffusion coefficient until $Re = 5$. After this flow case, the intensity of rotational flow profile is enhanced with rising flowrates. Trendlines show a convergent behaviour due to developing complex flow patterns and lessening diffusion effects. Notably, diffusive mixing becomes negligible when the highest flow condition is reached. Fluids are mainly mixed based on the chaotic flow profile formed. Therefore, the same amount of mixing efficiency is obtained at $Re = 40$ regardless of the diffusion magnitudes. In all configurations, the minimum mixing index is obtained at $Re = 5$ flow scenario ($D = D_1$). At this pivotal point, the degree of mixing is mostly controlled by the chaotic advection. The smallest diffusion constant yields 62% and 71% mixing efficiency in the CSCR-HS-AI and CSCR-VS-AI setups, respectively. Meanwhile, the maximum mixing value in each Re case is usually provided by the CSCR-VS-AI configuration. In most cases more than 80% homogenous fluid mixing is obtained. In very low flow conditions, mixing indexes are computed to be 92% and 84% for $Re = 0.1$ and 0.5, respectively ($D = D_1$). Relatively low mixing efficiencies are observed in the transition region, i.e., $Re = 1-10$ ($D = D_1$). The degree of mixing is quantified as 78% and 76.4% for $Re = 1$ and 10, respectively. Furthermore, nearly 83% and 85% mixing index is computed in the two most chaotic flow conditions, respectively, i.e., $Re = 20$ and 40. Outlet

concentration distributions of the CSCR micromixer configurations are shown in Figure 5.13.

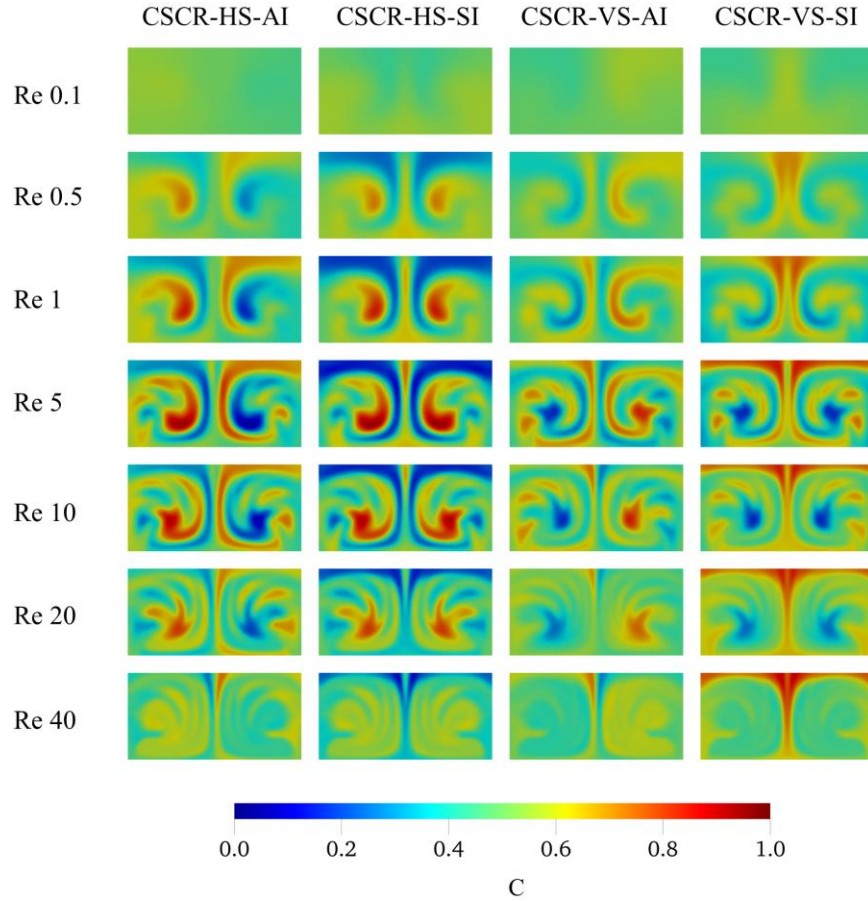


Figure 5.13 Concentration distributions at the outlet of the CSCR micromixer configurations examined ($D = D_1$).

The CSCR micromixer activates an effective, chaotic fluid flow with rising flowrates. Especially, in the flow cases where $Re = 20$ and 40 , fluid mixing is predominantly carried out based on strong deformation of fluid bodies. In other flow conditions, however, diffusive mixing affects the degree of mixing at different rates depending on the following factors: magnitude of molecular diffusion coefficient, fluid residence time, and the contact surface between fluids. The most challenging mixing conditions are observed in $Re = 1, 5$, and 10 scenarios when the molecular diffusion

constant is too small (i.e., $D = D_1$). Shortening residence time of fluids substantially inhibits the function of diffusivity whereas the contact surface is enlarged. Accordingly, fluids are largely mixed depending on the deformation rate of fluids in the rotations. Besides, in relatively very low flow conditions, i.e., $Re = 0.1$ and 0.5 , diffusive interaction is amplified due to high contact time over the contact surfaces of fluid bodies. Therefore, the mixing of fluids is primarily carried out by diffusive interaction.

In Figure 5.14a and Figure 5.14b, the CSCR and CT micromixers are compared in terms of mixing efficiency and mixing quality. Vertical split inlets and alternating injection modes are considered for both micromixer configurations. Accordingly, only the effect of semi-circular ridges, in convex position, is highlighted. Bar charts are obtained normalizing the outcomes of the CSCR-VS-AI by that of the CT-VS-AI. In addition, the development of mixing efficiencies along the mixing channels of the CSCR-VS-AI and CT-VS-AI micromixer configurations are shown in Figure 5.14c and Figure 5.14d, respectively ($D = D_2$). Notably, Figure 5.14a indicates that the CSCR design improved the degree of mixing is substantially over the CT micromixer. The maximum improvement is observed for the smallest molecular diffusion coefficient tested because fluid mixing is primarily carried out based on the chaotic action rather than molecular diffusion. In very low Re region, the ratios are found to be 1.23 and 2 for $Re = 0.1$ and 0.5 , respectively ($D = D_1$). Mixing efficiency is enhanced up to 7.3 times over the CT design under the toughest mixing conditions, i.e., $Re = 1-10$. In the most chaotic region, however, the CSCR micromixer provides around 8.7 times higher mixing values. The CSCR-VS-AI and CT-VS-AI micromixer configurations are also compared visually in Figure 5.15, which shows the

distribution of scalar concentration on the central x-y planes of all the flow scenarios simulated ($D = D_1$).

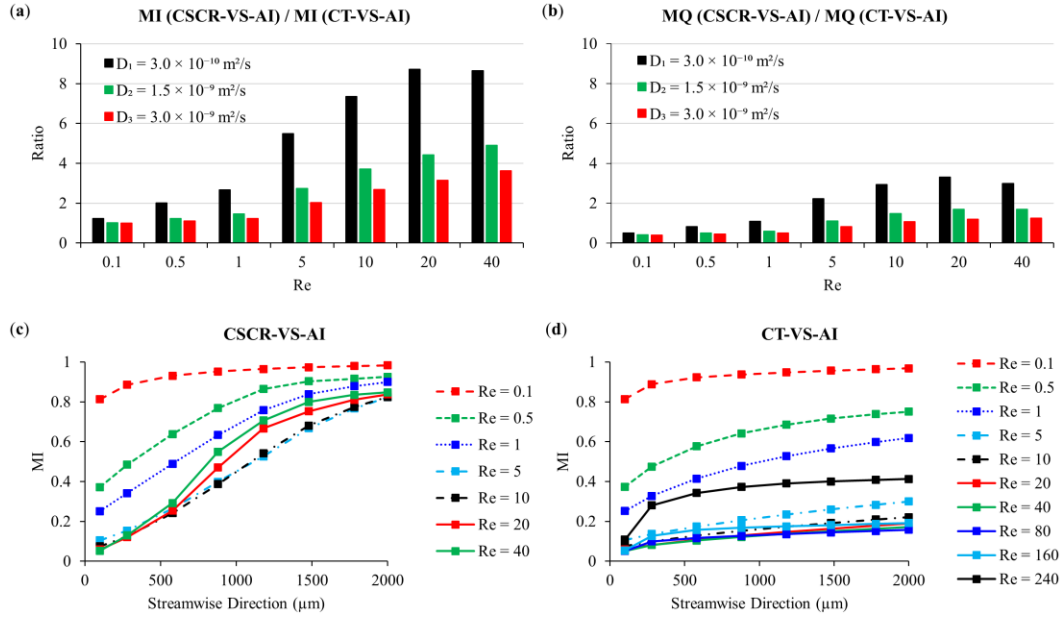


Figure 5.14 (a) and (b) the ratio of mixing index and mixing performance, respectively. Mixing values, obtained from CSCR-VS-AI micromixer, are normalized by that of CT-VS-AI; (c) and (d) the development of mixing index along the mixing channel for CSCR-VS-AI and CT-VS-AI configurations, respectively ($D = D_2$).

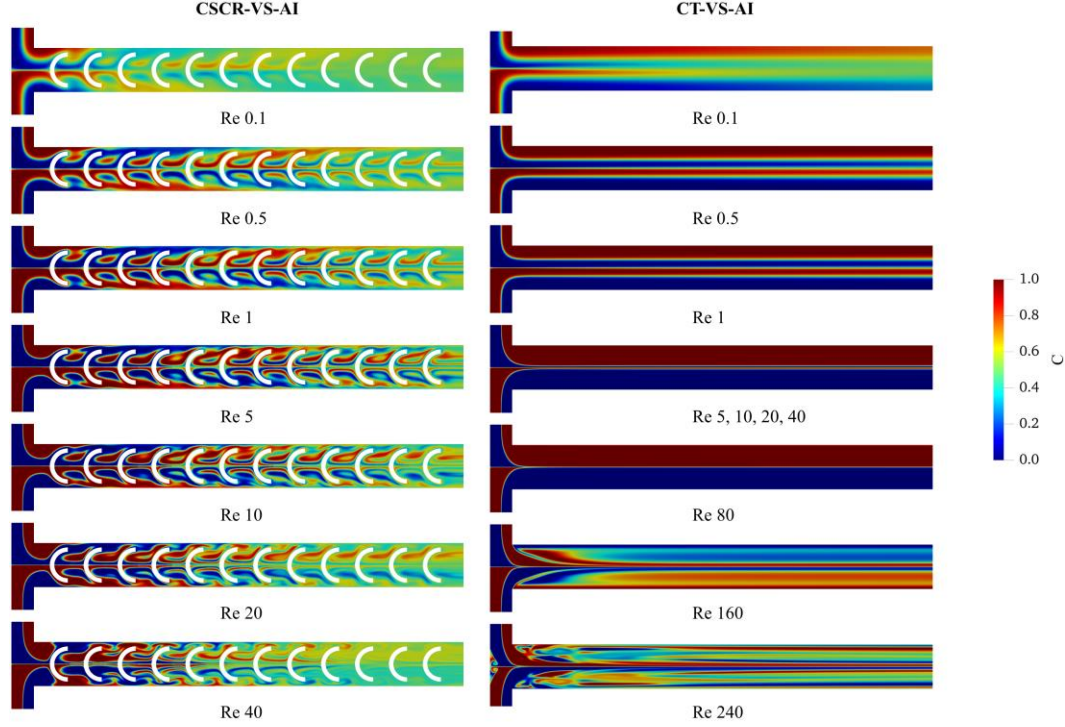


Figure 5.15 Scalar concentration distributions on the x-y plane at $z = 50 \mu\text{m}$ in CSCR-VS-AI (left) and CT-VS-AI (right) micromixer configurations for all the Re scenarios simulated ($D = D_1$). All planes are normal to the z-direction. In each plane, y-direction is shown between $y = +200 \mu\text{m}$ and $y = -200 \mu\text{m}$.

As illustrated in Figure 5.14b, when the pressure drops are considered, comparatively lower ratios are obtained in terms of the quality of mixing. The maximum ratio is observed as 3.3 at $\text{Re} = 20$. In the CSCR design, higher pressure drops are yielded as a result of mixing channel cross-section, confined by ridges. However, it should be noted that all the energy, spent in the CSCR micromixer, is utilized to form the helicoidal fluid motion. In contrast, CT micromixer results in lower pressure drops due to a smooth, segregated flow profile, developed in the unobstructed mixing channel.

As may be seen in Figure 5.14a and Figure 5.14b, the increase in mixing efficiency and mixing quality slows down with increasing diffusion magnitudes. Besides, the lowest ratios are observed in the very low flow conditions, i.e., $\text{Re} = 0.1, 0.5$, and 1. First and

foremost, the scarce contact time of fluids in the CSCR micromixer cause to yield lower ratios. Namely, fluid particles travel much faster in the CSCR micromixer due to the restriction of mixing channel cross-section. When Figure 5.6 and Figure 5.11 are evaluated together, it is evident that the trendlines, which belong to different diffusion constants, converge at $Re = 20$ and 160 in the CSCR-VS-AI and CT-VS-AI configurations, respectively, which indicates that while chaotic flow effects are dominant in the CSCR design, diffusive effects become more prominent in the CT micromixer. Therefore, while the CT design can respond to the increase of molecular diffusion constant by enhancing diffusive mixing, much lower fluid residence time in the CSCR micromixer limits the utilization of molecular diffusion. Second, the CSCR micromixer develop higher mixing efficiencies in a shorter distance as shown in Figure 5.14c and Figure 5.14d. Mixing length also decreases further when the magnitude of diffusion coefficient is increased. Correspondingly, the actual pressure drops lessen when the number of mixing elements is reduced. Therefore, the ratios will increase in cases that the design outcomes are compared before the exit of the micromixers.

5.4.4 *Alternative micromixer configurations*

In this chapter, alternative micromixer configurations are also examined as schematically shown in Figure 5.16. The same geometrical dimensions are preserved in A, B, C and D designs with that of the CSCR micromixer, i.e., L , W , H , H_r , D_r , t_r , and l_p . In the A, B, and C configurations, the different positioning effects of the semi-circular ridges are surveyed. In the design A, the mixing elements are positioned concavely on the bottom floor of the mixing channel. The same objects, however, are arranged as baffles with convex and concave orientations in the designs B and C, respectively. In both setups, odd-

and even-numbered ridges are located on the bottom and top floors of the mixing channel, respectively. Besides, the effect of rectangular ridges, which are aligned on the bottom floor of the mixing channel, is investigated in the design D. All configurations are tested in the two most chaotic flow region, i.e., $Re = 20$ and 40 , with vertical split inlets and alternating injection mode. Simulations are conducted for the smallest diffusion constant ($D = D_1$) by aiming to reveal the actual mixing characteristics based on the chaotic advection. The degree of mixing is quantified for each flow condition and presented along with outlet concentration distributions in Figure 5.16.

As given in Figure 5.16, the lowest mixing outcomes are obtained when rectangular ridges are employed in case D. Inlet streams predominantly flow around the central part of the mixing channel ($y = 0$) with slight fluctuations in the z -direction. Fluids, coming from the outer sub-inlets—red and blue colors at the center of the outlet cross-section—are partially diverted to the gaps at the first rectangular ridge. After this point, fluid flow is maintained above the gap area over several mixing elements. A slanting fluid motion is observed towards the center of the mixing channel ($y = 0$) around the sixth element, and it is kept until the exit. Therefore, a rather limited distortion occurred in fluid bodies. In the concave position of the semi-circular elements (i.e., case A), inlet streams are largely deflected to the center of the mixing channel ($y = 0$) due to inwards curvature of the ridges. As opposed to the convex orientation, fluid volumes are mostly raised at the center of the mixing elements. Later, two symmetrical, leaning flow patterns are followed towards the side channels of the mixing channel. In the meantime, fluids, in the gap regions, followed a path between consecutive ridges and merged with the mainstream, flowing at the center of the mixing channel ($y = 0$). Even though a rotational fluid behaviour is observed, the

alternation rates of fluid bodies are much lower than that of the CSCR micromixer. Meanwhile, baffle-type arrangements mixed the fluids without developing a periodic fluid flow in the mixing channel. Inlet streams are mixed intermittently by the mixing elements, located on the bottom and top floors. Fluid bodies are stretched and deflected depending on the position of the semi-circular elements. In convex and concave positions of the semi-circular ridges, fluid bodies are manipulated similarly by each mixing element as described in the CSCR and A configurations, respectively. In the baffle-type setups, however, leaning motions are created in the $+z$ and $-z$ directions by odd- and even-numbered mixing elements, respectively. Although a chaotic fluid flow is also created in the B and C configurations, distortion of fluids is considerably lower than that of the CSCR micromixer.

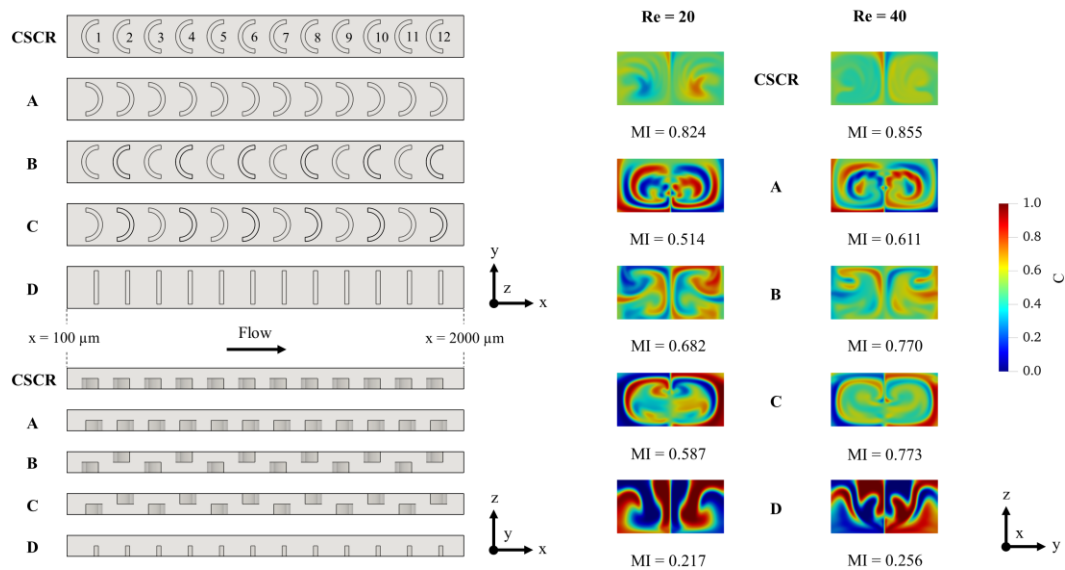


Figure 5.16 Alternative micromixer configurations with semi-circular (i.e., A, B, and C) and rectangular (i.e., D) ridges. Top and side views of the mixing channels (left). Outlet concentration distributions at $Re = 20$ and 40 for corresponding micromixer configurations (right).

5.4.5 Discussion

As shown in this chapter, the convex alignment of the semi-circular ridges yields a specific, helicoidal-shaped flow pattern. Compared to the alternative designing approaches, the highest deformation rate of fluid bodies is observed in the CSCR micromixer. The design dynamics develop an effective, chaotic flow state in a flow condition as low as $Re = 20$. In most cases simulated, well-mixed state of fluids with homogenous concentration distributions is reached in a distance less than $2000\ \mu m$. It should be emphasized that the CSCR passive micromixer design creates a helicoidal flow profile without depending on the inlet and injection types applied. For the same flow condition, different injection approaches only affect the mixing performance by changing the distribution of scalar concentration in the helicoidal flow profile. In this study, split inlets and different injection modes are only tested to show how to maximize the exploitation of chaotic fluid motion in the mixing channel. Therefore, as shown in Figure 5.17, the CSCR micromixer may be operated using several alternative injection strategies to improve the effective utilization of chaotic flow pattern in the mixing channel.

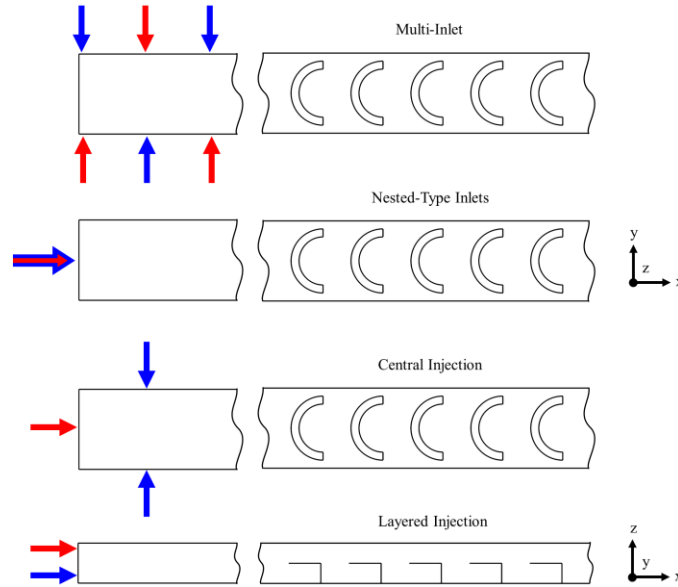


Figure 5.17 Alternative fluid injection types in the CSCR passive micromixer. Red and blue colors show different fluids.

To observe mixing effects of several design parameters in the CSCR micromixer, a parametric study was conducted on the CSCR-VS-AI micromixer configuration at $Re = 40$. Figure 5.18 shows parametric study outcomes in terms of mixing efficiency, pressure drop, and mixing quality. It should be noted that when the effect of a parameter was tested, all other parameter dimensions were kept constant as given in section 5.2. In all charts in Figure 5.18, central bars of each parameter correspond the actual dimensions that are used in the above CSCR micromixer configurations. According to the results, the height of the ridges (H_r) was found to be the most effective design parameter to control mixing efficiency and pressure drop in the CSCR micromixer. When ridge heights were reduced by a factor of $\frac{1}{2}$, the CSCR micromixer developed a relatively weak rotational fluid motion along the mixing channel which in turn caused nearly 57% mixing efficiency loss at the outlet. Besides, pressure drop value was dropped approximately 50% due to relaxed fluid flow in the mixing channel. When ridge heights increased by the same factor above, the

improvement of mixing efficiency was quite small (~8%) as opposed to a drastic pressure drop rise (~300%) in the CSCR micromixer. Therefore, the dimensions, given for semi-circular ridges in the CSCR micromixer design, are found to be almost optimum values to yield the maximum mixing efficiency with a reasonable pressure drop.

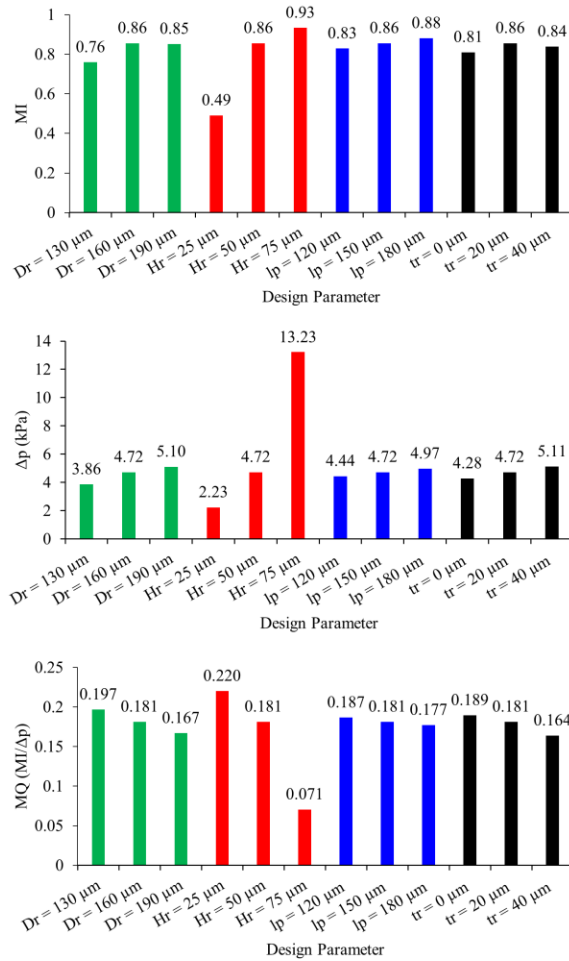


Figure 5.18 Parametric study outcomes for the CSCR-VS-AI micromixer configuration at $Re = 40$. Central values are the actual dimensions that are used in the CSCR micromixer design.

5.5 Conclusions

In this chapter, 3-D T-shaped passive micromixers were studied numerically and a novel micromixer design was proposed. Mixing characteristics were investigated under

several fluid flow and transport conditions. The effects of alternative inlet splitting, and injection strategies were examined. It was shown that the unobstructed classical-T micromixer develops chaotic fluid motion when Re number is greater than 40. However, the effect of complex flow patterns was rather limited to raise the degree of fluid mixing significantly. A mixing enhancement was observed in the engulfment flow type regardless of the inlet type, injection mode, and the magnitude of diffusion coefficient. Besides, inlet splitting helped to improve fluid mixing in vortex regimes, but the contribution of split inlets was more prominent in low Re number conditions.

The novel passive micromixer was designed employing semi-circular ridges. It was revealed that the alignment of ridges in convex position yields a specific, helicoidal-shaped fluid flow. The chaotic behaviour of fluids was observed in a Re range between 0.1 and 40. The intensity of rotations was boosted with growing flowrates. The maximum mixing results were obtained with vertical split inlets and alternating injection mode. In most cases simulated, more than 80% homogenous mixing efficiency was obtained. Well-mixed state of fluids was reached in a distance less than 2000 μm . Pressure drops were computed as 2.07 and 4.72 kPa in the two highest flow conditions, respectively, i.e., $\text{Re} = 20$ and 40. In comparison with the classical-T micromixer, the novel design increased mixing efficiency and mixing quality by the factors of 8.7 and 3.3, respectively.

Furthermore, alternative micromixer configurations were assessed. It was found that the use of rectangular ridges resulted in several times lower mixing index than the CSCR micromixer. In addition, although the concave positioning and baffle-type arrangements enhanced mixing efficiency, the deformation rate of fluid bodies was lower than that of the CSCR micromixer. It was also found that the dimensions, employed in the CSCR design,

are ideal to yield at least 80% mixing efficiency values with acceptable pressure drops. Consequently, the CSCR passive micromixer was proposed for microfluidic systems where a rapid and thorough fluid mixing is needed over a relatively short distance.

CHAPTER 6. NOVEL 3-D FLUID OVERLAPPING PASSIVE MICROMIXER DESIGN

6.1 Introduction

As discussed in Chapter 2 and Chapter 5, numerous alternative micromixer geometries have been designed to improve fluid mixing over short distances. The outcomes evidently show that mixing performance can be boosted in virtue of complex flow patterns, which are mostly generated at relatively high Re numbers (e.g., $Re > 10-20$). However, at low flow velocities (e.g., $Re < 5-10$) substantial mixing performance loss is seen as a result of small contact surfaces generated between fluids. This is mainly caused by layered flow conditions prevailing in the microchannels of these designs. For instance, in the previous chapter, an inflection point was observed at $Re = 5$ after which the effective utilization of advection was accelerated in the CSCR micromixer design. Although the CSCR micromixer geometry developed a complex flow profile even at very low flow conditions (e.g., $Re \leq 5$), and hence produced increased contact surface between fluids, short residence time of fluids reduced the diffusive activity across the interfacial area formed. Therefore, a diminishing mixing efficiency profile was observed between $Re = 0.1$ and 5. In several micromixer studies (Al-Halhouli et al., 2015; Bhagat et al., 2007; Fang et al., 2012; Ortega-Casanova and Lai, 2018), although some injection and design strategies are used to improve mixing at low Re numbers, overall micromixer length can still rise to the centimeter level to obtain an adequate mixing efficiency (e.g., 80%), which is not desired as noted earlier.

In this chapter, a novel 3-D fluid overlapping passive micromixer design is proposed to surpass the small interfacial area restrictions at low fluid flow velocity conditions. Unlike the conventional micromixer configurations, where the effective utilization of advection process is prioritized to improve contact surface, the novel design proposed enables the formation of a predefined interfacial area between fluid bodies in a compact geometry. Therefore, a rapid inter-diffusion between fluids is ensured, and mixing distance is decreased significantly.

6.2 Overlapping Micromixer Design

As shown in Figure 6.1, the circular-shaped fluid overlapping (CSFO) micromixer geometry consists of three main branches that are inlet channel, mixing units, and exit channel. The dimensions of the circular inlet and exit channels are equal with a length (l_i and l_e) and cross-section area (A_c) of $200\ \mu\text{m}$ and $2 \times 10^4\ \mu\text{m}^2$, respectively. In the CSFO design, five identical mixing units are used to observe the effect of fluid overlapping approach in a wide range of flow conditions. The height (h_u) and radius (r_u) of a single mixing unit are $60\ \mu\text{m}$ and $300\ \mu\text{m}$, respectively. Each mixing unit is divided equally in the z-direction with a solid, impermeable, and thin-plate disk element which is coaxial with the mixing unit and has a radius (r_d) of $270\ \mu\text{m}$. It is observed that the existence of physical joining parts between a disk element and mixing unit will affect the overlapping flow pattern trivially. Therefore, for the sake of designing convenience in the present study, these parts are excluded in the CSFO geometry. In physical applications of the CSFO design, the disk elements can be attached to mixing units from various points as indicated by the line arrows I, II, and III in Figure 6.1. Other than that, the mixing units are linked to each other via cylindrical extensions, in which height (h_c) is $10\ \mu\text{m}$ and radius (r_c) is equal

to that of inlet and outlet channels. However, it should be noted that the purpose of including these connection parts is only to assess mixing performance at the exit of mixing units. The contribution of these extensions to the actual mixing performance is negligible, and hence these additional parts can be omitted in a physical design. Meanwhile, the physical dimensions of the 3-D CSFO micromixer is consistent with that of used in the literature (Al-Halhouli et al., 2015; Lin et al., 2005; Ortega-Casanova and Lai, 2018) and multi-layer fabrication methods (X. Chen, 2018; M. Zhang et al., 2010) can be utilized in physical construction of the design proposed. Example micromixer studies may be seen in References (Gray et al., 1999; Lin et al., 2005; Yang et al., 2013) for detailed fabrication process of 3-D geometries at microscales.

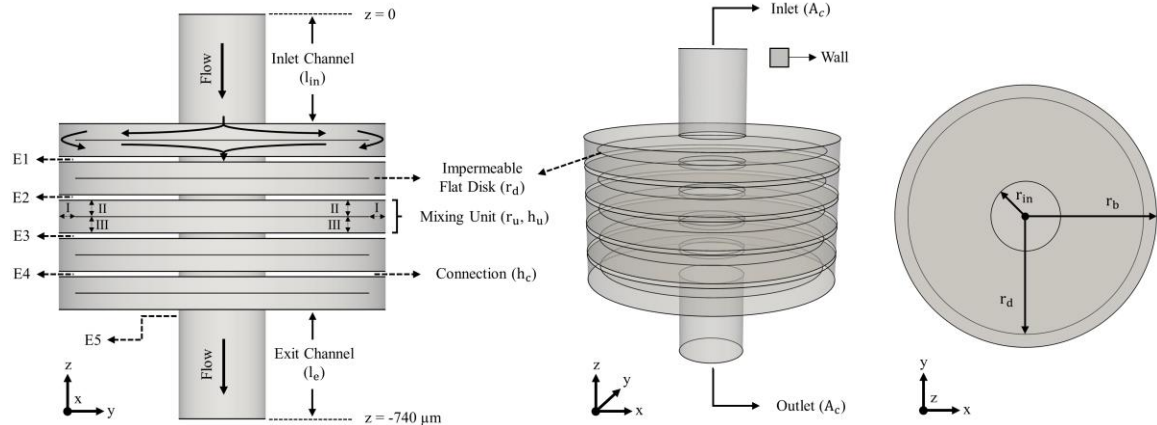


Figure 6.1 3-D CSFO micromixer geometry.

In the CSFO micromixer, nested-type inlets are used to create overlapping flow profile throughout the disk surfaces in mixing units. The core and outer segments of inlet surfaces are utilized to inject fluids as depicted in Figure 6.2. Note that these segments have an equal surface area in all injection types applied, and these surfaces are further split equally in injection B. The development of different injection patterns in both circular and

rectangular geometries can be seen from Figure 6.3 and Figure 6.4. In this research, both symmetrical and alternating injection patterns (see Figure 6.2 and Figure 6.4) are applied over the inlet boundary.

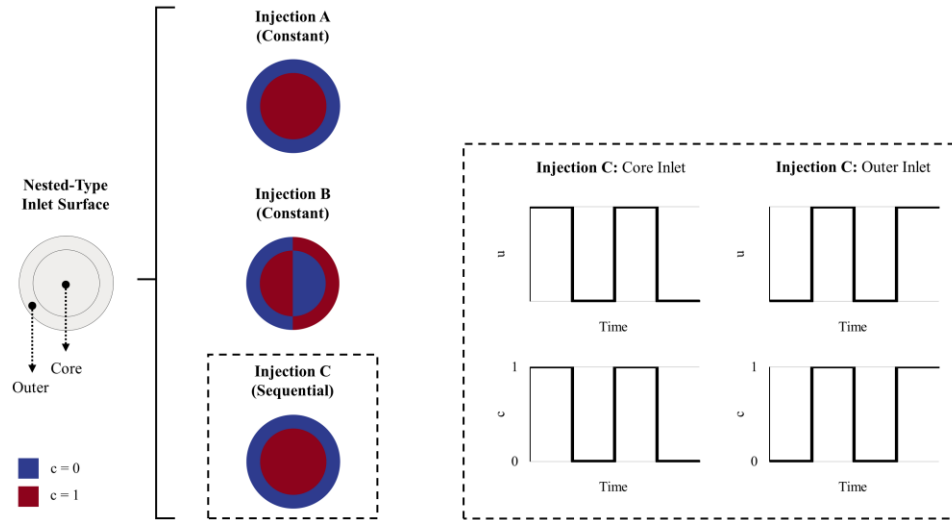


Figure 6.2 Injection types tested in the CSFO micromixer design.

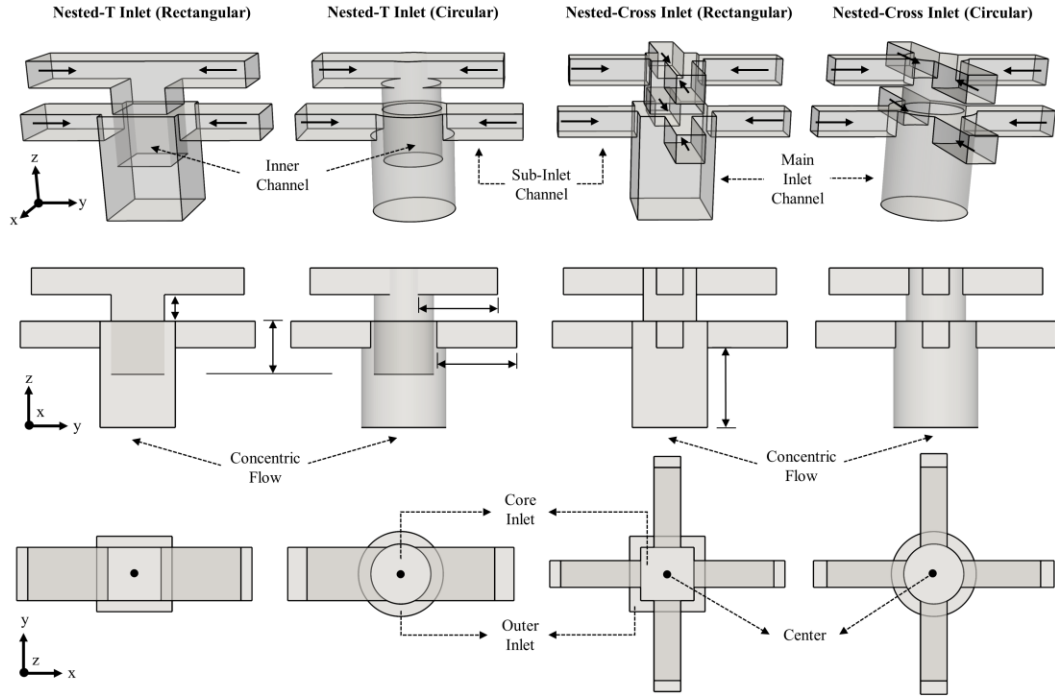


Figure 6.3 Circular and rectangular nested-type inlet structures.

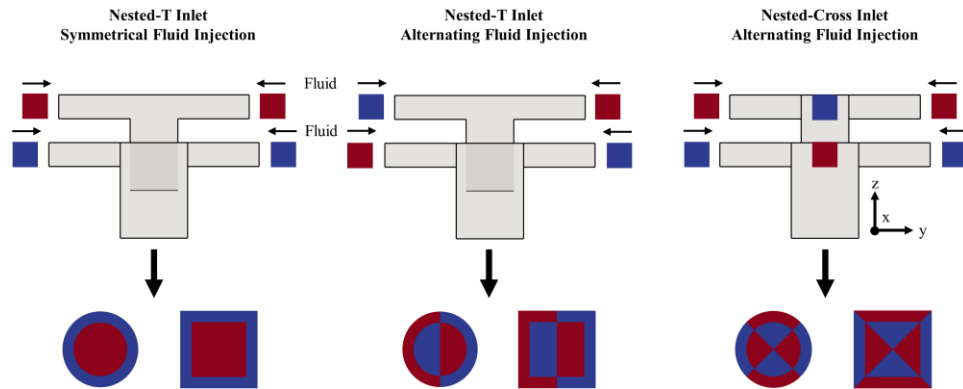


Figure 6.4 Alternative injection scenarios and distribution of fluids in microchannels.

6.3 Case Setup

Micromixer performance is examined extensively establishing several molecular diffusion constants in a broad range of flow conditions. Reynolds numbers with

corresponding inlet velocities, molecular diffusion constants, and Schmidt numbers that are tested as tabulated in Table 6.1. It should be noted that D_1 , D_2 , and D_3 molecular diffusion cases also correspond Sc_1 , Sc_2 , and Sc_3 scenarios, respectively. To maintain consistency throughout the present chapter, scalar transport simulations are evaluated with respect to different molecular diffusion constants instead of Schmidt numbers. In all mixing scenarios, equal amount of fluid is injected from each inlet segment in injection A, B, and C. To investigate fluid mixing in the micromixer, relative scalar concentrations, 0 and 1, are imposed on the inlet surface as described schematically in Figure 6.2. In injection A and B cases, fluid injection is kept constant over time, and therefore steady-state mixing domain is examined to evaluate the mixing performance of the CSFO micromixer. In injection C, fluids are injected over the core and outer inlet regions as a square wave with the same injection frequency (f). Thus, the time-dependent evolution of fluid mixing is observed in the micromixer. Note that, in transient numerical simulations, overall simulation times were chosen long enough—for a given flow condition, at least three times of the theoretical fluid mean residence time in the micromixer—to observe the complete development of fluid mixing in the micromixer. In the rest of this chapter, CSFO–A, –B and –C notations are used to describe the CSFO micromixer configurations with fluid injection modes A, B and C, respectively.

Table 6.1 Fluid flow and passive scalar transport test scenarios.

Fluid Flow		Passive Scalar Transport	
Reynolds Number	Inlet Velocity (m/s)	Molecular Diffusion Coefficient (m ² /s)	Schmidt Number
0.1	6.27×10^{-4}		
0.5	3.13×10^{-3}	$D_1 = 3.0 \times 10^{-10}$	$Sc_1 = 1/3 \times 10^4$
1	6.27×10^{-3}	$D_2 = 1.5 \times 10^{-9}$	$Sc_2 = 2/3 \times 10^3$
5	3.13×10^{-2}	$D_3 = 3.0 \times 10^{-9}$	$Sc_3 = 1/3 \times 10^3$
10	6.27×10^{-2}		

6.4 Results and Discussion

6.4.1 Grid study

In this chapter, hexahedron elements are used to discretize the computational domain in numerical simulations of the CSFO micromixer. A systematic grid study is performed by determining four different grid levels in the computational domain of the CSFO micromixer. The size of the mesh elements and total element numbers in L1, L2, L3, and L4 mesh levels are given in Table 6.2. Numerical simulations are carried out for the highest Pe number scenario examined in the CFSO–B micromixer configuration (i.e., $Pe = 3.33 \times 10^4$ when $Re = 10$ and $D = D_1 = 3.0 \times 10^{-10} \text{ m}^2/\text{s}$). To quantify the discrepancy between each mesh level and the finest mesh level, pressure drop (Δp) and outlet mixing index (MI) parameters are employed. Grid study outcomes are presented in Figure 6.5a, b, and c.

Table 6.2 Mesh properties used in the grid study.

Mesh Level	Grid Size, Δx (μm)	Total Elements
L1	3.2 - 2.2	3.90×10^6
L2	3.6 - 2.8	2.45×10^6
L3	4.2 - 3.2	1.58×10^6
L4	4.6 - 4.0	1.05×10^6

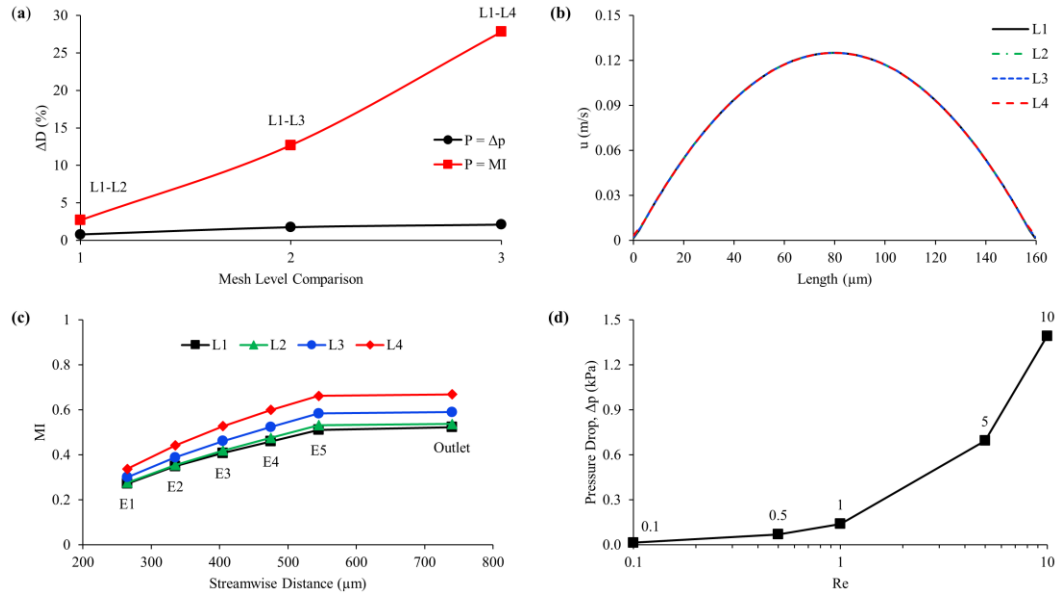


Figure 6.5 Grid study outcomes and the change of pressure drop in the CSFO micromixer: (a) difference, as a percentage, between L1 and L2, L3, L4 mesh densities with respect to Δp and MI parameters; (b) velocity distribution on the diameter of outlet cross-section obtained from L1, L2, L3, and L4 mesh level solutions; (c) development of mixing efficiency along the CSFO micromixer in L1, L2, L3, and L4 mesh solutions. MI values are computed on E1, E2, E3, E4, and E5 cross-sections which are normal to the z-direction; (d) Δp vs. Re number in the CSFO micromixer.

Figure 6.5a shows that there is a good agreement between the finest and coarser mesh levels, when the pressure drop is used to quantify the relative numerical errors in numerical solutions. The maximum variation is calculated as 2.1% between L1 and L4 meshes which evidently indicates that even the coarsest grid level, L4, can provide quite accurate results in fluid flow simulations. The same agreement between different mesh

level solutions is also seen in Figure 6.5b, which shows the distribution of velocity along the diameter of outlet plane. On the contrary, when outlet mixing efficiency is employed in error analysis, numerical solutions exhibit a high divergence as indicated by the rising trendline in Figure 6.5a. In fact, such a discrepancy between the two trendlines occurs due to quite different transport conditions in fluid flow and scalar transport simulations. While a mild Re number ($Re = 10$) in the former offers a better control of numerical errors even in relatively coarse grids, the latter is carried out at a very high Pe number ($Pe = 3.33 \times 10^4$), and hence much smaller mesh elements are required to approximate sharp scalar gradients accurately. Therefore, mesh study outcomes need to be evaluated in reference to scalar transport simulations to employ a suitable mesh density in the simulations. For the MI parameter given in Figure 6.5a, the differences in L1–L4, L1–L3, and L1–L2 comparisons are measured to be nearly 28, 13, and 2.7%, respectively. The lessening percentages indicate that false diffusion generation is suppressed noticeably with increasing mesh densities. The convergent trend of mesh refinement can also be seen in Figure 6.5c, which shows the development mixing efficiency along the CSFO micromixer for all mesh levels tested. Considering the small variation, i.e., 2.7%, against a large mesh density difference, i.e., 1.45×10^6 elements, between L1–L2 mesh levels, L2 mesh level is determined to conduct numerical simulations of the CSFO micromixer. Furthermore, this selection is also validated by estimating an effective diffusivity coefficient from the scalar transport solution of L2 mesh level. The ratio of effective diffusivity coefficient to molecular diffusion constant (D_E/D_M) is found to be 1.112 which is quite close to 1. Meaning that the molecular diffusion constant simulated is mostly recovered from the numerical solution and the amount of numerical diffusion errors is trivial. Therefore, the

use of L2 mesh density provides mostly physical mixing outcomes even in the worst-case scenario. Note that, in other mixing scenarios established in this chapter, numerical solutions will generate much less numerical diffusion due to diminishing magnitude of Pe number in mild scalar transport conditions.

6.4.2 Fluid mixing in the CSFO–A and CSFO–B micromixer configurations

At small Re numbers, ineffective manipulation of fluid bodies cause yielding a small contact area between fluid bodies, which in turn limits mixing by diffusion. To overcome this problem and enlarge the interfacial area between mixing fluids, a typical approach is to create several laminations in microchannels (Gray et al., 1999). In this method, main flows are divided into numerous sub-streams or layers of fluid sections which are aligned in microchannels to be in serial or parallel flow regions. In laminating micromixers (Hardt and Schönfeld, 2003; Tofteberg et al., 2009), the overall contact surface is proportional to the number of different fluid segments generated in the micromixer. Although diffusive mixing is promoted over the interfacial area shared by the fluid segments, usually a complex channel network is required to align fluids in microchannels. In the CSFO micromixer design proposed, the enhancement of contact area is ensured without generating multiple flow sectors in the flow domain. Instead, entire fluid bodies are overlapped and stretched in compact mixing units. As can be seen from Figure 6.6, which shows the flow pathlines and 3–D flow domain in the CSFO micromixer, fluids that are injected from core and outer inlet segments flow concentrically through the inlet channel and are stretched over the disk surface. During the fluid flow in the CSFO micromixer, the injected fluids occupy different volumes of the flow domain. As the core flow (shown by red color in Figure 6.6) follows a path around disk elements at the central

region of the micromixer, the outer flow (shown by blue color in Figure 6.6) develops between the core flow and micromixer walls. Therefore, a quite large interfacial area is generated between the two fluid bodies due to the encapsulation of the core flow by the outer flow across the CSFO micromixer domain. The development of contact surface in both upper and lower compartments of a single mixing unit is shown schematically in Figure 6.7.

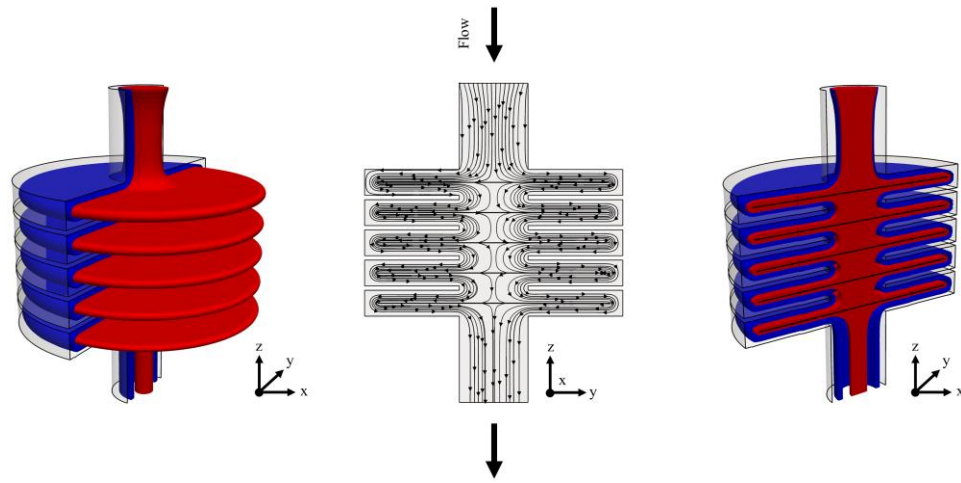


Figure 6.6 Flow pathlines on the yz-plane at the center of the CSFO micromixer (center) and 3-D flow domain in the CSFO micromixer (left and right). Red and blue colors show the fluids injected from core and outer inlets, respectively.

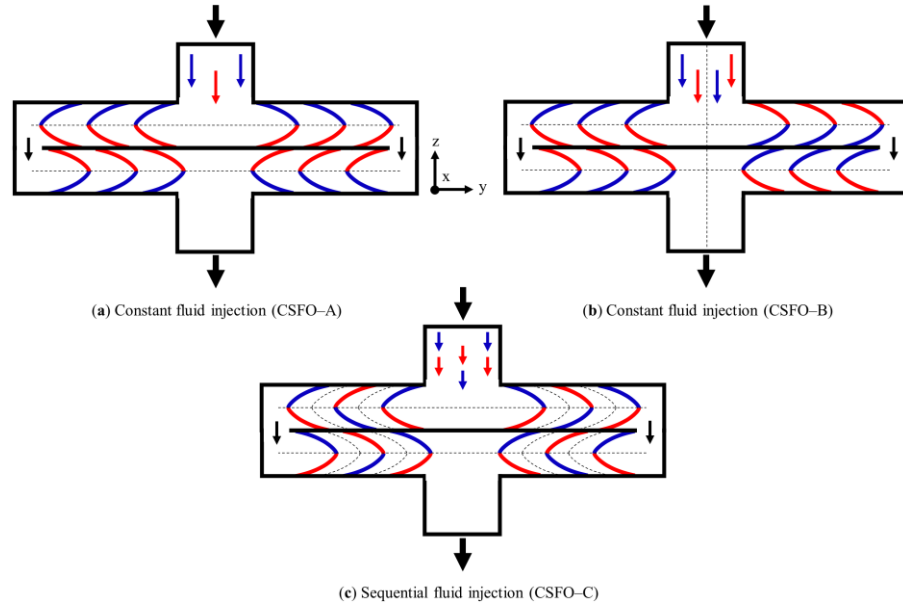


Figure 6.7 The distribution of injected fluids in the mixing units of the micromixer configurations (a) CSFO-A; (b) CSFO-B; and (c) CSFO-C. The dashed lines and curves show the contact surfaces formed between different fluids. Red and blue colors represent the fluids injected from core and outer inlets, respectively. Black arrows show flow directions.

In Figure 6.7 it is shown that the overlapping (or stratified) fluid pattern expands throughout the disk surface in the upper volume of mixing chamber and flows to the lower volume through the gap between the mixing chamber and the disk element. In the lower section, the above streams are converged at the exit of the cylindrical box and transferred to the next mixing unit. In all design configurations, the same flow cycle is repeated until the fluids are conveyed to the main exit channel of the micromixer. While both CSFO-A and CSFO-B configurations develop a contact surface on the horizontal plane, CSFO-B micromixer also forms an interface in the vertical direction due to alternating fluid injection imposed on the core and outer inlet segments. The horizontal and vertical contact areas formed between mixing fluids are represented by the dashed lines in Figure 6.7. Meanwhile, it should be noted that the total area of the gap region is approximately 2.7 times higher than that of exit cross-sections. Thus, the fluid flow is not restricted in the gap

region and the residence time of fluid particles in a single mixing unit is controlled by the area of the exit cross-section. In the present CSFO micromixer design, the surface area of inlet, outlet, and exit planes are kept equal as noted earlier.

When the mixing performance of micromixers are evaluated, the outcomes evidently show that diffusive mixing—in the vertical direction—is activated across the large interfacial areas formed. Figure 6.8 shows the development of fluid mixing along the CSFO–A and CSFO–B micromixers for all mixing conditions tested. Regarding the results shown in Figure 6.8, it can be said that the vertical contact surface formed in the CSFO–B micromixer affects the mixing performance trivially. The MI values of both configurations indicates that even the maximum difference is less than 5%. This is due to the fact that the degree of mixing is mainly controlled by the horizontal surface areas developed in the upper and lower sections of mixing boxes. The contribution of the additional interface to the diffusive mixing—in the horizontal direction—is more visible at low flow conditions, whereas this effect vanishes by lessening residence time of fluid particles at higher Re numbers. In the lowest flow velocity condition ($Re = 0.1$), almost a complete fluid mixing ($MI > 94\%$) is observed at the exit of the first mixing unit. Moreover, although it is not reflected in the plots, the distribution of scalar concentration in simulation results showed that the biggest portion of the mixing takes place only in the upper section of the first mixing box. In all molecular diffusion scenarios, more than 90% mixing efficiency is yielded in a distance less than $260\ \mu\text{m}$ in the main streamwise direction. At $Re = 0.5$, while at least two mixing units are required to provide more than 90% mixing value when the smallest diffusion constant is used, this is not the case in higher diffusivity conditions. In D_2 and D_3 mixing scenarios, more than 94% mixing efficiency is obtained at the exit of the

first mixing unit of the CSFO–A micromixer. As can be pursued from the change of the trendlines in increasing Re numbers, reducing contact time between fluid bodies suppresses the inter–diffusion continually, and hence more mixing units are required to enhance the degree of mixing in the micromixer. Notably, the combination of low contact times with small diffusion coefficients develop the most challenging mixing conditions in the micromixer. At $Re = 1$, while D_2 and D_3 diffusivities can still be tolerated against the fluid residence time reduced, the utilization of the smallest diffusion constant becomes difficult. In that case, the mixing distance increases to $400\text{ }\mu\text{m}$ (E3) and $470\text{ }\mu\text{m}$ (E4) to obtain nearly 86% and 93% MI, respectively. In all mixing scenarios tested, the lowest mixing efficiencies are obtained for the two highest flow conditions of the D_1 case as expected. The MI values at the exit of the micromixers are found to be nearly 65% and 54% for $Re = 5$ and 10, respectively. As mentioned previously, although the contact surface area is increased substantially in CSFO geometry, the development of mixing by diffusion is prohibited by rising flowrates. Nonetheless, the MI values are still promising for the higher molecular diffusion constants, D_2 and D_3 , as shown in Figure 5. At $Re = 5$, while D_2 scenario provides more than 86% mixing efficiency at the exit of the third mixing unit (E3), only two units are required to reach a MI value of nearly 91% (E2) in D_3 case. For the same diffusivity scenarios, D_2 and D_3 , the highest flow condition, $Re = 10$, yields 84% and 92% fluid mixing at E5 and E4 exits, respectively. For all mixing conditions examined, the distribution of scalar concentrations on the outlets of CSFO–A and CSFO–B micromixers are presented in Figure 6.9. In addition, for the smallest diffusion constant, D_1 , the development fluid mixing on different cross-sections along the CSFO–A configuration can be seen from Figure 6.10.

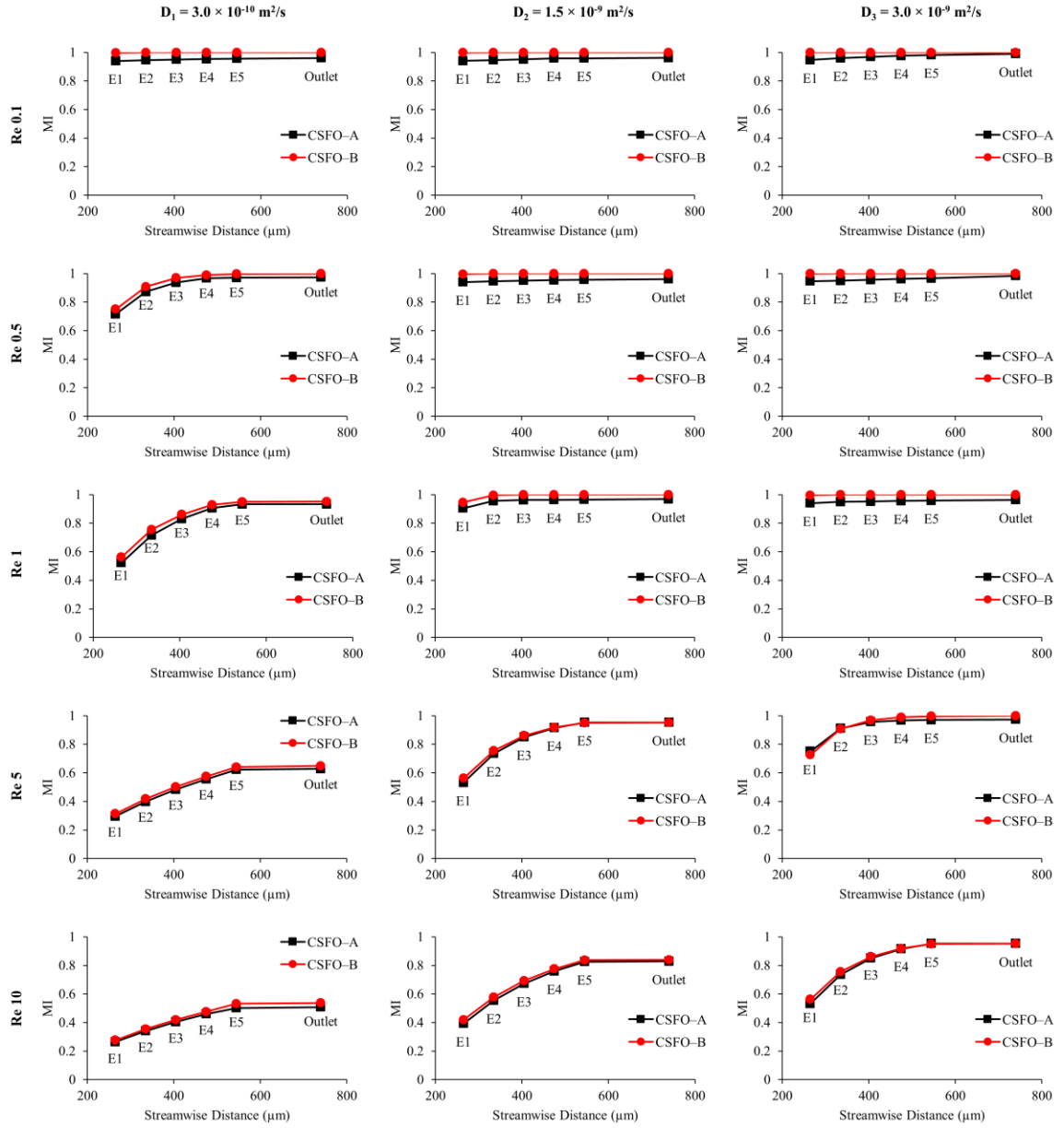


Figure 6.8 The development of MI along the CSFO-A and CSFO-B micromixer configurations for all flow conditions (i.e., $Re = 0.1, 0.5, 1, 5$, and 10) and molecular diffusion constants (D_1, D_2 , and D_3). MI values are calculated on the E1, E2, E3, E4, and E5 cross-sections which are normal to the z -direction.

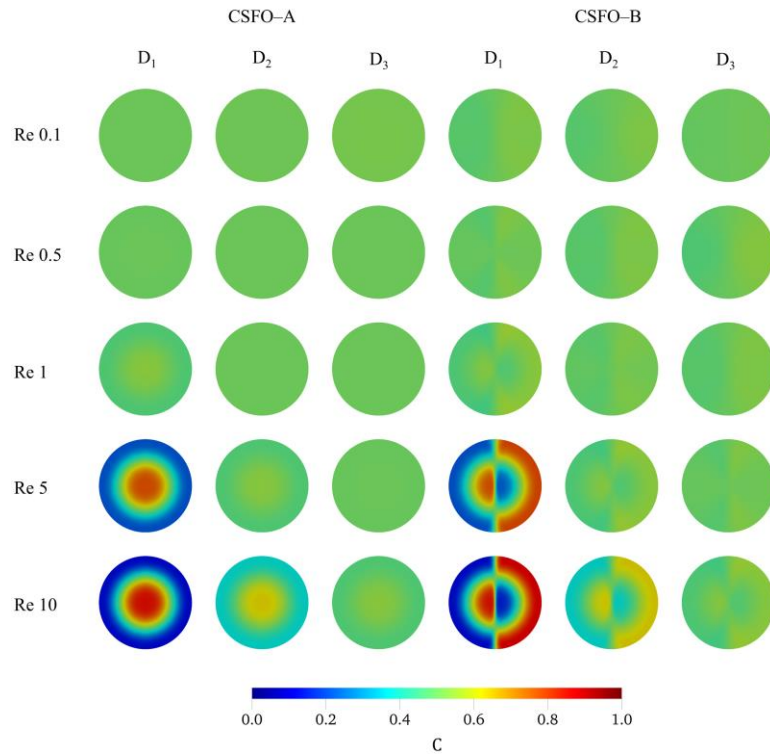


Figure 6.9 The distribution of scalar concentrations on the outlets of CSFO–A (first three columns on the left) and CSFO–B (last three columns on the right) micromixer configurations.

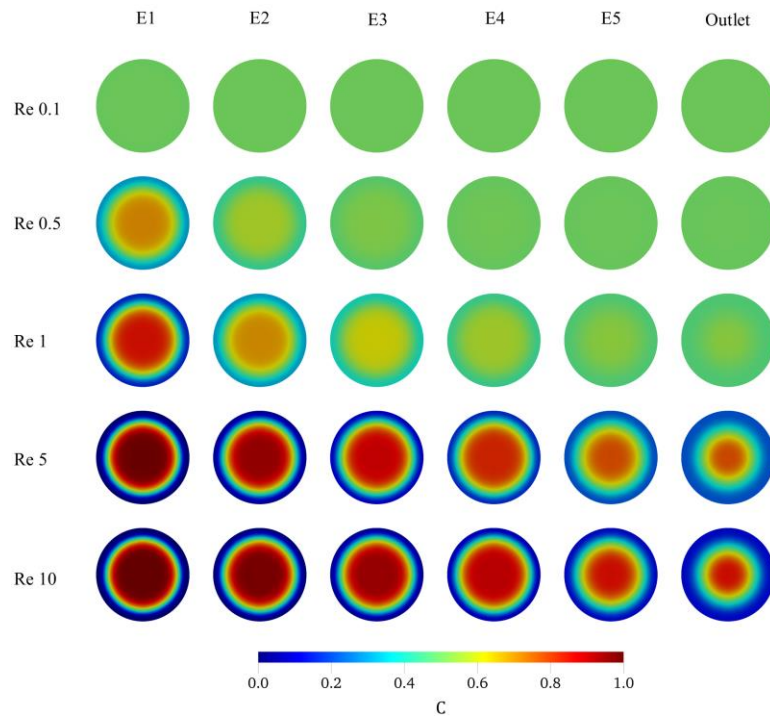


Figure 6.10 The development of fluid mixing along the CSFO–A micromixer configuration for all flow scenarios of D_1 diffusion constant. Planes show the distribution of scalar concentration. E1, E2, E3, E4, and E5 show exit cross-sections which are normal to the z-direction.

6.4.3 Fluid mixing in the CSFO–C micromixer configuration

As discussed above, when the CSFO micromixer is operated with constant fluid injection, large contact surfaces are developed between fluid bodies in the horizontal directions. However, in the CSFO design, the overall interfacial area can be enhanced further if the fluids are injected sequentially over the core and outer inlet segments as described in Figure 6.2. Sequential or pulse injection of fluids can be achieved by manipulating micropumps as described and used in References (C. Cortes-Quiroz et al., 2014; Fujii et al., 2003; Glasgow et al., 2004; Nguyen and Huang, 2005). In the case of sequential injection in CSFO–C configuration, the development of additional contact areas between consecutive fluid pairs is enabled as shown schematically in Figure 6.7c (see the dashed curves). In mixing units, these new interfaces move dynamically by expanding and shrinking in the upper and lower mixing sections, respectively, which creates a wave pattern throughout the disk surfaces. Therefore, in each half volume of the mixing units, diffusive mixing is also promoted in the horizontal directions. Meanwhile, it is worth noting that unlike the CSFO–A and CSFO–B configurations, where entire fluid bodies are overlapped on the horizontal plane, in the CSFO–C micromixer, different fluid segments develop the overlapped fluid structure due to wave pattern in the horizontal direction. The mixing performance of the CSFO–C configuration is investigated in various injection frequencies—between 10 and 250 Hertz (Hz) depending on the flow condition—for the most challenging mixing scenarios (i.e., $D = D_1$ and $Re = 1, 5$, and 10). Note that 1 Hz

defines one cycle per second. The evolution of mixing efficiencies is observed with respect to time at the exit of each mixing unit. The results are plotted in Figure 6.11. It should be mentioned that in Figure 6.11, $f = 0$ Hz plots show time-dependent numerical solutions of CSFO–A micromixer, in which fluid injection is constant over time as described in Figure 6.2. These solutions are utilized to compare the relative effects of constant and sequential fluid injections in the CSFO design.

Figure 6.11 evidently shows that the formation of additional contact surface areas accelerated diffusive mixing substantially. At $Re = 1$, even the lowest injection frequency, $f = 10$ Hz, is adequate to reduce the mixing distance ($MI > 90\%$) to the exit of the second mixing unit (E2). However, further increase of the injection frequency contributes to the overall mixing efficiency slightly. When the mixing outcomes are compared with that of CSFO–A micromixer, CSFO–C configuration ($f = 10$ Hz) provides a rapid fluid mixing over a very short distance. To reach a MI value around 85%, the time and distance required are “240 millisecond (ms) and $330\ \mu\text{m}$ ” and “640 ms and $400\ \mu\text{m}$ ” in CSFO–C and CSFO–A configurations, respectively. Therefore, the use of sequential injection reduces mixing time and distance by the factors of 2.7 and 1.2, respectively. Much higher improvements in mixing values are seen in $Re = 5$ and 10 flow conditions as indicated by the rising trendlines in Figure 6.11. Meanwhile, it needs to be explained that before reaching their steady values, the mixing efficiencies follow a declining and rising trend after a sharp increase at early stages. The spikes in the trendlines are observed at the exit of each mixing unit in both CSFO–A and CSFO–C micromixer configurations. These peak points essentially occur due to the following reason explained. At the beginning of the fluid flow in the inlet channel, the formation parabolic flow profile yields a relatively high contact

area and diffusive mixing starts developing on this surface. During the fluid flow, the diffusive mixing on the parabolic front travels in the micromixer and leaves the micromixer in the end. Therefore, the peak mixing efficiency, which is generated at the very early stage, is observed at the exit of the mixing units. After the peak values of MI, the declining and rising trends show the actual development of mixing efficiency in the micromixers.

At $Re = 5$, as constant fluid injection ($f = 0$ Hz) can only offer a MI value around 63% ($t = 280$ ms) at E5 location, more than 85% MI ($t = 120$ ms) is obtained at the exit of the second mixing unit (E2) by the use of sequential fluid injection in the CSFO geometry ($f = 25$ Hz). For higher injection frequencies, $f = 50$ and 100 Hz, the degree of mixing rises to 95% ($t = 160$ ms) and 98% ($t = 180$ ms) levels at the same location (E2), respectively. Unlike the $Re = 1$ flow condition, the effect of injection frequency is more visible at $Re = 5$. While $f = 25$ Hz case provides nearly 65% ($t = 140$ ms) mixing efficiency at the exit of the first mixing box (E1), the MI values reach 81% ($t = 120$ ms) and 90% ($t = 100$ ms) levels in $f = 50$ and 100 Hz scenarios, respectively. In the highest flow scenario, $Re = 10$, while nearly 53% MI ($t = 140$ ms) can be measured at the last exit location (E5) of the CSFO–A micromixer, CSFO–C configuration provides more than 61% MI ($t = 70$ ms) at the exit of the first mixing unit (E1) for the lowest injection frequency tested ($f = 50$ Hz). When the injection frequency is set to $f = 100$ and 250 Hz, the MI value reaches 77% ($t = 80$ ms) and 88% ($t = 100$ ms) on the same exit location (E1), respectively. As the best-case scenarios at $Re = 5$ ($f = 25$ Hz) and $Re = 10$ ($f = 50$ Hz), CSFO–C configuration develops approximately 85% ($t = 120$ ms) and 83% ($t = 70$ ms) mixing efficiencies in a distance less than 330 and 400 μm , respectively. When these mixing figures are compared with the outputs of the CSFO–A configuration, mixing conditions are improved significantly in

terms of efficiency, distance, and time. Notably, such an improvement could be achieved by means of the extra contact areas formed between consecutive fluid segments during the sequential injection.

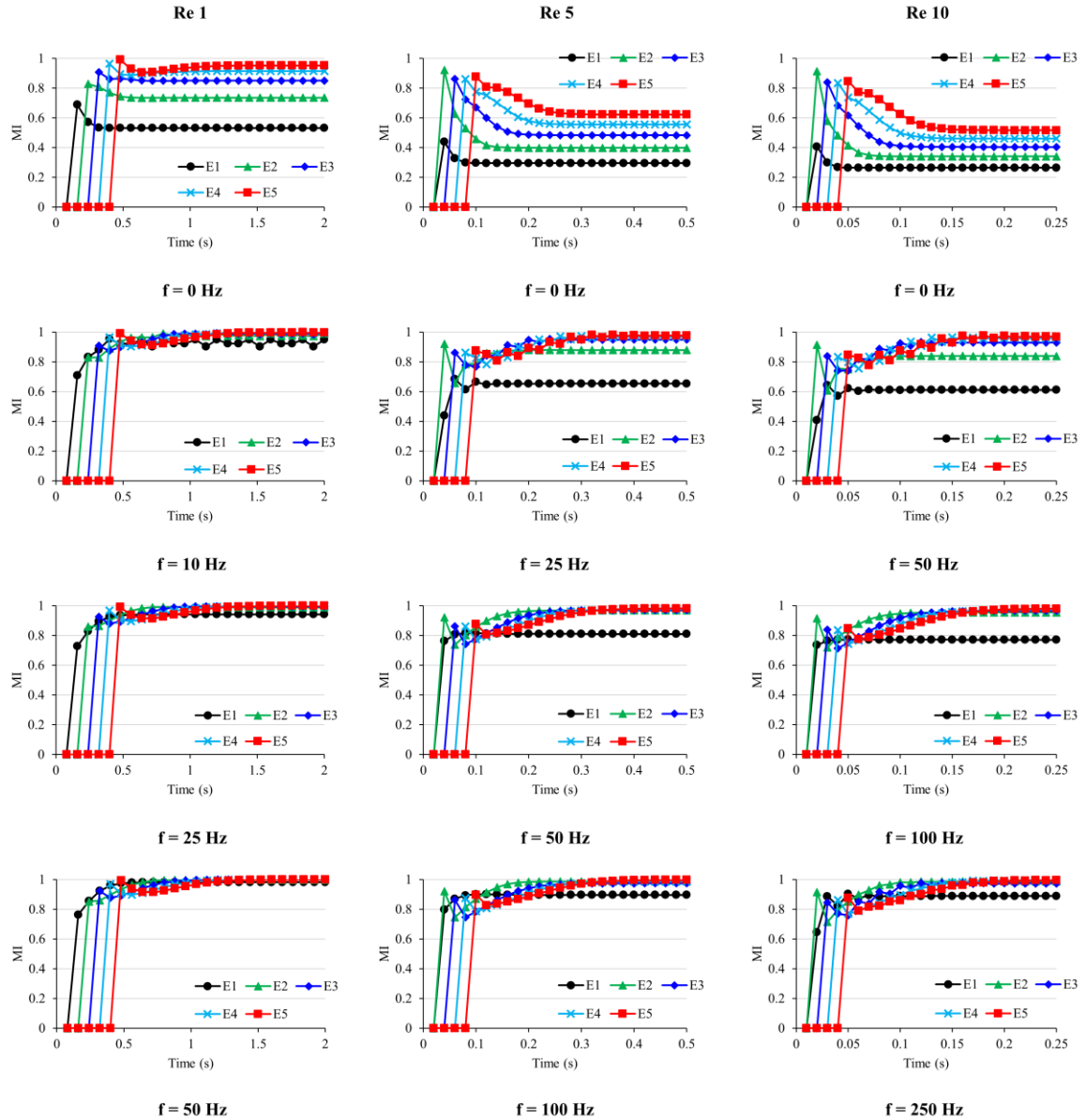


Figure 6.11 The development of fluid mixing with respect to time at the exit of mixing units in the CSFO–C micromixer configuration when $Re = 1, 5$, and 10 and $D = D_1$. $f = 0$ Hz plots (first row) show time-dependent solutions of CSFO–A micromixer. MI

values are calculated on the E1, E2, E3, E4, and E5 cross-sections which are normal to the z-direction.

6.4.4 Discussion

The CSFO micromixer and nested-type inlets developed in this research offer a novel design approach to mix fluids at microscale. Unlike the conventional micromixer designs, where the enhancement of interfacial area strongly depends on the effective manipulation of fluid flow in microchannels, the CSFO geometry inherently develops a large contact area without requiring a complex flow formation in the micromixer domain. Therefore, better operating conditions are yielded. As can be seen from Figure 6.5d, the CSFO design improves fluid mixing under reasonable pressure drop conditions. Even the highest flow condition, $Re = 10$, yields a pressure drop value of less than 1.4 kPa, which is quite acceptable compared to that of reported in the literature (Alam and Kim, 2013; Chung and Shih, 2007). The pressure values in Figure 6.5d can be decreased further if the number of mixing units are reduced in the design. When the mixing performance of the CSFO micromixer is compared with other studies in the literature, a substantial amount of mixing efficiency is achieved over a very short distance as presented in Table 6.3.

Table 6.3 The comparison of the CSFO–A configuration with the micromixers reported in the literature in terms of mixing performance in very low flow conditions ($Re < 10$).

Micromixer	Re	Mixing Efficiency (%)	Mixing Length (μm)	Reference[*]
Crossing Channels	0.1	88	6400	[1]
Multi–Inlet	0.1–0.29	90–80	5000	[2]
Serpentine	0.2	100	7500	[3]
Baffled	0.29	52	7200	[4]
T–Shaped ($f = 20$ Hz)	0.3	86.5	500	[5]
T–Shaped (split inlet)	0.5	42	2000	[6]
Vortex	0.5	50	1000	[7]
Rhombic	1	55	6000	[8]
Obstructed Channels	1	55	1180	[9]
	0.1	94	260	
CSFO–A (D_1)	0.5	94	400	[10]
	1	91	470	

^{*}[1] (Alam and Kim, 2013), [2] (Ortega-Casanova and Lai, 2018), [3] (Hossain et al., 2017), [4] (Fang et al., 2012), [5] (Glasgow and Aubry, 2005), [6] (Okuducu and Aral, 2019), [7] (Lin et al., 2005), [8] (Chung and Shih, 2007), [9] (Sadegh Cheri et al., 2013), [10] Present Study.

It should also be mentioned that the use of nested-type inlets is not only limited to the CSFO micromixer, but also can be used in any type of active or passive micromixer designs. Concentric flows that are developed in nested-type inlets basically provide two main advantages. First, when the fluids are injected concentrically, the deformation of fluid bodies in the micromixer becomes relatively much easy compared to the conventional fluid injections in separate channels. For instance, in split–and–recombination (SAR) micromixers (Mubashshir Ahmad Ansari et al., 2010; Raza et al., 2018), several mixing units are required to increase the distribution of inlet streams in sub-channels. When, however, fluids are injected concentrically, the distribution ratio of different fluids in the sub-channels is increased, and hence the number of mixing units required can be reduced.

Second, the nested-type inlets inherently create a contact area between the two fluids being injected. Thus, fluid mixing is initiated at the beginning of the inlet channel before fluids reach to the micromixer. The test simulations, which we do not report here, showed that the use of concentric flows in circular or rectangular channels improves diffusive mixing significantly when $Re \leq 0.1$. Therefore, in extremely slow flow conditions, only a straight or curved channel with a nested-type inlet can be utilized as a micromixer.

The CSFO micromixer can also function without employing the nested-type inlets when the fluid injection is sequential. In such a case, the entire inlet surface is utilized to feed the micromixer with different fluids sequentially. However, in this condition, the interfacial area on the horizontal plane is not formed and the overall contact surface is developed by the wave pattern as described schematically in Figure 6.12. Besides this function, the CSFO geometry can be modified to be operated at much higher flow conditions by generating chaotic advection in the micromixer. For this purpose, the disk elements can be redesigned with alternative grooves or obstacles to create complex flow patterns in the mixing units.

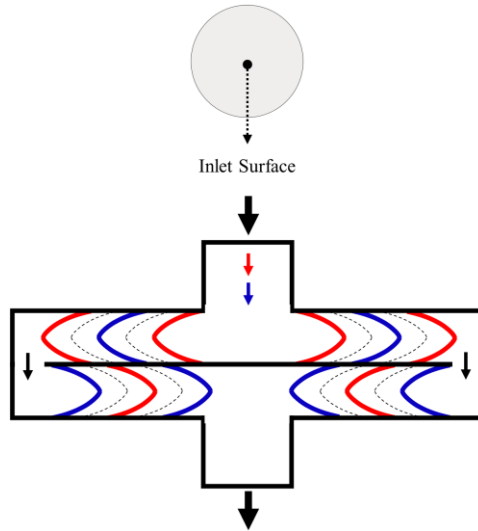


Figure 6.12 The distribution of fluids in a single mixing unit when the entire inlet surface is used to inject fluids sequentially.

In addition to the circular micromixer design, the fluid overlapping mixing approach can also be applied in rectangular or polygonal (e.g., pentagon, hexagon etc.) geometries. However, when a rectangular geometry is used, a non-uniform velocity distribution can develop on the rectangular plane that divides mixing box volume equally. As displayed in Figure 6.13, which shows the flow pathlines and the distribution of flow vectors in single-mixing-box circular and square designs ($Re = 10$), the two geometries render varying flow profiles. In contrast to smooth flow distribution in the circular design, the fluid flow is dominated at the center of the horizontal directions in the square geometry, which creates dead flow zones at the corner regions of the square box (see the dashed red lines). Although that variation in the flow structure does not affect the development of the fluid overlapping pattern in the mixing box, the diffusive interaction is diminished. That is due to the yield of a relatively a smaller contact area and increased flow velocity in central directions, which reduces contact time. Regarding the outcomes in Figure 6.13, the circular geometry appears to be an optimal shape for the fluid overlapping mixing approach.

Consequently, considering the plain design structure and high mixing performance, the CSFO passive micromixer can be integrated with microfluidic systems or used as a stand-alone device to mix fluids at microscales.

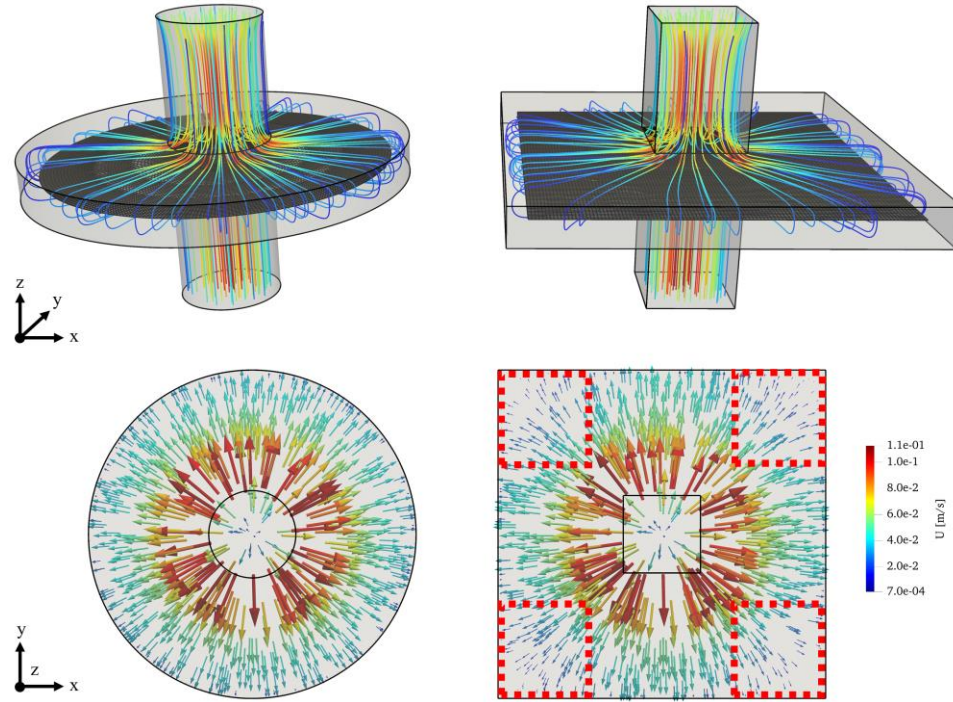


Figure 6.13 The distribution of flow vectors and flow pathlines in single-mixing-box circular and square design configurations ($Re = 10$).

6.5 Conclusions

In this chapter, fluid overlapping mixing approach and nested-type inlets were introduced for passive micromixers. A 3-D circular-shaped passive micromixer design was developed to enhance fluid mixing particularly at very low flow conditions that is $Re < 10$. The mixing performance of the CSFO micromixer was examined numerically in various fluid flow and molecular diffusion conditions. The effects of alternative design configurations and injection strategies were tested. Numerical simulation results indicate that the CSFO design creates a large contact surface between mixing fluids in the both

upper and lower volumes of each mixing unit. In the case of constant fluid injection, the overlapping fluid pattern develops an interfacial area throughout the disk elements on the horizontal plane. However, when the fluids are injected sequentially, additional contact areas are formed between consecutive fluids. While symmetrical and alternating fluid feeding types provide almost identical results in the constant injection scenarios, the mixing effect of injection frequency is increased with rising Re numbers in the sequential injection cases. In both injection conditions, high mixing efficiency values could be achieved with a reasonable pressure drop in the CSFO micromixer. The maximum pressure drop is found to be less than 1.4 kPa at $Re = 10$. For the smallest diffusion coefficient and constant fluid injection, more than 90% mixing efficiency is quantified in a distance of 260, 400, and 470 μm for $Re = 0.1$, 0.5, and 1 flow scenarios, respectively. The mixing distances are reduced further even in high flow conditions when fluids are injected sequentially. When the mixing outcomes are compared with that of reported in the literature, the CSFO design offers a high amount of fluid mixing over a very short distance. Therefore, the CSFO micromixer is proposed for next generation microfluidic systems, where short mixing distances will be required, to mix fluids at microscale.

CHAPTER 7. CONCLUSIONS AND FUTURE WORK

7.1 Conclusions

Passive micromixers are miniaturized mixing units that are employed in microscale flow systems to mix two or more fluids thoroughly by using flow energy in microchannels. In passive micromixers, ineffective manipulation of laminar flows and slow diffusing tendency of several biological or chemical substances cause the development of a tough mixing environment that is $Pe = 10^4$ – 10^6 . In this condition, mixing length increases significantly to obtain an adequate mixing efficiency, and hence a very long mixing channel is required which is not desirable due to the fact that increase in mixing length induces integration, high energy requirement, and long mixing time problems. In passive micromixers, enhancement of fluid mixing over a short distance is only possible by devising special geometries, in which fluid flow and molecular diffusion are exploited effectively. In addition to the difficulties in fluid mixing, numerical simulation of high Pe transport systems suffers from false diffusion errors which occur due to inaccurate approximation of sharp scalar gradients in the transport domain. In numerical solutions, these errors manifest themselves as molecular diffusion and increase fluid mixing unphysically. Therefore, in numerical passive micromixer studies, the complete characterization of false diffusion errors is critical to evaluate fluid mixing accurately and report reliable outcomes.

In the current literature, several passive micromixer designs are proposed to enhance fluid mixing and reduce mixing length. In most of these efforts, the improvement of mixing could be achieved as a trade-off between pressure-drop, mixing length, and design

complexity. In addition, in several numerical micromixer studies, although fluid mixing is investigated at very high Pe transport conditions, mixing efficiencies are reported without evaluating the contribution of false diffusion effects in numerical solutions. Regarding the above problems, in this thesis, we conducted an extensive research on the extent of false diffusion errors in microscale advection-dominant transport systems and developed two novel micromixer designs which improve fluid mixing without compromising the above parameters. The findings are of great importance for passive micromixer literature as highlighted below.

7.1.1 False diffusion errors in numerical passive micromixer studies

In FVM, numerical diffusion errors were examined in both unidirectional and complex flow systems. The outcomes showed that flow fields could be resolved quite similarly by all mesh levels in both flow types tested. This was due to very low numerical error production in mild Re numbers. In contrast, scalar transport simulations at very large Pe numbers produced considerably high numerical errors compared to the numerical solution of the flow field. Thus, since numerical solution of scalar transport domain is significantly affected by numerical diffusion errors, the use of flow parameters in grid studies should be avoided. Instead, mixing efficiency needs to be employed as the parameter to show the actual discrepancy between different grid levels and to determine a feasible grid size.

In unidirectional flow case, keeping the flow direction and grid boundaries aligned in the computational domain—by using hexahedron elements—produced a negligible amount of numerical diffusion in the solution of the AD equation. On the other hand, disoriented mesh

and flow direction—when tetrahedron and prism elements are used—caused significant amount numerical diffusion generation in the numerical solution of the concentration field at Re scenarios larger than 0.1. Therefore, numerical results showed that the false diffusion amount generated is mostly related to both transport condition and orthogonality between flow and grid lines. When prism and tetrahedral mesh structures are applied, the physical effect of the molecular diffusion constant tested was overshadowed by false diffusion errors that were generated during the numerical solution of AD equation. Regarding the outcomes, it is recommended that the use of prism and tetrahedron elements in scalar transport simulations should be limited strictly. In complex fluid flow conditions, even though computational domain is discretized with hexahedron elements, contribution of additional dimensions inherently prevented keeping a good mesh flow alignment in micromixers. Thus, the continuous violation of orthogonality in such flow regimes caused generating high amount of false diffusion in numerical solutions which in turn masked the physical effects of molecular diffusion and increased the performance of micromixer unphysically. It was also shown that numerical diffusion generation in complex flows depends on the magnitude of Pe_Δ and the flow pattern formed. When Pe_Δ number is larger than a certain value and grid–flow alignment is disturbed continuously, numerical schemes cannot resolve high scalar gradients accurately and produce unphysical numerical diffusion in the solution. Therefore, numerical simulations of complex flow systems need to be conducted carefully and the false diffusions generated should be quantified to avoid overestimating actual mixing efficiencies.

In FEM, the selection of an appropriate stabilization type, which is used to suppress the oscillations in the simulations, is crucial to control the false diffusion in numerical

solutions. It was shown that while the consistent stabilization method provides almost the same results with FVM for the resolution of both flow and transport domains, the inconsistent method, in which the physical diffusion constant is increased artificially, enhanced the mixing performance of the micromixer unphysically, and hence changed the physical problem examined. Therefore, when FEM is used in micromixer studies, the numerical stabilization technique should be chosen cautiously to avoid reporting unphysical mixing outcomes.

As shown in this dissertation, numerical diffusion errors can affect the solution significantly and change the physical problem examined. Therefore, quantification of numerical diffusion errors in numerical passive micromixer studies is crucial to report reliable and physical mixing outcomes.

7.1.2 The convex semi-circular-ridge (CSCR) passive micromixer design

In this thesis, a novel convex semi-circular-ridge passive micromixer was devised to improve fluid mixing and reduce mixing length. It was shown that when semi-circular ridges are aligned convexly on the bottom floor of the mixing channel, a specific, helicoidal fluid motion is generated along the mixing channel, which in turn enhances fluid mixing. The CSCR design helps to diminish inhomogeneity between fluid bodies by working in a two-way mixing mode depending on the flow condition in the micromixer. At low flow conditions, e.g., $Re < 5$, the CSCR micromixer ensures a rapid interdiffusion between fluid bodies by generating a high interfacial area. However, when flowrate is increased, e.g., $Re > 5$, the micromixer activates formation of chaotic advection and fluid mixing is enhanced with growing deformation rate of fluid bodies in helicoidal flow profiles. Simulation results

showed that the CSCR micromixer can mix the fluids homogenously and provide more than 80% mixing efficiency in a distance less than 2000 μm . The maximum pressure drop was found to be less than 5 kPa at $\text{Re} = 40$. When the outcomes are compared with that of the classical-T shaped passive micromixer, the novel design proposed increases mixing efficiency and mixing quality values by the factors of 8.7 and 3.3, respectively. It was also shown that different orientations of mixing elements in the mixing channel adversely affect the mixing performance by disturbing the formation of helicoidal-shaped flow profile. When the performance of the micromixer is compared with that of reported in the literature, the outcomes evidently indicates that CSCR micromixer improves fluid mixing substantially over a short distance and functions under very low pressure drop conditions. Consequently, we propose the CSCR design as a novel approach to create an effective chaotic advection at microscales and improve fluid mixing over a short distance.

7.1.3 The circular-shaped fluid overlapping (CSFO) passive micromixer design

In this thesis, a novel, 3-D circular-shaped passive micromixer design was developed to enhance fluid mixing particularly at very low flow conditions, where generation of chaotic fluid motion is difficult. It was shown that the CSFO design forms a quite large contact surface between fluid bodies and accelerates diffusive mixing in vertical and/or horizontal directions. While constant fluid injection can only create an interfacial area on the horizontal plane, sequential fluid injection forms additional contact surface between consecutive fluid pairs. The outcomes evidently showed that the CSFO micromixer design can be operated under low pressure drop conditions and reduce mixing distance significantly. In the highest flow condition investigated, the maximum pressure drop was found to be less than 1.4 kPa between the inlet and outlet of the CSFO micromixer. For

constant fluid injection case and the most difficult mixing conditions, almost complete mixing is observed in a mixing distance between 265 μm and 500 μm for $\text{Re} = 0.1, 0.5$ and 1 flow conditions, respectively. When higher molecular diffusion constants were tested, mixing distance could be reduced further to a level less than 265 μm . In the case of sequential fluid injection, a significant efficiency increase was observed due to the formation of extra contact surfaces in the mixing unit. For the lowest injection frequencies tested, at least 83% mixing performance was obtained in a distance less than 330 and 400 μm for $\text{Re} = 5$ and 10 flow conditions, respectively. The mixing times were found to be 120 ms and 70 ms for the same flow conditions, respectively. When the performance of the CSFO design is compared with the designs reported in the literature, the CSFO design offers a very high mixing efficiency over a very short distance. Therefore, the CSFO micromixer can be employed in microfluidic systems, where a rapid and efficient fluid mixing is needed in very low flow and diffusivity conditions. In addition, we propose the fluid overlapping method as a novel design approach in the passive micromixer literature.

7.2 Recommendations for Future Works

In this dissertation, although a comprehensive research was conducted on false diffusion errors in numerical solution of advection–dominant transport systems, the outcomes are valid only for non-reactive mixing systems. In terms of reactive transport modelling, false diffusion errors can significantly affect the accurate evaluation of reaction yields between reacting species. Therefore, characterization of false diffusion errors in these systems may become more important. In addition to that, the mixing performance of the CSCR and CSFO micromixer designs can also be investigated under reactive transport conditions. It should also be noted that the CSCR and CSFO micromixer designs can be

improved further in future studies. For instance, in the CSCR micromixer, the development helicoidal flow pair does not depend on the injection type and only controlled by the special alignment of semi-circular ridges. Therefore, the mixing performance of the CSCR design can be increased by feeding the helicoidal flows with alternative injection approaches as described in Chapter 5. As mentioned earlier, the CSFO micromixer design can also be used in much higher flow conditions by redesigning the disk elements to generate a chaotic flow in a mixing unit. In this case, the number of disk elements can be reduced. Lastly, for both micromixer designs, an optimization study can be conducted to find optimum design dimensions and operating conditions to maximize the fluid mixing performance.

APPENDIX A. PUBLISHED ARTICLES

Title: Performance Analysis and Numerical Evaluation of Mixing in 3-D T-Shape Passive Micromixers

Journal–Year: Micromachines (EISSN 2072-666X)–2018

DOI: <https://doi.org/10.3390/mi9050210>

Citations: 10



micromachines



Article

Performance Analysis and Numerical Evaluation of Mixing in 3-D T-Shape Passive Micromixers

Mahmut Burak Okuducu ¹ and Mustafa M. Aral ^{2,*}

¹ School of Civil and Environmental Engineering, Georgia Institute of Technology, Atlanta, GA 30332, USA; mbokuducu@gatech.edu

² Department of Civil Engineering, Bartin University, Bartin 74100, Turkey

* Correspondence: mustafaaral@bartin.edu.tr; Tel.: +90-738-223-5036

Received: 2 April 2018; Accepted: 25 April 2018; Published: 28 April 2018



Abstract: In micromixer devices, laminar characteristics of the flow domain and small diffusion constants of the fluid samples that are mixed characterize the mixing process. The advection dominant flow and transport processes that develop in these devices not only create significant challenges for numerical solution of the problem, but they are also the source of numerical errors which may lead to confusing performance evaluations that are reported in the literature. In this study, the finite volume method (FVM) and finite element method (FEM) are used to characterize these errors and critical issues in numerical performance evaluations are highlighted. In this study, we used numerical methods to evaluate the mixing characteristics of a typical T-shape passive micromixer for several flow and transport parameters using both FEM and FVM, although the numerical procedures described are also equally applicable to other geometric designs as well. The outcome of the study shows that the type of stabilization technique used in FEM is very important and should be documented and reported. Otherwise, erroneous mixing performance may be reported since the added artificial diffusion may significantly affect the mixing performance in the device. Similarly, when FVM methods are used, numerical diffusion errors may become important for certain unstructured discretization techniques that are used in the idealization of the solution domain. This point needs to be also analyzed and reported when FVM is used in performance evaluation of micromixer devices. The focus of this study is not on improving the mixing performance of micromixers. Instead, we highlight the bench scale characteristics of the solutions and the mixing evaluation procedures used when FVM and FEM are employed.

Keywords: micromixers; microfluidics; CFD; grid type; finite volume method; finite element method; numerical diffusion; artificial diffusion; false diffusion

Title: Computational Evaluation of Mixing Performance in 3-D Swirl-Generating Passive Micromixers

Journal–Year: Processes (EISSN 2227-9717)–2019


DOI: <https://doi.org/10.3390/pr7030121>

Citations: 3



Article

Computational Evaluation of Mixing Performance in 3-D Swirl-Generating Passive Micromixers

Mahmut Burak Okuducu ^{1,*}  and Mustafa M. Aral ²

¹ School of Civil and Environmental Engineering, Georgia Institute of Technology, Atlanta, GA 30332, USA

² Department of Civil Engineering, Bartın University, 74100 Bartın, Turkey; mustafaaral@bartin.edu.tr

* Correspondence: mbokuducu@gatech.edu; Tel.: +1-404-820-1588

Received: 31 January 2019; Accepted: 20 February 2019; Published: 27 February 2019



Abstract: Computational Fluid Dynamics (CFD) tools are used to investigate fluid flow and scalar mixing in micromixers where low molecular diffusivities yield advection dominant transport. In these applications, achieving a numerical solution is challenging. Numerical procedures used to overcome these difficulties may cause misevaluation of the mixing process. Evaluation of the mixing performance of these devices without appropriate analysis of the contribution of numerical diffusion yields over estimation of mixing performance. In this study, two- and four-inlet swirl-generating micromixers are examined for different mesh density, flow and molecular diffusivity scenarios. It is shown that mesh densities need to be high enough to reveal numerical diffusion errors in scalar transport simulations. Two-inlet micromixer design was found to produce higher numerical diffusion. In both micromixer configurations, when cell Peclet numbers were around 50 and 100 for Reynolds numbers 240 and 120, the numerical diffusion effects were tolerable. However, when large cell Peclet number scenarios were tested, it was found that the molecular diffusivity of the fluid is completely masked by false diffusion errors.

Keywords: micromixer; finite volume method; CFD; swirl; numerical diffusion; false diffusion

Title: Novel 3-D T-Shaped Passive Micromixer Design with Helicoidal Flows

Journal–Year: Processes (EISSN 2227-9717)–2019



DOI: <https://doi.org/10.3390/pr7090637>

Citations: 0



Article

Novel 3-D T-Shaped Passive Micromixer Design with Helicoidal Flows

Mahmut Burak Okuducu ^{1,*}  and Mustafa M. Aral ² 

¹ School of Civil and Environmental Engineering, Georgia Institute of Technology, Atlanta, GA 30332, USA

² Department of Civil Engineering, Bartın University, 74100 Bartın, Turkey; mustafaaral@bartin.edu.tr

* Correspondence: mbokuducu@gatech.edu; Tel.: +1-404-820-1588

Received: 4 September 2019; Accepted: 17 September 2019; Published: 19 September 2019



Abstract: Laminar fluid flow and advection-dominant transport produce ineffective mixing conditions in micromixers. In these systems, a desirable fluid mixing over a short distance may be achieved using special geometries in which complex flow paths are generated. In this paper, a novel design, utilizing semi-circular ridges, is proposed to improve mixing in micro channels. Fluid flow and scalar transport are investigated employing Computational Fluid Dynamics (CFD) tool. Mixing dynamics are investigated in detail for alternative designs, injection, and diffusivity conditions. Results indicate that the convex alignment of semi-circular elements yields a specific, helicoidal-shaped fluid flow along the mixing channel which in turn enhances fluid mixing. In all cases examined, homogenous concentration distributions with mixing index values over 80% are obtained. When it is compared to the classical T-shaped micromixer, the novel design increases mixing index and mixing performance values by the factors of 8.7 and 3.3, respectively. It is also shown that different orientations of ridges adversely affect the mixing efficiency by disturbing the formation of helicoidal-shaped flow profile.

Keywords: passive micromixer; microfluidics; CFD; engulfment flow; helicoidal flow; vortex flow; chaotic advection; T-micromixer

REFERENCES

- Abdollahi-Aghdam, A., Majidi, M. R., and Omid, Y. (2018). Microfluidic paper-based analytical devices (μ PADs) for fast and ultrasensitive sensing of biomarkers and monitoring of diseases. *BioImpacts : BI*, 8(4), 237-240.
- Afzal, A., and Kim, K.-Y. (2012). Passive split and recombination micromixer with convergent–divergent walls. *Chemical Engineering Journal*, 203, 182-192.
- Ahrens, J., Geveci, B., and Law, C. (2005). Paraview: An end-user tool for large data visualization. *The visualization handbook*, 717.
- Al-Halhouli, A. a., Alshare, A., Mohsen, M., Matar, M., Dietzel, A., and Büttgenbach, S. (2015). Passive Micromixers with Interlocking Semi-Circle and Omega-Shaped Modules: Experiments and Simulations. *Micromachines*, 6(7), 953-968.
- Alam, A., Afzal, A., and Kim, K.-Y. (2014). Mixing performance of a planar micromixer with circular obstructions in a curved microchannel. *Chemical Engineering Research and Design*, 92(3), 423-434.
- Alam, A., and Kim, K.-Y. (2012). Analysis of mixing in a curved microchannel with rectangular grooves. *Chemical Engineering Journal*, 181-182, 708-716.
- Alam, A., and Kim, K.-Y. (2013). Mixing performance of a planar micromixer with circular chambers and crossing constriction channels. *Sensors and Actuators B: Chemical*, 176, 639-652.
- Ali, M. E., Rahman, M. M., Dhahi, T. S., Kashif, M., Sarkar, M. S., Basirun, W. J., . . . Bhargava, S. K. (2016). Nanostructured Materials: Bioengineering Platforms for Sensing Nucleic Acids. In *Reference Module in Materials Science and Materials Engineering*: Elsevier.
- Ansari, M. A., and Kim, K.-Y. (2007). Shape optimization of a micromixer with staggered herringbone groove. *Chemical Engineering Science*, 62(23), 6687-6695.

- Ansari, M. A., and kim, K.-Y. (2009). Parametric study on mixing of two fluids in a three-dimensional serpentine microchannel. *Chemical Engineering Journal*, 146(3), 439-448.
- Ansari, M. A., Kim, K.-Y., Anwar, K., and Kim, S. M. (2010). A novel passive micromixer based on unbalanced splits and collisions of fluid streams. *Journal of Micromechanics and Microengineering*, 20(5), 055007.
- Ansari, M. A., Kim, K.-Y., Anwar, K., and Kim, S. M. (2012). Vortex micro T-mixer with non-aligned inputs. *Chemical Engineering Journal*, 181-182, 846-850.
- Ansari, M. A., Kim, K. Y., and Kim, S. M. (2018). Numerical and Experimental Study on Mixing Performances of Simple and Vortex Micro T-Mixers. *Micromachines (Basel)*, 9(5).
- Aubin, J., Ferrando, M., and Jiricny, V. (2010). Current methods for characterising mixing and flow in microchannels. *Chemical Engineering Science*, 65(6), 2065-2093.
- Bailey, R. T. (2017). Managing false diffusion during second-order upwind simulations of liquid micromixing. *International Journal for Numerical Methods in Fluids*, 83(12), 940-959.
- Bergman, T. L., Lavine, A. S., and Incropera, F. P. (2011). *Fundamentals of Heat and Mass Transfer, 7th Edition*: John Wiley & Sons, Incorporated.
- Bhagat, A. A. S., Peterson, E. T. K., and Papautsky, I. (2007). A passive planar micromixer with obstructions for mixing at low Reynolds numbers. *Journal of Micromechanics and Microengineering*, 17(5), 1017-1024.
- Bhopte, S., Sammakia, B., and Murray, B. (2008, 28-31 May 2008). *Geometric modifications to simple microchannel design for enhanced mixing*. Paper presented at the 2008 11th Intersociety Conference on Thermal and Thermomechanical Phenomena in Electronic Systems.
- Bhopte, S., Sammakia, B., and Murray, B. (2010, 2-5 June 2010). *Numerical study of a novel passive micromixer design*. Paper presented at the 2010 12th IEEE Intersociety Conference on Thermal and Thermomechanical Phenomena in Electronic Systems.

- Böhm, S., Greiner, K., Schlautmann, S., de Vries, S., and van den Berg, A. (2001, 2001//). *A Rapid Vortex Micromixer for Studying High-Speed Chemical Reactions*. Paper presented at the Micro Total Analysis Systems 2001, Dordrecht.
- Bothe, D., Stemich, C., and Warnecke, H.-J. (2006). Fluid mixing in a T-shaped micromixer. *Chemical Engineering Science*, 61(9), 2950-2958.
- Branebjerg, J., Gravesen, P., Krog, J. P., and Nielsen, C. R. (1996, 11-15 Feb. 1996). *Fast mixing by lamination*. Paper presented at the Proceedings of Ninth International Workshop on Micro Electromechanical Systems.
- Cai, G., Xue, L., Zhang, H., and Lin, J. (2017). A Review on Micromixers. *Micromachines*, 8(12), 274.
- Capretto, L., Cheng, W., Hill, M., and Zhang, X. (2011). Micromixing within microfluidic devices. *Top Curr Chem*, 304, 27-68.
- Carroll, G. T., Devereux, P. D., Ku, D. N., McGloughlin, T. M., and Walsh, M. T. (2010). Experimental validation of convection-diffusion discretisation scheme employed for computational modelling of biological mass transport. *Biomed Eng Online*, 9, 34.
- Castelain, C., Mokrani, A., Le Guer, Y., and Peerhossaini, H. (2001). «Experimental Study of Chaotic Advection Regime in a Twisted Duct Flow». *European Journal of Mechanics - B/Fluids*, 20, 205-232.
- Chen, J. J., and Chen, C. H. (2011). Investigation of Swirling Flows in Mixing Chambers. *Modelling and Simulation in Engineering*, 2011, 15.
- Chen, X. (2018). Fabrication and performance evaluation of two multi-layer passive micromixers. *Sensor Review*, 38(3), 321-325.
- Chung, C. K., and Shih, T. R. (2007). A rhombic micromixer with asymmetrical flow for enhancing mixing. *Journal of Micromechanics and Microengineering*, 17(12), 2495-2504.
- Clark, J., Kaufman, M., and Fodor, P. S. (2018). Mixing Enhancement in Serpentine Micromixers with a Non-Rectangular Cross-Section. *Micromachines*, 9(3), 107.

- Cortes-Quiroz, C., Azarbadegan, A., Johnston, I., and Tracey, M. (2014). *Analysis and design optimization of an integrated micropump-micromixer operated for bio-MEMS applications*.
- Cortes-Quiroz, C. A., Azarbadegan, A., and Zangeneh, M. (2014). Evaluation of flow characteristics that give higher mixing performance in the 3-D T-mixer versus the typical T-mixer. *Sensors and Actuators B: Chemical*, 202, 1209-1219.
- Demirel, E., and Aral, M. (2016). *Unified Analysis of Multi-Chamber Contact Tanks and Mixing Efficiency Evaluation Based on Vorticity Field. Part II: Transport Analysis* (Vol. 8).
- Fang, Y., Ye, Y., Shen, R., Zhu, P., Guo, R., Hu, Y., and Wu, L. (2012). Mixing enhancement by simple periodic geometric features in microchannels. *Chemical Engineering Journal*, 187, 306-310.
- Farra, R., Sheppard, N. F., McCabe, L., Neer, R. M., Anderson, J. M., Santini, J. T., . . . Langer, R. (2012). First-in-Human Testing of a Wirelessly Controlled Drug Delivery Microchip. *Science Translational Medicine*, 4(122), 122ra121.
- Freitas, C. J. (2002). The issue of numerical uncertainty. *Applied Mathematical Modelling*, 26(2), 237-248.
- Fu, L.-M., Wang, Y.-N., and Liu, C.-C. (2014). An integrated microfluidic chip for formaldehyde analysis in Chinese herbs. *Chemical Engineering Journal*, 244, 422-428.
- Fujii, T., Sando, Y., Higashino, K., and Fujii, Y. (2003). A plug and play microfluidic device. *Lab Chip*, 3(3), 193-197.
- G. Bessoth, F., J. deMello, A., and Manz, A. (1999). Microstructure for efficient continuous flow mixing. *Analytical Communications*, 36(6), 213-215.
- Gale, B. K., Jafek, A. R., Lambert, C. J., Goenner, B. L., Moghimifam, H., Nze, U. C., and Kamarapu, S. K. (2018). A Review of Current Methods in Microfluidic Device Fabrication and Future Commercialization Prospects. *Inventions*, 3(3), 60.

- Galletti, C., Roudgar, M., Brunazzi, E., and Mauri, R. (2012). Effect of inlet conditions on the engulfment pattern in a T-shaped micro-mixer. *Chemical Engineering Journal*, 185-186, 300-313.
- Gambhire, S., Patel, N., Gambhire, G., and Kale, S. (2016). A review on different micromixers and its micromixing within microchannel. *International Journal of Current Engineering and Technology*, 4, 409-413.
- Gervais, L., de Rooij, N., and Delamarche, E. (2011). Microfluidic Chips for Point-of-Care Immunodiagnostics. *Advanced Materials*, 23(24), H151-H176.
- Geuzaine, C., and Remacle, J. F. (2009). Gmsh: A 3-D finite element mesh generator with built-in pre- and post-processing facilities. *International Journal for Numerical Methods in Engineering*, 79(11), 1309-1331.
- Gidde, R. R., and Pawar, P. M. (2019). Flow feature and mixing performance analysis of RB-TSAR and EB-TSAR micromixers. *Microsystem Technologies*.
- Gidde, R. R., Pawar, P. M., Ronge, B. P., Misal, N. D., Kapurkar, R. B., and Parkhe, A. K. (2017). Evaluation of the mixing performance in a planar passive micromixer with circular and square mixing chambers. *Microsystem Technologies*.
- Glasgow, I., and Aubry, N. (2005). Dynamics of microfluidic mixing using time pulsing. *Discrete and Continuous Dynamical Systems*, 2005.
- Glasgow, I., Lieber, S., and Aubry, N. (2004). Parameters Influencing Pulsed Flow Mixing in Microchannels. *Analytical Chemistry*, 76(16), 4825-4832.
- Godunov, S. K., and Ryaben'kii, V. S. (1963). SPECTRAL STABILITY CRITERIA FOR BOUNDARY-VALUE PROBLEMS FOR NON-SELF-ADJOINT DIFFERENCE EQUATIONS. *Russian Mathematical Surveys*, 18(3), 1.
- Gray, B. L., Jaeggi, D., Mourlas, N. J., van Drieënhuizen, B. P., Williams, K. R., Maluf, N. I., and Kovacs, G. T. A. (1999). Novel interconnection technologies for integrated microfluidic systems1Paper presented as part of the SSAW-98 Workshop.1. *Sensors and Actuators A: Physical*, 77(1), 57-65.
- Gresho, P. M., and Lee, R. L. (1981). Don't suppress the wiggles—They're telling you something! *Computers & Fluids*, 9(2), 223-253.

- Hardt, S., and Schönfeld, F. (2003). Laminar mixing in different interdigital micromixers: II. Numerical simulations. *AIChE Journal*, 49(3), 578-584.
- Herold, K. E., and Rasooly, A. (2009). *Lab on a chip technology*. Norfolk, UK: Norfolk, UK : Caister Academic Press.
- Hossain, S., and Kim, K.-Y. (2010). Numerical Study on Mixing Performance of Straight Groove Micromixers. *International Journal of Fluid Machinery and Systems*, 3, 227-234.
- Hossain, S., and Kim, K.-Y. (2014). Mixing Analysis of Passive Micromixer with Unbalanced Three-Split Rhombic Sub-Channels. *Micromachines*, 5(4), 913-928.
- Hossain, S., and Kim, K.-Y. (2016). Parametric investigation on mixing in a micromixer with two-layer crossing channels. *SpringerPlus*, 5(1), 794.
- Hossain, S., Lee, I., Kim, S. M., and Kim, K.-Y. (2017). A micromixer with two-layer serpentine crossing channels having excellent mixing performance at low Reynolds numbers. *Chemical Engineering Journal*, 327, 268-277.
- Hu, J., Wang, S., Wang, L., Li, F., Pingguan-Murphy, B., Lu, T. J., and Xu, F. (2014). Advances in paper-based point-of-care diagnostics. *Biosensors and Bioelectronics*, 54, 585-597.
- Idelsohn, S. R., and Oñate, E. (1994). Finite volumes and finite elements: Two ‘good friends’. *International Journal for Numerical Methods in Engineering*, 37(19), 3323-3341.
- Izadpanah, E., Hekmat, M. H., Azimi, H., Hoseini, H., and Babaie Rabiee, M. (2018). Numerical simulation of mixing process in T-shaped and DT-shaped micromixers. *Chemical Engineering Communications*, 205(3), 363-371.
- Jain, M., Rao, A., and Nandakumar, K. (2013). Numerical study on shape optimization of groove micromixers. *Microfluidics and Nanofluidics*, 15(5), 689-699.
- Javaid, M., Cheema, T., and Park, C. (2018). Analysis of Passive Mixing in a Serpentine Microchannel with Sinusoidal Side Walls. *Micromachines*, 9(1), 8.

- Jian Chen, J., Ren Lai, Y., Tang Tsai, R., Der Lin, J., and Yang Wu, C. (2011). Crosswise ridge micromixers with split and recombination helical flows. *Chemical Engineering Science*, 66(10), 2164-2176.
- Kirby, B. J. (2010). *Micro- and Nanoscale Fluid Mechanics: Transport in Microfluidic Devices*.
- Kjeang, E., Djilali, N., and Sinton, D. (2009). Microfluidic fuel cells: A review. *Journal of Power Sources*, 186(2), 353-369.
- Kumar, V., Paraschivoiu, M., and Nigam, K. D. P. (2011). Single-phase fluid flow and mixing in microchannels. *Chemical Engineering Science*, 66(7), 1329-1373.
- Kuzmin, D. (2010). *A Guide to Numerical Methods for Transport Equations*.
- Le The, H., Le Thanh, H., Dong, T., Ta, B. Q., Tran-Minh, N., and Karlsen, F. (2015). An effective passive micromixer with shifted trapezoidal blades using wide Reynolds number range. *Chemical Engineering Research and Design*, 93, 1-11.
- Lee, C.-Y., and Fu, L.-M. (2018). Recent advances and applications of micromixers. *Sensors and Actuators B: Chemical*, 259, 677-702.
- Lee, C. Y., Chang, C. L., Wang, Y. N., and Fu, L. M. (2011). Microfluidic mixing: a review. *Int J Mol Sci*, 12(5), 3263-3287.
- Leonard, B. P. (1979). A stable and accurate convective modelling procedure based on quadratic upstream interpolation. *Computer Methods in Applied Mechanics and Engineering*, 19(1), 59-98.
- Li, J., Xia, G., and Li, Y. (2013). Numerical and experimental analyses of planar asymmetric split-and-recombine micromixer with dislocation sub-channels. *Journal of Chemical Technology & Biotechnology*, 88(9), 1757-1765.
- Li, T., and Chen, X. (2017). Numerical investigation of 3D novel chaotic micromixers with obstacles. *International Journal of Heat and Mass Transfer*, 115, 278-282.

- Lin, C.-H., Tsai, C.-H., and Fu, L.-M. (2005). A rapid three-dimensional vortex micromixer utilizing self-rotation effects under low Reynolds number conditions. *Journal of Micromechanics and Microengineering*, 15(5), 935-943.
- Lisak, G., Cui, J., and Bobacka, J. (2015). Paper-based microfluidic sampling for potentiometric determination of ions. *Sensors and Actuators B: Chemical*, 207, 933-939.
- Liu, K., Yang, Q., Chen, F., Zhao, Y., Meng, X., Shan, C., and Li, Y. (2015). Design and analysis of the cross-linked dual helical micromixer for rapid mixing at low Reynolds numbers. *Microfluidics and Nanofluidics*, 19(1), 169-180.
- Liu, M. (2011). Computational study of convective–diffusive mixing in a microchannel mixer. *Chemical Engineering Science*, 66(10), 2211-2223.
- Liu, Y., and Jiang, X. (2017). Why microfluidics? Merits and trends in chemical synthesis. *Lab on a Chip*, 17.
- Liu, Y. Z., Kim, B. J., and Sung, H. J. (2004). Two-fluid mixing in a microchannel. *International Journal of Heat and Fluid Flow*, 25(6), 986-995.
- Mansur, E. A., Ye, M., Wang, Y., and Dai, Y. (2008). A State-of-the-Art Review of Mixing in Microfluidic Mixers. *Chinese Journal of Chemical Engineering*, 16(4), 503-516.
- Matsunaga, T., and Nishino, K. (2013). Semi-Lagrangian Method for Numerical Analysis of Fluid Mixing in T-Shaped Micromixer. *JOURNAL OF CHEMICAL ENGINEERING OF JAPAN*, 46(10), 699-708.
- Matsunaga, T., Shibata, K., Murotani, K., and Koshizuka, S. (2015). Hybrid grid-particle method for fluid mixing simulation. *Computational Particle Mechanics*, 2(3), 233-246.
- Moukalled, F., Mangani, L., and Darwish, M. (2015). *The Finite Volume Method in Computational Fluid Dynamics: An Advanced Introduction with OpenFOAM and Matlab*: Springer Publishing Company, Incorporated.
- Neill, S. P., and Hashemi, M. R. (2018). Chapter 8 - Ocean Modelling for Resource Characterization. In S. P. Neill & M. R. Hashemi (Eds.), *Fundamentals of Ocean Renewable Energy* (pp. 193-235): Academic Press.

- Nguyen, N.-T. (2012a). Chapter 1 - Introduction. In N.-T. Nguyen (Ed.), *Micromixers (Second Edition)* (pp. 1-8). Oxford: William Andrew Publishing.
- Nguyen, N.-T. (2012b). Chapter 2 - Fundamentals of mass transport in the microscale. In N.-T. Nguyen (Ed.), *Micromixers (Second Edition)* (pp. 9-72). Oxford: William Andrew Publishing.
- Nguyen, N.-T. (2012c). Chapter 3 - Computational transport processes for micromixers*. In N.-T. Nguyen (Ed.), *Micromixers (Second Edition)* (pp. 73-112). Oxford: William Andrew Publishing.
- Nguyen, N.-T., and Huang, X. (2005). An analytical model for mixing based on time-interleaved sequential segmentation. *Microfluidics and Nanofluidics*, 1, 373-375.
- Nguyen, N.-T., and Huang, X. (2006). *Mixing in microchannels based on hydrodynamic focusing and time-interleaved segmentation: modeling and experiment* (Vol. 6036): SPIE.
- Nguyen, N.-T., and Wu, Z. (2005). Micromixers—a review. *Journal of Micromechanics and Microengineering*, 15(2), R1-R16.
- Nonino, C., Savino, S., and Del Giudice, S. (2009). Numerical Assessment of the Mixing Performance of Different Serpentine Microchannels. *Heat Transfer Engineering*, 30(1-2), 101-112.
- Okuducu, M. B., and Aral, M. M. (2018). Performance Analysis and Numerical Evaluation of Mixing in 3-D T-Shape Passive Micromixers. *Micromachines*, 9(5), 210.
- Okuducu, M. B., and Aral, M. M. (2019). Novel 3-D T-Shaped Passive Micromixer Design with Helicoidal Flows. *Processes*, 7(9), 637.
- Oñate, E., and Manzan, M. (2000). Stabilization techniques for finite element analysis of convection-diffusion problems. *Developments in Heat Transfer*, 7, 71-118.
- OpenFOAM. The OpenFOAM Foundation, OpenCFD Ltd. (Version v5). Bracknell, UK, 2015.

- Ortega-Casanova, J., and Lai, C. H. (2018). CFD study about the effect of using multiple inlets on the efficiency of a micromixer. Assessment of the optimal inlet configuration working as a microreactor. *Chemical Engineering and Processing - Process Intensification*, 125, 163-172.
- Ouro, P., Fraga, B., Viti, N., Angeloudis, A., Stoesser, T., and Gualtieri, C. (2018). Instantaneous transport of a passive scalar in a turbulent separated flow. *Environmental Fluid Mechanics*, 18(2), 487-513.
- Pandey, C. M., Augustine, S., Kumar, S., Kumar, S., Nara, S., Srivastava, S., and Malhotra, B. D. (2018). Microfluidics Based Point-of-Care Diagnostics. *Biotechnology Journal*, 13(1), 1700047.
- Park, J. M., Seo, K. D., and Kwon, T. H. (2009). A chaotic micromixer using obstruction-pairs. *Journal of Micromechanics and Microengineering*, 20(1), 015023.
- Patankar, S. V. (1980). *Numerical Heat Transfer and Fluid Flow*. New York, NY, USA: Hemisphere Publishing Corporation.
- Pérez-Mitta, G., Trautmann, C., Toimil-Molares, M. E., and Azzaroni, O. (2017). 3 - Single Ion Track-Etched Nanochannels for Analytical Applications. In M. Tagliazucchi & I. Szleifer (Eds.), *Chemically Modified Nanopores and Nanochannels* (pp. 61-83). Boston: William Andrew Publishing.
- Prescott, J. H., Lipka, S., Baldwin, S., Sheppard, N. F., Maloney, J. M., Coppeta, J., . . . Santini, J. T. (2006). Chronic, programmed polypeptide delivery from an implanted, multireservoir microchip device. *Nature Biotechnology*, 24(4), 437-438.
- Rasouli, M., Abouei Mehri, A., Goharimanesh, M., Lashkaripour, A., and Razavi Bazaz, S. (2018). Multi-criteria optimization of curved and baffle-embedded micromixers for bio-applications. *Chemical Engineering and Processing - Process Intensification*, 132, 175-186.
- Raza, W., Hossain, S., and Kim, K.-Y. (2018). Effective mixing in a short serpentine split-and-recombination micromixer. *Sensors and Actuators B: Chemical*, 258, 381-392.
- Reyes, D. R., Iossifidis, D., Auroux, P.-A., and Manz, A. (2002). Micro Total Analysis Systems. 1. Introduction, Theory, and Technology. *Analytical Chemistry*, 74(12), 2623-2636.

- Ritter, P., Osorio-Nesme, A., and Delgado, A. (2016). 3D numerical simulations of passive mixing in a microchannel with nozzle-diffuser-like obstacles. *International Journal of Heat and Mass Transfer*, 101, 1075-1085.
- Roudgar, M., Brunazzi, E., Galletti, C., and Mauri, R. (2012). Numerical Study of Split T-Micromixers. *Chemical Engineering & Technology*, 35(7), 1291-1299.
- S A Berger, L Talbot, a., and Yao, L. S. (1983). Flow in Curved Pipes. *Annual Review of Fluid Mechanics*, 15(1), 461-512.
- Sabotin, I., Tristo, G., Junkar, M., and Valentinčič, J. (2013). Two-step design protocol for patterned groove micromixers. *Chemical Engineering Research and Design*, 91(5), 778-788.
- Sackmann, E. K., Fulton, A. L., and Beebe, D. J. (2014). The present and future role of microfluidics in biomedical research. *Nature*, 507, 181.
- Sadegh Cheri, M., Latifi, H., Salehi Moghaddam, M., and Shahraki, H. (2013). Simulation and experimental investigation of planar micromixers with short-mixing-length. *Chemical Engineering Journal*, 234, 247-255.
- Shah, S. I. A., Kostiuk, L. W., and Kresta, S. M. (2012). The Effects of Mixing, Reaction Rates, and Stoichiometry on Yield for Mixing Sensitive Reactions—Part I: Model Development. *International Journal of Chemical Engineering*, 2012, 16.
- Sheu, T. S., Chen, S. J., and Chen, J. J. (2012). Mixing of a split and recombine micromixer with tapered curved microchannels. *Chemical Engineering Science*, 71, 321-332.
- Shih, T. R., and Chung, C. K. (2007). A high-efficiency planar micromixer with convection and diffusion mixing over a wide Reynolds number range. *Microfluidics and Nanofluidics*, 5(2), 175-183.
- Silva, J. P., dos Santos, A., and Semiao, V. (2017). Experimental characterization of pulsed Newtonian fluid flows inside T-shaped micromixers with variable inlets widths. *Experimental Thermal and Fluid Science*, 89, 249-258.
- Soleymani, A., Kolehmainen, E., and Turunen, I. (2008). Numerical and experimental investigations of liquid mixing in T-type micromixers. *Chemical Engineering Journal*, 135, S219-S228.

- St John, A., and Price, C. P. (2014). Existing and Emerging Technologies for Point-of-Care Testing. *The Clinical biochemist. Reviews*, 35(3), 155-167.
- Streets, A. M., and Huang, Y. (2013). Chip in a lab: Microfluidics for next generation life science research. *Biomicrofluidics*, 7(1), 011302.
- Suh, Y. K., and Kang, S. (2010). A Review on Mixing in Microfluidics. *Micromachines*, 1(3), 82-111.
- Sweby, P. K. (1984). High Resolution Schemes Using Flux Limiters for Hyperbolic Conservation Laws. *SIAM Journal on Numerical Analysis*, 21(5), 995-1011.
- Tofteberg, T., Skolimowski, M., Andreassen, E., and Geschke, O. (2009). A novel passive micromixer: lamination in a planar channel system. *Microfluidics and Nanofluidics*, 8(2), 209-215.
- Tran-Minh, N., Dong, T., and Karlsen, F. (2014). An efficient passive planar micromixer with ellipse-like micropillars for continuous mixing of human blood. *Comput Methods Programs Biomed*, 117(1), 20-29.
- Van Doormaal, J. P., and Raithby, G. D. (1984). ENHANCEMENTS OF THE SIMPLE METHOD FOR PREDICTING INCOMPRESSIBLE FLUID FLOWS. *Numerical Heat Transfer*, 7(2), 147-163.
- van Leer, B. (1979). Towards the ultimate conservative difference scheme. V. A second-order sequel to Godunov's method. *Journal of Computational Physics*, 32(1), 101-136.
- Vashist, S. K. (2017). Point-of-Care Diagnostics: Recent Advances and Trends. *Biosensors*, 7(4), 62.
- Vikhansky, A. (2004). Quantification of reactive mixing in laminar microflows. *Physics of Fluids*, 16(12), 4738-4741.
- Viktorov, V., and Nimafar, M. (2013). A novel generation of 3D SAR-based passive micromixer: efficient mixing and low pressure drop at a low Reynolds number. *Journal of Micromechanics and Microengineering*, 23(5), 055023.

- VIRK, M. S., and HOLDØ, A. E. (2016). Numerical analysis of fluid mixing in T-Type micro mixer. *2016*, 2(1).
- Waheed, S., Cabot, J. M., Macdonald, N. P., Lewis, T., Guijt, R. M., Paull, B., and Breadmore, M. C. (2016). 3D printed microfluidic devices: enablers and barriers. *Lab on a Chip*, 16(11), 1993-2013.
- Wang, C. T., Hu, Y. C., and Hu, T. Y. (2009). Biophysical micromixer. *Sensors (Basel)*, 9(7), 5379-5389.
- Wang, D., Ba, D., Liu, K., Hao, M., Gao, Y., Wu, Z., and Mei, Q. (2017). A Numerical Research of Herringbone Passive Mixer at Low Reynold Number Regime. *Micromachines*, 8(11), 325.
- Wang, L., Chen, W., Xu, D., Shim, B. S., Zhu, Y., Sun, F., . . . Kotov, N. A. (2009). Simple, rapid, sensitive, and versatile SWNT-paper sensor for environmental toxin detection competitive with ELISA. *Nano letters*, 9(12), 4147-4152.
- Wang, L., Liu, D., Wang, X., and Han, X. (2012). Mixing enhancement of novel passive microfluidic mixers with cylindrical grooves. *Chemical Engineering Science*, 81, 157-163.
- Wang, L., Yang, J.-T., and Lyu, P.-C. (2007). An overlapping crisscross micromixer. *Chemical Engineering Science*, 62(3), 711-720.
- Ward, K., and Fan, Z. H. (2015). Mixing in microfluidic devices and enhancement methods. *J Micromech Microeng*, 25(9).
- Warming, R. F., and Beam, R. M. (1976). Upwind Second-Order Difference Schemes and Applications in Aerodynamic Flows. *AIAA Journal*, 14(9), 1241-1249.
- Wong, S. H., Bryant, P., Ward, M., and Wharton, C. (2003). Investigation of mixing in a cross-shaped micromixer with static mixing elements for reaction kinetics studies. *Sensors and Actuators B: Chemical*, 95(1-3), 414-424.
- Wong, S. H., Ward, M. C. L., and Wharton, C. W. (2004). Micro T-mixer as a rapid mixing micromixer. *Sensors and Actuators B: Chemical*, 100(3), 359-379.

- Xia, H. M., Wan, S. Y. M., Shu, C., and Chew, Y. T. (2005). Chaotic micromixers using two-layer crossing channels to exhibit fast mixing at low Reynolds numbers. *Lab on a Chip*, 5(7), 748-755.
- Xu, Z., Li, C., Vadillo, D., Ruan, X., and Fu, X. (2011). Numerical simulation on fluid mixing by effects of geometry in staggered oriented ridges micromixers. *Sensors and Actuators B: Chemical*, 153(1), 284-292.
- Yang, J., Qi, L., Chen, Y., and Ma, H. (2013). Design and Fabrication of a Three Dimensional Spiral Micromixer. *Chinese Journal of Chemistry*, 31(2), 209-214.
- Zhang, J., and Luo, X. (2018). Mixing Performance of a 3D Micro T-Mixer with Swirl-Inducing Inlets and Rectangular Constriction. *Micromachines (Basel)*, 9(5).
- Zhang, M., wu, J., Wang, L., Xiao, K., and Wen, W. (2010). A simple method for fabricating multi-layer PDMS structures for 3D microfluidic chips. *Lab on a Chip*, 10, 1199-1203.